

**DEVELOPMENT AND VALIDATION OF THERMO-HYDRO-MECHANICAL
SIMULATOR MODEL FOR ENHANCED GEOTHERMAL SYSTEMS**

by
Dharmendra Kumar

Copyright © 2014
Dharmendra Kumar
All Right Reserved

A thesis submitted to the Faculty and the Board of Trustees of the Colorado School of Mines in partial fulfillment of the requirement of the degree of Doctor of Philosophy (Civil Engineering).

Golden, Colorado
Date: _____

Signed: _____
Dharmendra Kumar

Signed: _____
Dr. Marte Gutierrez
Thesis Advisor

Golden, Colorado
Date: _____

Signed: _____
Dr. John E. McCray
Professor and Head
Civil & Environmental Engineering

ABSTRACT

The thesis presents the development and validation of hydraulic fracturing and heat extraction models for Enhanced Geothermal Systems (EGS). The fracture models are developed using the Displacement Discontinuity (DD) Method which is an indirect Boundary Element approach. Two types fracture models are developed: based on the constant strength DD method and based on the Kelvin's fundamental-solution DD method. Analytical verification for each method is included. The DD model, based on the Kelvin's fundamental solution, presents a more robust and efficient technique for the fracture modeling. Various issues for the implementation of the Boundary Element Method for the fracture mechanics problems such as hyper-singularity and fracture tip singularity of stresses have been accounted in the numerical model. The Newtonian fracture fluid flow is modeled for steady and transient flow cases. Steady-state fracture fluid flow is modeled using implicit Finite Difference Method, and transient fluid flow is modeled based on the Galerkin's Finite Element approach. The fracture heat flow is modeled considering two cases: heat flow analysis during the fracture initiation and propagation processes, and long term heat circulation and extraction model for thermal energy production from an EGS reservoir. Two-dimensional and three-dimensional heat extraction models based on the Boundary Integral Equation formulations are formulated. In both the model, Laplace transform technique is used to deal with the time variable. The weak singularity cases have been considered for both two- and three-dimensional models. The thermal induced stresses due to differential cooling of the reservoir rocks are accounted for. Explicit hydro-mechanical and thermo-mechanical models for two-dimensional are established. Finally, the field validation of the heat circulation test is done using three-dimensional heat extraction. The validation of experimental result based on the analytical fracture model is also performed.

TABLE OF CONTENTS

ABSTRACT	iii
LIST OF FIGURES	ix
LIST OF TABLES	xv
LIST OF ABBREVIATIONS.....	xvi
ACKNOWLEDGEMENTS.....	xvii
CHAPTER 1.INTRODUCTION	1
1.1. Enhanced Geothermal Systems.....	1
1.2. Research Motivation	3
1.3. Research Objectives.....	4
1.4. Thesis Organization	4
CHAPTER 2.LITERATURE REVIEW	7
2.1. Introduction.....	7
2.2. Fracture Mechanics Theories for Hydraulic Fracturing.....	9
2.2.1. Griffith’s Energy Approach	10
2.2.2. Linear Elastic Fracture Mechanics (LEFM) Theory.....	12
2.3. Basic Phenomena and Mechanisms of Hydraulic Fracturing	19
2.3.1. Fracture Initiation.....	20
2.3.2. Fracture Initiation from a Circular Wellbore	21
2.3.3. Fracture Propagation.....	24
2.3.4. Fracture Fluid Flow.....	28
2.3.5. Fluid Diffusion and Leak-off	34
2.3.6. Fracture Heat Flow	35
2.4. Hydraulic Fracture Modeling.....	37
2.4.1. Two-Dimensional Fracture Models	38

2.4.2. Three-Dimensional Fracture Models	42
2.5. Computational Methods for Fracture Mechanics	45
2.5.1. Finite Element Method	45
2.5.2. Boundary Element Method.....	46
CHAPTER 3.FRACTURE DEFORMATION MODELING.....	48
3.1. Introduction.....	48
3.2. Basic Equations of Elasticity	48
3.3. Boundary Element Method for Elasticity	50
3.3.1. Kelvin’s Fundamental Solution	51
3.3.2. Betti’s Reciprocal Work Theorem	53
3.3.3. Somigliana’s Identity	54
3.3.4. The Boundary Integral Equation (BIE).....	56
3.3.5. Point Collocation and Galerkin’s Methods.....	56
3.3.6. Direct and Indirect Boundary Element Methods	57
3.4. Application of Boundary Element Method to Fracture Mechanics	58
3.4.1. Displacement Discontinuity Method	60
3.5. Constant Strength Displacement Discontinuity Model.....	61
3.5.1. Two-Dimensional Constant Strength DDM Model.....	62
3.5.2. Constant Strength Three-Dimensional DDM Model.....	72
3.6. DDM Models Based on Kelvin’s Fundamental Solution	75
3.6. 1. Numerical Implementation	76
3.6.2. Linear Equations of Discretized System.....	85
3.6.3. Numerical Example	87
3.6.4. Model Verification.....	90
3.6.5. Estimation of Stress Intensity Factor	92

3.7. Chapter Summary	93
CHAPTER 4.FLUID FLOW MODELING	94
4.1. Introduction.....	94
4.2. Steady State Fracture Fluid Flow.....	94
4.2.1. Governing Equations	95
4.2.2. Finite Difference Approximation.....	96
4.2.3. Numerical Example	99
4.3. Transient Fracture Fluid Flow	103
4.3.1. Governing Equations Fracture Fluid Flow	103
4.3.2. Finite Element Discretization	105
4.3.3. Numerical Implementation	106
4.3.4. Verification of Finite Element Program	107
4.4. Chapter Summary	113
CHAPTER 5.HEAT FLOW MODELING	115
5.1. Introduction.....	115
5.2. Heat Flow during Fracture Propagation.....	116
5.2.1. Governing Equations	116
5.2.2. Numerical Implementation	118
5.2.3. Numerical Example	119
5.2.4. Estimation of Thermal Induced-Stresses	121
5.3. Two-Dimensional Heat Extraction Model.....	123
5.3.1. Governing Equations	123
5.3.2. Laplace Transformation of Heat Flow Equations.....	124
5.3.3. Boundary Integral Equation Formulation	126
5.3.4. Integral Equation Solution	127

5.3.5. Numerical Implementation	128
5.3.6. Numerical Inverse of the Laplace Transform	129
5.3.7. Numerical Examples	130
5.4. Three-dimensional Heat Extraction Model.....	133
5.4.1. Governing Equations	134
5.4.2. Boundary Integral Equation (BIE) Formulation	135
5.4.4. Numerical Integration	137
5.4.5. Linear Equations of Discretized System.....	140
5.4.6. Numerical Examples.....	142
5.5. Chapter Summary	144
CHAPTER 6.COUPLED HYDRO-THERMO-MECHANICAL FRACTURE MODELING ...	145
6.1. Introduction.....	145
6.2. Hydro-Mechanical Coupling	146
6.2.1. Governing Equations	146
This section presents the governing equations for the one-dimensional fracture fluid flow and coupled fracture stress-deformation behavior.....	146
6.2.2. Explicit Coupling of Fracture Fluid Flow and Deformation	150
6.2.3. Numerical Example	153
6.3. Thermo-Mechanical Coupling.....	156
6.3.1. Effect of Thermal Stresses on KGD Model	156
6.3.2 Effect of Thermal Induced Stresses on 2D-DDM Model	160
6.4. Chapter Summary	162
CHAPTER 7.MODEL VALIDATION	163
7.1. Field Validation of Circulation Test	163
7.2. Experimental Validation of Fracture Model	167

7.3. Chapter Summary	171
CHAPTER 8.SUMMARY, CONCLUSIONS, & RECOMMENDATIONS	172
8.1. Summary	172
8.2. Conclusion	175
8.3. Future Recommendations	177
REFERENCES CITED	178
APPENDIX A	193
APPENDIX B	194

LIST OF FIGURES

Figure 1.1. Schematic of Enhanced Geothermal System (Department of Energy-Geothermal Technologies Program, 2011).....	2
Figure 2.1. Unfractured and fractured well system (API, 2009)	9
Figure 2.2. An elliptic hole in an infinite plate subjected to tension	11
Figure 2.3. Schematic of three modes of fracture opening: (a) Mode-I or opening mode (b) Mode-II or shearing mode (c) Mode-III or tearing mode (Irwin, 1957)	13
Figure 2.4. Stress state near a crack tip.....	14
Figure 2.5. Crack front spherical coordinate system	18
Figure 2.6. A circular wellbore under the action of in-situ stresses and wellbore pressure	22
Figure 2.7. A differential element representing radial, tangential, and shear stresses.....	22
Figure 2.8. Two-dimensional local crack tip coordinate system	25
Figure 2.9. Schematic of parallel plate fluid flow inside a fracture.....	31
Figure 2.10. Fluid flow velocity profile in a fracture approximated by two parallel plates	32
Figure 2.11. PKN constant height fracture model (Economides & Nolte, 2000).....	40
Figure 2.12. KGD constant fracture height model (Economides & Nolte, 2000)	42
Figure 2.13. Schematic of three-dimensional hydraulic fracture geometry (Yew, 1997)	44
Figure 3.1. Stress components on a three-dimensional infinitesimal element (Becker, 1992).....	50
Figure 3.2. Representation of source and field points and components of displacement and traction fundamental solution (Brebbia et al., 1984)	52
Figure 3.3. An elastic body subjected to two different systems of forces	54

Figure 3.4. Source point inside the domain and surrounded by a spherical region	55
Figure 3.5. Fracture geometry in an infinite domain (Aliabadi & Rooke, 1991)	59
Figure 3.6. Components of two-dimensional constant displacement discontinuity	63
Figure 3.7. Discretization of a fracture in NE number of elements (Crouch & Starfield, 1983)..	64
Figure 3.8. Displacement discontinuity components over an arbitrarily oriented fracture surface (Tao, 2010)	65
Figure 3.9. Displacement correlation for a parabolic fracture tip element (Nasab & Marji, 2007)	66
Figure 3.10. A pressurized planar fracture in an infinite region	68
Figure 3.11. Normal DD distribution along the pressurized fracture in an infinite plane	69
Figure 3.12. Normal stress distribution near tip of a pressurized planar fracture (along $y=0$)	69
Figure 3.13. An arbitrarily orientated fracture under far field stresses and internal fluid pressure	70
Figure 3.14. Normal and shear DD distribution along the pressurized arbitrarily oriented fracture in an infinite plane	71
Figure 3.15. Variation of analytical and numerical values of Mode-I and Mode-II stress intensity factors with orientation angle	71
Figure 3.16. Components of three-dimensional displacement discontinuities: (a) Mode-I fracture opening (b) Mode-II fracture shearing and (c) Mode-III fracture shearing (Vandamme & Curran, 1989)	73
Figure 3.17. Normal fracture opening for a square fracture using constant three-dimensional DD model	74

Figure 3.18. Mode-II shear opening for a square fracture using constant three-dimensional DD model	74
Figure 3.19. Continuous and semi-discontinuous rectangular elements.....	77
Figure 3.20. Representation of adaptive non-singular integration over an element	80
Figure 3.21. Variation of number of Gaussian point with R/L ratio (Davis & Gao, 2006)	81
Figure 3.22. Polar coordinates in parametric plane with singular node.....	83
Figure 3.23. Division of singular element into triangular sub-elements (Xiao & Yue, 2011)	85
Figure 3.24. Flow chart for three-dimensional displacement discontinuity model	86
Figure 3.25. Penny shaped fracture with uniform internal fluid pressure	88
Figure 3.26. Discretized circular fracture mesh (126 domain elements, 12 fracture front elements and 145 nodes).....	88
Figure 3.27. Surface plot of fracture normal opening.....	89
Figure 3.28. Comparison of numerical and analytical fracture normal opening (along $y=0$).....	91
Figure 3.29. Comparison of numerical and analytical normal stress distribution near fracture tip region (along $y=0$).....	91
Figure 3.30. Fracture front element and its spherical coordinates (Xiao & Yue, 2011).....	92
Figure 4.1. Schematic of two-dimensional fracture surface with injection and extraction wells.	96
Figure 4.2. Discretized fracture mesh for steady state fluid flow	97
Figure 4.3. Representation of a derivative boundary condition with a fictitious node.....	98
Figure 4.4. Surface plot of fracture fluid pressure distribution for a single well system.....	100
Figure 4.5. Fracture fluid flux vectors for a single injection well system	101

Figure 4.6. Surface plot of fracture fluid pressure distribution for injection and extraction well system	102
Figure 4.7. Fracture fluid flux vectors for the injection and extraction well system	102
Figure 4.8. Conservation of fracture fluid flow in a control volume rate (Yew, 1997).....	103
Figure 4.9. Boundary of fracture fluid flow domain (Hongren, 1987).....	104
Figure 4.10. Discretized reservoir domain for pore distribution	109
Figure 4.11. Variation of pore pressure distribution at middle node for 100 sec (Alpha=1).....	111
Figure 4.12. Variation of pore pressure distribution for 100 sec	111
Figure 4.13. Discretized fracture mesh for rectangular fracture fluid flow	112
Figure 4.14. Fluid pressure variation with time.....	113
Figure 5.1. Schematic of two-dimensional heat flow with one-dimensional fracture	117
Figure 5.2. Normalized temperature distribution inside the fracture.....	120
Figure 5.3. Surface plot of normalized temperature distribution.....	121
Figure 5.4. Thermal-induced normal stresses after 10 days	122
Figure 5.5. Schematic of a two-dimensional fracture connecting the injection and production extraction wells.....	123
Figure 5.6. Comparison of fracture temperature variation for fixed fracture length (After 1 year)	131
Figure 5.7. Variation of fracture temperature with time for fixed fracture length.....	132
Figure 5.8. Variation of thermal-induced stresses for a fixed fracture length (After 1 year)	133

Figure 5.9. Schematic of three-dimensional heat transport flow between the injection and extraction wells (Ghassemi et al., 2003).....	134
Figure 5.10. Non-singular and singular elements on a discretized fracture surface	138
Figure 5.11. Sub-division of quadrilateral element into triangular sub-elements.....	139
Figure 5.12. Transformation of a triangular sub-element to a degenerated square domain	140
Figure 5.13. Flow chart for three-dimensional heat extraction model.....	141
Figure 5.14. Surface plot of temperature distribution over the fracture surface.....	143
Figure 5.15. Change of temperature with time between injection and production well.....	144
Figure 6.1. Schematic of explicit coupling between the fracture aperture and fluid flow.....	146
Figure 6.2. Cell-centered Finite Difference discretization of 1D problem	148
Figure 6.3. Goodman joint model and a linear joint model (Sesetty & Ghassemi, 2013).....	149
Figure 6.4. Representation of effective stress acting on a fracture element (Tao, 2010)	150
Figure 6.5. Flow chart for explicit coupled hydro-mechanical model.....	152
Figure 6.6. Fracture fluid pressure after 1 sec of fluid injection.....	154
Figure 6.7. Fracture width after 1 sec of fluid injection.	154
Figure 6.8. Fracture fluid pressure after 2 sec of fluid injection.....	155
Figure 6.9. Fracture width after 2 sec of fluid injection	155
Figure 6.10. Initial fracture width from the KGD model.....	157
Figure 6.11. Initial fracture length the KGD model.....	157
Figure 6.12. Change in the fracture width due to thermal-induced stress (KGD model).....	159

Figure 6.13. Change in fracture volume due to thermal-induced stress (KGD model)	159
Figure 6.14. Thermal induced stresses after 10 days from boundary integral solution	161
Figure 6.15. Effect of the thermal induced stresses on the fracture normal opening in the 2D-DD model	161
Figure 7.1. Layout of position of wells and reservoirs at Hijiori EGS site (Kuriyagawa & Tenma, 1999)	164
Figure 7.2. Surface plot of temperature distribution for 90-day circulation test	166
Figure 7.3. Schematic of the tri-axial cell for laboratory hydraulic fracturing test	167
Figure 7.4. Variation of the fluid pressure with time during experimental hydraulic fracturing in triaxial cell (Frash, 2012).....	168
Figure 7.5. Variation of the fluid pressure with time during experimental hydraulic fracturing in triaxial cell (Frash, 2012).....	170
Figure 7.6. Variation of the fluid pressure with time during experimental hydraulic fracturing in triaxial cell (Frash, 2012).....	170

LIST OF TABLES

Table 3-1. Input parameters for constant three-dimensional DD model	73
Table 3-2. Input parameters for penny shaped fracture model	87
Table 4-1. Input parameters for steady state fracture fluid flow.....	99
Table 4-2. Reservoir and fluid properties for pore pressure distribution.....	110
Table 4-3. Input parameters for rectangular fracture fluid flow model	112
Table 5-1. Input parameters for 2D heat flow model.....	119
Table 5-2. Normalized temperature after 1 year ($L=300$ m).....	130
Table 5-3. Input Parameters for 2D heat extraction model.....	130
Table 5-4. Input parameters for 2D thermal induced stresses (Ghassemi, 2003).....	133
Table 5-5. Input Parameters for 3D heat extraction model (Yamaguchi, 1992).....	142
Table 6-1. Input parameters for explicit hydro-mechanical coupled model.....	153
Table 6-2. Input parameters for the KGD model.....	156
Table 7-1. 90-day circulation test data (Yamaguchi, 1992).....	164
Table 7-2. Input parameters for experimental hydraulic fracture test	168

LIST OF ABBREVAIIONS

API	American Petroleum Institute
BIE	Boundary Integral Equation
BEM	Boundary Element Method
DD	Displacement Discontinuity
DDM	Displacement Discontinuity Method
DEM	Discrete Element Method
EGS	Enhanced Geothermal System
FDM	Finite Difference Method
FEM	Finite Element Method
KGD	Khristianovich, Geertsma and de-Klerk Model
PKN	Perkins, Kern and Nordgren Model
P3D	Pseudo Three-dimensional Model
SIF	Stress Intensity Factor
SST	Singularity Subtraction Method
XFEM	Extended Finite Element Method

ACKNOWLEDGEMENTS

I owe a lot of gratitude to my advisor Dr. Marte Gutierrez. I am grateful to him for his support and guidance throughout my studies. I specially want to thank him for independence he gave in my research and allowing me to explore different research topic.

I would like to thank Dr. John R. Berger, Dr. Paul A. Matrin, Dr. Azra Tutuncu, & Dr. Yu-Shu Wu to be a part of my thesis committee and for providing guidance throughout my studies. I would also like to thank to Dr. Graham Mustoe & Dr. Ozkan for helping for some part of my research.

A very special thanks goes to the U.S. Department of Energy who provided continuous financial support throughout this study. The support is gratefully acknowledged.

In the last, I would like to thank my friends Utapendu Kuila, Dipankar Dwivedi, Sarthok Sircar , & Luke Frash who have supported and motivated me in many ways.

Dedicated to my Guru Late Shri. R.C. Shukla and to my parents!!!

I highly dedicate this thesis to my wife Khushboo Tewari, who has always supported & motivated me.

CHAPTER 1.

INTRODUCTION

Geothermal energy is basically the heat energy stored in the Earth's crust. It is a clean and sustainable energy source. Geothermal energy resources range from the shallow ground hot water and Hot Dry Rocks (HDR) found beneath the Earth's surface. In general, HDR resources occur at depths of 3 to 5 km from the Earth's surface. The heat energy from a geothermal system can be recovered to generate electricity mainly through two systems: hydrothermal systems or enhanced geothermal systems (EGS). Hydrothermal systems are naturally occurring hot reservoir with recharging water and sufficient reservoir permeability to allow water circulation. These reservoirs contains sufficient amount of water and steam at high temperature and pressure, which can be recovered to generate electricity. However, EGS reservoirs have no or negligible amount of water and permeability. Hence; for heat production, EGS reservoirs require enhancement of permeability and forced water circulation. Hydraulic fracturing is considered the primary means of creating functional EGS reservoirs at sites where the permeability of the rock mass is too limited to allow cost effective heat recovery. Due to high reservoir rocks temperature and high in-situ stresses at greater depth, hydraulic fracturing is a very challenging for the EGS. The research presented in this thesis mainly focuses on the accurate prediction of induced hydraulic fractures in EGS reservoirs and efficient heat extraction through the created fracture networks.

1.1. Enhanced Geothermal Systems

An approach to capture the heat energy from the Hot Dry Rocks (HDR) and low permeability reservoirs though forced water circulation is known as enhanced geothermal systems or engineered geothermal systems (EGS). EGS are formed by drilling system of

injection and extraction wells through the HDR reservoir and circulating cold water through the fracture networks. A schematic of an EGS along with surface facilities is shown in Figure 1.1. The thermal energy from the EGS is recovered through the extraction wells in the form of hot water and steam. The power plant unit at the surface uses the recovered hot water and steam to generate electricity. Finally, cooled water is recirculated to the reservoir through injection wells to complete the loop. For efficient heat energy production, the injector and extraction wells need to interconnect either through hydraulically induced or natural fractures. The heat extraction rate of such a system depends on the induced permeability so that fluid can contact the rock and extract the heat.

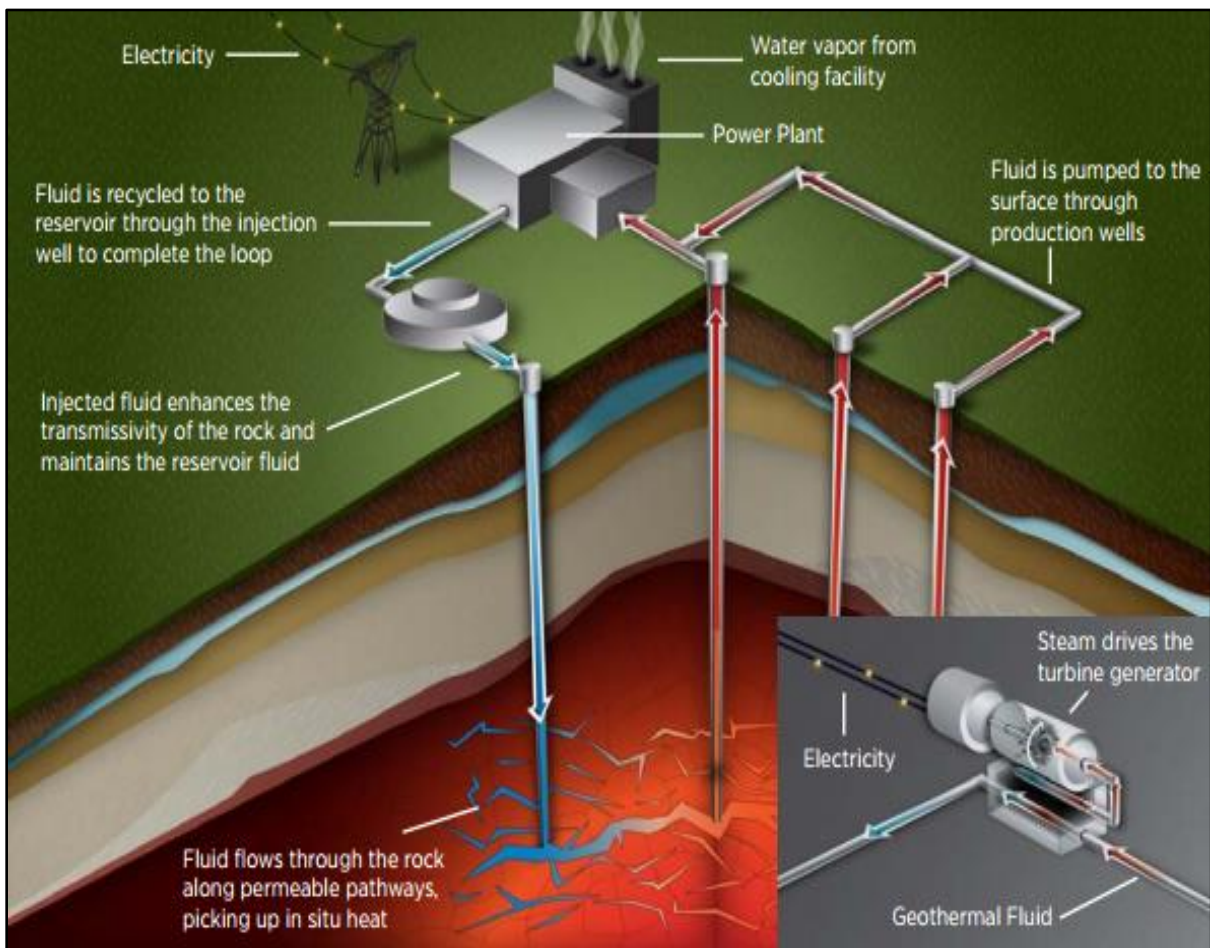


Figure 1.1. Schematic of Enhanced Geothermal System (Department of Energy-Geothermal Technologies Program, 2011)

1.2. Research Motivation

The development of Enhanced Geothermal Systems requires advanced methodology to stimulate low permeability reservoirs. For efficient thermal energy production from an EGS, large induced fractures that allow injection of large amount of water required. The natural and created fracture networks are needed to make sure that the circulated water is continuously in contact with high temperature reservoir rocks. Hydraulic fracturing is the most commonly used method to create large fracture network. The hydro-thermal-mechanical processes in the hydraulic fracturing of EGS reservoirs are a combination of many complicated physical phenomena, including fracture opening and closing in poro-elastic materials, non-linear behavior of injected slurry and its leak-off into the formation, fracture propagation in rock-mass, proppant transportation and its action to prevent fracture closure, and flow of fluid and heat through the fracture and surrounding rocks. Due to high reservoir temperature, the fracturing in an EGS requires rheologically controllable fracturing fluids, and temperature hardened proppants. Though, several numerical models have been developed for hydraulic fracture stimulation for the oil and gas industry; however, they have not sufficiently been demonstrated for the EGS reservoir creation. Insufficient data and measurements under geothermal conditions make it difficult to directly translate experience from the oil and gas industries to EGS applications. Hence, advanced simulator models are required for hydraulic fracturing the EGS. More specific motivations for this research are as follows:

1. Due to mostly brittle nature of the EGS reservoir rocks, fracturing in the EGS applications will have complex three-dimensional geometries
2. Due to complex fracture network geometries, efficient three-dimensional heat extraction models are required for the EGS.

3. The high reservoir temperature plays a critical role in the hydraulic fracturing process in the EGS reservoirs. It can affect the fracture propagation and initiation process and can change the fluid and rock physical properties.

1.3. Research Objectives

The overall objective of this research is to develop a numerical methodology for simulating the hydraulic fracture creation, including true three-dimensional geometry prediction, and heat extraction from an EGS. More specifically the research objectives are divided as follows:

1. To develop a true three-dimensional hydraulic fracture model. Three-dimensional fracture modeling will use the Displacement Discontinuity method which is an indirect Boundary Element Method.
2. To develop three-dimensional heat extraction model from hydraulically fractured EGS reservoirs. The three dimensional heat flow and transport model is based on the Boundary Integral Formulation.
3. To develop fracture fluid flow model. The two-dimensional fracture fluid flow model is developed using the Finite Element Method.
4. To develop coupled hydro-thermo-mechanical model of hydraulic fracturing.
5. To validate the hydraulic fracture and heat extraction models using experimental data and field EGS case studies.

1.4. Thesis Organization

This thesis is organized in eight chapters. The details of each individual chapter are as follows:

Chapter 1 introduces the Enhanced Geothermal Systems, and provides details of the motivations of this research and the specific research objectives.

Chapter 2 presents the detailed literature review for the hydraulic fracturing process, the fracture mechanics concepts applicable to hydraulic fracturing, and various processes involved in the hydraulic fracturing. A brief overview of the various numerical models and numerical approaches is provided.

Chapter 3 presents an introduction of the three-dimensional elasticity and the Boundary Element Method for the elasticity problems. The theoretical and numerical aspects of the Displacement Discontinuity (DD) method for fracture modeling are discussed. Two numerical models: constant strength DD model and point load DD models are developed and their analytical validations are included.

Chapter 4 presents the mathematical and numerical aspects of steady-state and transient fracture fluid flow. This chapter is basically a supportive chapter for the work on heat extraction modeling and coupled hydro-thermo-mechanical hydraulic fracture modeling.

Chapter 5 presents two types of heat flow model: heat flow analysis during fracturing and heat flow analysis for long term heat extraction. The heat extraction models have been divided in two parts: two-dimensional heat extraction model and three-dimensional heat extraction model. Methodologies to estimate thermal induced stresses on the fracture surfaces are discussed.

Chapter 6 presents hydro-mechanical and thermo-mechanical coupling methodologies for two dimensional hydraulic fracturing.

Chapter 7 presents the field validation of heat circulation test and experimental validation of the hydraulic fracturing.

Chapter 8 presents summary, conclusion from the thesis, and recommendations for future work.

CHAPTER 2.

LITERATURE REVIEW

This chapter presents an introduction to the hydraulic fracturing process and the fracture mechanics concepts applicable to the hydraulic fracturing. The main processes involved in the hydraulic fracture mechanism such as fracture initiation and propagation, fracture fluid and heat flow, and fluid diffusion from a fracture surface are discussed briefly. The various existing numerical models and their applicability and limitations are reviewed. A brief discussion on the main numerical techniques used to analyze the hydraulic fracturing process is provided

2.1. Introduction

Hydraulic fracturing is the most common technique used to enhance reservoir rock permeability. It is most commonly used to enhance production from hydrocarbon reservoirs. The process of fracture initiation and propagation in a rock mass by injection of a pressurized fluid from the wellbore is termed as hydraulic fracturing. In Petroleum Engineering, the created fractures provide conductive paths to the hydrocarbons stored in the reservoir rocks to the wellbore thereby increasing the production rates. Hydraulic fracture process presents a complex mathematical problem that involves the mechanical interaction of the propagating fracture with the fluid dynamics of the injected fluid. The hydraulic fractures play an important role to stimulate heat extraction from geothermal reservoirs by providing the pathways for the fluid and heat exchange (Wright & Tanigawa, 1994; Ghassemi et al., 2010). As a fracturing fluid travels between the injection and extraction wells through the fracture networks, it interacts with the reservoir rock which gives a rise to the chemical, thermo-elastic, and poro-elastic phenomena, all of which can affect the fracture geometry (Ghassemi et al., 2008).

First, hydraulic fracture treatment was started by the Dow Chemical Company in 1930's to fracture the rock formation in combination with acid stimulation enhance reservoir performance. In 1947, Pan American Petroleum Corporation started the first non-acidic fracturing treatment specifically designed to stimulate well production from a gas well in the Hugoton gas field, Kansas. Presently, hydraulic fracturing is extensively used to improve oil and gas production throughout the world. In US oil and gas reservoirs, large quantities of natural gases exist in low permeability rocks. Valko & Economides (1995) reported that in the North America since 1950, about 70% of gas wells and 50% of oil wells have been hydraulically stimulated. Outside of the oil and gas industry, hydraulic fracturing is also used in other applications such as for coal bed methane production, hazardous solid waste disposal, measurement of in-situ stresses, fault reactivations in mining, and for circulation of water in the Hot Dry Rocks (HDR) for geothermal energy production.

The hydraulic fracturing requires the process of pumping a high pressure fluid into a wellbore at a high injection rate. As the resistance to flow in the formation increases, the pressure in the wellbore increases to a critical value that exceeds the breakdown pressure of the formation. Once the formation breakdown occurs, a fracture is created and the injected fluid starts flowing along the fracture. In general, a main single fracture along with multiple small fractures is created and propagates in two opposite directions from the wellbore. The created hydraulic fractures improve the productivity of a well. A schematic of wellbore before and after hydraulic creation is shown in Figure 2.1. From upper part of the Figure 2.1, it is obvious that all of the oil or gas must converge radially to a very small area. However; the lower figure shows an increase of the flow path for the oil and gas flow. At early time of fracturing, the oil and gas enters into the fracture from all points along the fracture. The high conductive fracture path rapidly

transports fluids to the wellbore. However, at later time, the oil and gas in the reservoir flows towards an elliptical pressure sink and most of it enters near the tip of the fracture.

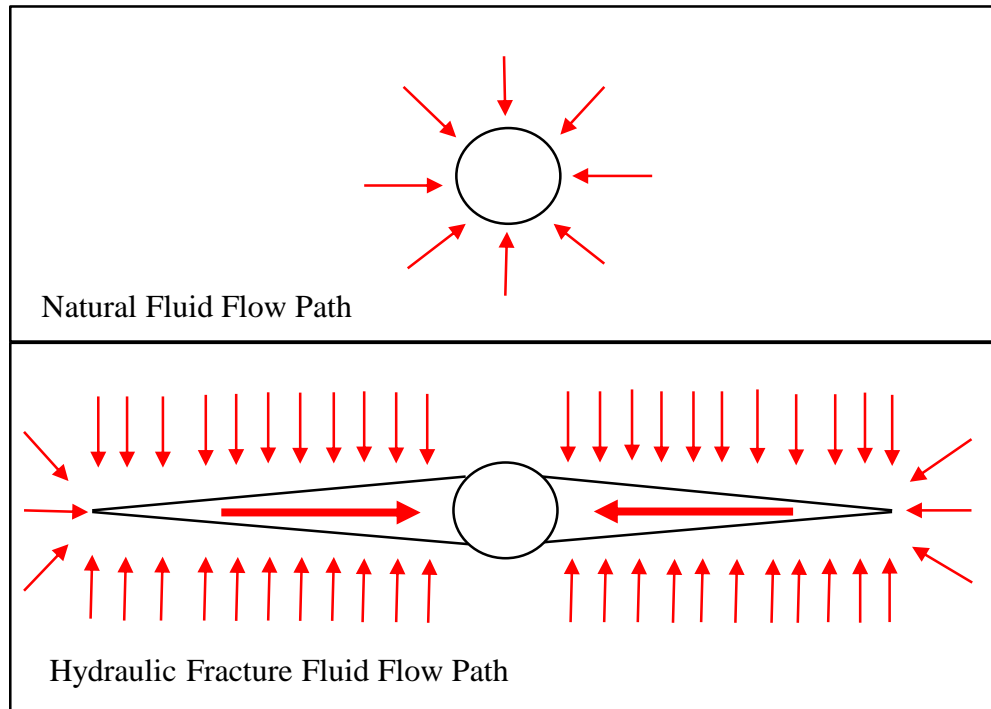


Figure 2.1. Unfractured and fractured well system (API, 2009)

A hydraulic fracture is induced in two phases. The first phase starts with creating perforations or weak points into the formation from a wellbore. Then a viscous fluid called as pad is pumped into the well. When the down-hole pressure goes beyond breakdown pressure, a fracture initiates from the perforated interval and goes into the surrounding reservoir rock. In second phase, proppants consisting of a slurry mixture of fluid and proppant, is injected into the well. The slurry mixtures extend the initiated fracture, keep it open, and transport the proppant deep into the fracture.

2.2. Fracture Mechanics Theories for Hydraulic Fracturing

Rock and fracture mechanics play important roles in the engineering design of hydraulic fracturing treatments (Adachi et al., 2007). Rock mechanical properties predict the stress

distribution at depth and elastic and strength properties control the created fracture geometry (Valko & Economides, 1995). The theory of hydraulic fracturing depends on an understanding of fracture initiation and propagation processes in a rock mass at greater depth (Gidley et al., 1989). Due to the brittle nature of reservoir rocks, the theories of elastic and brittle fracture mechanics are applicable to understand the behavior of the fracture equilibrium and propagation. The most commonly used fracture mechanics theories applied to understand the hydraulic fracture initiation and propagation are: the Griffith's energy approach (Griffith, 1921), and the linear elastic fracture mechanics (LEFM) (Orowan, 1952; Irwin, 1957). A brief description of the fracture mechanics theories is provided in the following sections.

2.2.1. Griffith's Energy Approach

Griffith (1921) had proposed the first theory for the crack behavior in a brittle material based on the assumptions that numerous minute flaws or weakness zones exist in materials which act as sources of stress concentration. The concept of stress concentration along with energy release rate approach introduced by Griffith started the era of modern fracture mechanics. Griffith extended the earlier work of Inglis (1913) for an elliptical crack in an infinite plate under tensile forces. Considering, a problem of a thin, linearly elastic, isotropic, infinite plate containing a thin elliptical hole which is subjected to a uniform tensile stress as shown in Figure 2.2. The normal stress developed due to applied stresses at the end of the major axis can be given as follows (Inglis, 1913):

$$\sigma_{yy} = \sigma \left(1 + \frac{2a}{b} \right) \quad (2.1)$$

where σ_{yy} is the normal stress, σ is the applied stress, $2a$ and $2b$ are the major and minor axes of the elliptical crack, respectively. In Eq. (2.1), if length b tends to zero, then it results in a line

crack and the normal stress σ_{yy} increases without limit, which results in unreasonable condition that any amount of applied stress would cause the crack growth.

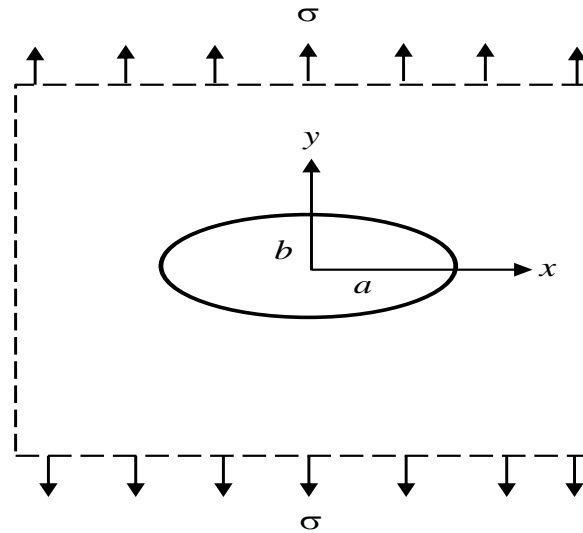


Figure 2.2. An elliptic hole in an infinite plate subjected to tension

Griffith suggested an energy balance criterion based on the assumption that the unstable propagation of a crack must result in a decrease in strain energy. The crack will propagate when the incremental release of energy due to crack extension becomes greater than the incremental increase of surface energy due to new crack surface formation. The crack propagation criteria can be given as follows:

$$dW \geq dW_s \quad (2.2)$$

where dW is the incremental increase due to crack extension and dW_s is the incremental increase of surface energy. The critical point for the crack propagation using Eq. (2.2) can be written as: $dW = dW_s$. If the energy from the crack plane is equal to or greater than the energy required to create a new crack surfaces, the crack can propagate will start (Sun & Jin, 2012). The surface energy for a crack of length $2a$ is given as follows:

$$W_s = 4aG_s \quad (2.3)$$

where G_s is the surface energy density. The total energy released due to presence of a crack of length $2a$ in an infinite two-dimensional body can be estimated as (Inglis, 1913):

$$W = \frac{\pi a^2 \sigma^2 (1-\nu^2)}{E} \quad ; \text{ Plane strain condition} \quad (2.4a)$$

$$W = \frac{\pi a^2 \sigma^2}{E} \quad ; \text{ Plane stress condition} \quad (2.4b)$$

where E is the Young's modulus and ν is the Poisson's ratio. Substitution of Eqs. (2.3) and (2.4) in Eq. (2.2) gives an estimate of the critical stress level at which the crack will start propagating. Mathematically, the critical stress σ_{cr} can be derived as follows:

$$\sigma_{cr} = \sqrt{\frac{2E\gamma}{\pi(1-\nu^2)a}} \quad ; \text{ Plane strain condition} \quad (2.5a)$$

$$\sigma_{cr} = \sqrt{\frac{2E\gamma}{\pi a}} \quad ; \text{ Plane stress condition} \quad (2.5b)$$

2.2.2. Linear Elastic Fracture Mechanics (LEFM) Theory

The linear elastic fracture mechanics (LEFM) is based on the Griffith's theory with modifications to include dissipative energy processes such as plastic flow and micro-cracking (Orowan, 1952; Irwin, 1957). The basic assumption of LEFM is that growth of a crack is controlled by stress fields at the crack tip. Irwin (1957) suggested that for a three-dimensional crack which is subjected to external loads, the crack tip relative displacement fields can be divided in components along the three coordinate directions. Irwin classified the relative crack tip displacements in three independent modes as shown in Figure 2.3, namely: Mode-I or

opening mode, Mode-II or shearing mode, and Mode-III or tearing mode. The crack growth process can be explained by superposition of these independent fracture opening modes.

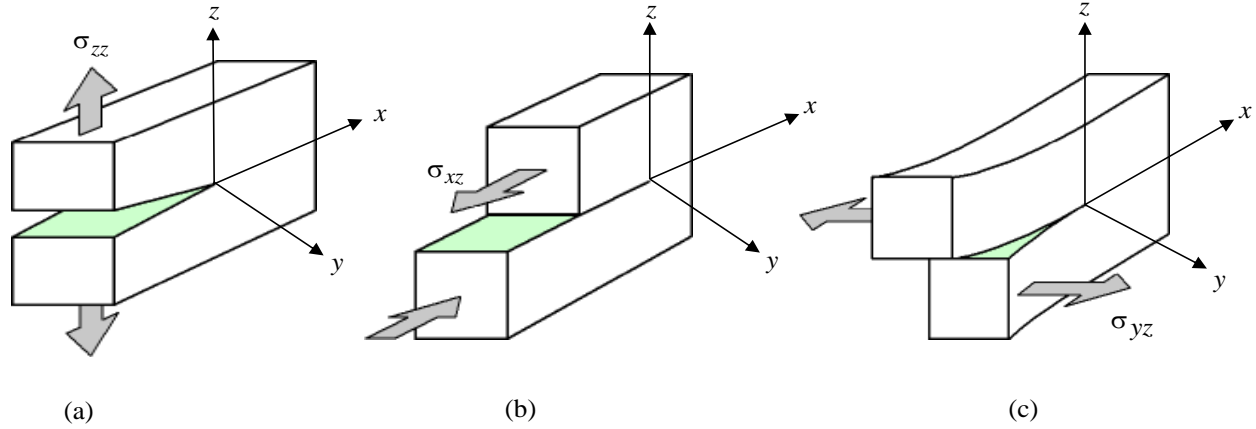


Figure 2.3. Schematic of three modes of fracture opening: (a) Mode-I or opening mode (b) Mode-II or shearing mode (c) Mode-III or tearing mode (Irwin, 1957)

1. Mode-I Fracture Opening

In case of Mode-I or opening mode, the tensile stresses perpendicular to the crack surfaces are applied on the body as shown in Figure 2.3 (a). The crack surfaces are pulled apart in the z direction and the deformations are symmetric with respect to the planes perpendicular to the x and y axes. The Mode-I stress and displacement fields in terms of polar coordinates (r, θ) for a crack tip as shown in Figure 2.4 can be given as follows (Irwin, 1957):

$$\begin{bmatrix} \sigma_{xx} \\ \sigma_{yy} \\ \sigma_{xy} \end{bmatrix} = \frac{K_I}{\sqrt{2\pi r}} \cos \frac{\theta}{2} \begin{bmatrix} 1 - \cos \frac{\theta}{2} \sin \frac{3\theta}{2} \\ 1 + \cos \frac{\theta}{2} \sin \frac{3\theta}{2} \\ \sin \frac{\theta}{2} \cos \frac{3\theta}{2} \end{bmatrix} \quad (2.6a)$$

$$\begin{bmatrix} \sigma_{zz} \\ \sigma_{xz} \\ \sigma_{yz} \end{bmatrix} = \begin{bmatrix} \nu' \cdot (\sigma_{xx} + \sigma_{yy}) \\ 0 \\ 0 \end{bmatrix}; \text{ for plane strain condition} \quad (2.6b)$$

$$\begin{bmatrix} \sigma_{zz} \\ \sigma_{xz} \\ \sigma_{yz} \end{bmatrix} = \begin{bmatrix} 0 \\ 0 \\ 0 \end{bmatrix} ; \text{ for plane stress condition} \quad (2.6c)$$

$$\begin{bmatrix} u_x \\ u_y \end{bmatrix} = \frac{K_I}{4G} \sqrt{\frac{r}{2\pi}} \begin{bmatrix} (2k-1) \cos \frac{\theta}{2} - \cos \frac{3\theta}{2} \\ -(2k-1) \sin \frac{\theta}{2} + \sin \frac{3\theta}{2} \end{bmatrix} \quad (2.6d)$$

$$u_z = -\frac{\nu'' z}{E} (\sigma_{xx} + \sigma_{yy}) \quad (2.6e)$$

where K_I is the Mode-I stress intensity factor, E and G are the Young's and shear modulus, respectively, the elastic constant are defined as:

$$k = \begin{cases} \frac{(3-\nu)}{(1+\nu)}, & \nu' = 0, \nu'' = \nu & ; \text{ for plane strain condition} \\ k = (3-4\nu), & \nu' = \nu, \nu'' = 0 & ; \text{ for plane stress condition} \end{cases} \quad (2.7)$$

where ν is the Poisson's ratio, ν' , ν'' and k represents the elasticity constants as defined in Eq. (2.7).

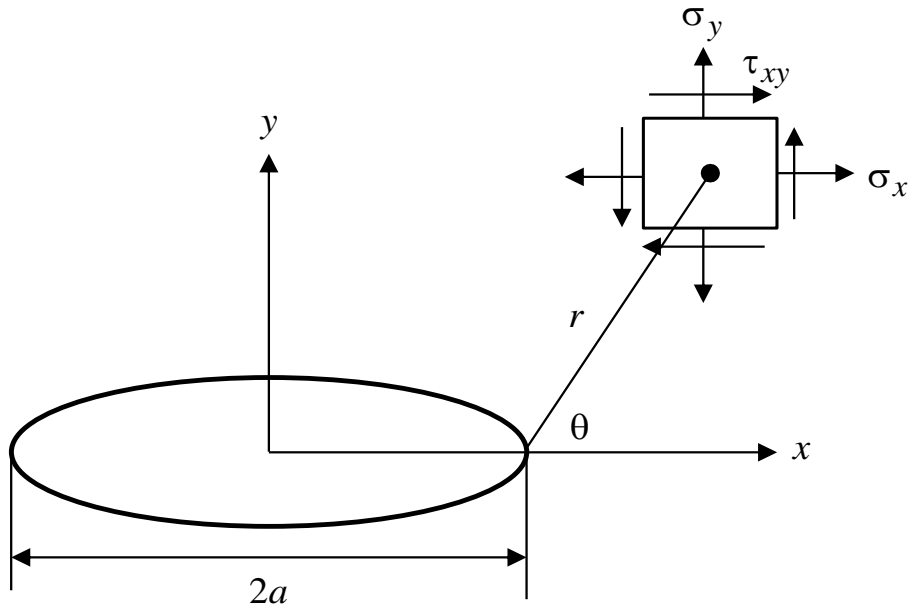


Figure 2.4. Stress state near a crack tip

2. Mode-II Fracture Opening

In case of Mode-II or sliding mode, the shear forces parallel to the crack surfaces are applied on the body as shown in Figure 2.3 (b). The crack deformations are symmetric with respect to the plane perpendicular to the z - axis and skew symmetric with respect to the plane perpendicular to y - axis. The Mode-II crack tip stresses and displacements fields can be written as (Irwin, 1957):

$$\begin{bmatrix} \sigma_{xx} \\ \sigma_{yy} \\ \sigma_{xy} \end{bmatrix} = \frac{K_{II}}{\sqrt{2\pi r}} \begin{bmatrix} -\sin \frac{\theta}{2} \left(2 + \cos \frac{\theta}{2} \cos \frac{3\theta}{2} \right) \\ \sin \frac{\theta}{2} \cos \frac{\theta}{2} \cos \frac{3\theta}{2} \\ \cos \frac{\theta}{2} \left(1 - \sin \frac{\theta}{2} \sin \frac{3\theta}{2} \right) \end{bmatrix} \quad (2.8a)$$

$$\begin{bmatrix} \sigma_{zz} \\ \sigma_{xz} \\ \sigma_{yz} \end{bmatrix} = \begin{bmatrix} \nu' \cdot (\sigma_{xx} + \sigma_{yy}) \\ 0 \\ 0 \end{bmatrix} ; \text{ for plane strain condition} \quad (2.8b)$$

$$\begin{bmatrix} \sigma_{zz} \\ \sigma_{xz} \\ \sigma_{yz} \end{bmatrix} = \begin{bmatrix} 0 \\ 0 \\ 0 \end{bmatrix} ; \text{ for plane stress condition} \quad (2.8c)$$

$$\begin{bmatrix} u_x \\ u_y \end{bmatrix} = \frac{K_{II}}{4G} \sqrt{\frac{r}{2\pi}} \begin{bmatrix} (2k+3) \sin \frac{\theta}{2} + \sin \frac{3\theta}{2} \\ -(2k-3) \cos \frac{\theta}{2} + \cos \frac{3\theta}{2} \end{bmatrix} \quad (2.8d)$$

$$u_z = -\frac{\nu'' z}{E} (\sigma_{xx} + \sigma_{yy}) \quad (2.8e)$$

where K_{II} is the Mode-II stress intensity factor.

3. Mode-III Fracture Opening

In case of Mode-III or tearing mode, the shear forces parallel to the crack front surfaces are applied on the body as shown in Figure 2.3 (c). The crack deformations are skew-symmetric with respect to the plane perpendicular to z - and y - axis. The Mode-III crack tip stresses and displacements can be written as (Irwin, 1957):

$$\begin{bmatrix} \sigma_{xz} \\ \sigma_{yz} \end{bmatrix} = \frac{K_{III}}{\sqrt{2\pi r}} \begin{bmatrix} -\sin \frac{\theta}{2} \\ \cos \frac{\theta}{2} \end{bmatrix} \quad (2.9a)$$

$$\begin{bmatrix} \sigma_{xx} \\ \sigma_{yy} \\ \sigma_{zz} \end{bmatrix} = \begin{bmatrix} 0 \\ 0 \\ 0 \end{bmatrix} \quad (2.9b)$$

$$u_x = u_y = 0 \quad (2.9c)$$

$$u_z = \frac{2K_{III}}{G} \sqrt{\frac{r}{2\pi}} \sin \frac{\theta}{2} \quad (2.9d)$$

where K_{III} is the Mode-III stress intensity factor.

4. Crack Front Elastic Field for a Three-Dimensional Crack

The elastic stress and displacement fields near a three-dimensional front crack can be represented using Williams' asymptotic solution (Williams, 1957). Hartranft & Sih (1977) suggested that by using geometrical analysis and series expansion, the stress and displacement fields for point outside the plane (\mathbf{n} , \mathbf{b}) can be expressed in terms of spherical coordinates as shown in Figure 2.5. The near crack tip stress fields for a three-dimensional can be represented as follows (Dell'sErba, 2002):

$$\sigma_n = \frac{K_I}{\sqrt{2\pi r \cos \varphi}} \cos \frac{\theta}{2} \left[1 - \sin \frac{\theta}{2} \sin \frac{3\theta}{2} \right] - \frac{K_{II}}{\sqrt{2\pi r \cos \varphi}} \sin \frac{\theta}{2} \left[2 + \cos \frac{\theta}{2} \cos \frac{3\theta}{2} \right] + O(1) \quad (2.10a)$$

$$\sigma_b = \frac{K_I}{\sqrt{2\pi r \cos \varphi}} \cos \frac{\theta}{2} \left[1 + \sin \frac{\theta}{2} \sin \frac{3\theta}{2} \right] + \frac{K_{II}}{\sqrt{2\pi r \cos \varphi}} \sin \frac{\theta}{2} \cos \frac{\theta}{2} \cos \frac{3\theta}{2} + O(1) \quad (2.10b)$$

$$\sigma_t = \frac{2\nu}{\sqrt{2\pi r \cos \varphi}} \left[K_I \cos \frac{\theta}{2} - K_{II} \sin \frac{\theta}{2} \right] + O(1) \quad (2.10c)$$

$$\sigma_{nb} = \frac{K_I}{\sqrt{2\pi r \cos \varphi}} \sin \frac{\theta}{2} \cos \frac{\theta}{2} \cos \frac{3\theta}{2} + \frac{K_{II}}{\sqrt{2\pi r \cos \varphi}} \cos \frac{\theta}{2} \left[1 - \sin \frac{\theta}{2} \sin \frac{3\theta}{2} \right] + O(1) \quad (2.10d)$$

$$\sigma_{nt} = -\frac{K_{III}}{\sqrt{2\pi r \cos \varphi}} \sin \frac{\theta}{2} + O(1) \quad (2.10e)$$

$$\sigma_{bt} = \frac{K_{III}}{\sqrt{2\pi r \cos \varphi}} \cos \frac{\theta}{2} + O(1) \quad (2.10f)$$

The displacement field is represented as follows:

$$u_n = \frac{(1+\nu)}{E} \sqrt{\frac{2r \cos \varphi}{\pi}} \left\{ K_I \cos \frac{\theta}{2} \left[(1-2\nu) + \sin^2 \frac{\theta}{2} \right] + K_{II} \sin \frac{\theta}{2} \left[2(1-\nu) + \cos^2 \frac{\theta}{2} \right] \right\} + O(r) \quad (2.11a)$$

$$u_b = \frac{(1+\nu)}{E} \sqrt{\frac{2r \cos \varphi}{\pi}} \left\{ K_I \sin \frac{\theta}{2} \left[2(1-\nu) - \cos^2 \frac{\theta}{2} \right] - K_{II} \cos \frac{\theta}{2} \left[(1-2\nu) - \sin^2 \frac{\theta}{2} \right] \right\} + O(r) \quad (2.11b)$$

$$u_t = 2 \frac{(1+\nu)}{E} \sqrt{\frac{2r \cos \varphi}{\pi}} K_{III} \sin \frac{\theta}{2} + O(r) \quad (2.11c)$$

where (r, θ, φ) are the spherical coordinate system, K_I , K_{II} , and K_{III} represent the stress intensity factors at the crack tip, $O(r)$ represent the terms tending to zero as $r \rightarrow 0$ and $O(1)$ are the bounded terms. From Eqs. (2.10) and (2.11) two important characteristics of the LEFM can be extracted, namely, $O(1/\sqrt{r})$ variation of the crack tip stress fields and $O(\sqrt{r})$ variation of the displacements field in plane perpendicular to the crack front.

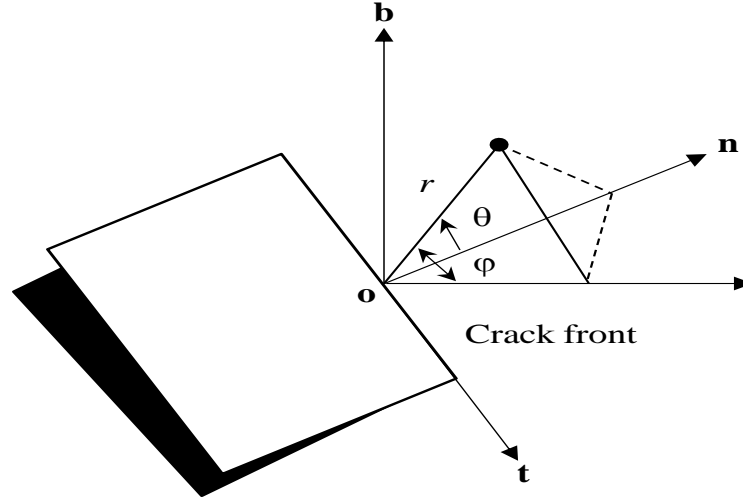


Figure 2.5. Crack front spherical coordinate system

5. Stress Intensity Factor

The stress intensity factor (SIF) is the most important parameter in fracture mechanics. The SIF basically represents a measure of strength of the near crack tip stress singularity which plays a critical role in the LEFM analysis. The value of the SIF depends on the applied load, geometry of the cracked structure, and position of estimation point along the crack front. The understanding of the SIF provides background for the analysis of the crack initiation and propagation processes. Therefore, the accurate estimation of the SIF values is the fundamental task of the LEFM analysis to any engineering problem. From Eq. (2.10), the stress field in vicinity of the crack front can be presented as follows (Mi, 1996):

$$\sigma_{ij}(r, \theta, \varphi) = \sum_{m=1}^{III} \frac{K_m}{\sqrt{2\pi r}} f_{ij}(r, \theta, \varphi) + O(1) \quad (2.12)$$

where f_{ij} is the functions from Eq. (2.10). Substituting, $\theta = \varphi = 0$ in Eq. (2.12), the stress intensity factors can be expressed as the limiting values of the stresses as $r \rightarrow 0$:

$$K_I = \lim_{r \rightarrow 0} \sqrt{2\pi r} \sigma_n(r, 0, 0) \quad (2.13a)$$

$$K_{II} = \lim_{r \rightarrow 0} \sqrt{2\pi r} \sigma_{nb}(r, 0, 0) \quad (2.13b)$$

$$K_{III} = \lim_{r \rightarrow 0} \sqrt{2\pi r} \sigma_{bt}(r, 0, 0) \quad (2.13c)$$

where K_I , K_{II} and K_{III} are the Mode-I, Mode-II and Mode-III stress intensity factors, respectively. The stress intensity factors can be also represented in terms of the displacements of the two opposite crack surfaces close to the crack front by substituting, $\theta = \pm\pi$; $\varphi = -\pi/2$ in Eq. (2.11) and neglecting $O(r)$ terms. The SIF values can be expressed as follows (Xiao & Yue, 2011):

$$K_I = \frac{E}{4(1-\nu^2)} \sqrt{\frac{\pi}{2r}} u_b(r, \theta = \pm\pi, \varphi = -\pi/2) \quad (2.14a)$$

$$K_{II} = \frac{E}{4(1-\nu^2)} \sqrt{\frac{\pi}{2r}} u_n(r, \theta = \pm\pi, \varphi = -\pi/2) \quad (2.14b)$$

$$K_{III} = \frac{E}{4(1+\nu)} \sqrt{\frac{\pi}{2r}} u_t(r, \theta = \pm\pi, \varphi = -\pi/2) \quad (2.14c)$$

2.3. Basic Phenomena and Mechanisms of Hydraulic Fracturing

The hydraulic fracturing mechanism represents a combination of several complex processes such as fracture initiation and propagation, mechanical deformation of rock mass due to the applied stresses and fluid pressure on the fracture surfaces, fluid flow inside the fracture, proppant flow and transport inside the fracture, fluid diffusion or leak-off into the reservoir, heat conduction between the reservoir rocks and fracture surfaces, and heat convection inside the fracture surface. The high reservoir rock temperature plays an important role in the fracture initiation and propagation processes in the geothermal reservoirs. The higher reservoir temperature can affect the physical and thermal properties of rock mass (e.g., rock mass density, thermal conductivity, elasticity and fracture toughness) and also alter the physical properties of

fracturing fluid (e.g., fluid density and viscosity). A detailed description of main mechanisms involved in the hydraulic fracturing of an EGS reservoir is discussed in following sections.

2.3.1. Fracture Initiation

The fracture initiation process in rock mass depends on the critical level of applied stresses and rock strength properties. A fracture initiation criterion basically gives a relationship between the effective principal stresses and represents a limiting case of stresses beyond which instability or fracture initiation will occur. Most commonly used failure criteria for the hydraulic fracture initiation are briefly described in following sections.

1. Maximum Tensile Stress Criterion

The maximum tensile stress criterion is commonly used for analysis of a hydraulic fracture initiation. This criterion suggests that the fracture initiation process will start when the minimum principal stress component of the applied stresses is equal to tensile strength of the rock mass. Mathematically, it can be given as follows (Valko & Economides, 1995):

$$\sigma_3 = -\sigma_t \quad (2.15)$$

where σ_3 is the minimum principal stress component (compression is assumed positive) and σ_t is the tensile strength of the rock mass.

2. Mohr-Coulomb Criterion

The Mohr-Coulomb criterion suggests that the shear stress at the failure is equal to sum of cohesion of the material and multiplication of friction coefficient and the effective normal stress acting on the failure plane. Mathematically, this criterion can be expressed as (Jaeger et al., 2007):

$$\tau = C_0 + \tan(\phi) \cdot (\sigma_n - p) \quad (2.16)$$

where τ represents the shear stresses, σ_n is the normal stress, C_0 is the cohesion, ϕ is the angle of internal friction, and p is the pore pressure.

2.3.2. Fracture Initiation from a Circular Wellbore

Consider a circular wellbore in a homogeneous, isotropic and linear elastic rock mass with axis parallel to the vertical stress as shown in Figure 2.6. The circumferential stresses on a differential element as shown in Figure 2.7 can be given by the Kirsch's solution (Herget, 1988) as follows (Valko & Economides, 1995):

$$\sigma_{rr} = \frac{\sigma_h + \sigma_v}{2} \left(1 - \frac{r_w^2}{r^2}\right) + \frac{\sigma_h - \sigma_v}{2} \left(1 - \frac{4r_w^2}{r^2} \frac{3r_w^4}{r^4}\right) \cos(2\theta) \quad (2.17a)$$

$$\sigma_{\theta\theta} = \frac{(\sigma_h + \sigma_v)}{2} \left(1 + \frac{r_w^2}{r^2}\right) - \frac{(\sigma_h - \sigma_v)}{2} \left(1 + \frac{3r_w^4}{r^4}\right) \cos(2\theta) \quad (2.17b)$$

$$\sigma_{r\theta} = -\frac{(\sigma_h + \sigma_v)}{2} \left(1 + \frac{2r_w^2}{r^2} - \frac{3r_w^4}{r^4}\right) \sin(2\theta) \quad (2.17c)$$

where σ_{rr} , $\sigma_{\theta\theta}$ and $\sigma_{r\theta}$ represent the radial, tangential, and shear stress components on the differential element, respectively, σ_v and σ_h are the minimum and maximum in-situ stresses, respectively, (r, θ) are the polar coordinates, and r_w represents the wellbore radius.

The stresses at the wall of wellbore can be obtained by substituting $r \rightarrow r_w$ in Eqs. (2.17) as follows:

$$\sigma_r = 0; \quad \tau_{r\theta} = 0 \quad (2.18a)$$

$$\sigma_\theta = (\sigma_h + \sigma_v) - 2(\sigma_h - \sigma_v) \cos 2\theta \quad (2.18b)$$

Considering, only the directions parallel and perpendicular to the minimum horizontal stress directions, Eqs. (2.18) can be represented as:

$$\sigma_{\theta} = 3\sigma_v - \sigma_h \quad ; \quad \theta = 0 \quad (2.19a)$$

$$\sigma_{\theta} = 3\sigma_h - \sigma_v \quad ; \quad \theta = \pi/2 \quad (2.19b)$$

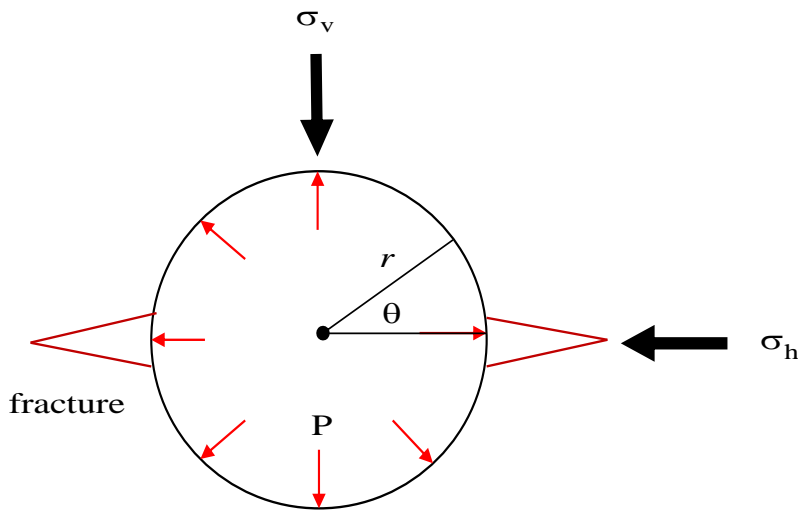


Figure 2.6. A circular wellbore under the action of in-situ stresses and wellbore pressure

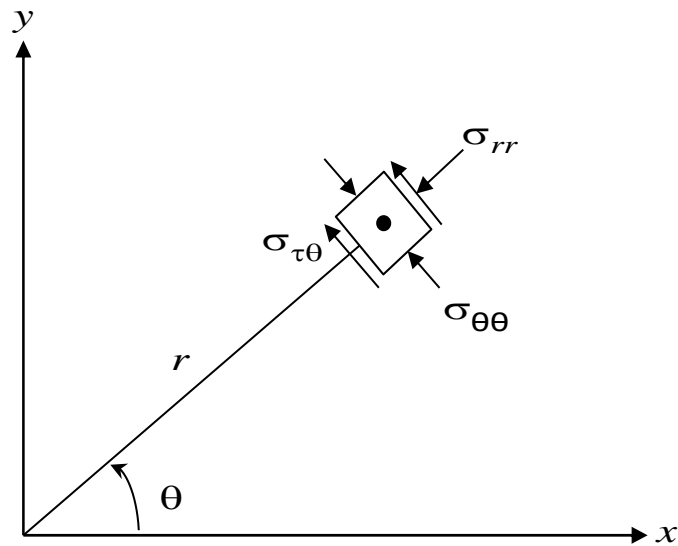


Figure 2.7. A differential element representing radial, tangential, and shear stresses

Based on the stress state near the circular wellbore, Hubbert & Willis (1957) presented a criterion for the hydraulic fracture initiation. This criterion suggests that the hydraulic fracture initiation will start when the effective tangential stress becomes equal to the tensile strength of the rock mass. The breakdown pressure for fracture initiation for an impermeable rock mass is given as follows (Hubbert & Willis, 1957):

$$p_b = 3\sigma_v - \sigma_h + \sigma_t \quad (2.20)$$

where p_b is the break down pressure, σ_t is tensile strength of the intact rock mass, $3\sigma_v - \sigma_h$ represents stress concentration as defined in Eq.(2.19). Schmidt & Zoback (1989) modified Eq. (2.20) using poro-elasticity theory to include influence of the rock porosity and pore pressure on breakdown pressure. The breakdown pressure for a poro-elastic media is given as follows:

$$p_b = \frac{3\sigma_v - \sigma_h + \sigma_t - \alpha p_p \left(\frac{1-2\nu}{1-\nu} \right)}{1 + \phi - \alpha \left(\frac{1-2\nu}{1-\nu} \right)} \quad (2.21)$$

where p_p is the pore pressure, ϕ is the porosity, ν is the Poisson's ratio, and α is the Biot's poro-elastic parameter which is defined as:

$$\alpha = 1 - \frac{K_m}{K_s} ; \quad 0 < \alpha \leq 1 \quad (2.22)$$

where K_m is the bulk modulus of dry rock and K_s is the bulk modulus of skeleton of material. In case of the EGS, the fracture initiation process is affected by induced thermal stresses. The breakdown pressure can be modified to include the effect of thermal induced stresses (Stephens & Voight, 1982). For an impermeable rock mass, the breakdown pressure can be given as follows:

$$p_b = 3\sigma_v - \sigma_h + \sigma_t + \frac{\alpha_T E \Delta T}{1-\nu} \quad (2.23a)$$

For a rock mass permeable to fracturing fluid, the breakdown pressure becomes:

$$p_b = \frac{3\sigma_v - \sigma_h + \sigma_t - \alpha p_p \left(\frac{1-2\nu}{1-\nu} \right) + \frac{\alpha_T E \Delta T}{1-\nu}}{1 + \phi - \alpha \left(\frac{1-2\nu}{1-\nu} \right)} \quad (2.23b)$$

where α_T is the coefficient of linear thermal expansion, and ΔT represents the change in temperature.

2.3.3. Fracture Propagation

One of the important components of fracture mechanics is the prediction of fracture growth rate and growth direction. The fracture propagation process needs to analyze and answer basically two main concerns: the condition under which the critical fracture propagation will start and under what condition an existing crack or fracture will lead to a critical condition (Mi, 1996). The main criterions to describe the hydraulic fracture propagation based on the Linear Elastic Fracture Mechanics (LEFM) are presented in following sections.

1. Maximum Principal Stress Criterion

The maximum principal stress criterion suggests that fracture will grow in a direction perpendicular to the maximum principal stress at the fracture tip (Erdogan & Sih, 1963). For a two-dimensional fracture as shown in Figure 2.8, the circumferential stresses in polar coordinate system can be given as follows (Aliabadi & Rooke, 1991):

$$\sigma_{\theta\theta} = \frac{1}{\sqrt{2\pi r}} \cos \frac{\theta}{2} \left[K_I \cos^2 \frac{\theta}{2} - \frac{3}{2} K_{II} \sin \theta \right] \quad (2.24a)$$

$$\sigma_{r\theta} = \frac{1}{\sqrt{2\pi r}} \cos \frac{\theta}{2} \left[\frac{1}{2} K_I \sin \theta + \frac{1}{2} K_{II} (3 \cos \theta - 1) \right] \quad (2.24b)$$

According to this theory, the fracture growth direction is obtained from condition $\sigma_{r\theta} = 0$ as:

$$K_I \sin \theta_0 + K_{II} (3 \cos \theta_0 - 1) = 0 \quad (2.25)$$

The fracture growth direction from Eq. (2.25) can be written as follows:

$$\tan \frac{\theta_0}{2} = \frac{1}{4} \left[\frac{K_I}{K_{II}} \pm \sqrt{\left(\frac{K_I}{K_{II}} \right)^2 + 8} \right] \quad (2.26)$$

For three-dimensional fracture propagation in mixed mode, the fracture propagation direction can be given as follows (Mi, 1996):

$$\tan \frac{\theta_0}{2} = \frac{1}{4} \left[\frac{K_{Ieff}}{K_{II}} \pm \sqrt{\left(\frac{K_{Ieff}}{K_{II}} \right)^2 + 8} \right] \quad (2.27)$$

where K_{Ieff} is the effective stress intensity factor from Mode-I and Mode-III stress intensity factors.

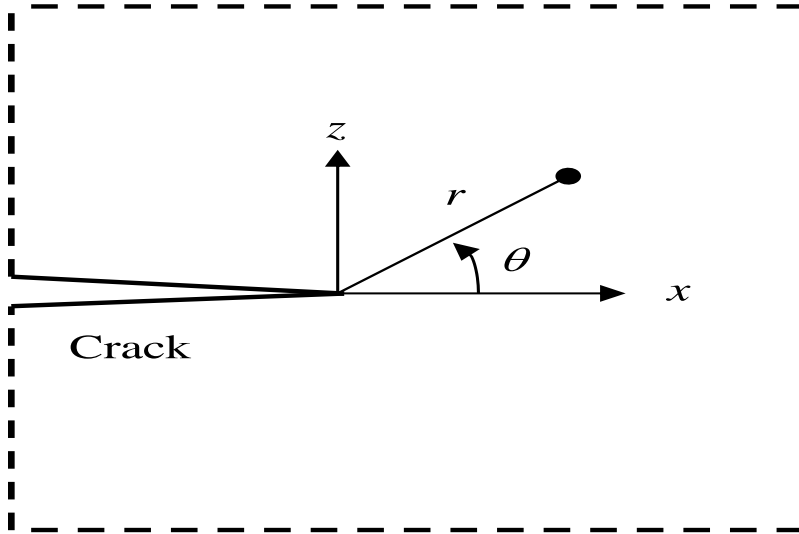


Figure 2.8. Two-dimensional local crack tip coordinate system

2. Maximum Energy Release Rate Criterion (G-Criterion)

Hussain et al. (1974) presented the maximum energy release criterion based on path independent integrals. This criterion is an extension of the Griffith fracture theory in that the fracture will grow in the direction along which the maximum potential energy is released. The fracture growth angle θ_0 is determined by maximizing the strain energy release rate with respect to θ as follows (Mi, 1996):

$$G(\theta) = \left[\frac{(1-\nu^2)}{E} (K_I^{(2)})^2 + \frac{(1-\nu^2)}{E} (K_{II}^{(2)})^2 + \frac{(1+\nu)}{E} (K_{III}^{(2)})^2 \right] \quad (2.28)$$

where the coefficient function as defined as follows:

$$K_I^{(2)}(\theta) = \left(\frac{4}{3 + \cos^2 \theta} \right) \cdot \left(\frac{1 - \theta/\pi}{1 + \theta/\pi} \right)^{\theta/\pi} \left[K_I \cos \frac{\theta}{2} + \frac{3}{2} K_{II} \sin \theta \right] \quad (2.29a)$$

$$K_{II}^{(2)}(\theta) = \left(\frac{4}{3 + \cos^2 \theta} \right) \cdot \left(\frac{1 - \theta/\pi}{1 + \theta/\pi} \right)^{\theta/\pi} \left[K_{II} \cos \frac{\theta}{2} - \frac{1}{2} K_I \sin \theta \right] \quad (2.29b)$$

$$K_{III}^{(2)}(\theta) = K_{III} \quad (2.29c)$$

If, the stress intensity factor values are given, the crack initiation angle θ_0 is obtained by numerically maximizing the above equations.

3. Strain Energy Density Criterion (S-Criterion)

Sih (1974) proposed a mixed-mode fracture propagation criterion based on the strain energy density concept. The strain energy stored in an element of unit thickness for two-dimensional fracture surface is given as follows (Sun & Jin, 2012):

$$dU = \left[\frac{1}{2G} \left\{ \frac{k+1}{8} (\sigma_{xx}^2 + \sigma_{yy}^2) - \left(\frac{3-k}{4} \right) \sigma_{xx} \sigma_{yy} + \sigma_{xy}^2 \right\} \right] dV \quad (2.30)$$

where the coefficient k is same as defined in Eq.(2.7) for plane strain and plane stress conditions. Substituting, the fracture tip stresses for the Mode-I and Mode-II opening from Eqs. (2.6) and (2.8) into Eq. (2.30) results as follows:

$$\frac{dU}{dV} = \frac{1}{r} \left[a_{11}K_I^2 + 2a_{12}K_I K_{II} + 2a_{22}K_{II}^2 \right] \quad (2.31)$$

where the coefficients are defined as (Mi,1996):

$$a_{11} = \frac{1}{16\pi G} [(k - \cos\theta)(1 + \cos\theta)] \quad (2.32a)$$

$$a_{12} = \frac{1}{16\pi G} \sin\theta [2\cos\theta - (k - 1)] \quad (2.32b)$$

$$a_{22} = \frac{1}{16\pi G} [(k + 1)(1 - \cos\theta) + (1 + \cos\theta)(3\cos\theta - 1)] \quad (2.32c)$$

The Eq. (2.31) shows that the strain energy density function has singularity of $O(r^{-1})$ near the fracture tip. The singular field intensity can be expressed using the strain energy density function defined as (Sih, 1974):

$$S = (a_{11}K_I^2 + 2a_{12}K_I K_{II} + a_{22}K_{II}^2) \quad (2.33)$$

The strain energy density criterion is based on two fundamental hypotheses: the fracture will extend in the direction of minimum strain energy density and the fracture extension occurs when the minimum strain density factor reaches to a critical value. The fracture growth direction can be determined based on conditions as follows (Sun & Jin, 2012):

$$\begin{aligned} \frac{\partial S}{\partial \theta} &= 0 ; \quad \text{at } \theta = \theta_0 \\ \frac{\partial^2 S}{\partial \theta^2} &> 0 ; \quad \text{at } \theta = \theta_0 \end{aligned} \quad (2.34)$$

2.3.4. Fracture Fluid Flow

The fluid flow process in a hydraulic fracture involves various complex phenomena of fluid mechanics such as rheologically-controlled flow, variation of the fracture cross-section with time and space, and the fluid diffusion into the reservoir rocks. In the case of the EGS, high reservoir temperatures introduce additional complexity in the fluid flow process by changing the fluid physical properties (e.g., viscosity and density). The fluid flow process in a hydraulic fracture is analyzed based on the combination of the mass and momentum conservation phenomenon, which are described below:

The mass conservation law suggests that for a fixed domain, the change of fluid mass with time is equal to zero. Mathematically, the statement of mass conservation can be represented based on continuity equation as follows (Reddy & Gartling, 1994):

$$\frac{D\rho}{Dt} + \rho \nabla \cdot \mathbf{V} = 0 \quad (2.35)$$

where $\mathbf{V} = (v_x, v_y, v_z)$ is the fluid velocity vector, ρ is the fluid density, ∇ is divergence operator, and the material derivative is defined as:

$$\frac{D}{Dt} = \frac{\partial}{\partial t} + v_x \frac{\partial}{\partial x} + v_y \frac{\partial}{\partial y} + v_z \frac{\partial}{\partial z} \quad (2.36)$$

For an incompressible fluid, the density changes following a fluid particle are negligible which results as $D\rho/Dt = 0$; hence, continuity equation (2.35) results in the incompressibility constraint as follows:

$$\nabla \cdot \mathbf{V} = 0 \quad (2.37)$$

The momentum conservation law, which is based on the Newton's second law of motion, suggests that the rate of change of linear momentum with time is equal to the sum of external

forces acting on the region. Mathematically, the statement of momentum conservation law can be represented as follows (Reddy & Gartling, 1994):

$$\rho \frac{D\mathbf{V}}{Dt} = \rho \mathbf{F} + \nabla \cdot \boldsymbol{\sigma} \quad (2.38)$$

where $\mathbf{F} = (f_x, f_y, f_z)$ is the body force vector, and $\boldsymbol{\sigma}$ is the Cauchy stress tensor.

3. Governing Equations for the Fracture Fluid Flow

Hydraulic fractures basically consist of narrow channels of variable cross-sections, spacing, and surface roughness (Ghassemi, 2003). A laminar fluid flow and the lubrication approximation can be assumed for a flow of high viscosity fluid with sufficiently small fluid injection rate. For an incompressible fluid, if we assume that the temperature effects are not important and neglecting the gravitational forces, the laminar fracture fluid flow is governed by the Navier-Stokes as follows (Currie, 2003):

$$\rho \frac{D\mathbf{V}}{Dt} = \rho \mathbf{F} - \nabla p + \mu \nabla^2 \mathbf{V} \quad (2.39)$$

where $\mathbf{V} = (v_x, v_y, v_z)$ is fluid velocity vector, p is the fluid pressure, ρ is the fluid density, μ is the fluid viscosity, $\mathbf{F} = (f_x, f_y, f_z)$ is the body force vector. In general, the hydraulic fracture width is very less as compare to the other two-dimensions: length and height; hence, the fluid flow essentially follows the Hele-Shaw's parallel plate model (Harr, 1962) as shown in Figure 2.9. Therefore, the fluid pressure variation across the fracture width is negligible and the derivatives of the velocity component in the x and y directions with respect to z direction are much larger. Neglecting the fluid pressure variation along z - axis, Eq. (2.39) in absence of inertia and body forces can be written as (Yew, 1997):

$$\rho \left(\frac{\partial v_x}{\partial t} + v_x \frac{\partial v_x}{\partial x} + v_y \frac{\partial v_x}{\partial y} \right) = \mu \nabla^2 v_x - \frac{\partial p}{\partial x} \quad (2.40a)$$

$$\rho \left(\frac{\partial v_y}{\partial t} + v_x \frac{\partial v_y}{\partial x} + v_y \frac{\partial v_y}{\partial y} \right) = \mu \nabla^2 v_y - \frac{\partial p}{\partial y} \quad (2.40b)$$

$$\frac{\partial p}{\partial z} = 0 \quad (2.40c)$$

Substituting $\frac{\partial v_x}{\partial t} = \frac{\partial v_y}{\partial t} = 0$ in the above equations, the fluid pressure variation for steady-state flow can be given as follows:

$$\frac{\partial p}{\partial x} = \mu \frac{\partial^2 v_x}{\partial z^2} \quad (2.41a)$$

$$\frac{\partial p}{\partial y} = \mu \frac{\partial^2 v_y}{\partial z^2} \quad (2.41b)$$

Integrating Eq. (2.41) twice with respect to z results to:

$$v_x = \frac{z^2}{2\mu} \frac{\partial p}{\partial x} + a_1 z + a_2 \quad (2.42a)$$

$$v_y = \frac{z^2}{2\mu} \frac{\partial p}{\partial y} + a_3 z + a_4 \quad (2.42b)$$

where a_1 , a_2 , a_3 and a_4 are integration constants.

Paterson (1983) suggested that the no-slip condition is important boundary condition for the Navier-Stokes equation, which states that at any boundary between the fluid and a solid, the velocity vector of the fluid must be equal to that of the solid. The no-slip condition implies that the fluid has zero velocity at the walls and at the top and bottom. Hence, Eq. (2.42) is subjected to following boundary conditions:

$$\frac{\partial v_x}{\partial z} = \frac{\partial v_z}{\partial z} = 0; \text{ at } z = 0$$

$$v_x = v_y = 0 \quad ; \quad \text{at } z = \pm \frac{w}{2}$$
(2.43)

where w is fracture width.

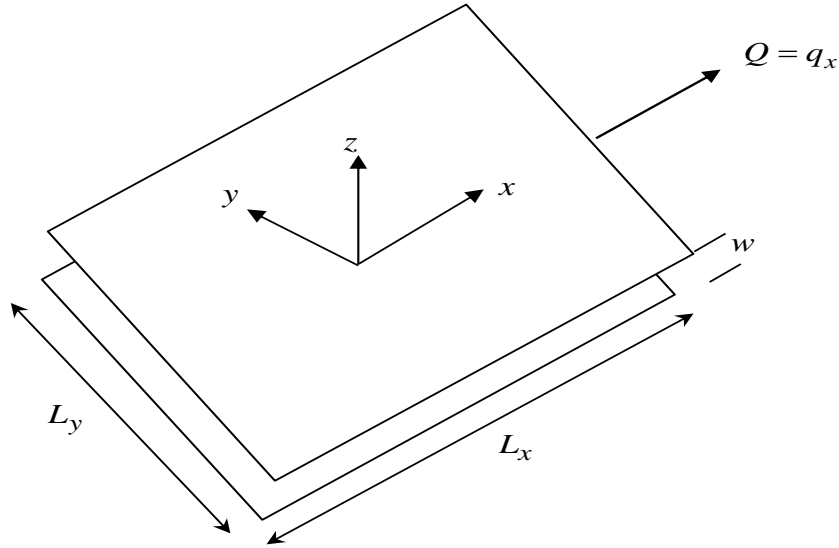


Figure 2.9. Schematic of parallel plate fluid flow inside a fracture

Applying the boundary conditions from Eq. (2.43), the fluid velocity components in x - and y -directions are given as:

$$v_x = -\frac{1}{2\mu} \left[\left(\frac{w}{2} \right)^2 - z^2 \right] \frac{\partial p}{\partial x}$$
(2.44a)

$$v_y = -\frac{1}{2\mu} \left[\left(\frac{w}{2} \right)^2 - z^2 \right] \frac{\partial p}{\partial y}$$
(2.44b)

Equation (2.44) represents a parabolic fluid flow variation along the fracture width as shown in Figure 2.10. It is obvious from Eq. (2.44) that the fluid flow has maximum velocity at middle of the fracture and it diminishes at the boundaries.

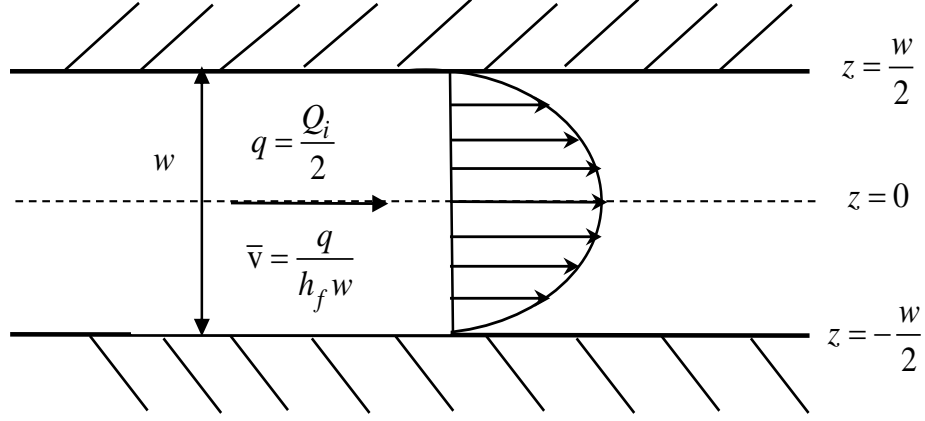


Figure 2.10. Fluid flow velocity profile in a fracture approximated by two parallel plates

The average velocity components can be obtained by integrating Eq. (2.44) over the fracture width as:

$$\bar{v}_x = -\frac{1}{2\mu w} \int_{-w/2}^{w/2} \left\{ \left[\left(\frac{w}{2} \right)^2 - z^2 \right] \frac{\partial p}{\partial x} \right\} dz \quad (2.45a)$$

$$\bar{v}_y = -\frac{1}{2\mu w} \int_{-w/2}^{w/2} \left\{ \left[\left(\frac{w}{2} \right)^2 - z^2 \right] \frac{\partial p}{\partial y} \right\} dz \quad (2.45b)$$

If b is the fracture length, then multiplication by cross-sectional area open to flow, bw the fluid flow components can be given as:

$$q_x = -\frac{bw^3}{12\mu} \frac{\partial p}{\partial x} \quad (2.46a)$$

$$q_y = -\frac{bw^3}{12\mu} \frac{\partial p}{\partial y} \quad (2.46b)$$

where q_x and q_y are fluid flow components in the x and y directions, respectively. The flow rate per unit fracture length is represented as follows:

$$q_i = -\frac{w^3}{12\mu} \frac{\partial p}{\partial x_i} ; \quad i = x, y \quad (2.47)$$

where p_i is the fluid pressure gradient in the i th direction. The above equation is known as the cubic law of fluid flow (Witherspoon et al., 1980). Detailed methodology for numerical implementation of Eq. (2.47) will be discussed in Chapter 4.

5. Rheological Behavior of Fracturing Fluids

Fluid rheology is basically the response of fluid due to applied stresses. Fluid rheology describes the relationship between applied forces, deformation, and time. Based on the rheological behavior, fluids can be classified in two categories as Newtonian or non-Newtonian. Newtonian fluids exhibit a direct proportionality between the shear stress and the shear rate in laminar fluid. The rheology for a Newtonian fluid can be given as follows (Valko & Economides, 1995):

$$\tau = \mu \dot{\gamma} \quad (2.48)$$

where τ is the shear stress, $\dot{\gamma}$ is the shear rate, and the proportionality constant μ is the fluid viscosity. Fluid viscosity is independent of the shear stress and it is a function of temperature and pressure of fluid system (Skelland, 1967). However, a non-Newtonian fluid shows a complex relationship between the shear stress and the shear rate. Several models are available to describe the shear stress response of non-Newtonian fluids. The simplest rheological for non-Newtonian fluids is the power law model, which has two constants: a power law index and a consistency index. Mathematically, the power-law model is given as follows (Whittaker, 1985):

$$\tau = K (\dot{\gamma})^n \quad (2.49)$$

where $\dot{\gamma}$ is shear rate, n is the power law index and K is the consistency index. For power-law fluid, the fluid apparent viscosity can be defined as:

$$\mu_a = K (\dot{\gamma})^{n-1} \quad (2.50)$$

The power law can describe the rheological behavior of both the pseudo-plastic as well as dilatant fluids. If $n < 1$, the fluid behaves as pseudo-plastic and if $n > 1$, it behaves as dilatant.

2.3.5. Fluid Diffusion and Leak-off

During hydraulic fracturing process, some of the injected fluids can be lost either due to fluid storage, or spurt loss or fluid diffusion or leak-off into the reservoir. The fluid storage is basically equal to the fracture volume. The spurt loss is defined as the fluid quantity used in wetting of the fracture surfaces, whereas, the fluid diffusion or leak-off is the fluid loss due to escape of injected fluid through preexisting cracks or thermal induced cracks. Mathematically, the total fluid loss through a fracture surface can be represented as follows (Wiles, 1986):

$$V_L = wL + 2S_p L + q_L \quad (2.51)$$

where V_L is the total fluid loss volume, w is the fracture aperture, L is the wetted fracture length which is normally equal to the fracture length, S_p is the spurt loss coefficient, and q_L is the fluid leak-off. One-dimensional fluid leak-off consideration is mostly used in the hydraulic fracture simulator models from the fracture surface. For a more accurate estimation of fluid leak-off, a pressure dependent model can be used.

Carter (1957) introduced a fluid leak-off model based on the assumption that the fluid leaks in one-dimensional steady state potential flow perpendicular to the fracture wall. The fluid leak-off rate can be represented using assumption that it decreases proportional to inverse of square root of the time from the fracture surface creation. Mathematically, the constant leak-off model can be represented as follows:

$$q_L(x, y, t) = \frac{2C_L}{\sqrt{t - \tau(x, y)}} \quad (2.52)$$

where C_L is the leak-off coefficient which can be determined experimentally, t is the current pumping time, and $\tau(x, y)$ is the time at which the fluid starts to leak-off at any location (x, y) of the fracture surface. For field application of constant leak-off model, the coefficient C_L is experimentally determined using mini-frac test, which can predict an average fluid leak-off over the fracture surface.

2.3.6. Fracture Heat Flow

The heat flow analysis in case of EGS reservoirs is important in two respects. Firstly, estimation of change in the fluid and rock temperature during the fracturing initiation and propagation process is important to account for the thermal-induced stresses over these processes and for modeling the temperature sensitive fluid flow. The change in the temperature can affect the physical properties of the fracturing fluid as well as of the reservoir rock. The temperature distribution inside the fracture can be estimated by the thermal conduction-advection equation (Clifton et al., 1989):

$$\frac{\partial}{\partial t} [\rho_f c_f T(x, y, t)] = K_r \nabla^2 T(x, y, t) - \nabla [\rho_f c_f \bar{v} T(x, y, t)] \quad (2.53)$$

where $T(x, y, t)$ is the fluid temperature at any given time and location, ρ_f and c_f are the fluid density and specific heat, respectively, K_r is the rock thermal conductivity, \bar{v} is the average fluid velocity. Equation (2.53) can be solved numerically with the appropriate initial and boundary conditions for the temperature distribution in the fractures. Once, the temperature distribution inside the fracture is known it can be coupled with the fracturing and fluid flow models.

The second important aspect of the heat flow analysis in the EGS reservoirs is the heat extraction modeling for estimation of thermal energy production. The thermal energy from an EGS reservoir is recovered by circulating water through the reservoir fracture network. The injection of the fluid with different temperature from the reservoir rock temperature induces heat conduction and advection processes. The heat flow inside the fracture occurs mainly by advection process due to fluid mass movement. However, heat conduction and convection (e.g. due to fluid leak-off into reservoir) process occurs between the host reservoir rock and the fracture surface. Since most of the reservoir rocks in case of the EGS have very limited or negligible permeability no fluid leak-off condition can be assumed for the heat flow analysis. Therefore, the heat flow between the reservoir and the fracture surface is mainly conduction-dominated. The mathematical description of the heat conduction and advection processes in the EGS heat flow modeling is provided in the following sections.

1. Heat Conduction between the Fracture and the Reservoir Rocks

The heat conduction process between the fracture surface and the reservoir rocks can be represented by the transient diffusion equation as follows (Carslaw & Jaeger, 1959):

$$\frac{\partial}{\partial x} \left[k_x(T) \frac{\partial T}{\partial x} \right] + \frac{\partial}{\partial y} \left[k_y(T) \frac{\partial T}{\partial y} \right] + \frac{\partial}{\partial z} \left[k_z(T) \frac{\partial T}{\partial z} \right] + Q_i = \rho_r c_r \frac{\partial T}{\partial t} \quad (2.54)$$

where T represents temperature, ρ_r and c_r are the rock density and specific heat, respectively, Q_i is the internal heat generation per unit volume, and $k_x(T)$, $k_y(T)$, $k_z(T)$ are the temperature-dependent thermal conductivities in the x , y and z directions, respectively. The thermal conductivities can be function of space and temperature. For a homogeneous and isotropic rock mass with temperature-independent thermal conductivity, in absence of the heat internal heat generation Eq. (2.54) can be written as follows:

$$\frac{\partial^2 T}{\partial x^2} + \frac{\partial^2 T}{\partial y^2} + \frac{\partial^2 T}{\partial z^2} = \frac{\rho_r c_r}{K_r} \frac{\partial T}{\partial t} \quad (2.55)$$

2. Heat Advection-Diffusion inside the Fracture

The heat flow process inside the fracture is governed by the heat advection-conduction process. Cheng et al. (2001) described in their work that the fluid diffusion can be neglected in case of continuous injection of cooling fluid and large advection velocities. Based on these assumptions, the governing equation for fluid flow inside the fracture can be given as follows (Ghassemi et al., 2005):

$$\rho_f c_f \nabla \cdot [\mathbf{q}(x, y) T(x, y, 0, t)] = \left[2K_r \frac{\partial T(x, y, z, t)}{\partial z} \Big|_{z=0^+} + \rho_f c_f \sum_{i=1}^{N_w} Q_i T(x_i, y_i, 0, t) \cdot \delta(x-x_i, y-y_i) \right] \quad (2.56)$$

where $\mathbf{q}(x, y)$ is the fluid flow vector, Q_i is the source or sink intensity, and δ is Dirac delta function.

2.4. Hydraulic Fracture Modeling

The theoretical modeling of hydraulic fracturing started in late 1950's. Khristianovich & Zheltov (1955) presented the first hydraulic fracture model based on the assumption of constant height growth of fracture planes. One of the milestones in two-dimensional hydraulic fracture modeling was given by Perkins & Kern (1961) based on the classic Sneddon's plane strain crack solution (Sneddon, 1946). Geertsma & de-Klerk (1969) presented the Khristianovich, Geertsma & de-Klerk Model (KGD model) based on the earlier work of Khristianovich & Zheltov. Nordgren (1972) modified the Perkins and Kern's model by including the effect of fluid losses on the fracture geometry and presented the generalized Perkins, Kern, and Nordgren model (PKN model) (Perkins & Kern, 1961). These earlier models are based on the assumption that the hydraulic fractures propagates essentially in two-dimensional planes. However, from the field

and experimental observations it can be concluded that in general hydraulically induced fractures grow in three-dimensional planes with varying fracture height, length, aperture and shape. Therefore, for accurate prediction of fracture geometries, three-dimensional modeling of the hydraulic fracture process is required. Three-dimensional models started to appear in the fracture modeling community since 1980's. A brief description of several hydraulic fracture models are provided in following sections.

2.4.1. Two-Dimensional Fracture Models

Two types of constant fracture height fracture models are used for two-dimensional hydraulic fracture modeling: the PKN and KGD models. Both the PKN and KGD models assume that the fracture toughness (or tensile strength) is sufficiently small and the fracture growth is mainly controlled by the fluid viscosity. The fracture height during propagation is assumed to be constant for both the models. A brief mathematical description of the PKN and the KGD model is discussed in the following sections.

1. Perkins, Kern and Nordgren (PKN) Model

The PKN model is based on the assumption that the cross-section of the fracture in vertical plane, perpendicular to the long axis of the fracture, maintains an elliptical configuration and plane strain condition exists in the vertical plane. A schematic of the PKN fracture geometry is shown in Figure 2.11. The fluid pressure inside the fracture is assumed to be constant and proportional the fracture aperture. The net fluid pressure and fracture aperture are related as follows (Sneddon, 1946):

$$w(x,t) = \frac{(1-\nu)p_{net}h_f}{G} \sqrt{1 - \left(\frac{x}{L}\right)^2} \quad (2.57)$$

where $w(x,t)$ is the fracture aperture at any given time, p_{net} is the net fluid pressure, h_f and L are the fracture height and length, G is the shear modulus and ν is the Poisson's ratio. Considering, the mass conservation condition and assuming incompressible Newtonian fluid flow inside the fracture, the fracture propagation condition in absence of fluid leak-off is given as follows (Gidley et al., 1989):

$$\frac{G}{64(1-\nu)\mu h_f} \frac{\partial^2 w^2}{\partial x^2} - \frac{\partial w}{\partial t} = 0 \quad (2.58)$$

where μ is the fluid viscosity. The above equation is subjected to following initial and boundary conditions:

$$w(x,0) = 0; \quad \text{for } t = 0 \quad (2.59a)$$

$$w(x,t) = 0; \quad \text{for } x \geq L(t) \quad (2.59b)$$

The analytical solution of Eq. (2.58) for the fracture aperture, fracture length and maximum wellbore pressure for constant fluid injection rate are given as follows (Nordgren, 1972):

$$w_0(0,t) = 2.5 \left[\frac{(1-\nu)\mu Q_i^2}{G h_f} \right]^{1/5} \cdot t^{1/5} \quad (2.60a)$$

$$L(t) = 0.68 \left[\frac{G Q_i^3}{(1-\nu)\mu h_f^4} \right]^{1/5} \cdot t^{4/5} \quad (2.60b)$$

$$p_{net,w}(0,t) = 2.5 \left[\frac{G^4 \mu Q_i^2}{(1-\nu)^4 h_f^4} \right]^{1/5} \cdot t^{1/5} \quad (2.60c)$$

where $w_0(0,t)$ is the maximum wellbore aperture, $L(t)$ is the fracture length, and $p_{net,w}(0,t)$ is the fluid pressure at the wellbore. The shape of the fracture takes the form as:

$$w(x,t) = w(0,t) \cdot \left(1 - \frac{x}{L}\right)^{1/4} \quad (2.61)$$

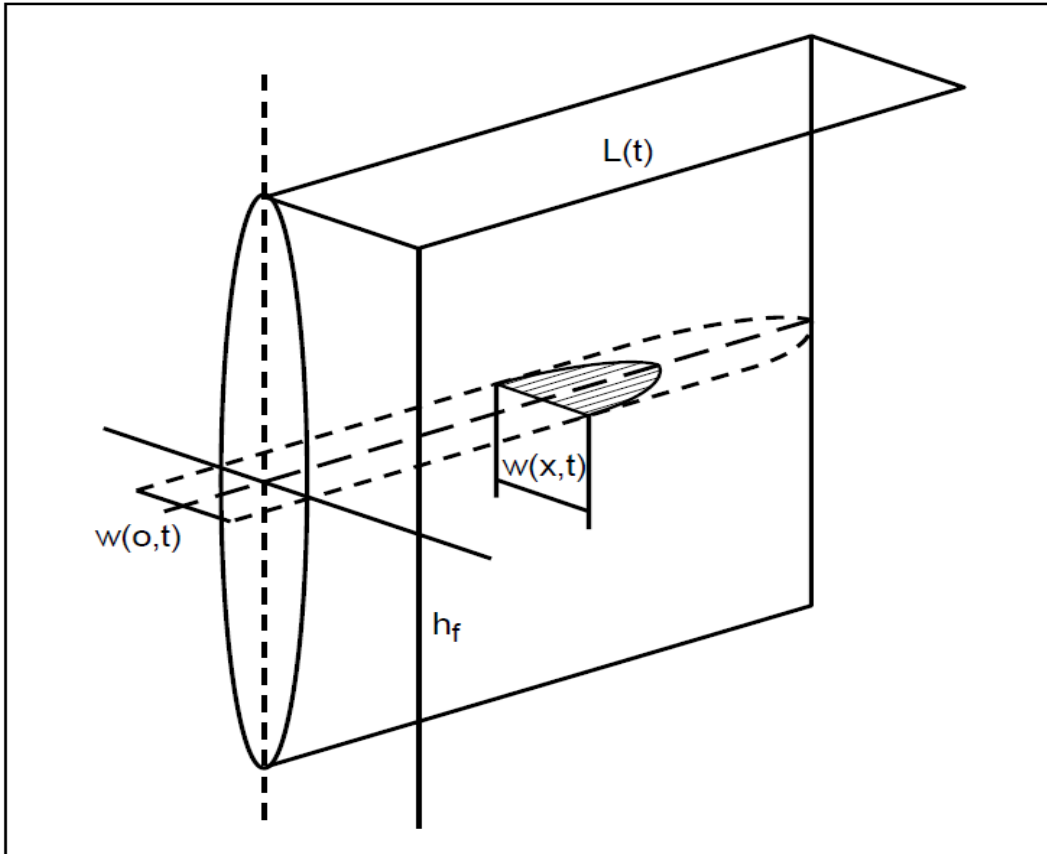


Figure 2.11. PKN constant height fracture model (Economides & Nolte, 2000)

2. Khristianovich, Geertsma and de-Klerk Model (KGD) Model

The KGD model assumes an approximately elliptical configuration in the horizontal plane and a rectangular shape in the vertical plane as shown in Figure 2.12. Plane strain condition is assumed in the horizontal cross-section of the fracture surface. For a rectangular cross section, the pressure gradient is given as follows (Economides & Nolte, 2000):

$$\frac{\partial p}{\partial x} = -\frac{12\mu Q_i}{h_f w^3(x,t)} \quad (2.62)$$

Integrating above equation over the fracture length as:

$$p_{net} = \frac{6\mu Q_i}{h_f} \int_0^L \frac{dx}{w^3(x,t)} \quad (2.63)$$

Applying, Barenblatt's tip condition which requires smooth closing of the fracture tip, results as follows (Barenblatt, 1962):

$$\int_0^L \frac{p_{net}(x)}{\sqrt{1-(x/L)^2}} dx = 0 \quad (2.64)$$

The maximum fracture aperture for constant height and infinite extension as suggested by Sneddon & Elliot (1946) can be given as follows:

$$w = \frac{2p_{net}h_f(1-\nu^2)}{E} \quad (2.65)$$

Substituting $h_f = 2L$, gives width profile for a constant net pressure over the entire fracture surface. Mathematically, it can be represented as:

$$w_0 = \frac{4p_{net}L(1-\nu^2)}{E} \quad (2.66)$$

The analytical solution based on above equations for the fracture aperture, fracture length and maximum wellbore pressure for constant fluid injection rate are given as follows (Geertsma & de Klerk, 1969):

$$w_0(0,t) = 1.87 \left[\frac{(1+\nu)\mu Q_i^3}{Gh_f^3} \right]^{1/6} \cdot t^{1/3} \quad (2.67a)$$

$$L(t) = 0.68 \left[\frac{GQ_i^3}{\mu(1-\nu)h_f^3} \right]^{1/6} \cdot t^{2/3} \quad (2.67b)$$

fracture geometry. The hydraulic fracture models which can address the main constraints of the classical two-dimensional models are categorized as: pseudo three-dimensional (P3D) models, planar three-dimensional model, and general or truly three-dimensional model.

The P3D models are based on the assumption that the fracture length is sufficiently large relative to its height, hence effective rock elastic stiffness is independent of the fracture length and the horizontal distance from the cross section of the crack front (Adachi et al., 2007). The vertical fluid flow is included in P3D model which allows the fracture height variation with time and distance from the wellbore (Ben-Naceur, 1989). Warpinski (1993) classified P3D models in two categories: cell based and lump based models. The cell based P3D models are basically extension of the PKN type model. The fracture length is sub-divided into series of cells with each having their own compacted height. The plain strain condition can be assumed at any cross section. The fluid flow is assumed to be essentially horizontal along the fracture length. However; in case of lumped based P3D models, the fracture geometry at each time step consists of two half-ellipses. These ellipses are joined at their center in the fracture length direction.

Several hydraulic fracturing simulator models have been developed based on two-dimensional, pseudo three-dimensional, and planar three-dimensional approach. These models work very well in cases where fracture geometries are limited to single planes and which are which defined (Carter et al., 2000). However, in case of complex fracture geometry such as those emanating from deviated wellbores with arbitrary crack front, advanced fracture simulation models are required. Two-dimensional or P3D models are not capable of addressing two important characteristics of the hydraulic fracturing process: height growth and out-of plane fracture propagation. Settari (1979) & Cleary et al. (1983) developed planar three-dimensional models, which can address the height growth issue. However; to account for the constraints of

simplified fracture geometries, fully three-dimensional models are required (Vandamme & Curran, 1989). Clifton & Sayed (1981), Cleary et al. (1983), and Wiles & Curran (1982) presented three-dimensional fracture models based on the integral equation formulation. Due to increased use of deviated wellbores in petroleum industry, the fully three-dimensional fracture prediction models are very vital for stimulation prediction. Hydraulic fracturing is often less effective for deviated wellbores as compared to traditional vertical wells, due to a poor understanding of the mechanics of fracture initiation and propagation from a deviated. The main components of three-dimensional hydraulic fracture geometry are shown in Figure 2.13.

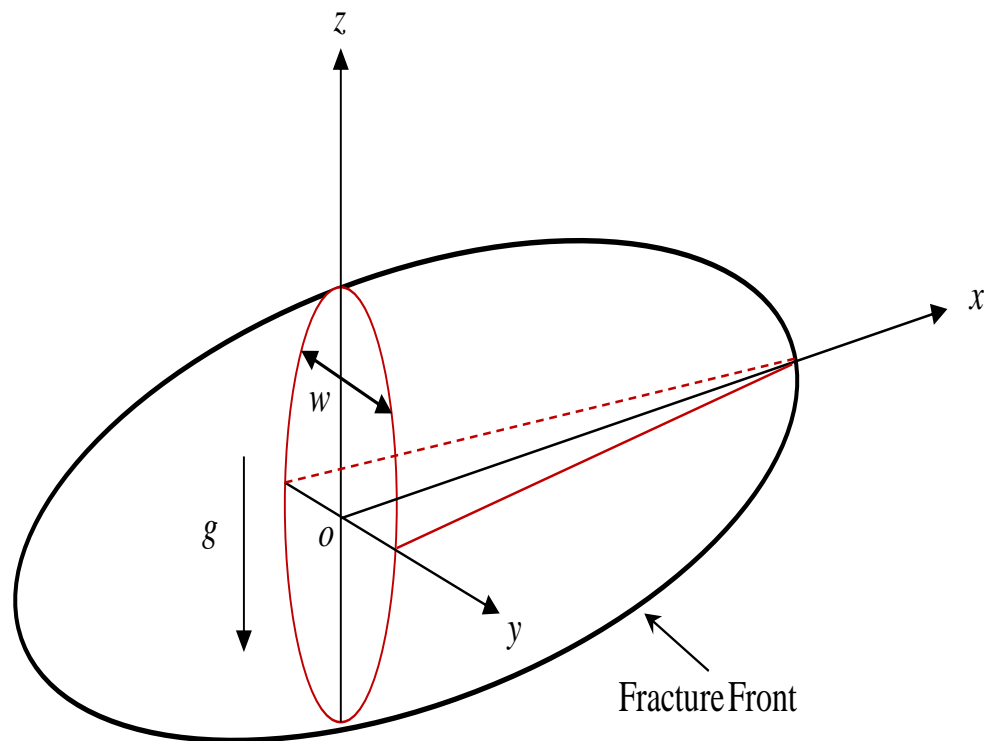


Figure 2.13. Schematic of three-dimensional hydraulic fracture geometry (Yew, 1997)

2.5. Computational Methods for Fracture Mechanics

The Finite Element, Finite Difference, Boundary Element and Discrete Element methods are the main numerical approaches to solve the fracture mechanics problems. The Finite Difference Method (FDM), which is mainly applicable to solving difference equations on domains of regular geometry, has demonstrated limited application in elasticity problems. The Discrete Element Method (DEM) is mostly applied when continuity of a medium cannot be assumed for discontinuous separated domains. The behavior of discontinuities between the bodies is analyzed with the solution of contact and impact between multiple bodies (Pande et al., 1990). The Finite Element Method (FEM) has become widely known and has widespread acceptance for the fracture mechanics analysis. The Boundary Element Method (BEM), which is a relatively newer approach than the other methods, has emerged as a powerful alternative to the FEM. A brief description of the applicability of the FEM and the BEM in the fracture mechanics is provided in following sections.

2.5.1. Finite Element Method

In the FEM, the elastic continuum medium is replaced by a finite number of structural elements of finite size and interconnected only at their nodal points (Zienkiewicz, 1971). By analyzing these individual elements and assembling them, an approximate solution of the actual problem can be obtained. In the FEM, the problem domain can be discretized using triangular or quadrilateral elements in two-dimensional analysis and tetrahedral or brick elements in three-dimensional analysis. The process of discretization results in a system of linear algebraic equations which forms a symmetric and banded matrix. By applying appropriate initial and boundary conditions, these systems of equations can be solved for unknown nodal variables using standard techniques of matrix elimination. Chan et al. (1970) implemented the FEM in

fracture mechanics problems to calculate the stress intensity factor. One of the main difficulties in the fracture mechanics problems is the accurate estimation of the near-crack behavior of the stresses and displacement fields. Henshell & Shaw (1975) introduced quarter point element to improve the accuracy of the stress and displacement fields near the crack tip. The quarter point elements gives quite accurate results of the crack-tip stresses, and is very simple to implement in existing computer programs. In the quarter point element, only the middle node of the quadratic element is required to be replaced at $l/4$ distance from the crack, where l is the length of the crack tip. Later, several crack tip singular elements have been introduced to account for the crack tip behavior (Barsoum, 1976). In fracture propagation problems, near crack tip fracture mesh plays a critical role which needs remeshing after each propagation step. An advanced alternative method to overcome time consuming remeshing process in the conventional FEM is the Extended Finite Element Method (Benzley, 1974). The Extended Finite Element Method (XFEM) eliminated remeshing requirement of the fracture tip region by adding enrichment elements which can be expressed using analytical expressions.

2.5.2. Boundary Element Method

The Boundary Element Method (BEM) presents a powerful numerical method to solve the boundary value problems form various disciplines (Brebbia et al., 1984). The BEM can be applied to fracture mechanics problems by overcoming the limitations associated with the FEM (Aliabadi & Rooke, 1991). The BEM transforms the problem to the boundaries, which eliminates the domain discretization. This significantly reduces the number of elements and avoids the difficulty of domain discretization. The formulation for the BEM problems depends on the fundamental solutions for the class of problems being solved. For elasticity problems, the most commonly used fundamental solution is the Kelvin's solution for displacements and tractions at

a point in an infinite elastic medium due to a unit load applied at another point. The discretization of the boundary converts the set of integral equations into a system of algebraic equations which with appropriate boundary conditions can be solved for unknown variables using standard elimination or iterative solvers. A detailed description of theoretical and numerical aspects of the BEM implementation for the fracture mechanics problems is presented in Chapter 3.

CHAPTER 3.

FRACTURE DEFORMATION MODELING

This chapter presents an introduction to three-dimensional elasticity theory and the Boundary Element Method for the solution of fracture mechanics problems. The Displacement Discontinuity Method (DDM), which is an indirect Boundary Element Method, is discussed in detail as applied to fracture modeling. The formulation and detailed methodology for numerical implementation of two types of DD models, namely, constant strength DD model and generalized point load DD model, are presented. Both the DD models are validated using analytical solution.

3.1. Introduction

The main objective of a hydraulic fracture deformation modeling is to estimate change in the fracture geometry (e.g., aperture, length and height) due to the applied stresses and fluid pressure. The fracture dimensions and propagation characteristics of a hydraulic are important considerations in the design of fracturing operation (Yew, 1997). This section describes fracture models using constant fluid pressure and the main concern is given to change in the fracture aperture.

3.2. Basic Equations of Elasticity

For an infinitesimal three-dimensional element as shown Figure 3.1, equations of equilibrium in terms of stress components can be given as follows (Cruse, 1988):

$$\frac{\partial \sigma_{ij}}{\partial x_j} + b_i = 0 ; \quad i, j = x, y, z \quad (3.1)$$

where σ_{ij} represents the stress components and b_i is the body force vector. The relationship between the strain-displacement is given by the compatibility equation (Timoshenko & Goodier, 1970):

$$\varepsilon_{ij} = \frac{1}{2} \left(\frac{\partial u_i}{\partial x_j} + \frac{\partial u_j}{\partial x_i} \right) \quad (3.2)$$

where ε_{ij} are the strain components and u_i are the displacement components. The constitutive equations or generalized Hooke's law relates stresses to strains of an isotropic and linearly elastic solid as follows (Timoshenko & Goodier, 1970):

$$\sigma_{ij} = \lambda \delta_{ij} \varepsilon_{mm} + 2G \varepsilon_{ij} \quad (3.3)$$

where λ represents the Lamé's elasticity constant, G is the shear modulus, ν is Poisson's ratio, ε_{mm} represents summation of strain components, and δ_{ij} is the Kronecker delta function, which is defined as:

$$\delta_{ij} = \begin{cases} 1; & \text{if } i = j \\ 0; & \text{if } i \neq j \end{cases} \quad (3.4)$$

The shear modulus and Lamé's elasticity constant are related to the Young's modulus and Poisson's ratio as follows:

$$\lambda = \frac{\nu E}{(1 + \nu)(1 - 2\nu)} \quad (3.5a)$$

$$G = \frac{E}{2(1 + \nu)} \quad (3.5b)$$

Substitution of Eq. (3.2) in Eq. (3.3) gives a relationship between stresses and displacements as follows:

$$\sigma_{ij} = \lambda \delta_{ij} \left(\frac{\partial u_m}{\partial x_m} \right) + G \left(\frac{\partial u_i}{\partial x_j} + \frac{\partial u_j}{\partial x_i} \right) \quad (3.6)$$

Substituting, Eq. (3.6) in Eq. (3.1) results in the Navier differential equation for displacements as follows (Becker, 1992):

$$G \frac{\partial^2 u_i}{\partial x_j \partial x_j} + \left(\frac{G}{1-2\nu} \right) \frac{\partial^2 u_j}{\partial x_i \partial x_j} + b_i = 0 \quad (3.7)$$

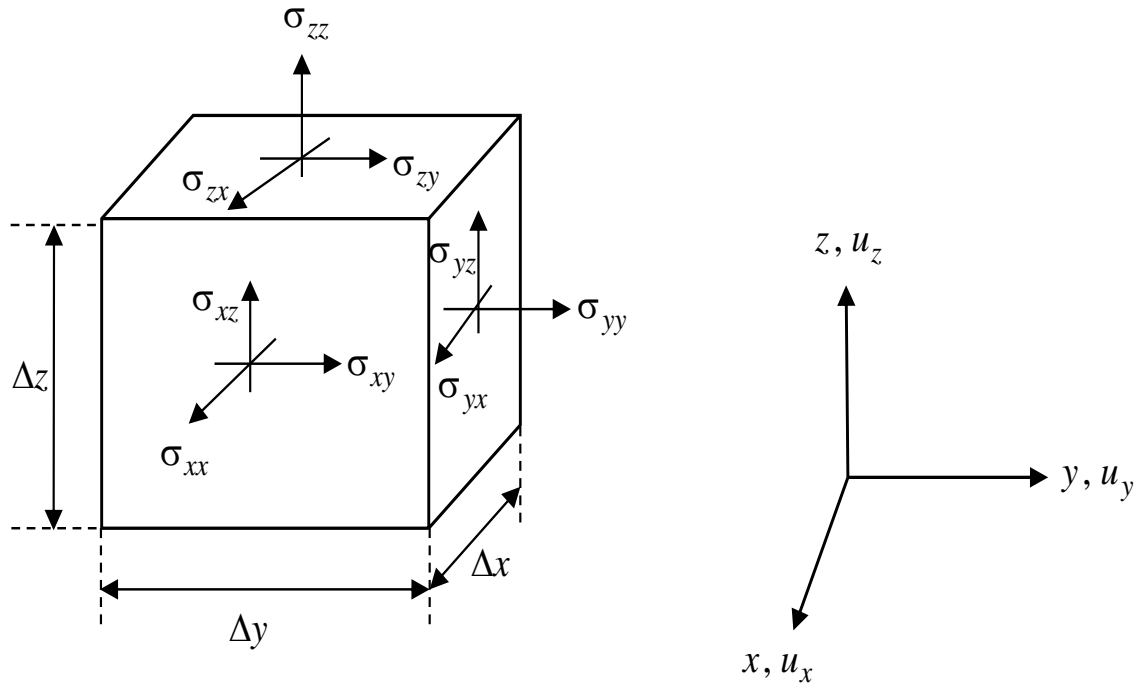


Figure 3.1. Stress components on a three-dimensional infinitesimal element (Becker, 1992)

3.3. Boundary Element Method for Elasticity

The Boundary Element Method (BEM) provides a superior numerical scheme as compared to other numerical scheme (e.g., Finite Element Method, Finite Difference, & Discrete Element Method) for fracture mechanics problems due to its high calculation accuracy and less required unknowns in the numerical solution. The BEM eliminates discretization of the whole domain, which results in a less expensive computational method. The fundamental governing equations for linear elastic, isotropic and homogenous solids and the basic concepts and theorems for the BEM application for the elasticity problems are presented in following sections.

3.3.1. Kelvin's Fundamental Solution

Proposed by Lord Kelvin, the fundamental solutions represents the solutions which satisfies the Navier's displacement differential displacement equation (Love, 1944). The BEM formulation for a particular problem depends mainly on nature of the fundamental solution. For the solution of the Navier differential equation, another displacement vector termed as the *Galerkin vector* is introduced as follows (Brebbia et al., 1984):

$$u_i = \frac{\partial^2 \mathbf{G}_i}{\partial x_j \partial x_j} - \left(\frac{1}{1-2\nu} \right) \frac{\partial^2 \mathbf{G}_j}{\partial x_i \partial x_j} \quad (3.8)$$

where \mathbf{G} is the Galerkin vector. Substituting Eq. (3.8) in Eq. (3.7) results in a bi-harmonic equation as follows:

$$\nabla^2 (\nabla^2 \mathbf{G}_i) + \frac{b_i}{G} = 0 \quad (3.9)$$

where G represents the shear modulus and b_i is the body force vector. Applying a unit force at the source point $\mathbf{x} = (x, y, z)$ to get its effect on the field point $\mathbf{x}' = (x', y', z')$ as shown in Figure 3.2, then this problem is known as the Kelvin's problem. The Kelvin's problem can be solved based on two basic conditions of the fundamental solutions: the stress must become infinite as the distance between the source point and field point tends to zero and the stresses become zero as the distance tends to infinite. Based on these two fundamental conditions, Cruse (1977) proposed an analytical solution of Eq. (3.9) based on the Galerkin vector as follows:

$$\mathbf{G}_i = \frac{1}{8\pi(1-\nu)} R(\mathbf{x}, \mathbf{x}') \quad (3.10)$$

where $R(\mathbf{x}, \mathbf{x}')$ is the distance between the source and field points. Substituting, the fundamental solution from above equation in Eq. (3.8) gives the displacement vector as follows:

$$u_i = U_{ij}(\mathbf{x}, \mathbf{x}') \cdot \mathbf{n}_j \quad (3.11)$$

where \mathbf{n}_j is the unit vector in the j th direction and $U_{ij}(\mathbf{x}, \mathbf{x}')$ represents the displacement fundamental solutions for the Kelvin problem, which is defined as follows (Aliabadi & Rooke, 1991):

$$U_{ij}(\mathbf{x}, \mathbf{x}') = \frac{1}{16\pi G(1-\nu)R} \left\{ (3-4\nu)\delta_{ij} + R_{,i} R_{,j} \right\} \quad (3.12)$$

where the distance R between the source and field points and its derivatives are given as follows (Beer, 2001):

$$R = \sqrt{(x-x')^2 + (y-y')^2 + (z-z')^2} \quad (3.13a)$$

$$R_{,1} = \frac{x-x'}{R} ; R_{,2} = \frac{y-y'}{R} ; R_{,3} = \frac{z-z'}{R} \quad (3.13b)$$

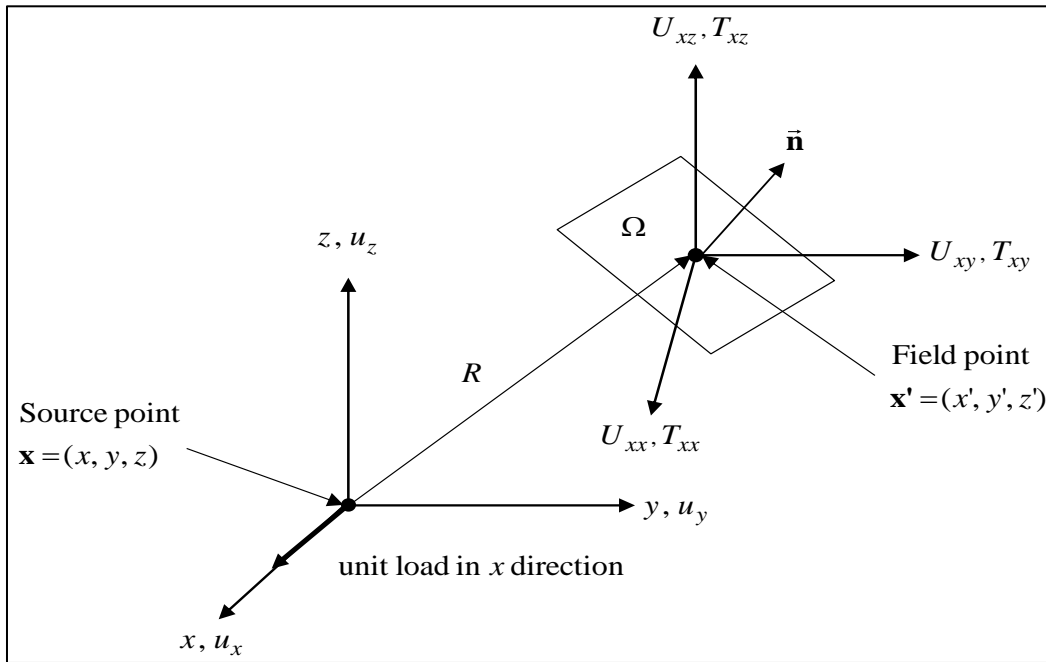


Figure 3.2. Representation of source and field points and components of displacement and traction fundamental solution (Brebbia et al., 1984)

The traction vector arising from the fundamental solution can be obtained by differentiating the displacement fundamental solution in Eq. (3.12) and substituting them in the Hooke's law in Eq. (3.3). The resultant traction vector is given as follows:

$$t_i = T_{ij}(\mathbf{x}, \mathbf{x}') \cdot \mathbf{n}_j \quad (3.14)$$

where $T_{ij}(\mathbf{x}, \mathbf{x}')$ are the traction fundamental solutions for the Kelvin's problem, which are defined as follows (Aliabadi & Rooke, 1991):

$$T_{ij}(\mathbf{x}, \mathbf{x}') = \frac{-1}{8\pi(1-\nu)R^2} \left\{ \frac{\partial R}{\partial \mathbf{n}} \left[(1-2\nu)\delta_{ij} + 3R_{,i} R_{,j} + (1-2\nu)(n_j R_{,i} - n_i R_{,j}) \right] \right\} \quad (3.15)$$

where $\frac{\partial R}{\partial \mathbf{n}}$ represents the derivatives of distance with respect to normal vector as follows:

$$\frac{\partial R}{\partial \mathbf{n}} = R_{,i} n_i + R_{,j} n_j + R_{,k} n_k \quad (3.16)$$

where $R_{,i}$, $R_{,j}$, $R_{,k}$ and n_i , n_j , n_k are the derivatives distance with respect and unit normal in the i th, j th and k th directions, respectively.

3.3.2. Betti's Reciprocal Work Theorem

Betti's reciprocal theorem forms the basis for the BEM formulation for elasto-static problems (Ameen, 2005). Consider a body under equilibrium with two different sets of stresses and strains as shown in Figure 3.3: set (a) which has the stresses and strains as $(\sigma_{ij}^{(a)}, \varepsilon_{ij}^{(a)})$ and set (b) which has the stresses and strains as $(\sigma_{ij}^{(b)}, \varepsilon_{ij}^{(b)})$. The Betti's reciprocal theorem states that work done by the stresses of set (a) on the strains of set (b) is equal to work done by the stresses of set (b) on the strains of set (a). Mathematically, this statement can be represented as follows (Banerjee & Butterfield, 1981):

$$\int_{\Omega} \sigma_{ij}^{(a)} \varepsilon_{ij}^{(b)} d\Omega = \int_{\Omega} \sigma_{ij}^{(b)} \varepsilon_{ij}^{(a)} d\Omega \quad (3.17)$$

Following the strain and displacement relationship, the above equation can be written as follows:

$$\frac{1}{2} \int_{\Omega} \sigma_{ij}^{(a)} \left(\frac{\partial u_i}{\partial x_j} + \frac{\partial u_j}{\partial x_i} \right)^{(b)} d\Omega = \frac{1}{2} \int_{\Omega} \sigma_{ij}^{(b)} \left(\frac{\partial u_i}{\partial x_j} + \frac{\partial u_j}{\partial x_i} \right)^{(a)} d\Omega \quad (3.18)$$

Integrating both sides of Eq. (3.18) following Green's theorem and using the strain-displacement and body forces, the expression for Betti's theorem follows as:

$$\int_{\Omega} b_i^{(a)} u_i^{(b)} d\Omega + \int_{\Gamma} t_i^{(a)} u_i^{(b)} d\Gamma = \int_{\Omega} b_i^{(b)} u_i^{(a)} d\Omega + \int_{\Gamma} t_i^{(b)} u_i^{(a)} d\Gamma \quad (3.19)$$

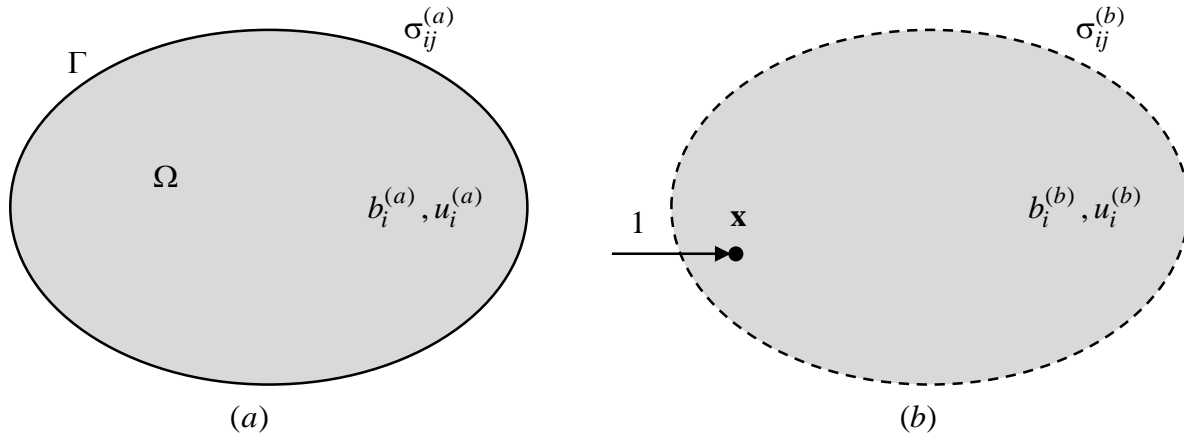


Figure 3.3. An elastic body subjected to two different systems of forces

3.3.3. Somigliana's Identity

Somigliana's identity can be derived from the Betti's reciprocal theorem and by using Kelvin's fundamental solutions. If the first set of displacements, tractions and body forces acting in a domain Ω and boundary Γ , as shown in Figure 3.3, are u_i, t_i, b_i and the second set are chosen as the fundamental fields at an internal point \mathbf{x}' , then the Betti's reciprocal Eq. (3.19) can be written as follows:

$$\int_{\Gamma+\Gamma_\varepsilon} U_{ij}(\mathbf{x}, \mathbf{x}') t_j(\mathbf{x}') d\Gamma(\mathbf{x}') + \int_{\Omega} U_{ij}(\mathbf{x}, \mathbf{x}') b_j(\mathbf{x}) d\Omega(\mathbf{x}) = \int_{\Gamma+\Gamma_\varepsilon} T_{ij}(\mathbf{x}, \mathbf{x}') u_j(\mathbf{x}') d\Gamma(\mathbf{x}') \quad (3.21)$$

where U_{ij} and T_{ij} are the displacement and the traction kernel fundamental solutions, respectively. As these kernel functions depend on the reciprocal of the distance between the

source point \mathbf{x} and field point \mathbf{x}' , the Kelvin solution becomes unbounded or singular if the source point approaches to field point. Therefore, a special treatment for these singularity cases must be included in Eq. (3.21) for accurate solution. To overcome this problem, the interior source point \mathbf{x} is surrounded by an infinitesimal spherical area with radius ε as shown in Figure 3.4 and the integrals are evaluated taking limit $\varepsilon \rightarrow 0$. Cruse (1977) derived the following relationships by taking limits of the surface integrals:

$$\lim_{\varepsilon \rightarrow 0} \int_{\Gamma_\varepsilon} U_{ij}(\mathbf{x}, \mathbf{x}') t_j(\mathbf{x}') d\Gamma(\mathbf{x}') = 0 \quad (3.22a)$$

$$\lim_{\varepsilon \rightarrow 0} \int_{\Gamma_\varepsilon} T_{ij}(\mathbf{x}, \mathbf{x}') u_j(\mathbf{x}') d\Gamma(\mathbf{x}') = u_i(\mathbf{x}) \quad (3.22b)$$

Using limit values in Eqs. (3.22), the boundary integral equation (3.21) can be written as:

$$u_i(\mathbf{x}) = \int_{\Gamma} U_{ij}(\mathbf{x}, \mathbf{x}') t_j(\mathbf{x}') d\Gamma(\mathbf{x}') - \int_{\Gamma} T_{ij}(\mathbf{x}, \mathbf{x}') u_j(\mathbf{x}') d\Gamma(\mathbf{x}') + \int_{\Omega} U_{ij}(\mathbf{x}, \mathbf{x}) b_j(\mathbf{x}) d\Omega(\mathbf{x}) \quad (3.23)$$

Equation (3.23) is known as the Somigliana identity for the displacement, which along with the Betti's reciprocal theorem forms the bases for the Boundary Element analysis for elasticity problems.

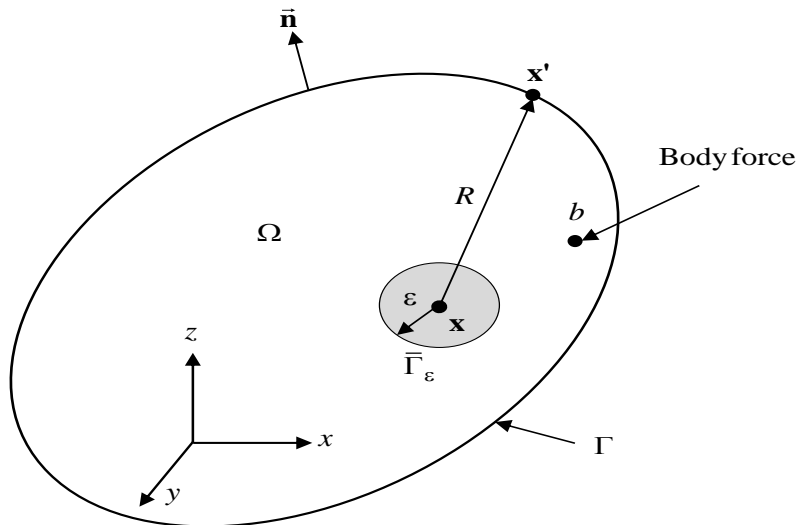


Figure 3.4. Source point inside the domain and surrounded by a spherical region

3.3.4. The Boundary Integral Equation (BIE)

Betti's reciprocal work theorem and the Somigliana identity for the displacement can be used to derive an integral equation for the displacements at the source point \mathbf{x} due to tractions and displacements on the surface at the boundary point \mathbf{x}' . In the absence of body forces, the BIE in Eq. (3.23) can be given as follows:

$$u_i(\mathbf{x}) = \int_{\Gamma} U_{ij}(\mathbf{x}, \mathbf{x}') t_j(\mathbf{x}') d\Gamma(\mathbf{x}') - \int_{\Gamma} T_{ij}(\mathbf{x}, \mathbf{x}') u_j(\mathbf{x}') d\Gamma(\mathbf{x}') \quad (3.24)$$

A similar BIE for stress at the source point \mathbf{x} can be obtained by differentiating Eq. (3.24) with respect to displacement and substituting the derivatives in the Hooke's law of Eq. (3.3) results as:

$$\sigma_{ij}(\mathbf{x}) = \int_{\Gamma} D_{ijk}(\mathbf{x}, \mathbf{x}') t_k(\mathbf{x}') d\Gamma(\mathbf{x}') - \int_{\Gamma} S_{ijk}(\mathbf{x}, \mathbf{x}') u_k(\mathbf{x}') d\Gamma(\mathbf{x}') \quad (3.25)$$

where $D_{ijk}(\mathbf{x}, \mathbf{x}')$ and $S_{ijk}(\mathbf{x}, \mathbf{x}')$ are the third order tensor kernel function for stresses, which are defined as follows (Becker, 1992):

$$D_{ijk}(\mathbf{x}, \mathbf{x}') = -\frac{1}{8\pi(1-\nu)R^2} \left\{ (1-2\nu) \left[\delta_{jk} R_{,i} + \delta_{ik} R_{,j} - \delta_{ij} R_{,k} \right] + 3R_{,i} R_{,j} R_{,k} \right\} \quad (3.26)$$

$$S_{ijk}(\mathbf{x}, \mathbf{x}') = \frac{-G}{4\pi(1-\nu)R^3} \left\{ \begin{array}{l} n_i \left[3\nu R_{,j} R_{,k} + (1-2\nu) \delta_{jk} \right] + n_j \left[3\nu R_{,i} R_{,k} + (1-2\nu) \delta_{ik} \right] \dots \\ \quad + n_k \left[3(1-2\nu) R_{,i} R_{,k} - (1-4\nu) \delta_{ij} \right] \dots \\ + 3 \frac{\partial R}{\partial \mathbf{n}} \left[(1-2\nu) \delta_{ij} + \nu \left(\delta_{jk} R_{,i} + \delta_{ik} R_{,j} \right) - 5R_{,i} R_{,j} R_{,k} \right] \end{array} \right\} \quad (3.27)$$

3.3.5. Point Collocation and Galerkin's Methods

The point collocation and the Galerkin's methods are the two basic procedures generally used to reduce the continuous boundary integral equations to a finite system. In mathematical terminology, the point collocation represents a strong-form solution, whereas the Galerkin's method represents a weak-form solution. In point collocation methodology, the boundary

integral equations are explicitly satisfied at a certain number of points in the domain. Generally, the collocation points are chosen equal to the nodes in the discretized the boundary. The point collocation approximation can be mathematically stated as (Sutradhar et al., 2008):

$$F(P_k) = 0 \quad ; \quad 1 \leq k \leq N \quad (3.28)$$

where P_k represent the collocation point, N is the total number of nodes, and the function F can be defined using Eq.(3.24) as follows:

$$F(\mathbf{x}) = \left\{ u_i(\mathbf{x}) - \int_{\Gamma} U_{ij}(\mathbf{x}, \mathbf{x}') t_j(\mathbf{x}') d\Gamma(\mathbf{x}') + \int_{\Gamma} T_{ij}(\mathbf{x}, \mathbf{x}') u_j(\mathbf{x}') d\Gamma(\mathbf{x}') \right\} \quad (3.29)$$

If the boundary displacements and tractions are interpolated from their values at these N nodes, $u_i(P_k)$ and $t_i(P_k)$, then the boundary conditions provide N of these $3N$ equation with $3N$ unknowns. The point collocation technique results in fully populated non-symmetric matrices. However; the Galerkin approach does not require that the integral equations to be satisfied at any point. These equations are enforced in a weighted average sense. Mathematically, the Galerkin's approach can be represented as follows (Sutradhar et al., 2008):

$$\int_{\Omega} \phi_k(P) F(P) dP = 0 \quad (3.30)$$

where $\phi_k(P)$ are the weight functions. The required $3N$ equations can be generated by an appropriate choice of N weight functions.

3.3.6. Direct and Indirect Boundary Element Methods

Based on the types of integral equation formulations, the BEM analysis can be classified into two types: the direct and indirect BEM (Ameen, 2005). The direct BEM uses the actual physical variables (e.g., displacements and tractions for elasticity problems) in the given problem to form the boundary integral equations. For a well-posed problem, if half of the boundary variables are known, then the remaining unknown variables are obtained directly from the

solution of the integral equations. Once the values of the variables are known on the boundaries, the variables inside the domain can be calculated from the boundary variables by integration. Most of the present-day Boundary Element modeling favors this method.

On the other hand, the indirect BEM uses certain fictitious density function, which may not have any direct physical significance. The boundary integral equations are expressed entirely in terms of a unit singular solution of the original differential equations distributed at a specific density over the boundary (Shah, 1992). The density function is solved first using numerical solution procedures. The unknown variables as well as the values of the variables in the domain are then obtained indirectly from the density functions by integration. One of the most commonly used indirect BEM for the fracture mechanics analysis is the Displacement Discontinuity Method.

3.4. Application of Boundary Element Method to Fracture Mechanics

The applications of the Boundary Element Method for the fracture mechanics problems have been demonstrated by several researches. Cruse (1977) implemented the direct BEM for the fracture mechanics problems; Snyder (1975) used a Green's function approach to analyze the fracture mechanics problem. Crouch (1976) and Weaver (1977) introduced the Displacement Discontinuity method. Portela (1992) developed a dual BEM for two-dimensional fracture problem. The dual BEM was successfully extended for three-dimensional fractures problems by Portela et al. (1992; 1993), and Mi & Aliabadi (1993). The direct application of the boundary integral equations for fracture analysis results in mathematical difficulties due to similar opposing fracture surfaces. Cruse (1978) presented a methodology to deal with the degeneracy problems using two opposite limiting fracture surfaces. Based on the Somigliana identity, the displacements at an interior point \mathbf{x} can be given as follows (Aliabadi & Rooke, 1991):

$$u_i(\mathbf{x}) = \int_{\Gamma + \Gamma_c^+ + \Gamma_c^-} U_{ij}(\mathbf{x}, \mathbf{x}') t_j(\mathbf{x}') d\Gamma(\mathbf{x}') - \int_{\Gamma + \Gamma_c^+ + \Gamma_c^-} T_{ij}(\mathbf{x}, \mathbf{x}') u_j(\mathbf{x}') d\Gamma(\mathbf{x}') \quad (3.31)$$

where the two opposite fracture surfaces can be identified as: a positive surface Γ_c^+ and a negative surface Γ_c^- , and Γ represents the remaining boundary as shown in Figure 3.5.

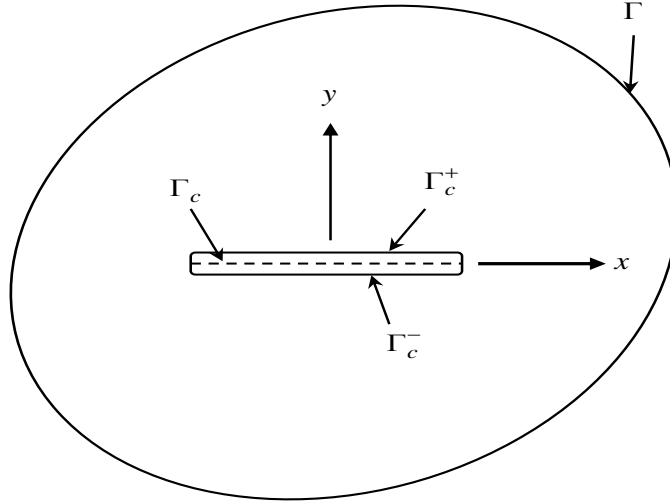


Figure 3.5. Fracture geometry in an infinite domain (Aliabadi & Rooke, 1991)

Based on the properties of the fundamental solutions, the displacement and traction kernel for points on the positive \mathbf{x}^+ and negative \mathbf{x}^- fracture surfaces can be given as follows:

$$U_{ij}(\mathbf{x}, \mathbf{x}^+) = +U_{ij}(\mathbf{x}, \mathbf{x}^-) \quad (3.32a)$$

$$T_{ij}(\mathbf{x}, \mathbf{x}^+) = -T_{ij}(\mathbf{x}, \mathbf{x}^-) \quad (3.32b)$$

The traction kernels in Eq. (3.32b) for two surfaces have opposite sign due to fact that the normal are in opposite direction. The boundary integral equation for combined fracture can be given as follows:

$$u_i(\mathbf{x}) = \int_{\Gamma} U_{ij}(\mathbf{x}, \mathbf{x}') t_j(\mathbf{x}') d\Gamma(\mathbf{x}') - \int_{\Gamma} T_{ij}(\mathbf{x}, \mathbf{x}') u_j(\mathbf{x}') d\Gamma(\mathbf{x}') + \int_{\Gamma_c} U_{ij}(\mathbf{x}, \mathbf{x}') \sum t_j(\mathbf{x}') d\Gamma(\mathbf{x}') - \int_{\Gamma_c} T_{ij}(\mathbf{x}, \mathbf{x}') \Delta u_j(\mathbf{x}') d\Gamma(\mathbf{x}') \quad (3.33)$$

where,

$$\Delta u_j(\mathbf{x}') = \Delta u_j(\mathbf{x}^{+'}) - \Delta u_j(\mathbf{x}^{-'}) \quad (3.34a)$$

$$\sum t_j(\mathbf{x}') = t_j(\mathbf{x}^{+'}) + t_j(\mathbf{x}^{-'}) \quad (3.34b)$$

For a traction free fracture surface or in other words when applied tractions are equal but in opposite directions, the Somigliana identify can be written as follows (Aliabadi & Rooke, 1991):

$$u_j(\mathbf{x}) - \frac{\Delta u_j(\mathbf{x})}{2} = \int_{\Gamma} U_{ij}(\mathbf{x}, \mathbf{x}') t_j(\mathbf{x}') d\Gamma(\mathbf{x}') - \int_{\Gamma} T_{ij}(\mathbf{x}, \mathbf{x}') u_j(\mathbf{x}') d\Gamma(\mathbf{x}') \dots \quad (3.35)$$

$$+ \int_{\Gamma_c} T_{ij}(\mathbf{x}, \mathbf{x}') \Delta u_j(\mathbf{x}') d\Gamma(\mathbf{x}')$$

The above equation has two major difficulties for direct application in fracture mechanics problems. First, application of equal tractions on the opposite surfaces of the fracture will result in same equation. Secondly, Eq. (3.35) has two unknown displacement variables $u_j(\mathbf{x})$ and Δu_j . Several techniques have been suggested to deal with these deficiencies of Eq. (3.35) such as sub-region method (Blandford et al. 1981), dual boundary element method and displacement discontinuity method.

3.4.1. Displacement Discontinuity Method

The Displacement Discontinuity (DD) method is an indirect BEM, which depends on the fundamental solution of the stress-strain relationship of an infinite elastic medium. The DD method was originally developed for rock mechanics analysis in mining engineering, however, later the DD method has been successfully applied in other areas such as fracture mechanics, slope stability analysis, hydraulic fracturing and wellbore stability. The DD method is based on the concept that the continuous displacement along a fracture surface can be discretized into a continuous distribution of displacement discontinuities. Considering, a fracture surface with two

surfaces lying on top of one another with opposing normal as shown in Figure (3.6), then the BIE in Eq. (3.24) can be given as follows (Mach, 1992):

$$u_i(\mathbf{x}) = \int_{\Gamma} U_{ij}(\mathbf{x}, \mathbf{x}') [t_j(\mathbf{x}'^+) + t_j(\mathbf{x}'^-)] d\Gamma(\mathbf{x}') - \int_{\Gamma} T_{ij}(\mathbf{x}, \mathbf{x}') [u_j(\mathbf{x}'^+) - u_j(\mathbf{x}'^-)] d\Gamma(\mathbf{x}') \quad (3.36)$$

where two opposite surfaces of fracture can be identified as: a positive surface Γ^+ and a negative surface Γ^- as represented in Figure 3.5. Considering the symmetry in the kernel functions U_{ij} and T_{ij} , the first term in Eq. (3.36) vanishes because the tractions on the two surfaces are equal and opposite in direction. Hence, Eq. (3.36) follows as:

$$u_i(\mathbf{x}) = - \int_{\Gamma} T_{ij}(\mathbf{x}, \mathbf{x}') D_j(\mathbf{x}') d\Gamma(\mathbf{x}') \quad (3.37)$$

where D_j is the j th component of DD which can be defined as:

$$D_j(\mathbf{x}') = [u_j(\mathbf{x}'^+) - u_j(\mathbf{x}'^-)] \quad (3.38)$$

The stresses generated by the DD's at any point can be obtained by differentiation of the above equation with respect to the coordinates and using the Hooke's law, which results as follows:

$$\sigma_{ij}(\mathbf{x}) = \int_{\Gamma} S_{ijk}(\mathbf{x}, \mathbf{x}') D_k(\mathbf{x}') d\Gamma(\mathbf{x}') \quad (3.39)$$

where $S_{ijk}(\mathbf{x}, \mathbf{x}')$ are the third order stress kernel functions as defined in Eq.(3.27). Equation (3.38) and (3.39) forms the basis for the DD analysis. A detailed description and numerical implementation procedures of two types of the DD Method namely, constant DD and point load DD, have been provided the in following sections.

3.5. Constant Strength Displacement Discontinuity Model

The concept of the constant line strength Displacement Discontinuity for an infinite elastic media was introduced by Crouch & Starfield (1983) using a concept from Salamon (1963). The DD concept is based on the solution of a constant line or square DD in an infinite

elastic medium. This method has been applied to various engineering problems due to its simplified analytical mathematical formulation and implementation procedures. The problem of a constant DD over a finite line element in the x - and y - plane of an infinite elastic solid is specified by the condition that the displacements be continuous everywhere except over the line element. The DD over an element for the Mode-I and Mode-II opening as shown in Figure 3.6, can be defined as follows (Wen, 1996):

$$u_x(x, 0^+) - u_x(x, 0^-) = \begin{cases} D_x & ; \quad -a \leq x \leq a \\ 0 & ; \quad \text{otherwise} \end{cases} \quad (3.40a)$$

$$u_y(x, 0^+) - u_y(x, 0^-) = \begin{cases} D_y & ; \quad -a \leq x \leq a \\ 0 & ; \quad \text{otherwise} \end{cases} \quad (3.40b)$$

where the positive sign represent the analysis point which belongs to the upper positive surface and the negative sign to the lower negative surface, a represents element half-length, D_x and D_y represents the normal and shear components of the DD.

3.5.1. Two-Dimensional Constant Strength DDM Model

The basic solutions of the displacements and the stresses at a point (x, y) generated by a constant DD sources on the line segment $|x| \leq a, y = 0$ can be given as follows (Crouch & Starfield, 1983):

The displacement components are given as:

$$u_x = D_x [2(1-\nu)f_{,y} - yf_{,xx}] + D_y [-(1-2\nu)f_{,x} - yf_{,xy}] \quad (3.41a)$$

$$u_y = D_x [(1-2\nu)f_{,x} - yf_{,xy}] + D_y [2(1-\nu)f_{,y} - yf_{,yy}] \quad (3.41b)$$

The stress components are given as:

$$\sigma_{xx} = 2GD_x [2f_{,xy} + yf_{,xyy}] + 2GD_y [f_{,yy} + yf_{,yyy}] \quad (3.42a)$$

$$\sigma_{yy} = 2GD_x[-yf_{,xyy}] + 2GD_y[f_{,yy} - yf_{,yyy}] \quad (3.42b)$$

$$\sigma_{xy} = 2GD_x[f_{,yy} + yf_{,yyy}] + 2GD_y[-yf_{,xyy}] \quad (3.42c)$$

where u_x and u_y are the displacement components in x - and y - directions, respectively, σ_{xx} , σ_{yy} and σ_{xy} are the normal and shear stresses, G is the shear modulus, and ν is the Poisson's ratio.

The function $f(x, y)$ is defined using the Green's function approach as (Crouch, 1976):

$$f(x, y) = \frac{-1}{4\pi(1-\nu)} \int_{-a}^a \text{Ln} \sqrt{(x-\xi)^2 + y^2} d\xi \quad (3.43)$$

The integration of Eq. (3.43) and derivative of functions of $f(x, y)$ with respect to x - and y - have been listed in **Appendix A**.

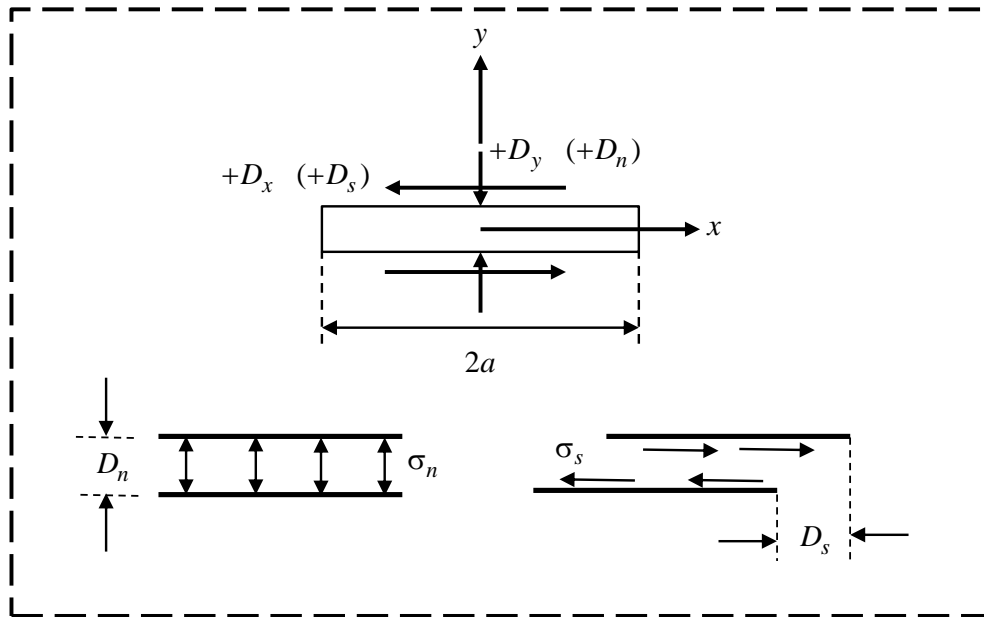


Figure 3.6. Components of two-dimensional constant displacement discontinuity

1. Numerical Implementation

A numerical procedure for solving a two-dimensional fracture problem can be developed by means of Eqs. (3.41) and (3.42). The fracture surface is discretized in NE number of elements as shown in Figure 3.7. The mid-point of each line element is defined as the element coordinate.

The shear and normal stresses at the midpoint of the i th element as shown in Figure 3.8, can be expressed in terms of the DD components at the j th element as follows:

$$\sigma_s^i = \sum_{j=1}^{NE} A_{ss}^{ij} D_s^j + \sum_{j=1}^{NE} A_{sn}^{ij} D_n^j \quad (3.44a)$$

$$\sigma_n^i = \sum_{j=1}^{NE} A_{ns}^{ij} D_s^j + \sum_{j=1}^{NE} A_{nn}^{ij} D_n^j \quad (3.44b)$$

where σ_s^i and σ_n^i are the shear and normal, respectively, and A_{ss}^{ij} etc. are the boundary influence coefficients for the stresses. If, we specify the values of stresses for each element, then Eq. (3.43) results in a system of $2NE$ simultaneous linear equations with $2NE$ unknown DD 's. The resultant system of equations can be solved standard Gauss elimination or any linear solver method for solution of linear system of equations. After solving Eq. (3.44) for the DD values, the stresses and displacements at any point in the body can be found using the method of superposition.

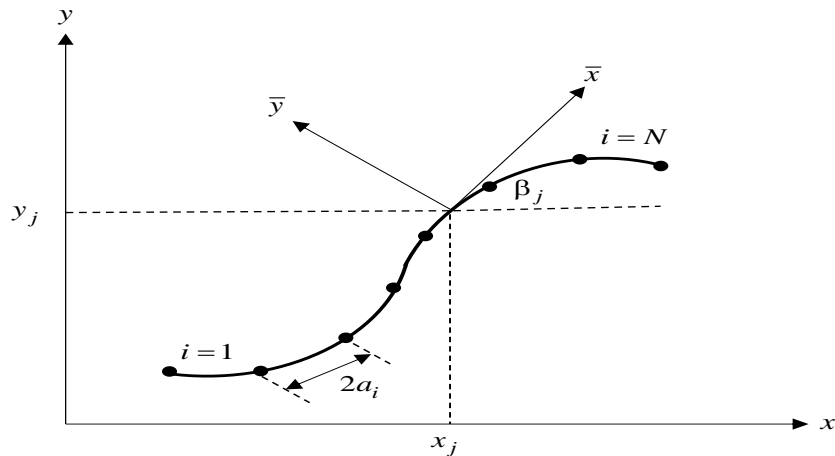


Figure 3.7. Discretization of a fracture in NE number of elements (Crouch & Starfield, 1983)

2. Coordinate Transformations for Arbitrarily Oriented Fracture

For generalization of Eq. (3.44) for an arbitrary oriented fracture surface, the elemental DD 's must be defined with respect to a local coordinate system (\bar{x}, \bar{y}) as shown in Fig. 3.8. The

transformation of coordinates from the global system (x, y) to the local system (\bar{x}, \bar{y}) can be obtained as follows:

$$\bar{x} = (x - x_j) \cos^j \beta + (y - y_j) \sin^j \beta \quad (3.45a)$$

$$\bar{y} = -(x - x_j) \sin^j \beta + (y - y_j) \cos^j \beta \quad (3.45b)$$

Similarly, the stresses can be transformed using following relationship:

$$\sigma_{\bar{x}\bar{x}} = \sigma_{xx} \cos^2 \beta + \sigma_{yy} \sin^2 \beta + \sigma_{xy} \sin 2\beta \quad (3.46a)$$

$$\sigma_{\bar{y}\bar{y}} = \sigma_{xx} \sin^2 \beta + \sigma_{yy} \cos^2 \beta - \sigma_{xy} \sin 2\beta \quad (3.46b)$$

$$\sigma_{\bar{x}\bar{y}} = -\sigma_{xx} \sin \beta \cos \beta + \sigma_{yy} \sin \beta \cos \beta + \sigma_{xy} (\cos^2 \beta - \sin^2 \beta) \quad (3.46c)$$

where (x_j, y_j) represents the midpoint of the j th element and β is the inclination of midpoint of the j th element from the positive x - axis.

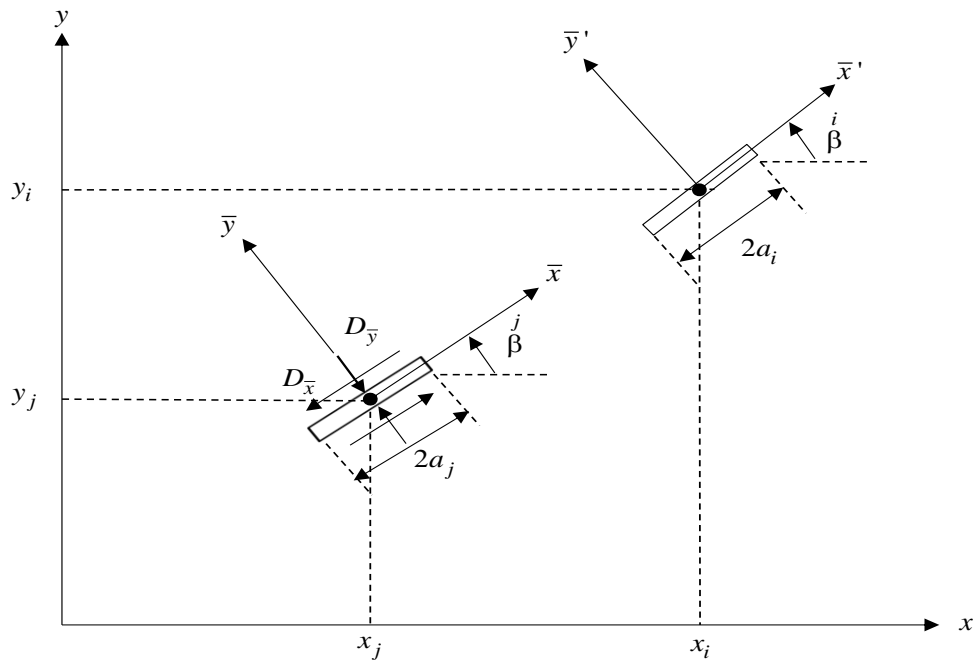


Figure 3.8. Displacement discontinuity components over an arbitrarily oriented fracture surface (Tao, 2010)

3. Fracture Tip Element and Stress Intensity Factor

For accurate estimation of near fracture tip behavior of the stresses and displacements a special tip must be included in analysis. Analytical solution to fracture problems for various loading conditions shows that the stresses at distance r from the fracture tip always vary as $1/\sqrt{r}$ to satisfy the LEFM criterion. Crouch & Starfield (1983) suggested a parabolic tip element as shown in Figure 3.9, and the DD variation for these elements can be given as follow:

$$D_i(\xi) = D_i(a)\sqrt{\frac{\xi}{a}}; \quad i = x, y \quad (3.47)$$

where ξ represents the distance from the fracture tip. Substituting, Eq. (3.47) in Eq. (3.43) the function $f(x, y)$ can be modified for the fracture tip element as follows:

$$f_c(x, y) = \frac{-1}{4\pi(1-\nu)} \int_0^{2a} \sqrt{\frac{\xi}{a}} \text{Ln} \sqrt{[(x-\xi)^2 + y^2]} d\xi \quad (3.48)$$

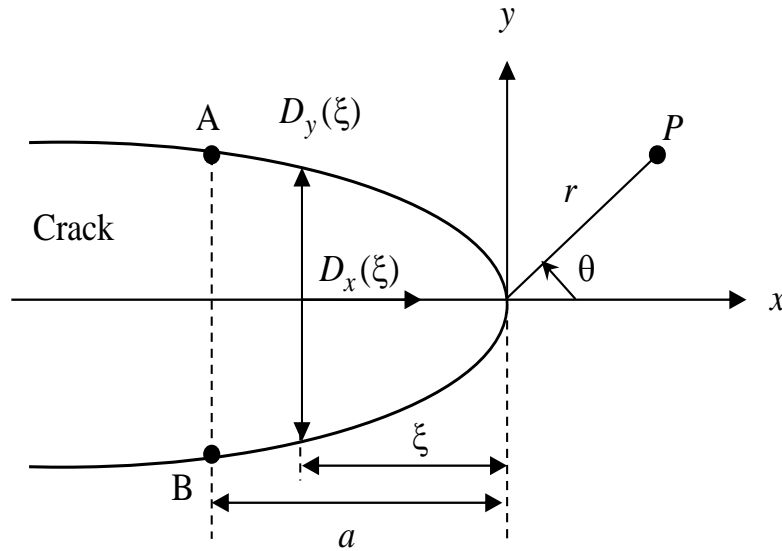


Figure 3.9. Displacement correlation for a parabolic fracture tip element (Nasab & Marji, 2007)

Once the DD values at the fracture tip are solved numerically, the stress intensity factors (SIF) can be obtained using the normal and shear displacement discontinuities for the constant elements as follows (Shou & Crouch, 1995):

$$K_I = \frac{E}{4(1-\nu^2)} \sqrt{\frac{\pi}{2a}} \cdot D_n(a) \quad (3.50a)$$

$$K_{II} = \frac{G}{4(1-\nu^2)} \sqrt{\frac{\pi}{2a}} \cdot D_s(a) \quad (3.50b)$$

where K_I and K_{II} are the Mode-I and Mode-II stress intensity factors, respectively, a is the half length of the fracture tip element.

4. Numerical Example

For numerical implementation and verification of two-dimensional DDM model, two numerical examples: planar pressurized fracture and arbitrary orientated pressurized fracture have been considered. For both models, the Young's modulus equal is to 37.5 GPa and the Poisson's ratio equal to 0.25 is used. The fracture length is equal to 2 m and it is divided in 20 numbers of equal elements.

4.1. Planar Pressurized Fracture

A two-dimensional DD model for a planar pressurized fracture in an infinite region as shown in Figure 3.10 is developed. The far field stresses $\sigma_{yy}=15$ MPa and internal fluid pressure $p=20$ MPa is applied on the fracture surface. The normal fracture opening results from the DDM model has been compared with the analytical solution for this problem as given by Sneddon (1951):

$$w(r) = \frac{2(1-\nu)}{G} P a \cdot \sqrt{1 - \left(\frac{x}{a}\right)^2} \quad (3.51)$$

where $P = p - \sigma_{yy}$ is the resultant of the fluid pressure and far field stresses, x is the distance along the fracture and a is the fracture half length.

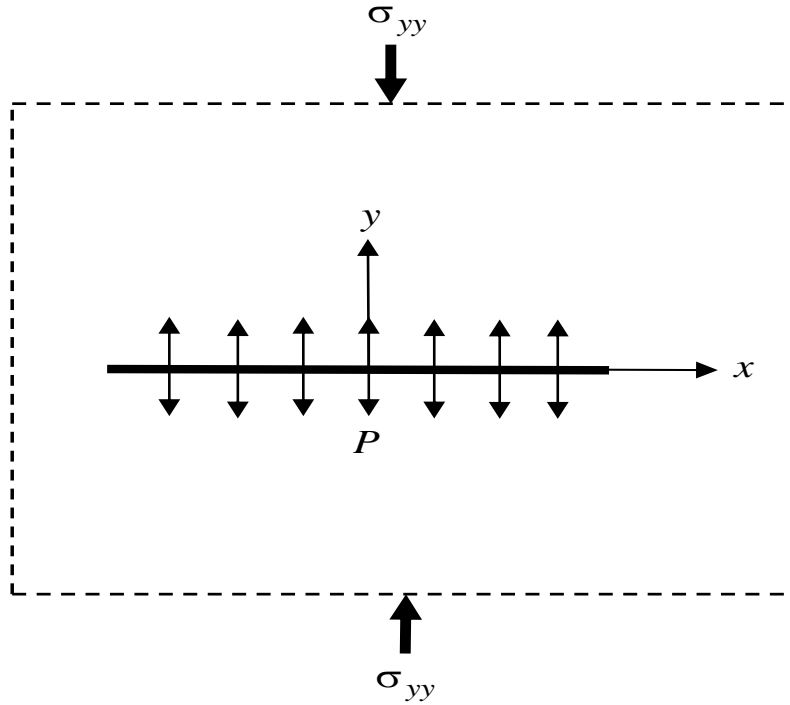


Figure 3.10. A pressurized planar fracture in an infinite region

A comparison of the numerical and analytical results for fracture normal opening is shown in Figure 3.11, which shows a very good agreement. The maximum fracture opening occurs at the wellbore and it tends to zero near the fracture tip. Another validation of the DDM model can be given by comparing the normal stress distribution near fracture tip. An analytical solution for the near fracture tip normal stress distribution can be given as follows (Valko & Economides, 1995):

$$\sigma_{yy} = -\frac{Px}{\sqrt{x^2 - a^2}} - P; \quad |x| > a \quad (3.52)$$

The normal stress distributions from the DDM model and from analytical solution from Eq. (3.52) are shown in Figure 3.12, which shows a good agreement. The maximum normal stresses occur very close to fracture tip region, the normal stress becomes infinite as $(x - a) \rightarrow 0$.

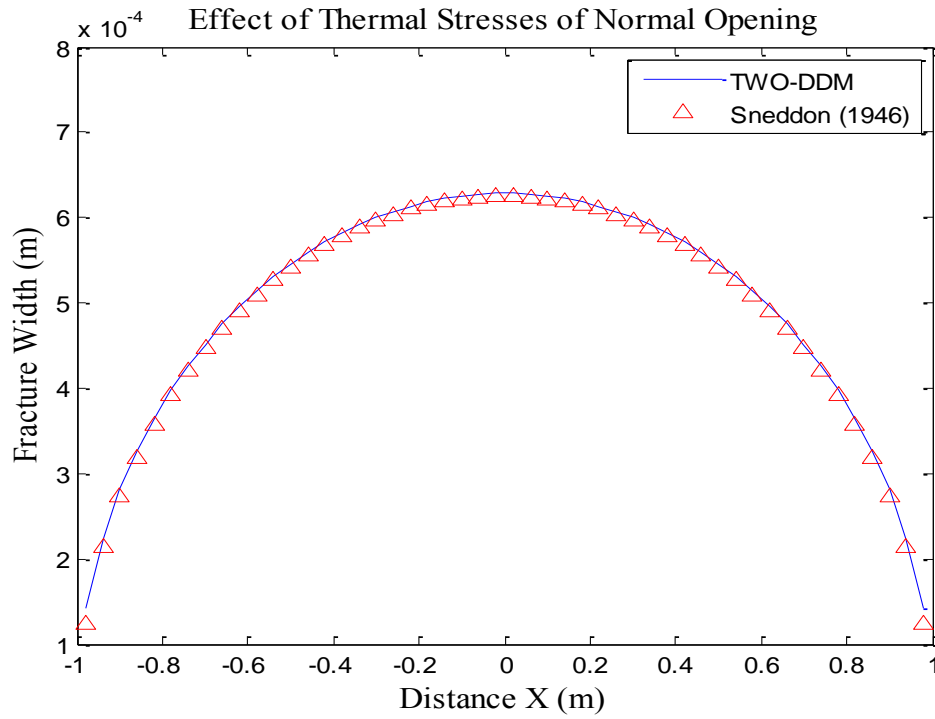


Figure 3.11. Normal DD distribution along the pressurized fracture in an infinite plane

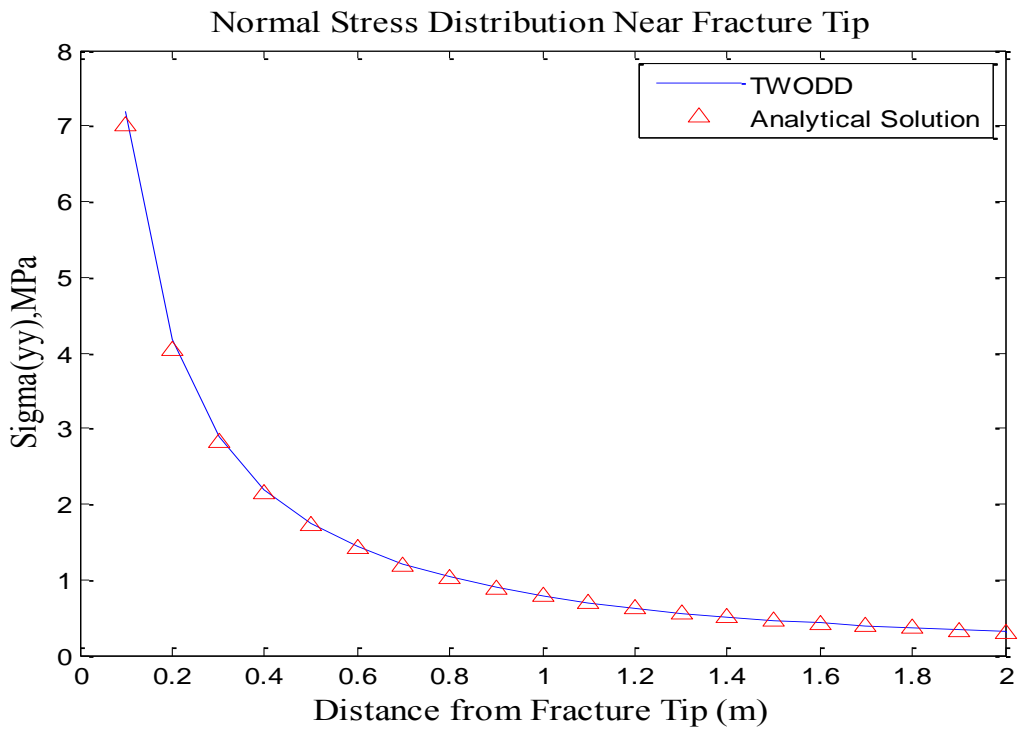


Figure 3.12. Normal stress distribution near tip of a pressurized planar fracture (along $y=0$)

4.2. Oriented Pressurized Fracture

A two-dimensional generalized DD model for an oriented fracture in an infinite region as shown in Figure 3.13 is developed. The far-field stresses $\sigma_{xx}=10$ MPa, $\sigma_{yy}=5$ MPa are applied, and internal fluid pressure $p=15$ MPa is assumed. A plot of distribution of the normal fracture opening and shear opening for oriented fracture with $\beta = \pi/3$ is represented in Figure 3.14. A verification of this model was done by estimating the stress intensity factor (SIF) at the fracture tip. For a pressurized oriented fracture the mode-I and mode-II SIF can be given as follows (Rice, 1968):

$$K_I = \sqrt{\pi a} \left[P - (\sigma_{xx} \sin^2(\beta) + \sigma_{yy} \cos^2(\beta)) \right] \quad (3.53a)$$

$$K_{II} = \frac{\sqrt{\pi a}}{2} \left[(\sigma_{xx} - \sigma_{yy}) \sin(2\beta) \right] \quad (3.53b)$$

where K_I and K_{II} represents the mode-I and mode-II SIF values.

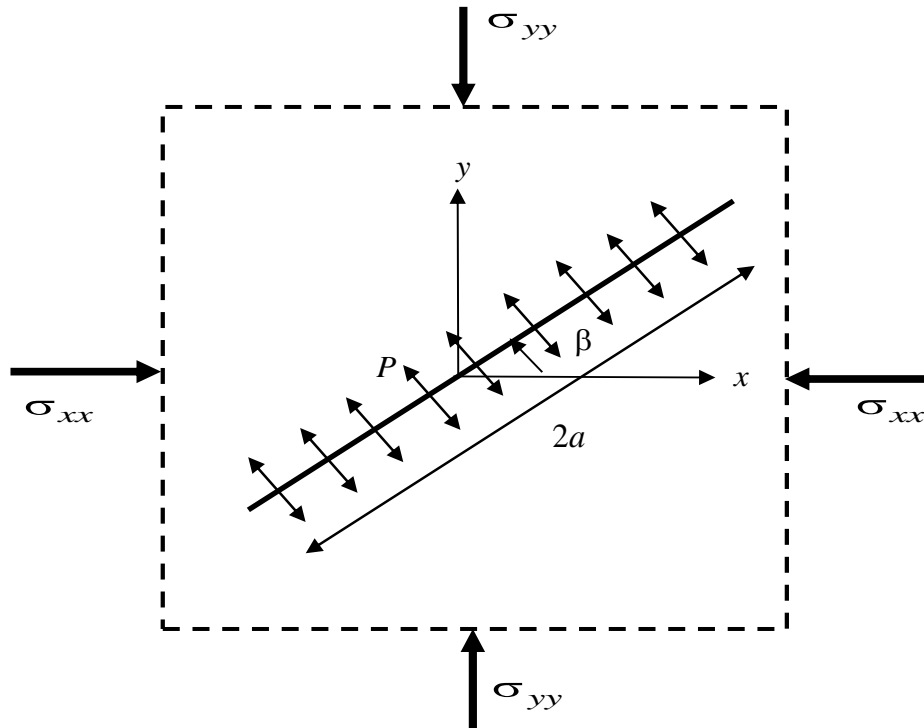


Figure 3.13. An arbitrarily orientated fracture under far field stresses and internal fluid pressure

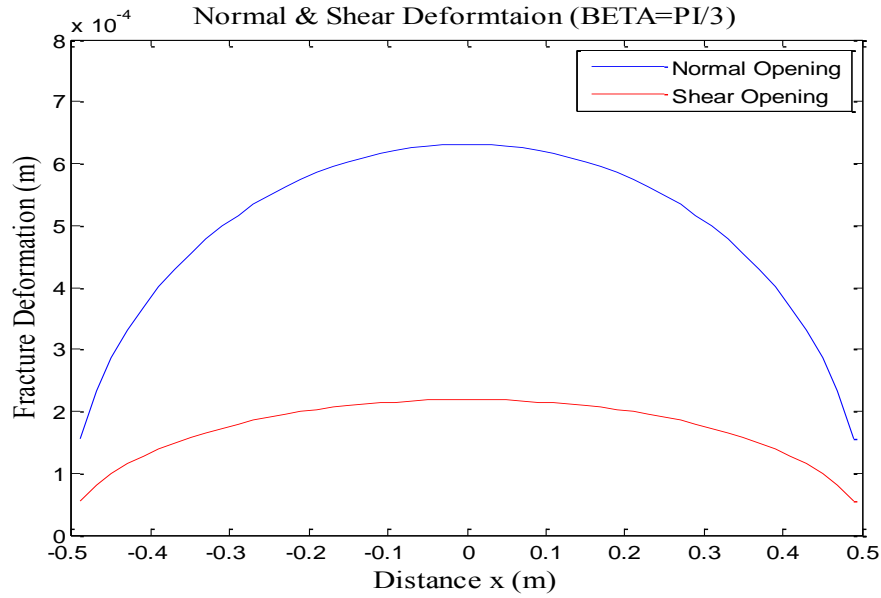


Figure 3.14. Normal and shear DD distribution along the pressurized arbitrarily oriented fracture in an infinite plane

Variations of the numerical and analytical SIF values for the mode-I and mode-II fracture openings with orientation angle are shown in Figure 3.15. The numerical SIF values show a good match with the analytical solution.

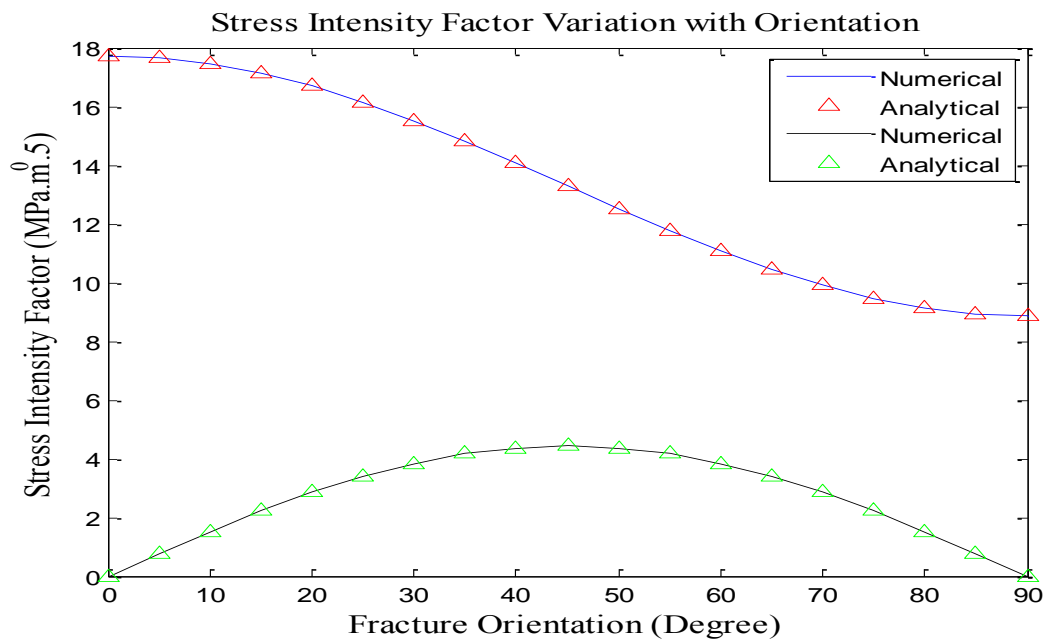


Figure 3.15. Variation of analytical and numerical values of Mode-I and Mode-II stress intensity factors with orientation angle

3.5.2. Constant Strength Three-Dimensional DDM Model

Similar to the constant two-dimensional DD model, Crouch & Starfield (1983) gave a formulation for the three-dimensional problems based on the constant DD formulation over a square or rectangular element. The three-components of the DD for three-dimensional problems namely: normal fracture opening and two shear rides are shown in Figure 3.16. For three dimensional problems, by placing NE unknown constant displacement element within the boundaries of the region to be analyzed and having known v boundary condition along the elements, a system of $3NE$ linear algebraic equations can be set up as follows:

$$\sigma_{s1}^i = \sum_{j=1}^{NE} A_{ss1}^{ij} D_{s1}^j + \sum_{j=1}^{NE} A_{ss2}^{ij} D_{s2}^j + \sum_{j=1}^{NE} A_{sn}^{ij} D_n^j \quad (3.54a)$$

$$\sigma_{s2}^i = \sum_{j=1}^{NE} A_{ss1}^{ij} D_{s1}^j + \sum_{j=1}^{NE} A_{ss2}^{ij} D_{s2}^j + \sum_{j=1}^{NE} A_{sn}^{ij} D_n^j \quad (3.54b)$$

$$\sigma_n^i = \sum_{j=1}^{NE} A_{ns1}^{ij} D_{s1}^j + \sum_{j=1}^{NE} A_{ns2}^{ij} D_{s2}^j + \sum_{j=1}^{NE} A_{nn}^{ij} D_n^j \quad (3.54c)$$

where NE is the total number of elements, σ_{s1} , σ_{s2} , σ_n represents the shear and normal forces on the fracture surface, D_n is the normal fracture opening, D_{s1} , D_{s2} represents the mode-II and mode-III shear rides, and A_{ss1} etc. are the three-dimensional influence coefficients.

1. Numerical Implementation

For numerical implementation of Eqs. (3.54), a square fracture surface of size 2m·2m in an infinite three-dimensional space is discretized using square element. The input parameters for this model are listed in Table 3-1. A surface plot for normal fracture opening is shown in Figure 3.17, which shows maximum normal opening of 0.001 m at the center of the fracture and minimum opening of 0.00019 m at the corners. A surface of the mode-II shear opening is also shown in Figure 3.18, which shows a maximum shear slip of 0.002 m at the center of the fracture

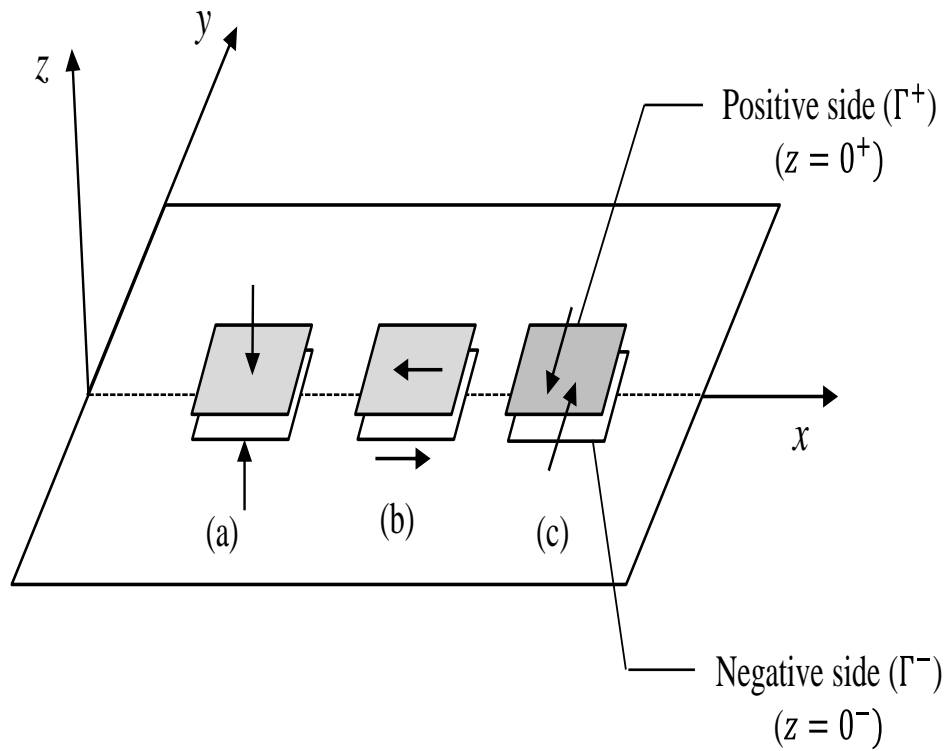


Figure 3.16. Components of three-dimensional displacement discontinuities: (a) Mode-I fracture opening (b) Mode-II fracture shearing and (c) Mode-III fracture shearing (Vandamme & Curran, 1989)

Table 3-1. Input parameters for constant three-dimensional DD model

No.	Parameter	Unit	Value
1	Young's modulus (E)	GPa	60
2	Poisson's ratio (ν)	-	0.25
3	Maximum horizontal stress (σ_{xx})	MPa	50
4	Minimum horizontal stress (σ_{yy})	MPa	40
5	Vertical stress (σ_{zz})	MPa	30
6	Fluid pressure (P)	MPa	10
7	Fracture dimensions	m·m	2·2

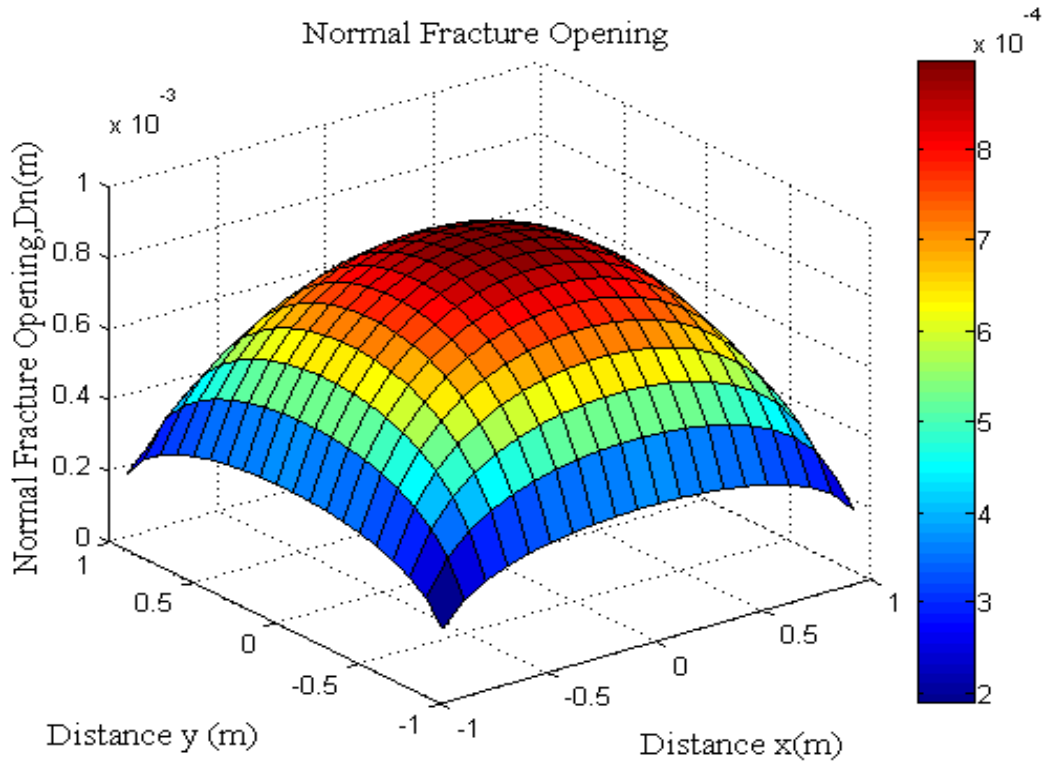


Figure 3.17. Normal fracture opening for a square fracture using constant three-dimensional DD model

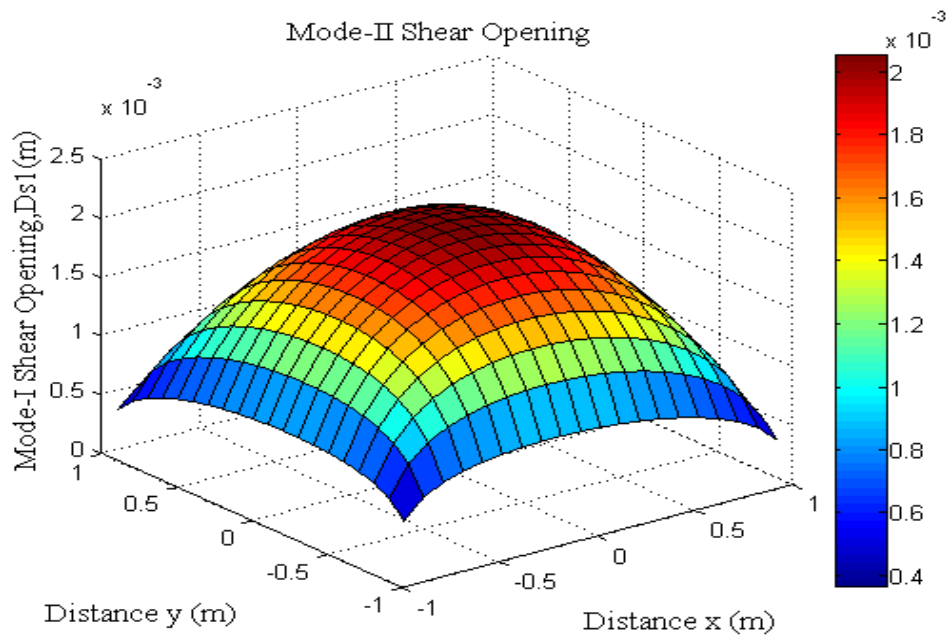


Figure 3.18. Mode-II shear opening for a square fracture using constant three-dimensional DD model

3.6. DDM Models Based on Kelvin's Fundamental Solution

Wiles & Curran (1982) and Vandamme & Curran (1989) presented a generalization of the DD method based on the point load DD using the Kelvin's fundamental solution for the elasticity problems. The generalized method eliminates the constant element constraint of the earlier DD models and can be easily extended for any geometrical shape for more accurate results. The DD values for a three-dimensional problem are defined as follows (Vandamme & Curran, 1989):

$$D_{kn}(\mathbf{x}') = \lim_{z \rightarrow -0} u_k(\mathbf{x}') - \lim_{z \rightarrow +0} u_k(\mathbf{x}') = \delta(\mathbf{x}') \cdot D_{kn}(\mathbf{x}'); \quad k, n = x, y, z \quad (3.55)$$

where $\mathbf{x}' = (x', y', z')$ is any point on the fracture surface, $u_k(\mathbf{x}')$ is the k th component of displacement, $\delta(\mathbf{x}')$ is the Dirac delta function and $D_k(\mathbf{x}')$ are the intensity tensor of the DD's.

The DD's for a three-dimensional fracture surface can be resolved into three components along the coordinate axes. The three DD components are comprised of a normal component that is perpendicular to the plane of the discontinuity, and two shear components that lie in the discontinuity plane as shown in Figure 3.16. The displacements and stresses at source point \mathbf{x} induced by the concentrated point source of DD at field point \mathbf{x}' can be given as follows (Vandamme & Curran, 1989):

$$u_i(\mathbf{x}) = G_{ikn}(\mathbf{x}, \mathbf{x}') \cdot D_{kn}(\mathbf{x}') \quad (3.56a)$$

$$\sigma_{ij}(\mathbf{x}) = S_{ijkn}(\mathbf{x}, \mathbf{x}') \cdot D_{kn}(\mathbf{x}') \quad (3.56b)$$

where $u_i(\mathbf{x})$ and $\sigma_{ij}(\mathbf{x})$ are the displacements and stresses induced at source point \mathbf{x} , respectively, and $G_{ikn}(\mathbf{x}, \mathbf{x}')$ & $S_{ijkn}(\mathbf{x}, \mathbf{x}')$ represents the three-dimensional displacement and stress kernel function as defined in Eqs. (3.26) and (3.27), respectively. The displacements and

stresses induced by the fracture in the finite area of the DD can be estimated by integration of right hand side of Eq. (3.56) over the fracture surface Ω as follows (Yamamoto et al., 2000):

$$u_i(\mathbf{x}) = \int_{\Omega} G_{ikn}(\mathbf{x}, \mathbf{x}') \cdot D_{kn}(\mathbf{x}') d\Omega(\mathbf{x}') \quad (3.57a)$$

$$\sigma_{ij}(\mathbf{x}) = \int_{\Omega} S_{ijkn}(\mathbf{x}, \mathbf{x}') \cdot D_{kn}(\mathbf{x}') d\Omega(\mathbf{x}') \quad (3.57b)$$

3.6. 1. Numerical Implementation

The boundary integral equations in Eq. (3.57) represent a relationship between the unknown DD components and displacements and stresses. The DD values can be solved either using displacement equation (Eq.3.57a) or stress boundary integral equation (Eq.3.57b) with appropriate boundary conditions. In case of the fracture mechanics problems, it is more convenient to specify the stress or traction as boundary conditions and solve Eq. (3.57b) for the unknown DD's. Subsequently, the displacements can be calculated using Eq. (3.57a). For numerical solution, the boundary surface can be divided in number of elements and each element is defined by certain number of nodal points. The methodology and important numerical issues for the numerical implementation of Eq. (3.57b) are provided in following sections.

1. Boundary Surface Discretization

The boundary or surface of the solution domain is divided into a number of connected elements. A linear variation of geometry and variable (e.g., displacement discontinuities and stresses) over each element is assumed. The fracture surface discretization is done using two types of elements; 4-node continuous quadrilateral elements for the fracture domain and 4-node semi-discontinuous quadrilateral for the fracture from elements as shown in Figure 3.19. The use of semi-discontinuous elements insures the specific characteristics of the displacement and stresses near a fracture front that is \sqrt{r} variation of displacements and $1/\sqrt{r}$ variation of

stresses or tractions. The shape functions for a bilinear continuous element can be given as follows (Zienkiewicz et al., 2005):

$$\phi_1(\xi, \eta) = 0.25 \cdot (1 - \xi)(1 - \eta) \quad (3.58a)$$

$$\phi_2(\xi, \eta) = 0.25 \cdot (1 + \xi)(1 - \eta) \quad (3.58b)$$

$$\phi_3(\xi, \eta) = 0.25 \cdot (1 + \xi)(1 + \eta) \quad (3.58c)$$

$$\phi_4(\xi, \eta) = 0.25 \cdot (1 - \xi)(1 + \eta) \quad (3.58d)$$

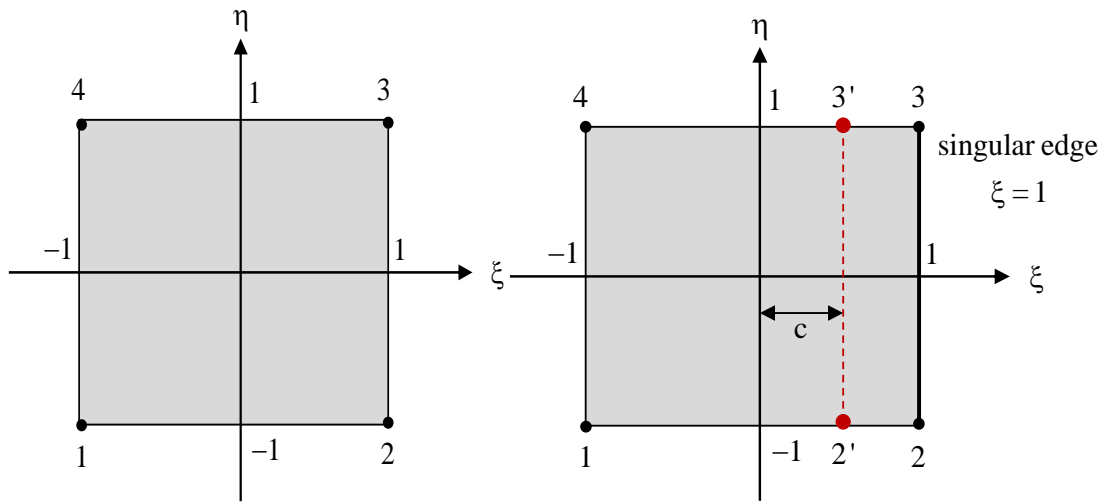


Figure 3.19. Continuous and semi-discontinuous rectangular elements

The shape functions for the 4-node semi-discontinuous elements are defined as (Guzina et al., 2006):

$$\phi_1^g(\xi, \eta) = \frac{(c - \xi) \cdot (1 - \eta)}{2(1 + c)} \quad (3.59a)$$

$$\phi_2^g(\xi, \eta) = \frac{(1 + \xi) \cdot (1 - \eta)}{2(1 + c)} \quad (3.59b)$$

$$\phi_3^g(\xi, \eta) = \frac{(1 + \xi) \cdot (1 + \eta)}{2(1 + c)} \quad (3.59c)$$

$$\phi_4^g(\xi, \eta) = \frac{(c - \xi) \cdot (1 + \eta)}{2(1 + c)} \quad (3.59d)$$

where c represents a shifting parameter for the fracture front nodes as shown in Figure. 3.19. For numerical integration, the elements in global coordinate system (x, y) are mapped into local coordinate system $\{\xi, \eta: -1 \leq \xi, \eta \leq 1\}$ using appropriate shape functions. A discretized form of Eq. (3.57b) can be given as follows:

$$\sigma_{ij}(\mathbf{x}) = \sum_{e=1}^{NE} \left\{ \sum_{l=1}^N \int_{\Omega_e} S_{ijkl}[\mathbf{x}, \mathbf{x}'(\xi, \eta)] g(\xi, \eta) \phi_l(\xi, \eta) J(\xi, \eta) D_{kn}^l(\xi, \eta) d\xi d\eta \right\} \quad (3.60)$$

where ϕ are the shape functions, J is the Jacobian of transformation, $g(\xi, \eta)$ is the multiplication coefficient for the fracture front elements. If fracture front is along singular edge $\xi=1$, the coefficients $g(\xi, \eta)$ for a 4-node semi-discontinuous element are defined as follows (Xiao & Yue, 2011):

$$g(\xi, \eta) = \begin{cases} 1 & ; \quad \text{Domain elements} \\ \sqrt{1 - \xi} & ; \quad \text{Fracture front elements} \end{cases} \quad (3.61)$$

2. Numerical Integration

The fundamental solution kernels in Eq. (3.60) depend on the distance R between the source point \mathbf{x} and field point \mathbf{x}' . Depending on the location of the source and field points, the numerical integration can be divided in two categories as: non-singular integration and singular integration. In the case, where the source point \mathbf{x} and field point \mathbf{x}' lies on different elements, the integrand is non-singular or well-behaved which can be evaluated using standard Gauss quadrature integration. However; in the case, where the source point \mathbf{x} and the field point \mathbf{x}' lies on the same integration element, integrand is unbounded as distance $R = \|\mathbf{x} - \mathbf{x}'\| \rightarrow 0$ and as a resultant integrand tends to infinity. An accurate evaluation of these integrals is critically important in the

BEM implementation. In mathematical terms these cases are known as hyper-singular, which can be estimated using the Hadamard principal-value integrals (Aliabadi & Brebbia, 1993). Methodologies for numerical evaluation of non-singular and hyper-singular integration have been discussed in following sections.

2.1. Non-Singular Integration

The numerical integration even for the non-singular kernel is a computationally expensive task which needs to be optimized. In this research, numerical integrations over the non-singular elements were performed using the adaptive Gaussian integration scheme (Davis & Gao, 2006). The adaptive integration technique is based on optimization of number of Gaussian points in each direction depending on the ratio of element length in that direction and its minimum distance from the collocation point as shown in Figure 3.20. Lachat & Watson (1976) suggested an algorithm to automatically select the order of integration over a boundary element based on the upper-bound analysis of the Gauss quadrature error. A generalization of the Lachat & Watson's method was presented by Mustoe (1984) to obtain required number optimum of Gaussian point in each direction. Davis & Bu (1995) modified Mustoe's scheme and presented an alternative empirical approach which gives more accurate results. The number of required Gaussian points based on this approach is given as follows (Gao & Davis, 2000):

$$m_i = p' \left[-0.1 \cdot \text{Ln}(e_i / 2) \left\{ \left(\frac{8L_i}{3R_{\min}} \right)^{3/4} + 1 \right\} \right] \quad (3.62)$$

where m_i is the required number of Gauss integration points in the i th direction, e_i is the prescribed tolerance, L_i is the element length along the i th local coordinate direction, R_{\min} is the minimum distance from the collocation point, and p' is related to order of singularity of as follows:

$$p' = \sqrt{\frac{2}{3}p + \frac{2}{5}} \quad (3.63)$$

where p represents the order of singularity of the kernel function.

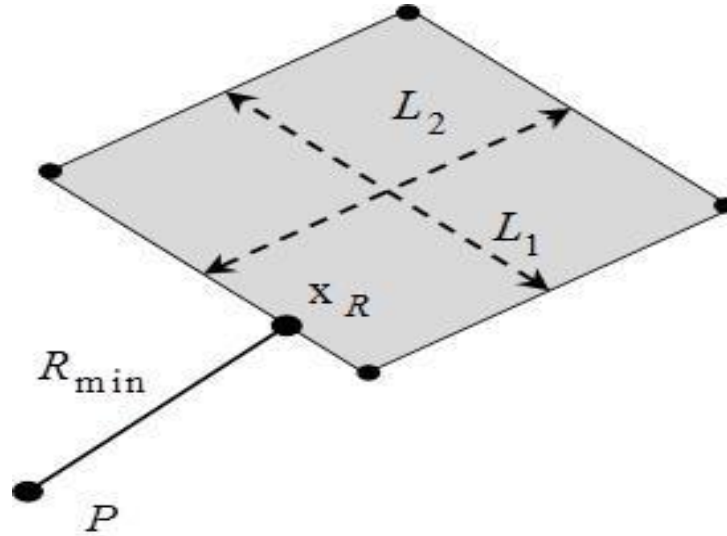


Figure 3.20. Representation of adaptive non-singular integration over an element

For numerical implementation of Eq. (3.62), first the minimum distance between the collocation point and integration element is calculated using Newton-Raphson iterative scheme (Griffiths & Smith, 2006), and then number of required number Gaussian point for a particular direction and for a fixed tolerance limit is obtained using Eq. (3.62). If, the calculated number of Gaussian point exceeds an optimum number of Gaussian point (e.g., $N=12$ in this case), then the element is sub-divided into small elements and this process is repeated till each sub-element satisfies the criterion of optimum number of Gaussian point. The adaptive integration with element subdivision can be used for near-singular integrals in the elasticity problems. A variation of number of Gaussian point with ration of distance and length for three difference order of singularities and fixed tolerance $e=10^{-4}$ is shown in Figure 3.21, which as the ratio of distance and length goes below to 0.2, the number of required Gaussian points goes very high.

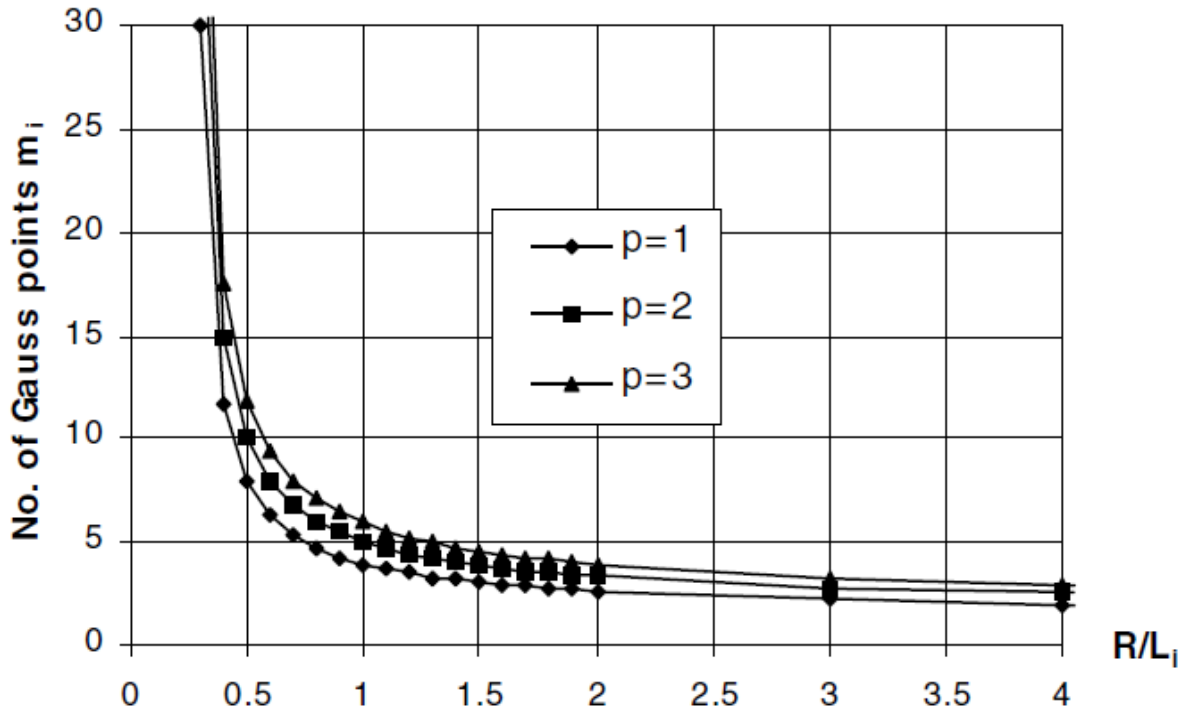


Figure 3.21. Variation of number of Gaussian point with R/L ratio (Davis & Gao, 2006)

2.2. Hyper-Singular Integration

The effective integration of the singular integrals is a critical issue in the application of the BEM for the fracture mechanics problems. Many techniques have been proposed for numerical evaluation of hyper-singular functions. The most commonly used methods are the singularity subtraction technique (Guiggiani et al., 1992), non-linear coordinate transformation (Telles, 1987) or special quadrature scheme (Kutt, 1975). In a recent publication, Xiao & Yue (2011) suggested that a combination of one-dimensional Gaussian quadrature and special Kutt's quadrature can be used for estimation of hyper-singular integrations. This scheme is relatively simple for application, but it fails in case of curved or irregular elements. The singularity subtraction technique which is a robust technique is adapted in this research. The singularity subtraction technique (SST) is based on the Taylor series expansions of the singular kernel

functions about the singular node (Aliabadi et al., 1991). The basic idea behind the SST is that the singular or unbounded parts of the kernels are first subtracted from the kernels which results in a well behaved integrand and can be integrated using standard Gaussian quadrature. Subsequently, the subtracted parts are integrated analytically or semi-analytically and added back. The hyper-singular integrand of Eq. (3.60) can be written as follows (Mi & Aliabadi, 1992):

$$I = \int_{-1}^1 \int_{-1}^1 S_{ijkn} \left[\mathbf{x}(\xi^c, \eta^c), \mathbf{x}'(\xi, \eta) \right] g(\xi, \eta) \phi_l(\xi, \eta) J(\xi, \eta) d\xi d\eta \quad (3.64)$$

where $\mathbf{x}(\xi^c, \eta^c)$ is the local coordinate of the singular node as shown in Figure 3.22. Introducing a polar coordinate system around the singular node $\mathbf{x}(\xi^c, \eta^c)$ as follows (Cruse, 1977):

$$\xi = \xi^c + \rho \cos \theta \quad (3.65a)$$

$$\eta = \eta^c + \rho \sin \theta \quad (3.65b)$$

$$d\xi d\eta = \rho d\rho d\theta \quad (3.65c)$$

where ρ and θ are the components of polar system. In terms of polar coordinates, Eq. (3.61) can be given as follows:

$$I = \int_0^{2\pi} \int_{\alpha(\varepsilon, \theta)}^{R(\theta)} F_{ijkn}(\rho, \theta) d\rho d\theta \quad (3.66)$$

where $\alpha(\varepsilon, \theta)$ is the equation of distorted neighborhood (Figure 3.22) and the integrand $F_{ijkn}(\rho, \theta)$ represents multiplication of the fundamental solution, shape functions, and Jacobian as follows:

$$F_{ijkn}(\rho, \theta) = S_{ijkn} \left[\mathbf{x}(\xi^c, \eta^c), \mathbf{x}'(\rho, \theta) \right] g(\rho, \theta) \phi_l(\rho, \theta) J(\rho, \theta) \rho \quad (3.67)$$

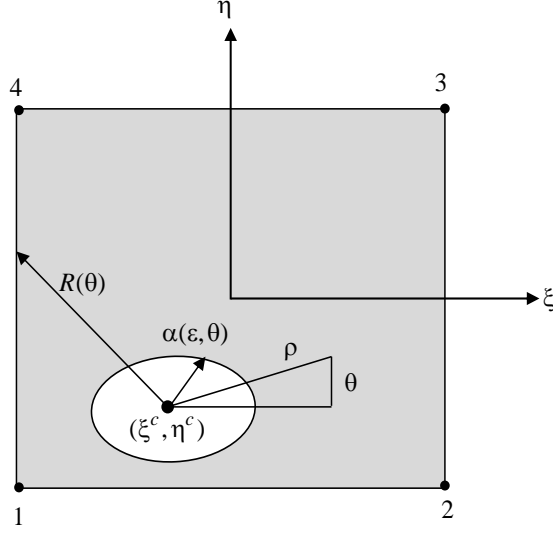


Figure 3.22. Polar coordinates in parametric plane with singular node

The polar coordinate transformation results in reduction of singularity of the integrand by $O(\rho^{-1})$; hence, Eq. (3.64) has a reduced singularity of order $O(\rho^{-2})$. Expanding Eq. (3.64) with respect to ρ using the Laurent series expansion as follows (Guiggiani, 1998):

$$F_{ijkn}(\rho, \theta) = \frac{F_{-2}(\theta)}{\rho^2} + \frac{F_{-1}(\theta)}{\rho} + O(1) \quad (3.68)$$

where $F_{-1}(\theta)$ and $F_{-2}(\theta)$ are the first and second terms in the Taylor's series expansion. The dependence on angle θ is crucial for expansion of above equation for accurate representation of asymptotic behavior of the integrand in neighborhood of the singular node ($\rho \rightarrow 0$). The Taylor series expansion of equation of distorted region $\alpha(\epsilon, \theta)$ with respect to ϵ can be given as follows:

$$\rho = \alpha(\epsilon, \theta) = \epsilon\beta(\theta) + \epsilon^2\gamma(\theta) + O(\epsilon^3) \quad (3.69)$$

A methodology to obtain expressions $F_{-1}(\theta)$, $F_{-2}(\theta)$, $\beta(\theta)$, and $\gamma(\theta)$ are explained in

Appendix B. Equation (3.68) can be written as follows:

$$I = I_0 + I_{-1} + I_{-2} \quad (3.70)$$

where functions I_0 , I_{-1} and I_{-2} are defined as follows:

$$I_0 = \int_0^{2\pi} \int_{\alpha(\varepsilon, \theta)}^{R(\theta)} \left[F_{ijk}(\rho, \theta) - \left(\frac{F_{-2}(\theta)}{\rho^2} + \frac{F_{-1}(\theta)}{\rho} \right) \right] d\rho d\theta \quad (3.71a)$$

$$I_{-1} = \lim_{\varepsilon \rightarrow 0} \int_0^{2\pi} \int_{\alpha(\varepsilon, \theta)}^{R(\theta)} \frac{F_{-1}(\theta)}{\rho} d\rho d\theta \quad (3.71b)$$

$$I_{-2} = \lim_{\varepsilon \rightarrow 0} \int_0^{2\pi} \int_{\alpha(\varepsilon, \theta)}^{R(\theta)} \frac{F_{-2}(\theta)}{\rho^2} d\rho d\theta \quad (3.71c)$$

A procedure to evaluate limits of functions I_{-1} and I_{-2} are given in **Appendix B**. Substituting Eqs. (3.71) in Eq. (3.68), the final formulation for hyper-singular integrals can be given as follows (Guiggiani et al., 1992):

$$I = \sum_m \left\{ \int_{\theta_1^m}^{\theta_2^m} \int_0^{R_m(\theta)} \left[F_{ijk}^m(\rho, \theta) - \left(\frac{F_{-2}^m(\theta)}{\rho^2} + \frac{F_{-1}^m(\theta)}{\rho} \right) \right] d\rho d\theta + \int_{\theta_1^m}^{\theta_2^m} \left[F_{-1}(\theta) \ln \left| \frac{R_m(\theta)}{\beta(\theta)} \right| - F_{-2}(\theta) \left(\frac{\gamma(\theta)}{\beta^2(\theta)} + \frac{1}{R(\theta)} \right) \right] d\theta \right\} \quad (3.72)$$

where m represents the number of triangular sub-elements as shown in Fig. 3.23. Equation (3.72) is completely bounded and can be applied for any type of element provided that the necessary continuity requirements for displacements: $u \in C^{0,\alpha}$ for Cauchy principal value and $u \in C^{1,\alpha}$ for Hadamard principal value (where α is a constant) are satisfied at each collocation point. The numerical integrations should be evaluated for individual triangular sub-element. Finally, the hyper-singular integral can be obtained by a summation of all triangular sub-element integrations.

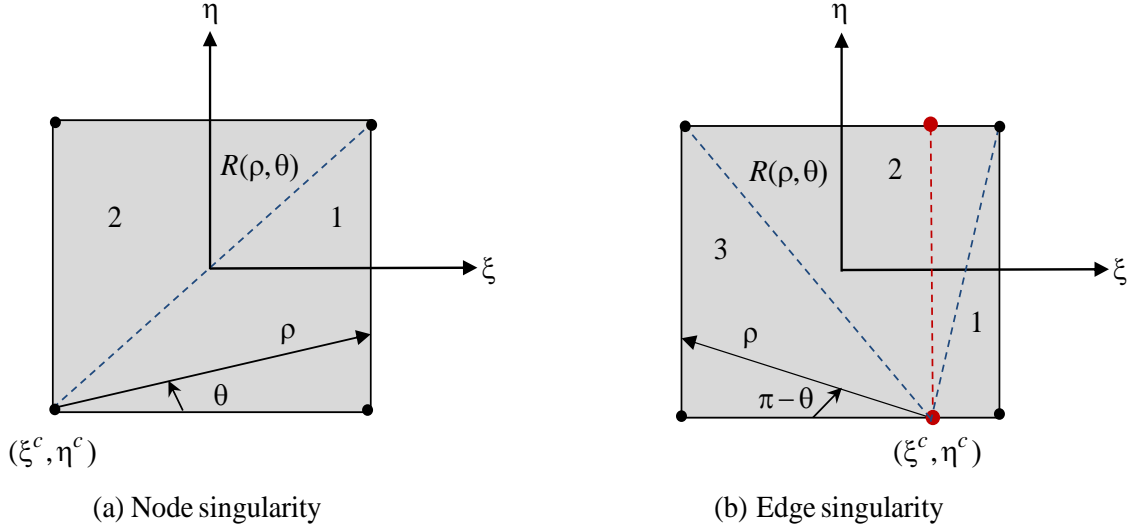


Figure 3.23. Division of singular element into triangular sub-elements (Xiao & Yue, 2011)

3.6.2. Linear Equations of Discretized System

By applying numerical integration and coordinates transformation, Eq. (3.60) can be written as vector-matrix equation as follows (Yamamoto et al., 2004):

$$\sigma_{ij}^I = \sum_{e=1}^{NE} \sum_{l=1}^N A_{ijk}^{IJ(l)} \cdot D_j^{J(l)} \quad (3.73)$$

where I represents the node number of collocation point, J represents the node number of field point, A_{ijk}^{IJ} is the influence matrix between the node I and node J which is derived by numerical integrations, and D_j^J represents the unknown DD vector. Assuming, that we have total NP number of nodal points on the boundary with each node having three unknown DD variables, then we will have a total of $3NP$ unknown variables. Following point collocation technique, Eq. (3.73) results in $3NP$ number of linear system of equations with $3NP$ unknowns. The linear system of equations with appropriate boundary conditions can be solved for unknown DD values using either direct or iterative linear equation solver. The stabilized bi-conjugate method is used in this analysis (Griffiths & Smith, 2006). A Matlab computer program has been developed for

three-dimensional DDM model in this research and a detailed flow chart for program is provided in Figure 3.24.

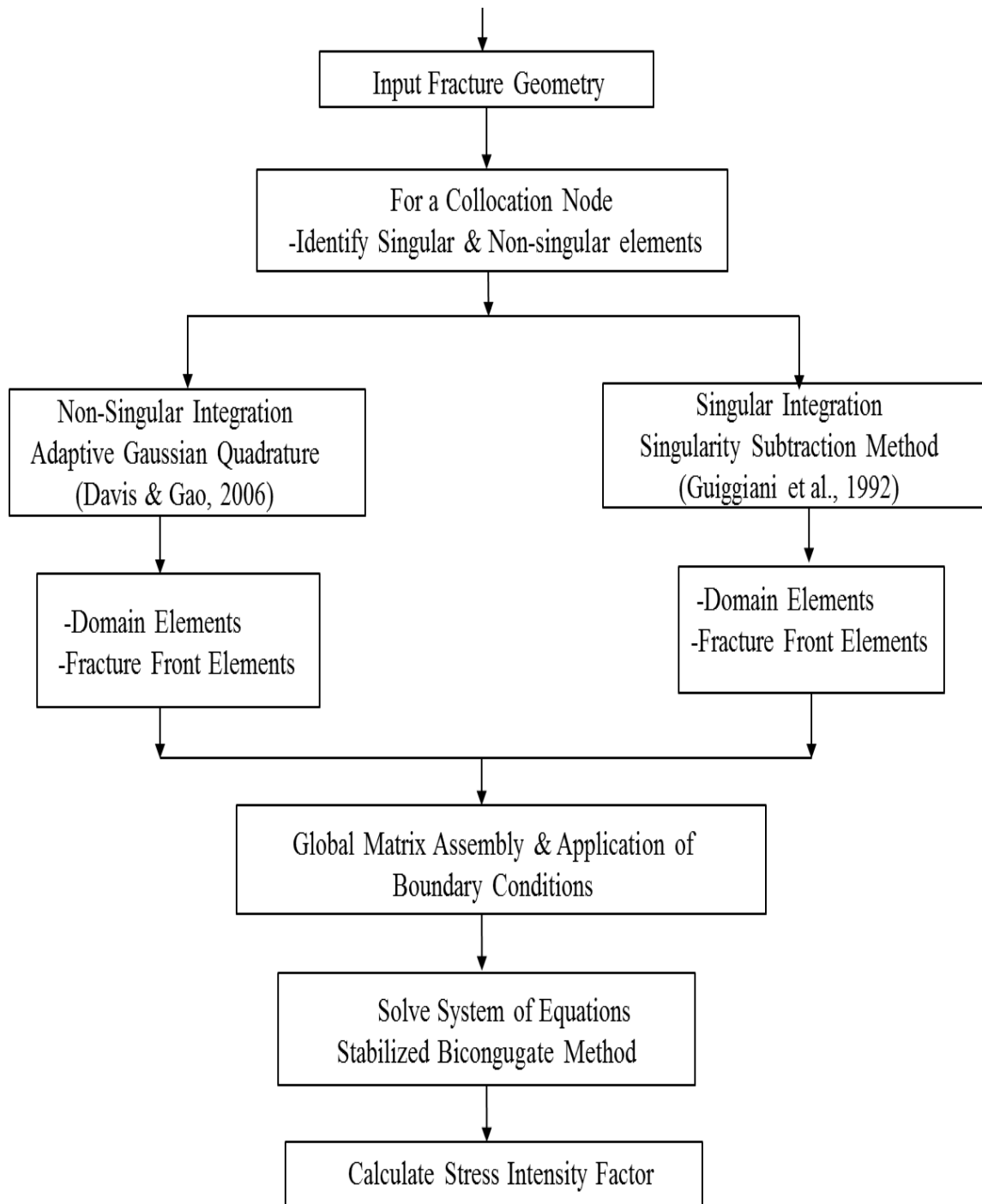


Figure 3.24. Flow chart for three-dimensional displacement discontinuity model

3.6.3. Numerical Example

For numerical implementation of Eq. (3.73), a pressurized penny shaped fracture as shown in Figure 3.25 is considered. The fracture surface is discretized using 4-node continuous elements for the domain elements and 4-node semi-discontinuous element for the fracture front element. A discretized fracture surface for this problem is shown in Figure 3.26. The input parameters for this model are listed in Table 3-2. A surface plot of the fracture normal fracture opening is shown Figure 3.27. Maximum fracture opening at the fracture center is equal to 0.0038 m and minimum fracture opening near the fracture tip (at shifted collocation point for the fracture front element) is equal to $3.61 \cdot 10^{-6}$ m, which can be used for the stress intensity factor estimation.

Table 3-2. Input parameters for penny shaped fracture model

No.	Parameter	Unit	Value
1	Young's modulus (E)	GPa	60
2	Poisson's ratio (ν)	-	0.25
3	Maximum horizontal stress (σ_{xx})	MPa	50
4	Minimum horizontal stress (σ_{yy})	MPa	50
5	Vertical stress (σ_{zz})	MPa	30
6	Fluid pressure (P)	MPa	20
7	Fracture radius	m	10
8	Number of angular division	-	12
9	Number of radial division	-	12

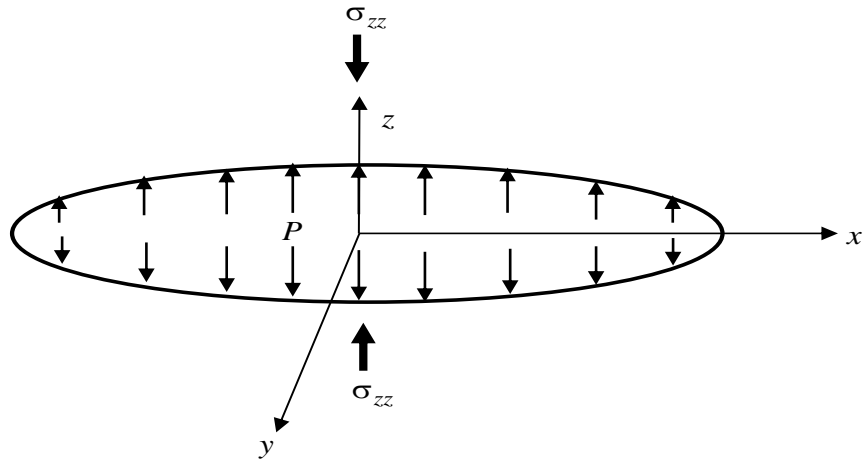


Figure 3.25. Penny shaped fracture with uniform internal fluid pressure

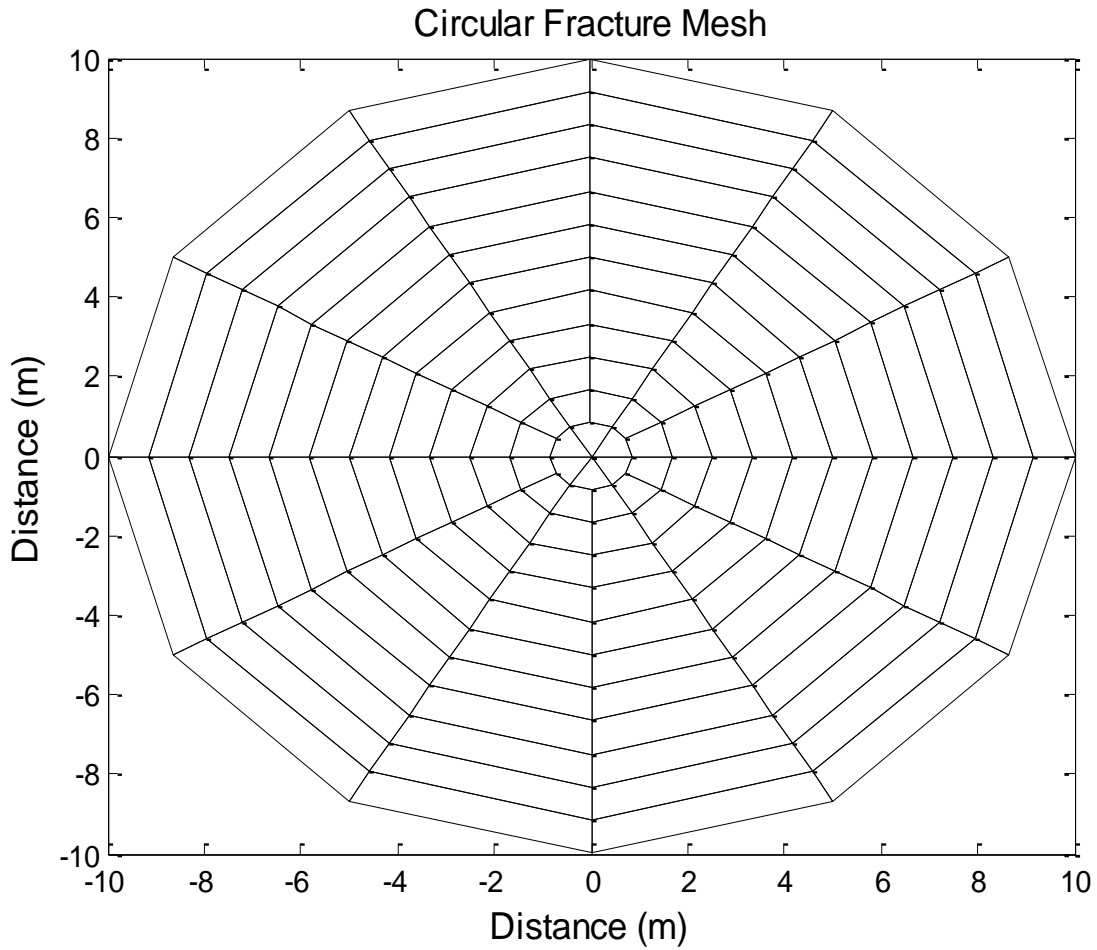


Figure 3.26. Discretized circular fracture mesh (126 domain elements, 12 fracture front elements and 145 nodes)

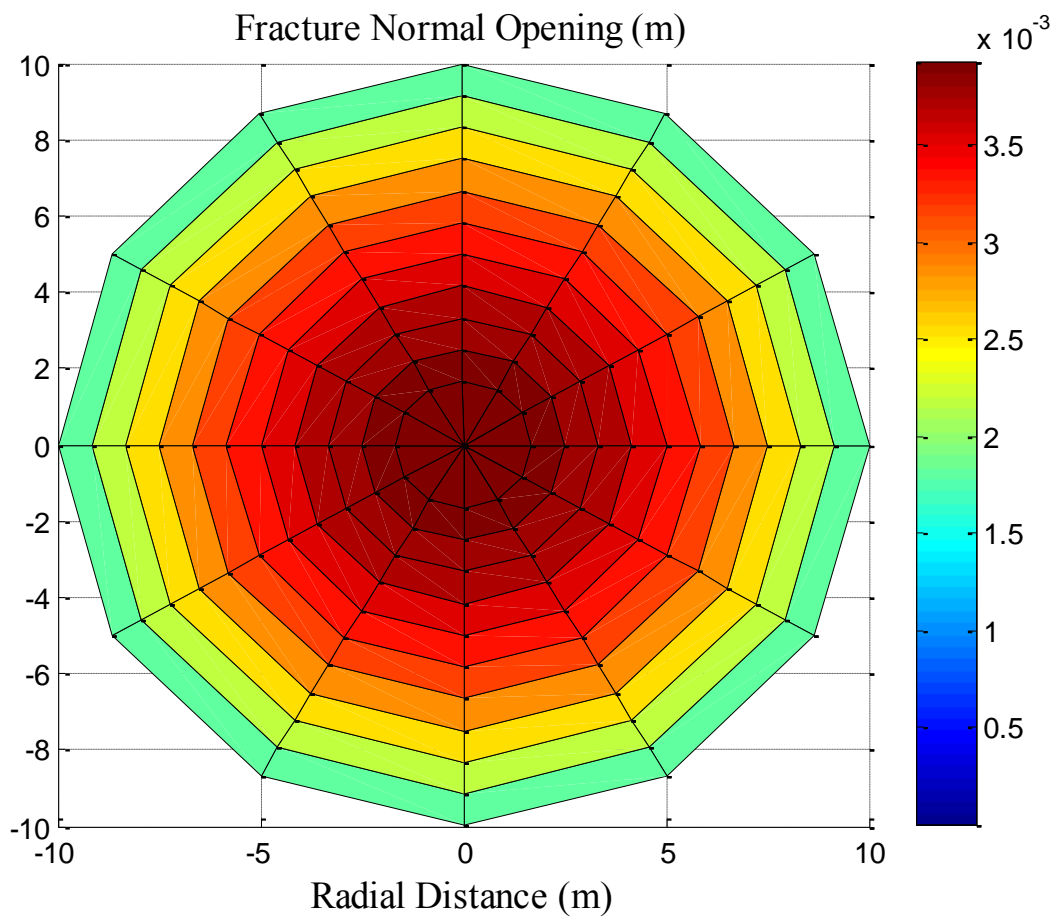


Figure 3.27. Surface plot of fracture normal opening

3.6.4. Model Verification

An analytical verification of three-dimensional DDM model is done by comparing numerical results with analytical results for a penny shaped fracture as proposed by Sneddon (1946) as follows:

$$w(r) = \frac{4(1-\nu)}{\pi G} P R \cdot \sqrt{1 - \left(\frac{r}{R}\right)^2} \quad (3.74)$$

where $w(r)$ represents the fracture normal opening, G and ν are the shear modulus and Poisson's ratio, respectively, r is the distance of any point from center of fracture, and R is the fracture radius. A comparison of numerical and analytical fracture normal opening results is shown in Figure 3.28, which shows a good agreement. Some deviation in the fracture opening is observed near the fracture tip region, which can be adjusted by using gradual changing mesh near the fracture tip region. Another, verification is done by estimating the fracture near tip stress distribution. An analytical solution for the normal stress distribution is given as follows (Li et al., 2001):

$$\sigma_{zz} = -\frac{2P}{\pi} \left[\sin^{-1}\left(\frac{R}{r}\right) - \frac{1}{\sqrt{(r/R)^2 - 1}} \right] ; r > R \quad (3.75)$$

where σ_{zz} represents the normal stresses near fracture tip, P is resultant forces on the fracture surface which a resultant of the applied fluid pressure and in-situ stress, R is the fracture radius, and r is the distance from the fracture tip. A comparison of the numerical and analytical normal stress distribution near the fracture tip is shown in Figure 3.29, which shows a good match. From Figure 3.29 it can be observed that the near fracture tip stresses becomes tremendously high as distance $r \rightarrow 0$.

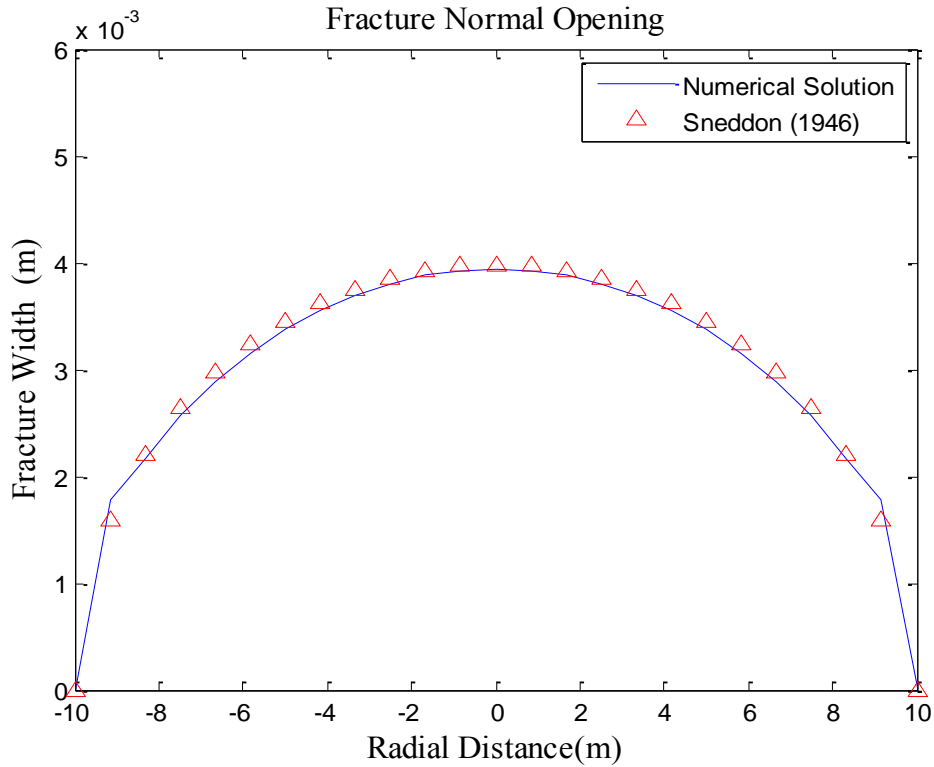


Figure 3.28. Comparison of numerical and analytical fracture normal opening (along $y=0$)

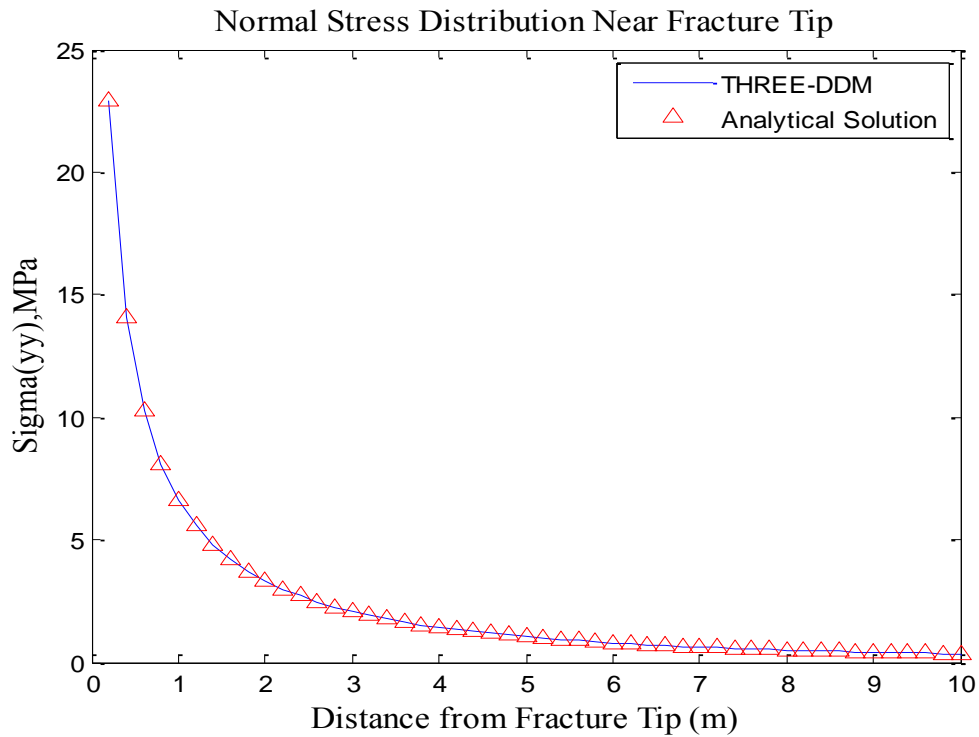


Figure 3.29. Comparison of numerical and analytical normal stress distribution near fracture tip region (along $y=0$)

3.6.5. Estimation of Stress Intensity Factor

Once the DD values are known from numerical solution of Eq. (3.73), the stress intensity factor values for a three-dimensional fracture front can be evaluated using one-point formulae or extrapolation technique coupled with special crack tip element. The SIF values are the critical parameters for the fracture propagation process; it's highly accurate estimation is desired. Based on one point formulae, SIF values are evaluated as follows (Mi, 1996):

$$K_I = \frac{E}{4(1-\nu^2)} \sqrt{\frac{\pi}{2r}} \cdot D_n(r, \theta = \pm\pi, \varphi = -\pi/2) \quad (3.76a)$$

$$K_{II} = \frac{E}{4(1-\nu^2)} \sqrt{\frac{\pi}{2r}} \cdot D_{s2}(r, \theta = \pm\pi, \varphi = -\pi/2) \quad (3.76b)$$

$$K_{III} = \frac{E}{4(1+\nu)} \sqrt{\frac{\pi}{2r}} \cdot D_{s1}(r, \theta = \pm\pi, \varphi = -\pi/2) \quad (3.76c)$$

where K_I, K_{II} , and K_{III} are the Mode-I, Mode-II, and Mode-III SIF values, respectively, and (r, θ, φ) represent the spherical coordinates of the fracture front element as shown in Figure 3.30.

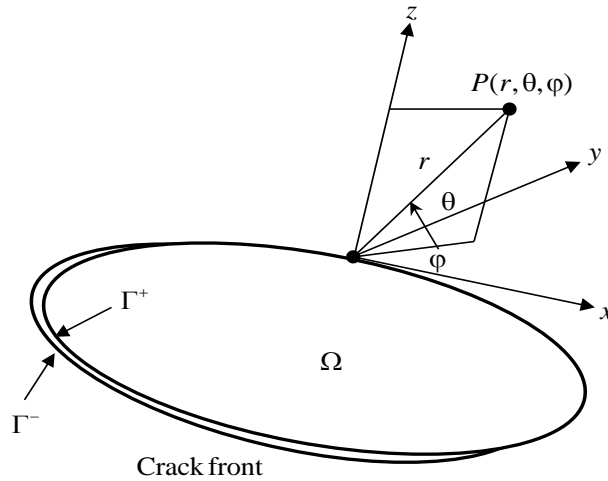


Figure 3.30. Fracture front element and its spherical coordinates (Xiao & Yue, 2011)

3.7. Chapter Summary

This chapter presented detailed methodologies for numerical implementation of the constant and point load DD models. The constant DD models provide a computationally simple methodology for the fracture modeling, but these models are not applicable for any type of fracture geometry (e.g., only for simple geometry) and have less accurate results as compared to point load DD models. The generalized DD models based on the Kelvin's fundamental solutions present a robust model and can be easily extended to any type of fracture geometry. The 4-node semi-discontinuous element used in this study presents an easy implementation of fracture front element. The hyper-singular scheme used is robust technique for singularity removal; it can efficiently handle curved elements. Since, the linear variation of DD's over is assumed, which gives nodal DD values; hence, this model can be directly communicated with the fluid model using the same mesh.

CHAPTER 4.

FLUID FLOW MODELING

This chapter presents the work on steady and transient fracture fluid flow modeling. The steady state fluid flows models are developed for fluid flux components as an input for the heat extraction model in Chapter 5. The transient fluid flow model is developed for coupled hydro-mechanical analysis of the fracture propagation. For both the models, Newtonian fluid behavior and constant fluid properties are assumed. Details of the governing equations for the fracture fluid flow and their numerical implementation are discussed in the following sections.

4.1. Introduction

In general, hydraulically-driven fractures have very narrow aperture as compared to other dimensions. Hence, fluid flow inside the fracture can be simulated by fluid flow in large channel with narrow aperture. The small fluid injection rate and high fluid viscosity suggests that laminar fluid flow exists and the lubrication approximation can be applied for the fracture fluid flow process. The fluid is assumed incompressible and follows Newtonian behavior. Depending on the application, two types of fluid models, namely, steady state flow model and transient flow model are developed in this research.

4.2. Steady State Fracture Fluid Flow

This section presents governing equations for steady state fracture fluid flow. The fracture fluid pressure is solved using Finite Difference approximation and fluid flow components are obtained as secondary variables.

4.2.1. Governing Equations

The steady state fluid flow for a fracture with constant or slight varying aperture can be represent using the ‘cubic law’ of parallel plate flow model as follows (Witherspoon et al., 1980):

$$\mathbf{q}(\mathbf{x}) = -\frac{w^3(x,y)}{\pi^2\mu} \nabla \mathbf{p}(\mathbf{x}) ; \quad \mathbf{x} = (x,y) \in \Gamma \quad (4.1)$$

where \mathbf{q} is the fluid flux vector, \mathbf{p} is the fluid pressure vector, w is the fracture aperture, μ is the fluid dynamic viscosity, and Γ represents the fracture surface as shown in Figure 4.1. In case of the EGS with injection and extraction well system, the fluid flow inside the fracture surface can be analyzed using a fluid source (for the injecting well) or sink (for the producing well) system. The fluid continuity equation based on the mass conservation can be given as follows (Liggett & Liu, 1983):

$$\nabla \cdot \mathbf{q}(\mathbf{x}) = -[Q_i \delta(\mathbf{x}_i) - Q_e \delta(\mathbf{x}_e) - q_L] \quad (4.2)$$

where Q_i is the fluid injection rate, Q_e is the fluid extraction rate q_L is the fluid leak-off into the reservoir, δ is the Dirac delta function, $\mathbf{x}_i = (x_i, y_i)$ and $\mathbf{x}_e = (x_e, y_e)$ represents the locations of the injection and extraction wells, respectively. Due to impermeable nature of the EGS reservoir rocks, no fluid leak-off condition is assumed. Substitution of Eq. (4.1) in Eq. (4.2) results in the lubrication equation for the fluid flow as follows (Ghassemi et al., 2005):

$$\nabla^2 p(x,y) = -\frac{\pi^2\mu}{w^3(x,y)} Q_i \cdot [\delta(\mathbf{x}_i) - \delta(\mathbf{x}_e)] \quad (4.3)$$

The above equation is subjected to boundary condition at the fracture front as follows:

$$\frac{\partial p}{\partial n} = 0 ; \quad \text{on } \partial\Gamma \quad (4.4)$$

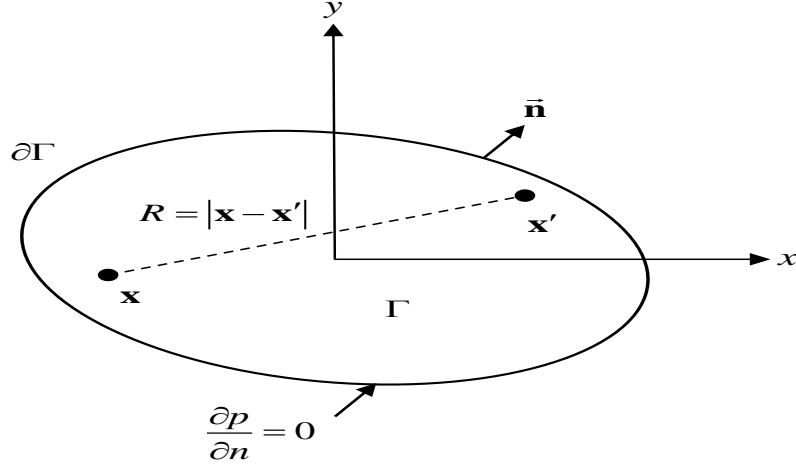


Figure 4.1. Schematic of two-dimensional fracture surface with injection and extraction wells

4.2.2. Finite Difference Approximation

The fluid flow equation (4.3) represents the Poisson's formulation with non-zero force vector (Greenberg, 1998). Expanding, Laplace operator in Eq. (4.3) results as in:

$$\frac{\partial^2 p}{\partial x^2} + \frac{\partial^2 p}{\partial y^2} = -R(x, y) \quad (4.5)$$

where $R(x, y)$ represents the right hand side of Eq.(4.3). The Finite Difference Method is used for numerical implementation of Eq. (4.5) in this research. The second order derivatives of the fluid pressure in Eq. (4.5) can be approximated using the central difference scheme in spatial variables as follows (Strack, 1989):

$$\left[\frac{\partial^2 p}{\partial x^2} \right]_{i,j} = \frac{p_{i-1,j} - 2p_{i,j} + p_{i+1,j}}{(\Delta x)^2} \quad (4.6a)$$

$$\left[\frac{\partial^2 p}{\partial y^2} \right]_{i,j} = \frac{p_{i,j-1} - 2p_{i,j} + p_{i,j+1}}{(\Delta y)^2} \quad (4.6b)$$

where (i, j) represents the location of a grid point as shown in Figure 4.2, Δx and Δy represent grid size in x - and y - directions, respectively. Substituting, the above equations in Eq. (4.5) results as:

$$\frac{p_{i-1,j} - 2p_{i,j} + p_{i+1,j}}{(\Delta x)^2} + \frac{p_{i,j-1} - 2p_{i,j} + p_{i,j+1}}{(\Delta y)^2} = -R_{i,j} \quad (4.7)$$

Assuming, $\Delta x = \Delta y$ for a square element grid, the fluid pressure for node (i, j) can be given as follows:

$$p_{i,j} = \frac{1}{4} [p_{i-1,j} + p_{i+1,j} + p_{i,j-1} + p_{i,j+1} + (\Delta x)^2 R_{i,j}] \quad (4.8)$$

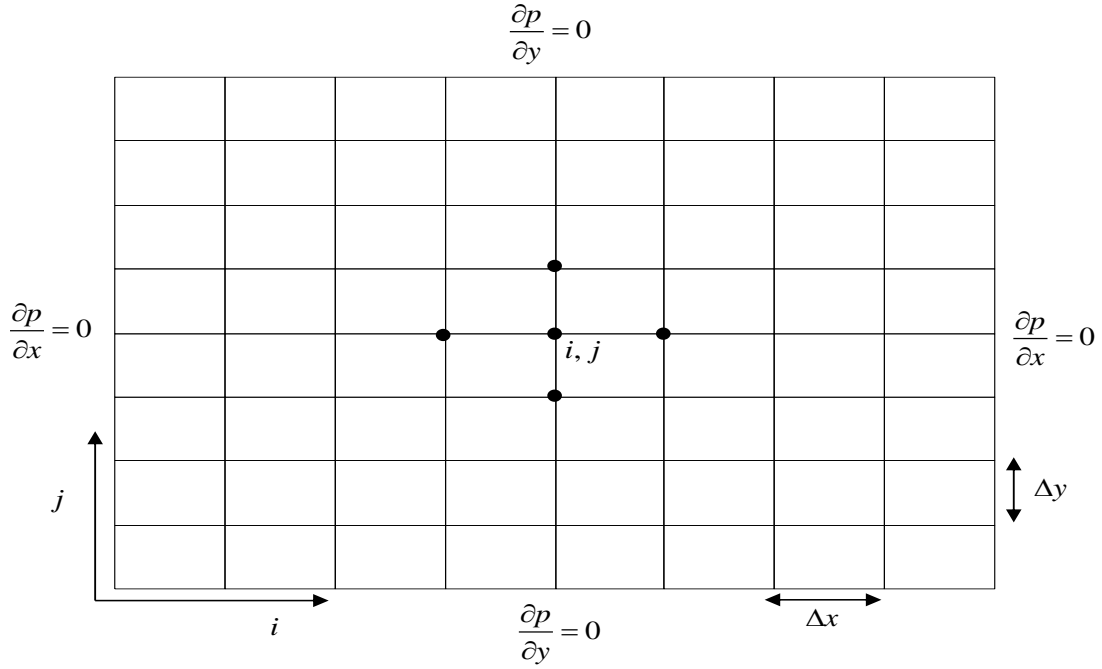


Figure 4.2. Discretized fracture mesh for steady state fluid flow

1. Numerical Implementation

Application of Eq. (4.8) for each nodal point in the grid results in a linear system of equations, which can be solved using direct or iterative solver. The Gauss-Seidel iterative method with successive over relaxation (SOR) is used in this research (Wang & Anderson, 1982). Based on SOR method, Eq. (4.8) can be written as follows:

$$p_{i,j}^{m+1} = (1-\omega)p_{i,j}^m + \frac{\omega}{4} [p_{i-1,j}^{m+1} + p_{i+1,j}^{m+1} + p_{i,j-1}^m + p_{i,j+1}^m + (\Delta x)^2 R(x,y)] \quad (4.9)$$

where ω is the relaxation factor which in general varies as $1 \leq \omega \leq 2$.

2. Flux Boundary Conditions

The derivative boundary conditions (Eq. 4.4) along the fracture front can be implemented by introducing a fictitious node outside the domain boundary as shown in Figure 4.3. Considering, the case of fracture boundary along $i=1$, normal derivative of fluid pressure using fictitious node can be written as follows:

$$\left[\frac{\partial p}{\partial n} \right]_{1,j} = \left[\frac{\partial p}{\partial x} \right]_{1,j} = \frac{p_{2,j} - p_{0,j}}{2\Delta x} \quad (4.10a)$$

$$p_{0,j} = p_{2,j} - 2\Delta x \left[\frac{\partial p}{\partial n} \right]_{1,j} \quad (4.10b)$$

Substituting Eq. (4.10b) in Eq. (4.9), the fluid pressure distribution for the fracture front along $i=1$ can be given as follows:

$$p_{1,j}^{m+1} = (1-\omega)p_{1,j}^m + \frac{\omega}{4} \left[p_{1,j-1}^{m+1} + 2p_{2,j}^m + p_{1,j+1}^m + (\Delta x)^2 R(x, y) \right] \quad (4.11)$$

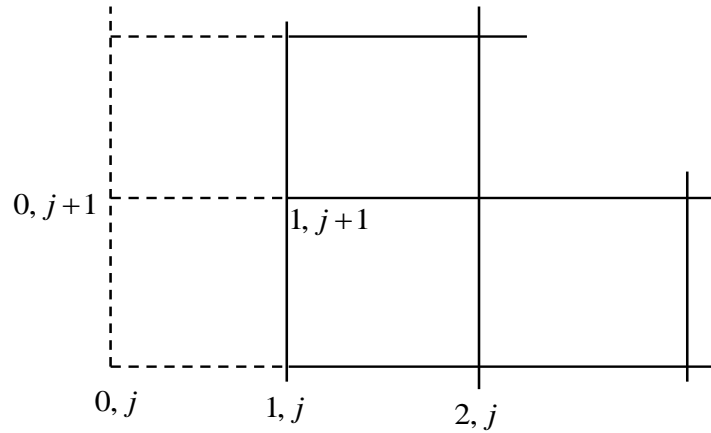


Figure 4.3. Representation of a derivative boundary condition with a fictitious node

3. Fluid Flow Components

Once the nodal fluid pressure are known from numerical solution of Eq. (4.9), the fluid flow components can be obtained based on the Darcy's Law:

$$q_x = -\frac{w^3}{\pi^2\mu} \frac{\partial p}{\partial x} \quad (4.12a)$$

$$q_y = -\frac{w^3}{\pi^2\mu} \frac{\partial p}{\partial y} \quad (4.12b)$$

where q_x and q_y represents the fluid flow components in x - and y - directions, respectively. The above equations as can approximate using central finite difference scheme as follows (Chapra & Canale, 1998):

$$q_x = -\frac{w^3}{\pi^2\mu} \left[\frac{P_{i+1,j} - P_{i-1,j}}{2\Delta x} \right] \quad (4.13a)$$

$$q_y = -\frac{w^3}{\pi^2\mu} \left[\frac{P_{i,j+1} - P_{i,j-1}}{2\Delta y} \right] \quad (4.13b)$$

4.2.3. Numerical Example

For numerical implementation of Eq. (4.9), two cases are considered: first with single injection well in an infinite reservoir and second an EGS system with the injection and extraction wells. The input parameters for these models are listed in Table 4-1.

Table 4-1. Input parameters for steady state fracture fluid flow

No.	Parameter	Unit	Value
1	Fluid viscosity (μ)	Pa·sec	0.001
2	Fluid injection rate(Q)	m ³ /sec	0.01
3	Fracture aperture (w)	m	0.001
4	Fracture size	m·m	50·50

1. Single Injection Well System

A single injection well system in an infinite reservoir is considered in this case. Though, the reservoir domain extends to infinity, but a long enough fracture extension is

considered for numerical modeling. A surface plot of fracture fluid pressure distribution is shown in Figure 4.4, which shows a maximum fluid pressure near the injection well and it shows minimum value at fracture boundary region. Once, the pressure distribution is known over the fracture surface, the fluid flux components can be obtained as secondary variables using Eqs. (4.13). A vector plot of fluid flux components is shown in Figure 4.5. The fluid components will be used as input for the heat extraction modeling.

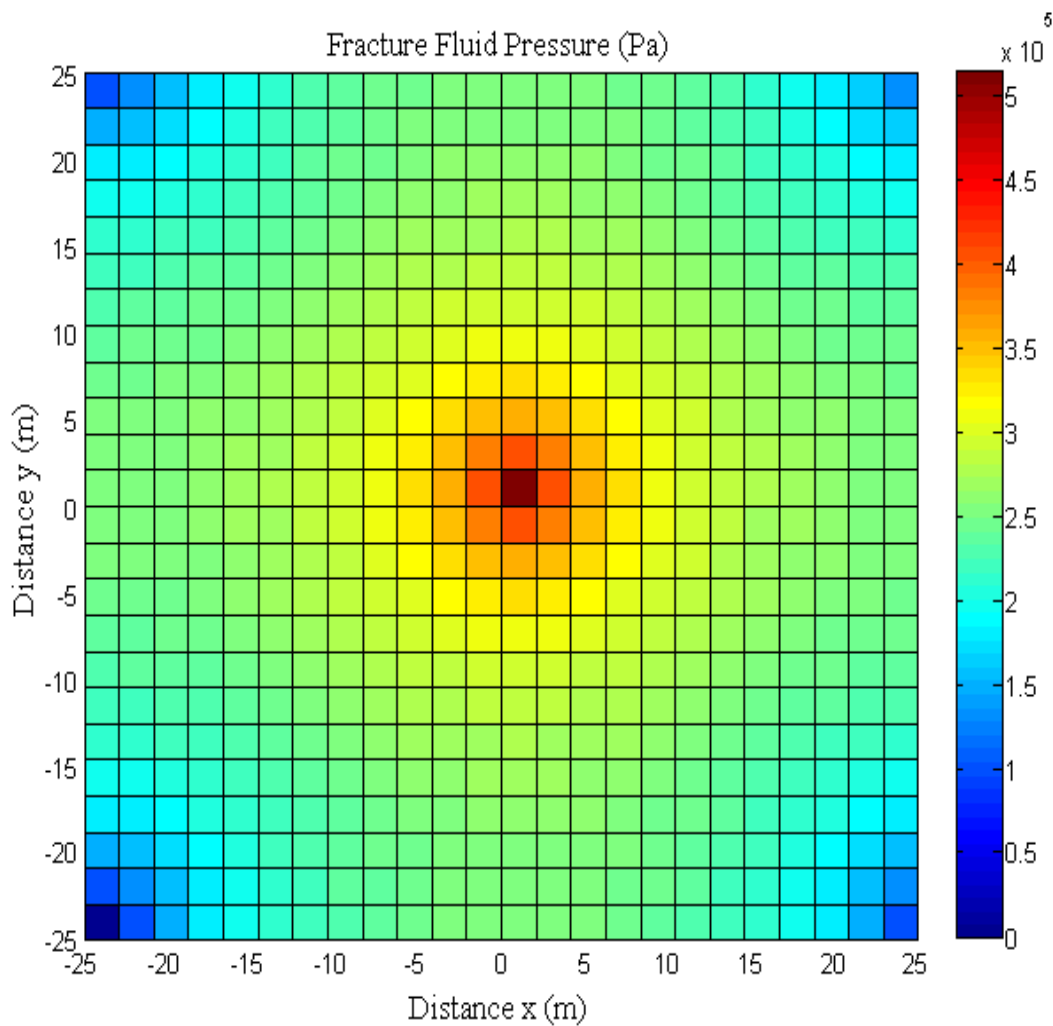


Figure 4.4. Surface plot of fracture fluid pressure distribution for a single well system

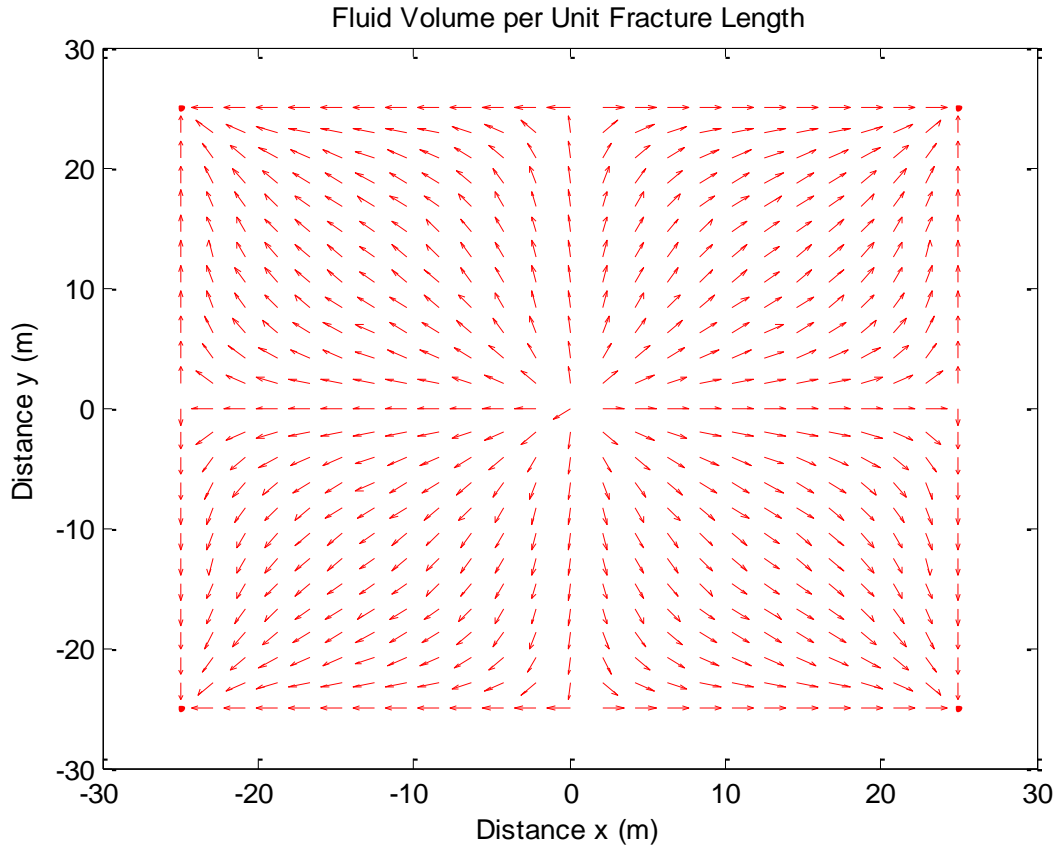


Figure 4.5. Fracture fluid flux vectors for a single injection well system

2. Injection and Extraction Well System

For numerical implementation of Eq. (4.8), an injection and extraction well system is considered. The boundary conditions are used as shown in Figure 4.2, for the fracture pressure distribution. A surface plot of fracture fluid pressure distribution is shown in Figure 4.6, which shows a maximum fluid pressure near the injection well and it shows minimum value at the extraction well. Once, the pressure distribution is known over the fracture surface, the fluid flux components can be obtained as secondary variables using Eqs. (4.13). A vector plot of fluid flux components is shown in Figure 4.7.

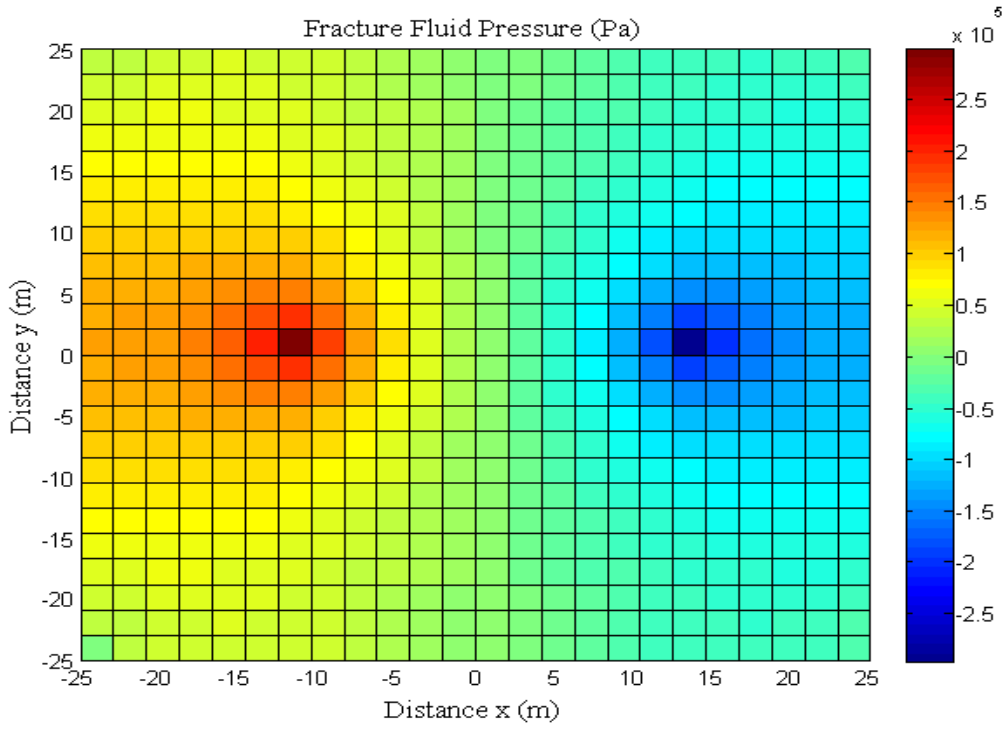


Figure 4.6. Surface plot of fracture fluid pressure distribution for injection and extraction well system

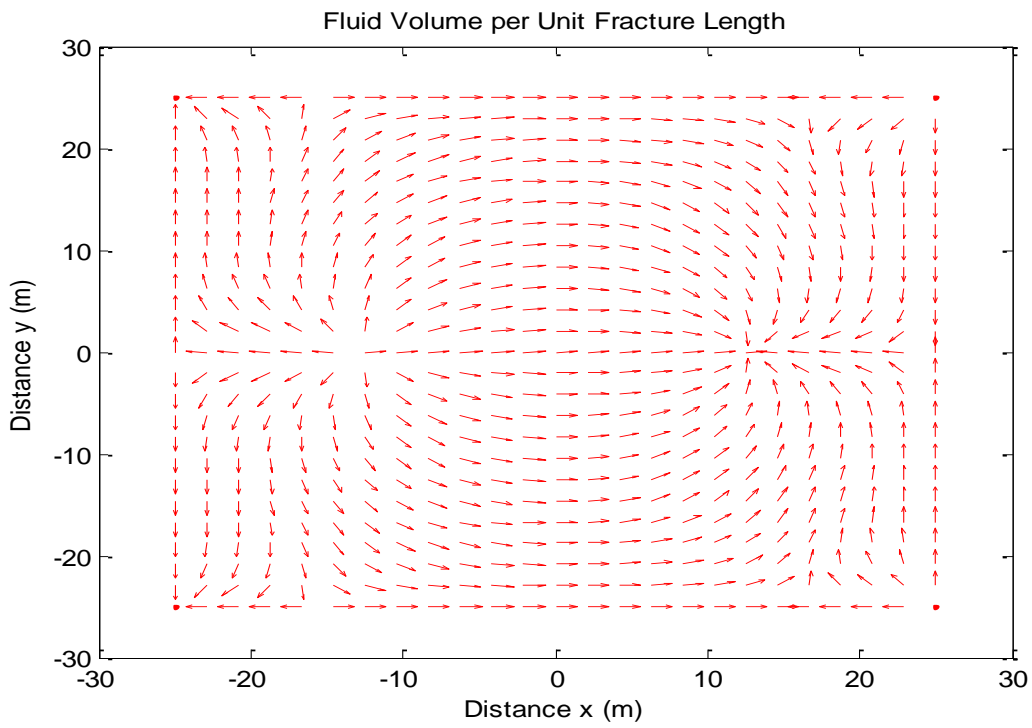


Figure 4.7. Fracture fluid flux vectors for the injection and extraction well system

4.3. Transient Fracture Fluid Flow

This section presents governing equations for the transient fracture fluid. The fluid flow equations are discretized and implemented using the Galerkin's Finite Element approximation.

4.3.1. Governing Equations Fracture Fluid Flow

Considering, a differential control volume in the fluid flow domain is shown in Figure 4.8, applying fluid mass conservation results as follows (Clifton & Sayed, 1981; Yew, 1997):

$$\frac{\partial q_x}{\partial x} + \frac{\partial q_y}{\partial y} + \frac{\partial w}{\partial t} + q_L = 0 \quad (4.14)$$

where q_x and q_y represents the fluid flux components in x - and y - directions, respectively, $\frac{\partial w}{\partial t}$ represents the fracture volume increase rate, and q_L is the fluid leak-off through fracture surfaces which can be expressed using one-dimensional model as follows (Carter, 1957):

$$q_L = \frac{2C_L}{\sqrt{t - \tau(x, y)}} \quad (4.15)$$

where C_L is an empirical fluid leak-off constant, t is current time, $\tau(x, y)$ represent the time at which any location of the fracture first time exposed for fluid leak-off.

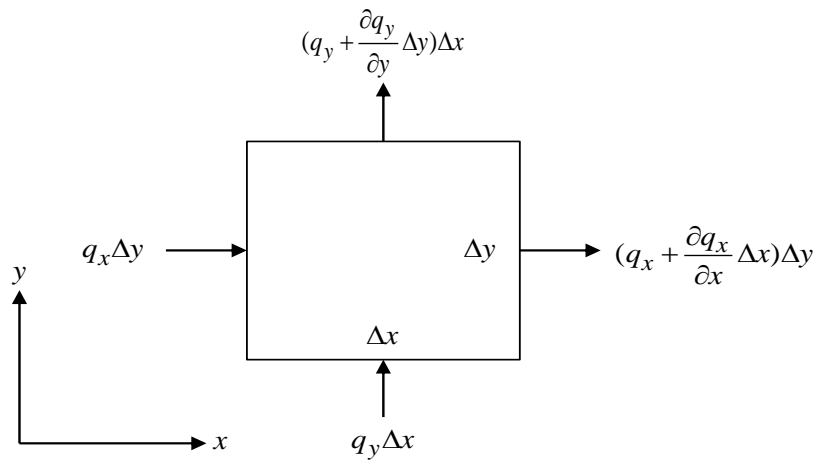


Figure 4.8. Conservation of fracture fluid flow in a control volume rate (Yew, 1997)

Substituting, the fluid flux components from Eq. (4.12) and fluid leak-off from Eq. (4.15) in Eq. (4.14) results as follows:

$$\frac{\partial}{\partial x} \left(\frac{w^3}{12\mu} \frac{\partial p}{\partial x} \right) + \frac{\partial}{\partial y} \left(\frac{w^3}{12\mu} \frac{\partial p}{\partial y} \right) = \frac{\partial w}{\partial t} + \frac{2C_L}{\sqrt{t - \tau(x, y)}} \quad (4.16)$$

The above equations represent the governing equation for two-dimensional Newtonian fluid flow inside a fracture. The following boundary conditions are subjected to Eq. (4.16):

$$-\frac{w^3}{\pi^2 \mu} \frac{\partial p}{\partial n} = Q_0; \quad \text{at Wellbore} \quad (4.17a)$$

$$\frac{\partial p}{\partial n} = 0; \quad \text{on symmetry line} \quad (4.17b)$$

$$\frac{\partial p}{\partial n} = 0; \quad \text{on fracture front} \quad (4.17c)$$

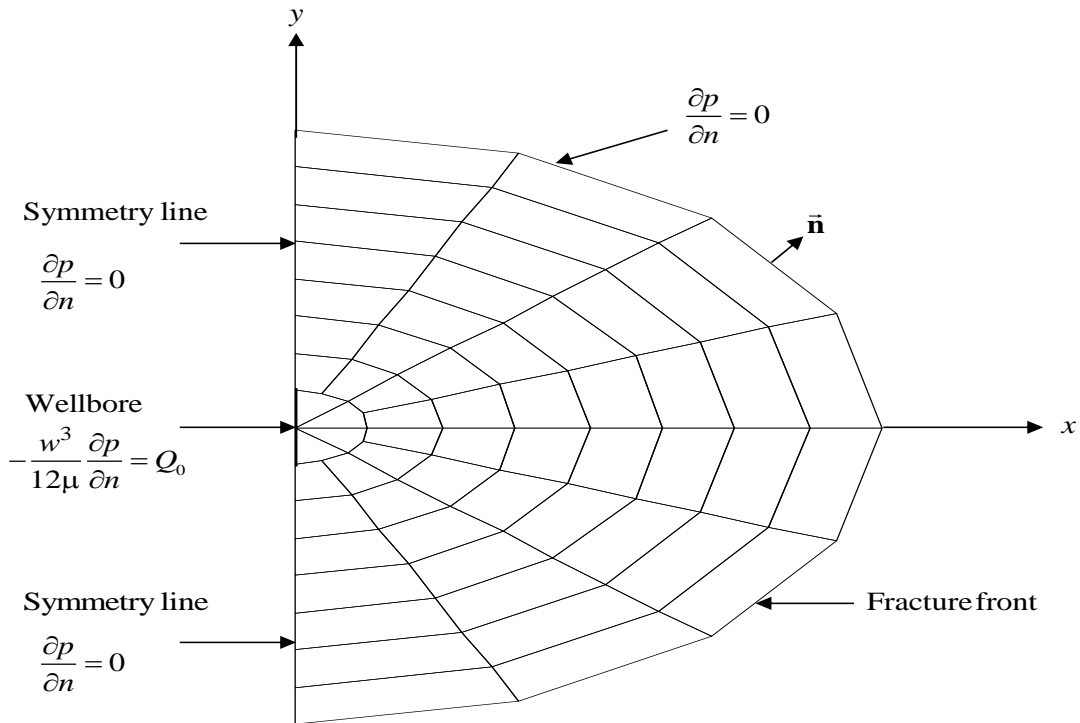


Figure 4.9. Boundary of fracture fluid flow domain (Hongren, 1987)

4.3.2. Finite Element Discretization

Equation (4.16) can be discretized using the standard Galerkin Finite Element Method (Zienkiewicz, 2005; Becker et al., 1981). Multiplying both side of Eq. (4.16) by basis functions results in:

$$\int_{\Omega} \phi_i \left[\frac{\partial}{\partial x} \left(\frac{w^3}{12\mu} \frac{\partial p}{\partial x} \right) + \frac{\partial}{\partial y} \left(\frac{w^3}{12\mu} \frac{\partial p}{\partial y} \right) \right] d\Omega = \int_{\Omega} \phi_i \frac{\partial w}{\partial t} d\Omega + \int_{\Omega} \phi_i q_L d\Omega \quad (4.18)$$

where ϕ represent the basis functions which depends on the type of elements used for mesh discretization. Integration equation (4.18) by parts over the fracture domain results as follows:

$$\int_{\Omega} \frac{w^3}{12\mu} \left[\frac{\partial p}{\partial x} \frac{\partial \phi_i}{\partial x} + \frac{\partial p}{\partial y} \frac{\partial \phi_i}{\partial y} \right] d\Omega = - \int_{\Omega} \phi_i \frac{\partial w}{\partial t} d\Omega - \int_{\Omega} \phi_i q_L d\Omega + \int_{\Omega_s} \phi_i \frac{w^3}{12\mu} \frac{\partial p}{\partial n} d\Omega_s \quad (4.19)$$

Applying boundary condition from Eq. (4.17a) results as:

$$\int_{\Omega} \frac{w^3}{12\mu} \left[\frac{\partial p}{\partial x} \frac{\partial \phi_i}{\partial x} + \frac{\partial p}{\partial y} \frac{\partial \phi_i}{\partial y} \right] d\Omega = - \int_{\Omega} \phi_i \frac{\partial w}{\partial t} d\Omega - \int_{\Omega} \phi_i q_L d\Omega + \int_{\partial\Omega_s} \phi_i Q_0 d\Omega_s \quad (4.20)$$

The above equation is subjected to the boundary conditions as given in Eqs. (4.17b), and (4.17c). Since, the entire fracture boundary is subjected to only the flux boundary condition; hence, it is Neumann problem. Becker et al. (1981) suggested that the Neumann problems can be only solve within a constant and using a necessary compatibility condition. A necessary compatibility condition for Eq. (4.20) can be given by conservation of the global flow rate as follows (Ouyang et al., 1997):

$$- \int_{\Omega} q_L d\Omega - \int_{\Omega} \frac{\partial w}{\partial t} d\Omega + \int_{\Omega_s} Q_0 d\Omega_s = 0 \quad (4.21)$$

The above condition implies that for an incompressible fluid, the summation of the fracture volume increase rate at any time and the fluid leak-off rate through the fracture surfaces is equal to the fracturing fluid injected into the fracture.

4.3.3. Numerical Implementation

For numerical implementation of Eq. (4.20), assuming a linear variation of the fluid pressure and the fracture width over an element as follows (Kwon & Bang, 2000):

$$p(x, y) = \sum_{i=1}^N \phi_i p_i \quad (4.22a)$$

$$w(x, y) = \sum_{i=1}^N \phi_i w_i \quad (4.22b)$$

where ϕ represent the shape functions, N is the number of nodes per element, p_i and w_i represent the nodal fluid pressure and fracture width, respectively. Using Eq. (4.22), the discretized fluid flow equation for an element can be written as follows:

$$\frac{1}{12\mu} \int_{\Omega_e} \left(\sum_{k=1}^N \phi_k w_k \right)^3 \left[\frac{\partial \phi_i}{\partial x} \frac{\partial \phi_j}{\partial x} + \frac{\partial \phi_i}{\partial y} \frac{\partial \phi_j}{\partial y} \right] p_j d\Omega_e = - \int_{\Omega_e} \phi_i \frac{\partial w}{\partial t} d\Omega - \int_{\Omega_e} \phi_i q_L d\Omega + \int_{\partial\Omega_s} \phi_i Q_0 d\Omega_s \quad (4.23)$$

The fracture width derivatives with respect to time variable in above equation can be approximated using implicit FD scheme as follows (Chapra & Canale, 1998):

$$\left. \frac{\partial w}{\partial t} \right|_{n+1} = \frac{w(t_{n+1}) - w(t_n)}{\Delta t} ; \Delta t = t_{n+1} - t_n \quad (4.24)$$

where $w(t_{n+1})$ and $w(t_n)$ represent the fracture widths at t_{n+1} and t_n time steps, respectively, and $t_{n+1} - t_n = \Delta t$ represent the time increment. Substituting, Eq. (4.24) in Eq. (4.23), the resultant equation can be written as (Carter et al., 2000):

$$\begin{aligned} \frac{1}{12\mu} \int_{\Omega_e} \left(\sum_{k=1}^N \phi_k w_k \right)^3 \left[\frac{\partial \phi_t}{\partial x} \frac{\partial \phi_j}{\partial x} + \frac{\partial \phi_t}{\partial y} \frac{\partial \phi_j}{\partial y} \right] p_j d\Omega_e = \\ - \int_{\Omega_e} \phi_t \left[\sum_{j=1}^N \phi_j \frac{w(t_{n+1}) - w(t_n)}{\Delta t} \right] d\Omega_e - \int_{\Omega_e} \phi_t q_L d\Omega_e + \int_{\partial\Omega_s} \phi_t Q_0 d\Omega_s \end{aligned} \quad (4.25)$$

The above equation can rearranged as follows:

$$\begin{aligned} \int_{\Omega_e} \phi_t \left[\sum_{j=1}^N \phi_j \frac{w_j(t_{n+1})}{\Delta t} \right] d\Omega_e + \frac{1}{12\mu} \int_{\Omega_e} \left(\sum_{k=1}^N \phi_k w_k \right)^3 \left[\frac{\partial \phi_t}{\partial x} \frac{\partial \phi_j}{\partial x} + \frac{\partial \phi_t}{\partial y} \frac{\partial \phi_j}{\partial y} \right] p_j d\Omega_e = \\ \int_{\Omega_e} \phi_t \left[\sum_{j=1}^N \phi_j \frac{w_j(t_n)}{\Delta t} \right] d\Omega_e - \int_{\Omega_e} \phi_t q_L d\Omega_e + \int_{\partial\Omega_s} \phi_t Q_0 d\Omega_s \end{aligned} \quad (4.26)$$

The left hand side of above equation has fluid pressure and fracture width as unknown for (n+1)th time step; whereas the right hand side of equation has all known quantities form previous time step. Equation (4.26) can be rewritten in non-linear vector form as follows:

$$[\mathbf{B}]\{\mathbf{w}\} + [\mathbf{K}(w)]\{\mathbf{p}\} = \mathbf{F} \quad (4.27)$$

The vector matrix can be written as follows:

$$K_{ij} = \frac{1}{12\mu} \int_{\Omega_e} \left(\sum_{k=1}^N \phi_k w_k \right)^3 \left[\frac{\partial \phi_t}{\partial x} \frac{\partial \phi_j}{\partial x} + \frac{\partial \phi_t}{\partial y} \frac{\partial \phi_j}{\partial y} \right] d\Omega_e; \quad B_{ij} = \int_{\Omega_e} \phi_t \left[\sum_{j=1}^N \phi_j \frac{1}{\Delta t} \right] d\Omega_e \quad (4.28a)$$

$$f_{ij} = \int_{\Omega_e} \phi_t \left[\sum_{j=1}^N \phi_j \frac{w_j(t_n)}{\Delta t} \right] d\Omega_e - \int_{\Omega_e} \phi_t q_L d\Omega_e + \int_{\partial\Omega_s} \phi_t Q_0 d\Omega_s \quad (4.28b)$$

4.3.4. Verification of Finite Element Program

A verification of the Finite Element program developed for the fracture fluid flow equation (4.26) is done using pore pressure distribution in a reservoir. The pore pressure distribution in the reservoir is given as follows (Gutierrez & Hansteen, 1994):

$$\nabla^T \frac{k}{n\mu} \nabla p = C_t \frac{\partial p}{\partial t} \quad (4.29)$$

where p is the pore pressure, k is the matrix permeability, n is the porosity, μ is the fluid viscosity, and C_t is total reservoir compressibility. Rewriting above equation in expanded form as follows:

$$\frac{\partial^2 p}{\partial x^2} + \frac{\partial^2 p}{\partial y^2} = \frac{1}{\alpha} \frac{\partial p}{\partial t}; \quad \alpha = \frac{k}{n\mu C_t} \quad (4.30)$$

Based on the Galerkin's Finite Element scheme Eq. (4.30a) can be written can as follows:

$$[\mathbf{M}]\{\dot{p}\}^t + [\mathbf{K}]\{p\}^t = \{\mathbf{F}\}^t \quad (4.31)$$

where,

$$\mathbf{K} = \alpha \int_V \nabla^T \phi \cdot \nabla \phi dV \quad (4.32a)$$

$$\mathbf{M} = \int_V \phi^T \cdot \phi dV \quad (4.32b)$$

$$\mathbf{F} = \int_{\Gamma} \phi \cdot f_i d\Gamma \quad (4.32c)$$

where ϕ are the shape functions. The derivative of pressure with respect to time variables can be approximated using implicit finite difference approximation as follows:

$$\{\dot{p}\}^{t+\Delta t} = \frac{\{p\}^{t+\Delta t} - \{p\}^t}{\Delta t} \quad (4.33)$$

Substituting, Eq. (4.33) in Eq. (4.31) results as follows:

$$([\mathbf{M}] + \Delta t [\mathbf{K}])\{p\}^{t+\Delta t} = \Delta t \{\mathbf{F}\}^{t+\Delta t} + [\mathbf{M}]\{p\}^t \quad (4.34)$$

1.

2. Numerical Implementation

For numerical implementation of Eq. (4.34), a reservoir domain was discretized using 4-noded rectangular elements as shown in Figure 4.10. The reservoir has initial zero pore pressure. Suddenly, the left and right boundary pressures are increased to 200 Pa and maintained at this pressure. The top and bottom boundary of the reservoir are at no flow condition. We are interested to get pressure distribution in the domain with time. An analytical solution for this problem, which is similar to the transient heat diffusion is given as follows (Greenberg, 1998):

$$p(x,t) = p_1 + (p_2 - p_1) \frac{x}{L} + \sum_{m=1}^{\infty} K_m \sin\left(\frac{m\pi x}{L}\right) \cdot \exp\left\{-\left(\frac{m\pi\alpha}{L}\right)^2 t\right\} \quad (4.35a)$$

$$K_n = \frac{2}{L} \int_0^L F(x) \sin\left(\frac{n\pi x}{L}\right) dx \quad (4.35b)$$

where $p(x,t)$ represent the pressure variation at any location with time, p_1 and p_2 are the pore pressures at two ends, respectively, L is the domain length, and $F(x)$ represent the source strength.

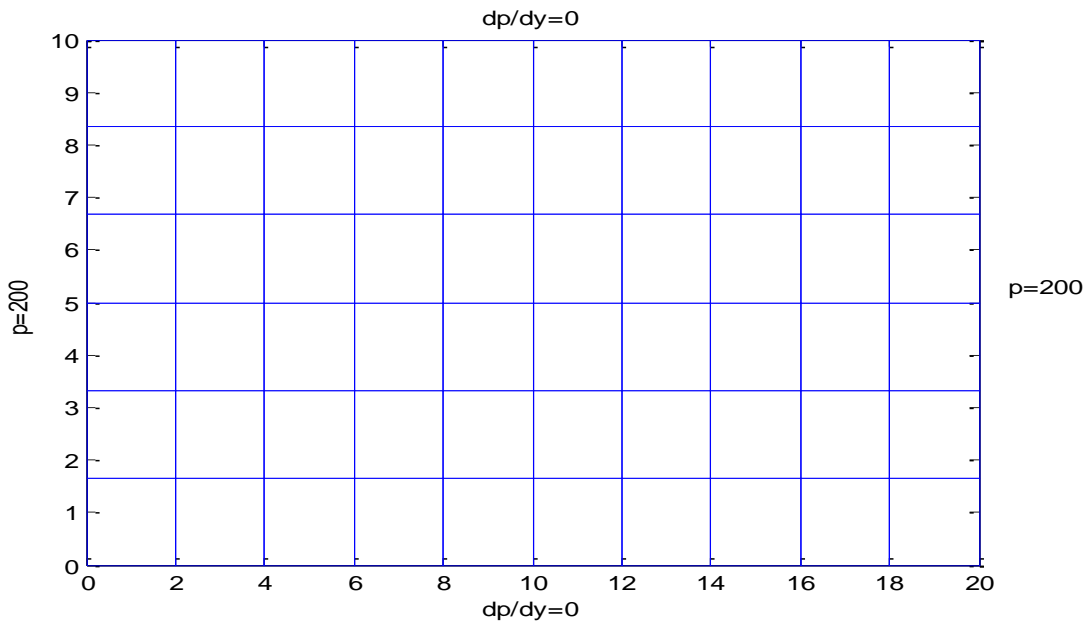


Figure 4.10. Discretized reservoir domain for pore distribution

3. Numerical Example 1

Two numerical examples for this problem are considered. In first case, the coefficient α is assumed equal to 1 and pore pressure distribution at middle node for 100 sec was observed. A plot of pore pressure distribution from the numerical solution and the analytical solution is shown in Figure 4.11, which shows a very good match. After 100 sec, a pore pressure equal to 180 Pa was recorded at the middle node. In second case, the coefficient α is calculated using Eq. (4.30b) using the reservoir parameter as listed in Table 4-2. The result of pore pressure distribution at middle node for 100 sec is shown in Figure 4.12. This case some deviation between the numerical analytical solution is observed. After 100 sec, a pore pressure of about 195 Pa was recorded by numerical model. From comparison of numerical and analytical solution of pore pressure distribution in above two cases, it can be concluded that the Finite Element program works well. It can be easily extended for the fracture fluid flow modeling in case of coupled hydro-mechanical models.

Table 4-2. Reservoir and fluid properties for pore pressure distribution

No.	Parameter	Unit	Value
1	Bulk modulus (K)	Pa	$7.6925 \cdot 10^8$
2	Poisson's ratio (ν)	-	0.20
3	Porosity (n)	-	0.30
4	Permeability (k)	mD	150
5	Biot's constant (β)	-	1
6	Fluid viscosity (μ)	cp	5
7	Reservoir length (L)	m	20
8	Reservoir width (D)	m	10

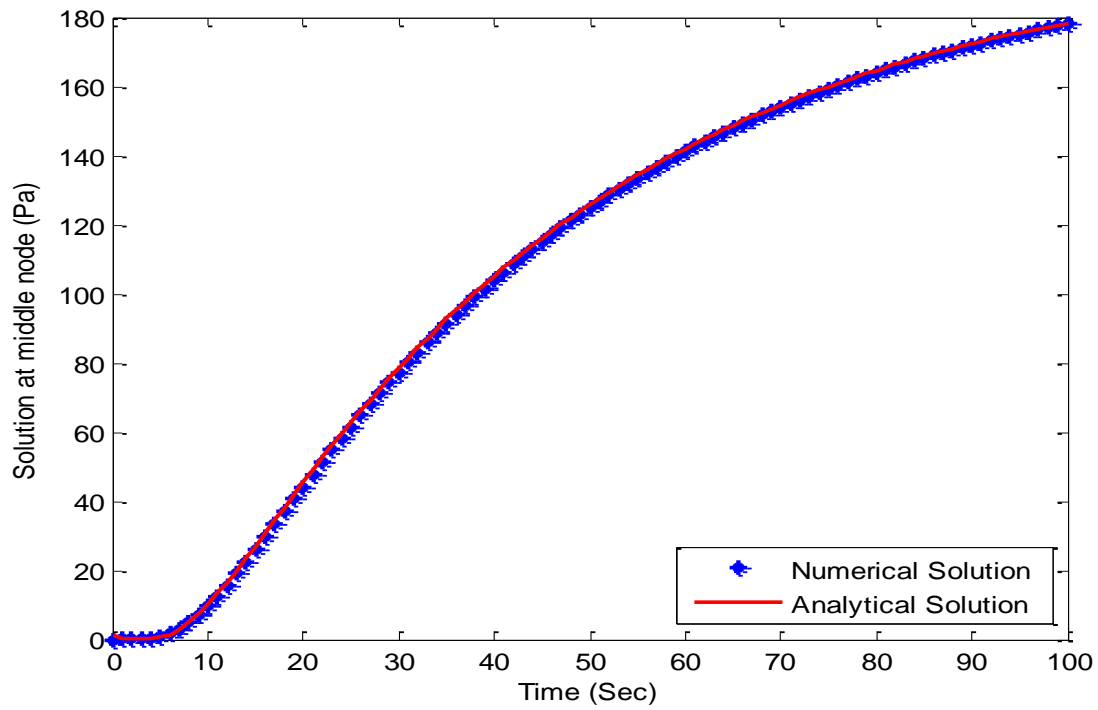


Figure 4.11. Variation of pore pressure distribution at middle node for 100 sec ($\alpha=1$)

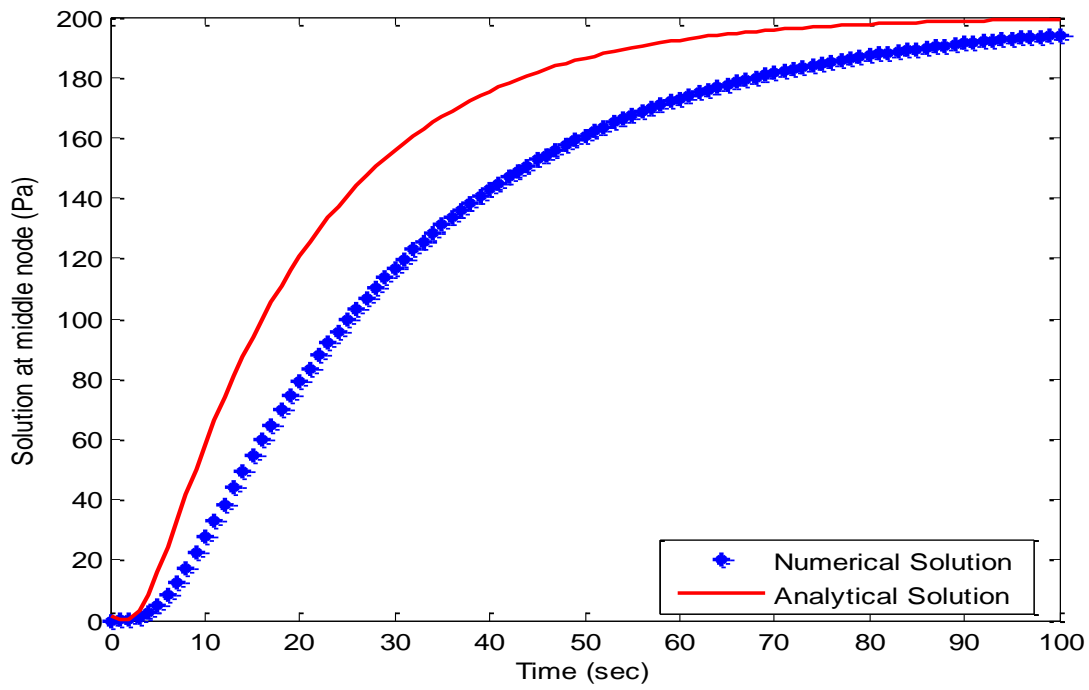


Figure 4.12. Variation of pore pressure distribution for 100 sec

4. Numerical Example 2

For second numerical example an hypothetical hydraulic fracture model is considered as shown in Figure 4.13. For this model a small uniform increase in the fracture width with time is assumed and the fluid equation (4.20) is solved for the fluid pressure distribution. The reservoir rocks are assumed impermeable; hence, no fluid leak-off condition is assumed. The boundary conditions for this model are same as shown Figure 4.9. The input parameters for this model are listed in Table 4-3.

Table 4-3. Input parameters for rectangular fracture fluid flow model

No.	Parameter	Unit	Value
1	Fluid injection rate (Q_i)	m ³ /sec	0.01
2	Minimum in-situ stress (σ_3)	MPa	30
3	Initial fracture width(w)	m	0.001
4	Change in fracture width	m/time step	0.0001
5	Time increment	min	1
6	Fluid viscosity (μ)	cp	5

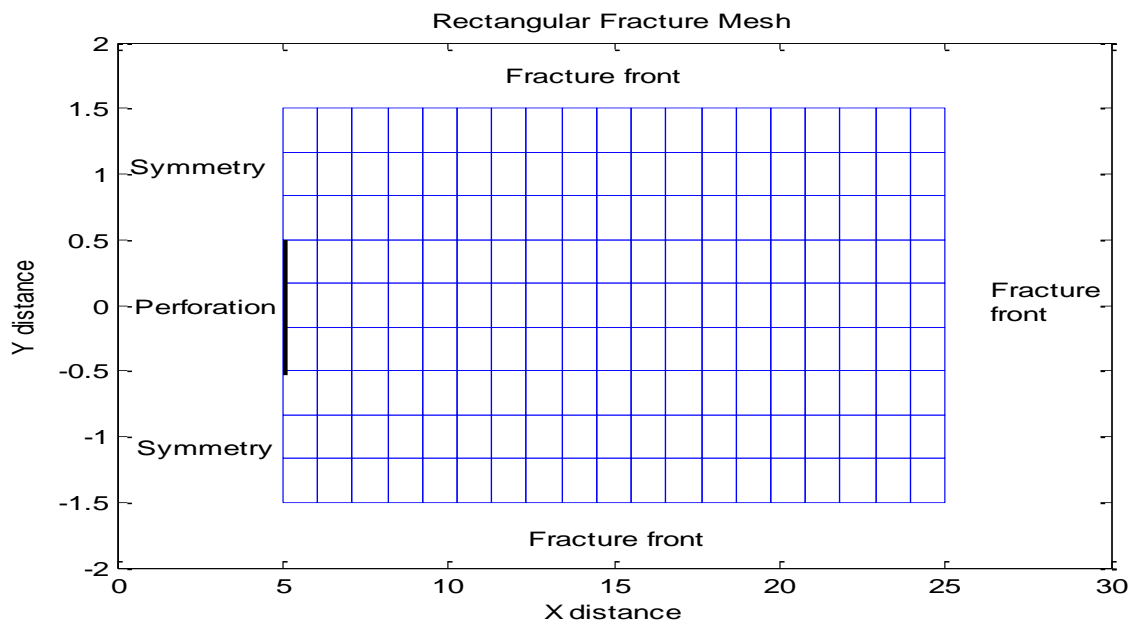


Figure 4.13. Discretized fracture mesh for rectangular fracture fluid flow

The fluid pressure variation for this hypothetical fracture model at three different locations: at the wellbore, near the wellbore and near the fracture tip is shown in Figure 4.14. The pressure variation from this model shows a similar behavior with a typical coupled hydraulic fracture model. All three pressure variation plots shows zero net fluid pressure condition at the fracture tip.

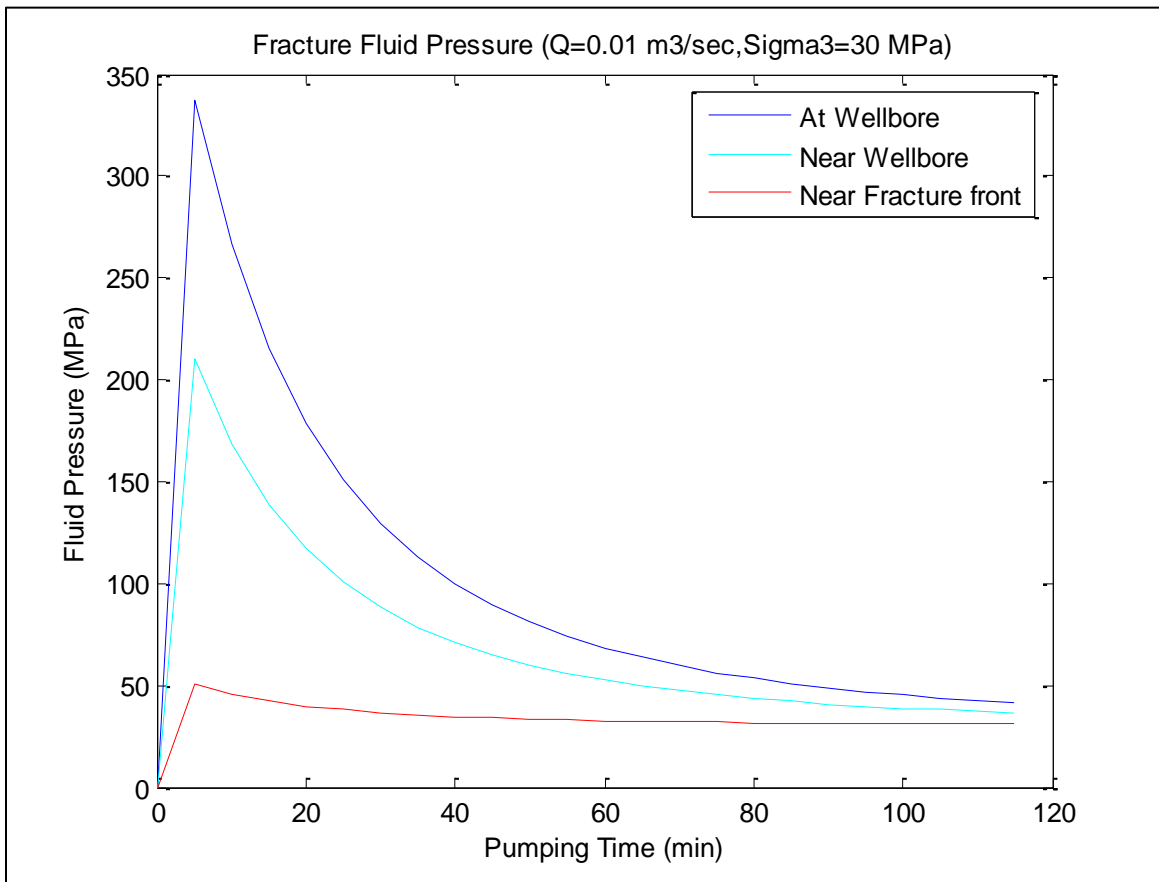


Figure 4.14. Fluid pressure variation with time

4.4. Chapter Summary

The numerical scheme presented for steady state flow presents a simple and efficient method for fluid flux computation, which can be directly used for the heat extraction models. For transient flow, the comparison of numerical and analytical solution of pore pressure distribution in two cases concludes that the Finite Element program works well. It can be easily extended for

the fracture fluid flow modeling in the coupled models. The example for hypothetical fracture model also demonstrated the validity of the fracture fluid flow program.

CHAPTER 5.

HEAT FLOW MODELING

The chapter presents two-dimensional and three-dimensional heat flow models. The heat flow in an EGS reservoir occurs by combination of heat conduction and advection processes. Two types of heat flow models are presented in this chapter: (1) early time heat flow model to investigate effect of thermal stresses on the fracture initiation and propagation processes, and (2) long-term heat extraction models for estimation of thermal energy output from an EGS reservoir.

5.1. Introduction

Several analytical and numerical approaches have been developed to estimate the heat production from Hot Dry Rock (HDR) reservoirs. Most of these models are based on an analytical solution and assume that one-dimensional heat conduction takes place perpendicular to the fracture surfaces. These analytical schemes can only model the case of simple fracture geometries and a steady-state flow in a single or in parallel fracture systems (Lauwerier, 1995; Gringarten & Sauty, 1975). Gringarten (1975) presented an analytical solution for the heat flow through a cluster of parallel fractures. Elsworth (1989) proposed a conceptual model for the heat extraction based on the spherical shape of reservoir. One of the first coupled three-dimensional heat flow numerical models based on the Finite Element Method was presented by Kolditz (1995). Kolditz and Clauser (1998) were able to model the heat circulation test at Rosemanowes (U.K.) HDR site. Ghassemi et al. (2003) presented a three-dimensional heat extraction model based on the Boundary Integral Equation formulation which completely eliminated the reservoir domain discretization. Hence, it is a computationally efficient method, since discretization of infinite reservoirs has always been a challenging task in the conventional heat flow models.

The injection of fracturing fluid during reservoir stimulation with different temperatures from the target rock temperature will induce heat conduction and advection processes. Inside the fracture, heat transfer will take place mainly due to advection of fluid mass. However, in direction perpendicular to fracture surface, heat transfer will be due to conduction in the rock formation and convection due to fluid leak-off into the reservoir (if formation is permeable). In all the models, the reservoir rock is assumed homogeneous with constant rock thermal and physical properties. Two types of heat flow models: heat flow during fracture propagation, and long term heat extraction models have been developed in the following sections.

5.2. Heat Flow during Fracture Propagation

The reservoir rock temperature plays an important role in the fracture initiation and propagation process in the EGS reservoirs. The reservoir temperature can affect the fluid properties of fracturing fluid and rock properties. The thermal induced stresses may affect fracture propagation and may lead to secondary fracturing due to rotation of principal stresses (Zhou et al., 2010). The fracture heat flow model developed in this section can be used the thermal component in the hydro-thermo-mechanical models for the fracture propagation. In development of the heat flow scheme, a stationary fracture is considered in this section.

5.2.1. Governing Equations

The heat flow process inside the fracture is governed by advection-conduction processes. For one-dimensional heat flow the advection-conduction equation can be given as follows (Zhang & Bennett, 2002):

$$\frac{\partial T(x,t)}{\partial t} = D_L \frac{\partial^2 T(x,t)}{\partial x^2} - v \frac{\partial T(x,t)}{\partial x} ; \quad x \in \Gamma \quad (5.1)$$

where D_L is the longitudinal dispersion coefficient, v is the average fluid velocity, and Γ represents the fracture surface as shown in Figure 5.1. In the right hand side of Eq. (5.1), the first term corresponds to heat conduction, and the second term is the advective heat flow.

The heat conduction between the reservoir rocks and the fracture surfaces is governed by transient diffusion process. For two-dimensional heat flow, the diffusion equation can be expressed as follow (Carslaw & Jaeger, 1986):

$$\frac{\partial^2 T(x, y, t)}{\partial x^2} + \frac{\partial^2 T(x, y, t)}{\partial y^2} = \frac{\rho_r c_r}{K_r} \frac{\partial T(x, y, t)}{\partial t} ; \quad x, y \in \Omega \quad (5.2)$$

where ρ_r and c_r are the rock density and the specific heat, respectively, $T(x, y, t)$ is the temperature at any location, K_r is the rock thermal conductivity, and Ω represents the reservoir domain as shown in Figure 5.1.

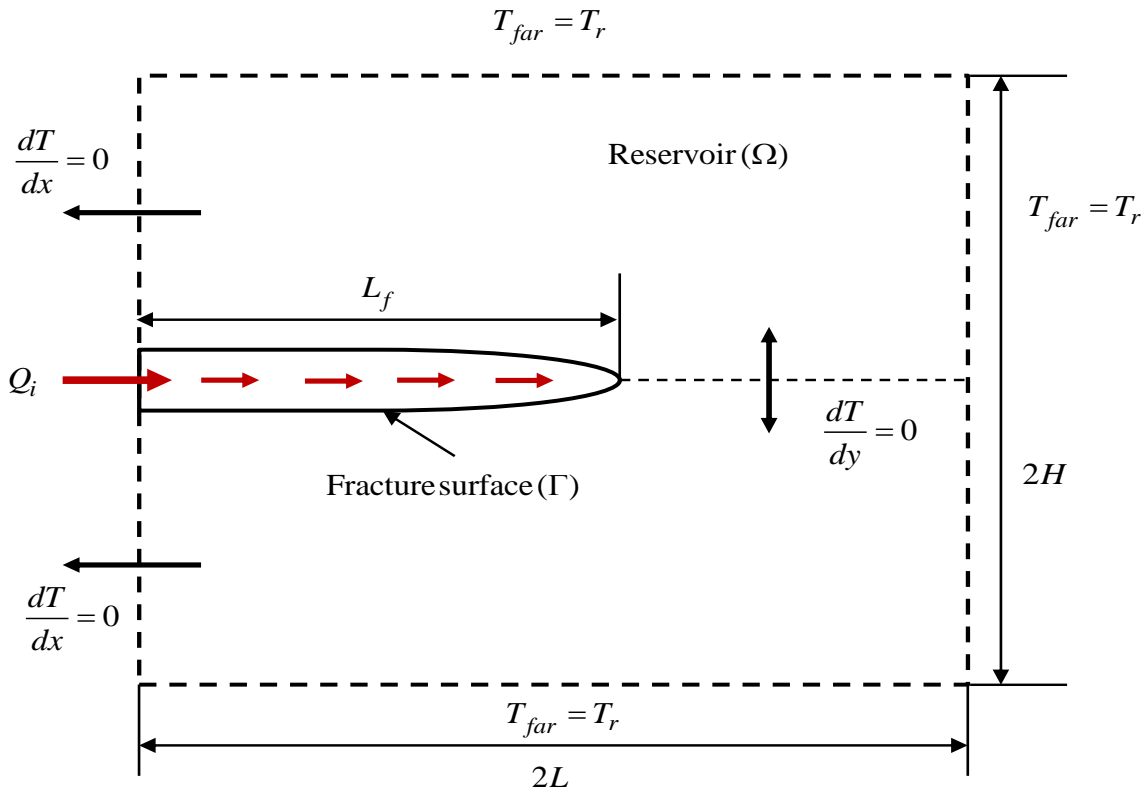


Figure 5.1. Schematic of two-dimensional heat flow with one-dimensional fracture

5.2.2. Numerical Implementation

For numerical implementation of Eq. (5.2), it can be discretized using implicit finite difference approximation both in spatial and time variables. The finite difference approximation using implicit difference in the time variable and central difference in the space variables can be written as follows (Chapra & Canale, 2006):

$$\frac{T_{i-1,j}^{n+1} - 2T_{i,j}^{n+1} + T_{i+1,j}^{n+1}}{(\Delta x)^2} + \frac{T_{i,j-1}^{n+1} - 2T_{i,j}^{n+1} + T_{i,j+1}^{n+1}}{(\Delta y)^2} = \frac{\rho_r c_r}{K_r} \frac{T_{i,j}^{n+1} - T_{i,j}^n}{\Delta t} \quad (5.3)$$

where Δx and Δy represent the domain length along x - and y - axis, respectively. The above equation can be rewritten as follows:

$$T_{i,j}^{n+1} = \frac{1}{1+4a} \left[aT_{i-1,j}^{n+1} + aT_{i+1,j}^{n+1} + aT_{i,j-1}^{n+1} + aT_{i,j+1}^{n+1} + T_{i,j}^n \right] \quad (5.4)$$

where coefficient a is given as:

$$a = \frac{K_r \Delta t}{\rho_r c_r (\Delta x)^2}$$

An analytical solution of Eq. (3.1) was given by Ogata & Banks (1961) as follows:

$$\frac{T}{T_R} = \frac{1}{2} \left[\operatorname{erfc} \left(\frac{x - vt}{\sqrt{4D_L t}} \right) + \exp \left(\frac{xv}{D_L} \right) \operatorname{erfc} \left(\frac{x + vt}{\sqrt{4D_L t}} \right) \right] \quad (5.5)$$

where erfc is the complementary error function and other variables are same as defined earlier. A sequential numerical procedure is used for this problem, first the temperature distribution inside the fracture is obtained by analytical solution from Eq. (5.5). Subsequently, Eq. (5.4) is solved for temperature change in the reservoir due to fluid injection inside the fracture. The temperature distribution from Eq. (5.5) is considered as boundary conditions along the fracture surface as shown in Figure 5.1. By changing the fracture length and fluid flow velocity, this model can account for moving mesh boundaries during hydraulic fracture propagation. A

numerical solution of coupled hydro-thermo-mechanical process can be developed by coupling this heat flow model with fracture deformation and fluid flow models.

5.2.3. Numerical Example

A numerical solution of Eqs. (5.3) and (5.5) is developed for a fixed fracture length and aperture. The effect of fluid injection on the fracture surface temperature and surrounding reservoir surfaces temperature after 10 days of fracture creation is analyzed. Due to symmetry along the fracture surface, only the upper part of the model in Figure 5.1 is considered. The input parameters for this model are listed in Table 5-1.

Table 5-1. Input parameters for 2D heat flow model

No.	Parameter	Unit	Value
1	Young's modulus (E)	GPa	37.5
2	Poisson's ratio, ν	-	0.25
3	Coefficient of linear expansion, α_T	$1/^\circ\text{C}$	0.0000008
4	Thermal diffusivity (c^*)	$\text{W/m}^\circ\text{C}$	2
5	Rock density (ρ_r)	kg/m^3	2700
6	Water density (ρ_w)	kg/m^3	1000
7	Specific heat of rock (c_r)	$\text{J/kg}^\circ\text{K}$	1000
8	Specific heat of water (c_w)	$\text{J/kg}^\circ\text{K}$	4200
9	Fracture length (L)	m	100
10	Fracture width (b)	m	0.003
11	Fluid velocity (v)	m/sec	1
12	Reservoir Temperature (T_r)	$^\circ\text{C}$	270
13	Water temperature (T_w)	$^\circ\text{C}$	40

A normalized temperature distribution inside the fracture is shown in Figure. 5.2, which shows that even after 10 days of fracture creation, about one third of fracture length is still filled with hot fluid. Hence, it can be noticed from this result that during small injection time, the temperature inside the fracture will probably not change significantly due to low thermal diffusivity of the EGS reservoirs. The temperature change in the reservoir due to fluid injection is modeled using Eq. (5.4). The boundary conditions for application of Eq. (5.4) are shown in Figure 5.1. A surface plot of normalized reservoir temperature distribution is shown in Figure 5.3, which also shows that only a local reservoir area near the fracture surface is affected by the injected fluid.

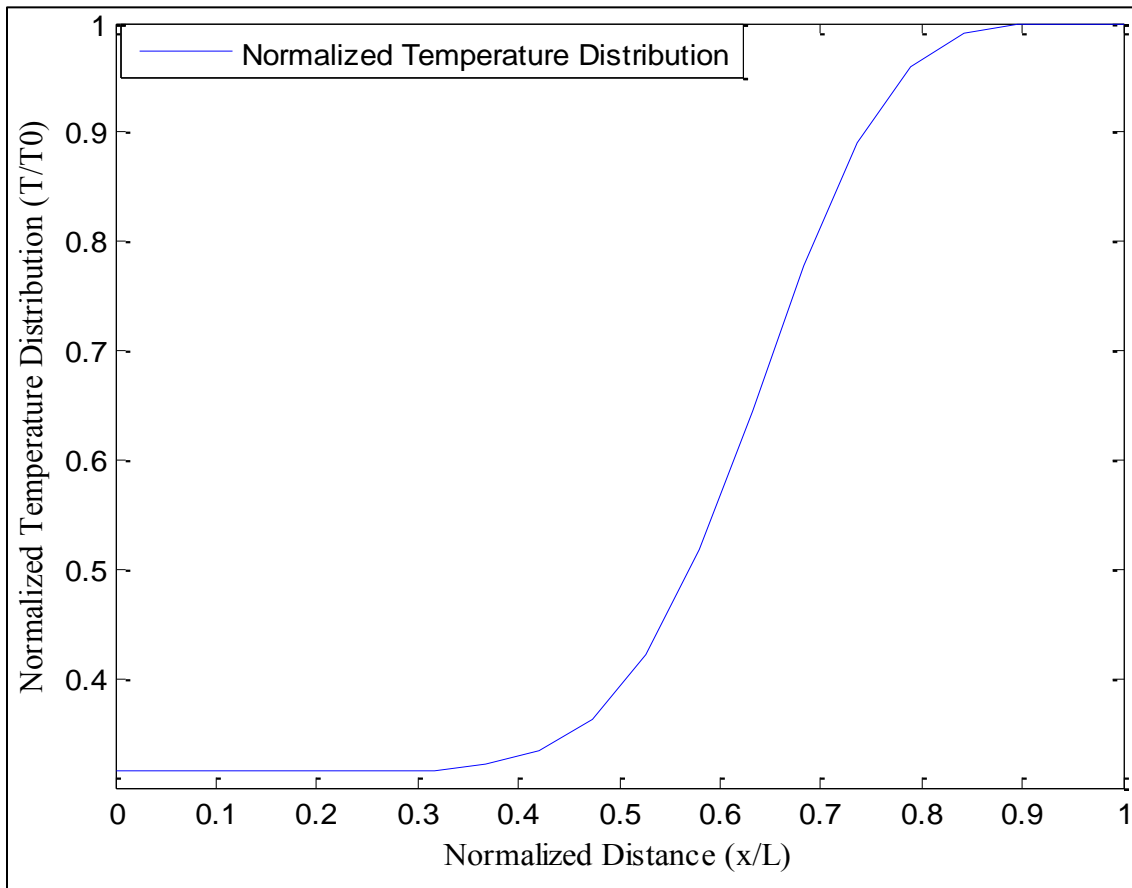


Figure 5.2. Normalized temperature distribution inside the fracture

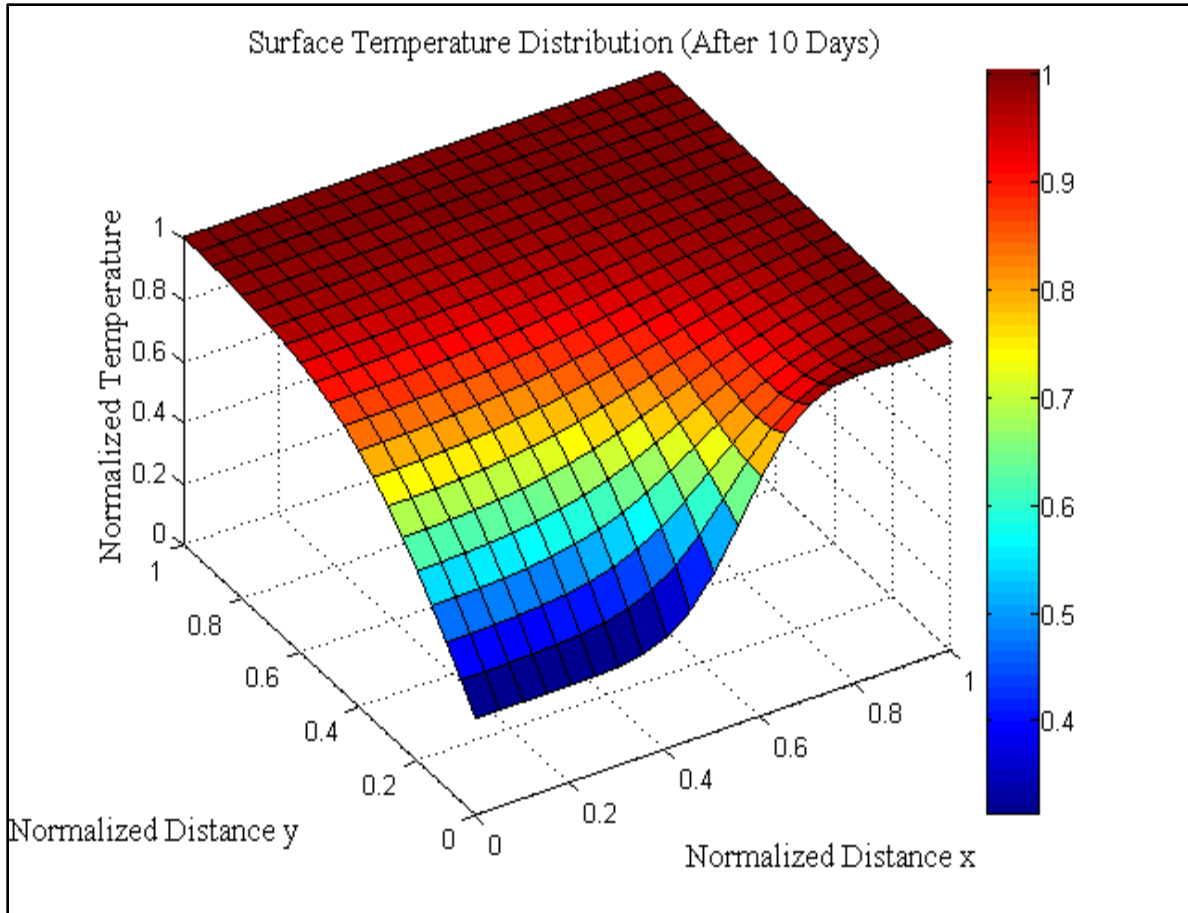


Figure 5.3. Surface plot of normalized temperature distribution

5.2.4. Estimation of Thermal Induced-Stresses

The temperature change of reservoir rock due to fluid injection induces thermal stresses which can affect the stress state in the reservoir and even can lead to secondary fracture formation. The thermo-elastic stresses changes in the reservoir based on the uniaxial strain assumption can be estimated as follows (Prats, 1981):

$$\Delta\sigma_{ij}^T = \frac{E\alpha_T}{1-\nu} \Delta T \cdot \delta_{ij} \quad (5.6)$$

where E is the Young's modulus, ν is the Poisson's ratio, and α_T is the coefficient of linear thermal expansion, ΔT is the change in the reservoir temperature, and δ_{ij} represents the

Kronecker delta function. For this case, a steady state change in the reservoir temperature (ΔT) is considered; however, for the application of this model in case of the fracture propagation process, the transient state change in the temperature should be considered. The thermal induced stresses along the fracture were estimated with three different fluid injection temperatures (e.g. 80°C, 85°C, and 90°C). All other parameters are kept constant. A plot of thermal induced stresses after 10 days is shown in Figure 5.4, which shows that induced stresses are increasing with time and decreasing with distance from the injection well. From Figure 5.4, it can be observed that the rate of thermal induced stress decreases with decrease in temperature difference between the reservoir and the injected fluid.

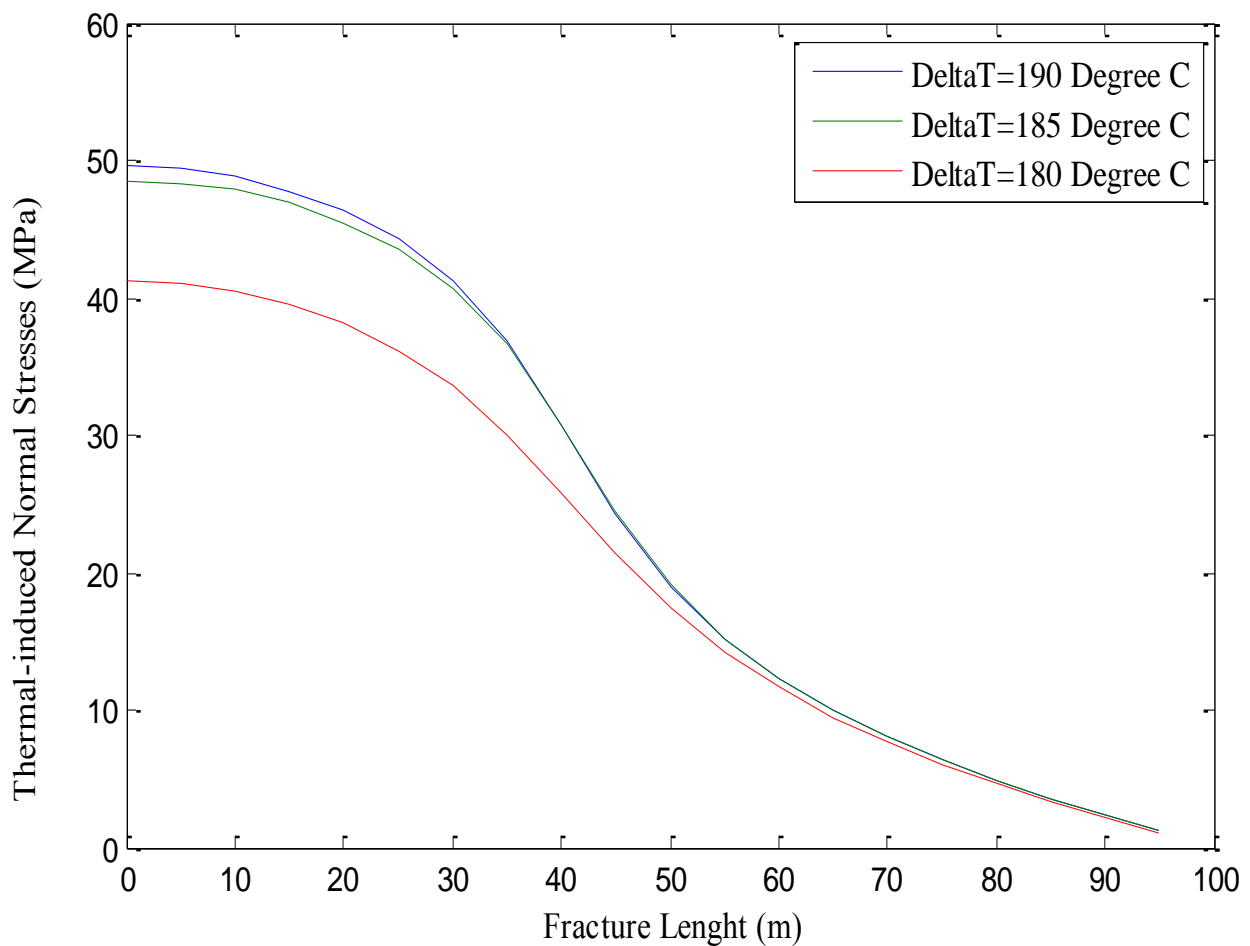


Figure 5.4. Thermal-induced normal stresses after 10 days

5.3. Two-Dimensional Heat Extraction Model

A two-dimensional heat extraction model based on the boundary integral formulation by Cheng et al. (2001) is developed in this section. Reservoir rock is assumed infinite and has homogenous rock physical properties and constant thermal properties. A Newtonian steady-state fluid flow is assumed inside the fracture. A pair of injection and production well connected by a long two-dimensional fracture with constant aperture is considered. A schematic for two-dimensional heat extraction model is shown in Figure 5.5.

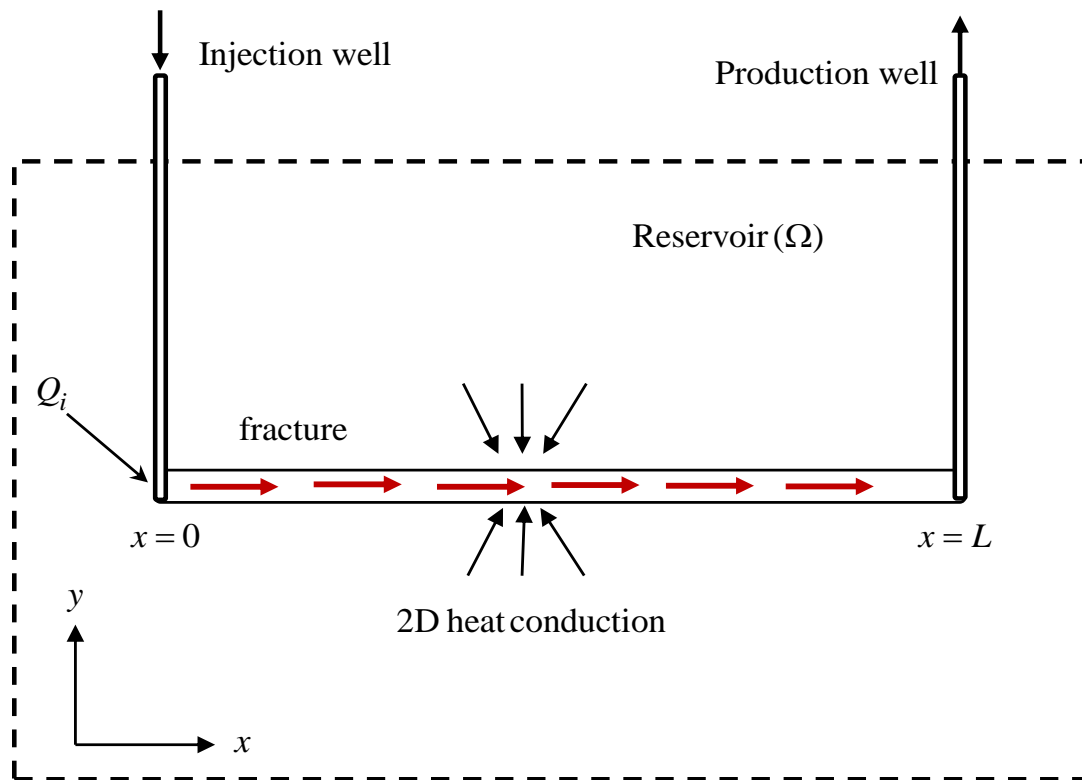


Figure 5.5. Schematic of a two-dimensional fracture connecting the injection and production extraction wells

5.3.1. Governing Equations

The heat flow and transport in two-dimensional fracture in presence of advection, dispersion, heat storage and conduction through the fracture walls can be given as follows (Cheng et al., 2001):

$$\frac{\partial T(x,0,t)}{\partial t} + v(x,t) \frac{\partial T(x,0,t)}{\partial x} - D_L \frac{\partial^2 T(x,0,t)}{\partial x^2} = \frac{2K_r}{\rho_f c_f w(x,t)} \frac{\partial T(x,y,t)}{\partial y} \Big|_{y=0}; \quad 0 \leq x \leq L \quad (5.7)$$

where ρ_f and c_f are the fluid density and specific heat, respectively, $w(x,t)$ is the fracture width, L is the fracture length, $v(x,t)$ is the average fluid velocity, D_L is the longitudinal heat dispersion coefficient, K_r is the rock thermal conductivity, and $T(x,y,t)$ is the temperature which is same for both the reservoir rocks and fracture fluid. In case of a typical laminar fluid flow, the heat transport is mainly dominated by the heat advection inside the fracture and heat diffusion into the reservoir. Hence, dropping the heat dispersion and storage terms in Eq. (5.7), it can be written as follows:

$$\frac{\partial T(x,0,t)}{\partial x} = \frac{2K_r}{\rho_f c_f v w} \frac{\partial T(x,y,t)}{\partial y} \Big|_{y=0} \quad (5.8)$$

The one-dimensional heat conduction between the fracture surface and the reservoir can be expressed as follows:

$$\frac{\partial T(x,y,t)}{\partial t} = \frac{K_r}{\rho_r c_r} \frac{\partial^2 T(x,y,t)}{\partial y^2} \quad (5.9)$$

Equations (5.8) and (5.9) are subjected to following initial and boundary conditions:

$$\begin{aligned} T(x,y,0) &= T_r \quad ; \text{ Reservoir temperature} \\ T(x_i, y_i, t) &= T_f \quad ; \text{ Injection fluid temperature} \end{aligned} \quad (5.10)$$

5.3.2. Laplace Transformation of Heat Flow Equations

A powerful method to solve the diffusion equations is based on the Laplace transform of the time variable (Banerjee, 1994). Rizzo & Shippy (1970) introduced the Laplace transformation for transient heat flow analysis in conjunction with the Boundary Element Method. The main advantage of this technique is that it reduces one-dimension of differential

equations by transforming the time variable to a scalar quantity. The Laplace transform of a function is defined as follows (Greenberg, 1998):

$$\tilde{F}(s) = \int_0^{\infty} f(t) \exp(-st) dt \quad (5.11)$$

where $f(t)$ is the function in time variable, $\tilde{F}(s)$ is the function in the Laplace transformed space and s is the transform parameter which is a real and positive number. The numerical solutions in the Laplace space are non-transient and explicitly depend on the transform parameter. This parameter can now simply be treated as a constant for further heat flow analysis. Applying the Laplace transform to Eq. (5.11) results as follows (Divo & Kassab, 2003):

$$\frac{K_r}{\rho_r c_r} \frac{\partial^2 \tilde{T}(x, y, s)}{\partial y^2} - s \tilde{T}(x, y, s) = -T(x, y, 0) \quad (5.12)$$

where $\tilde{T}(x, y, s)$ is the temperature in the Laplace transformed space. The right-hand side of Eq. (5.12) can be eliminated by defining a normalized temperature as follows (Gringarten et al., 1975):

$$T_N(x, y, t) = \frac{T_r - T(x, y, t)}{T_r - T_f} \quad (5.13)$$

Substituting, Eq. (5.13) in Eq. (5.12), results as:

$$\frac{K_r}{\rho_r c_r} \frac{\partial^2 \tilde{T}_N(x, y, t)}{\partial y^2} = s \tilde{T}_N(x, y, t) \quad (5.14)$$

The initial condition in Eq. (5.10) has been absorbed in the Laplace transformation of Eq. (5.12) and the boundary condition can be represented in the Laplace transform space as follows:

$$\tilde{T}_N(x_i, y_i, 0, s) = \frac{1}{s} \quad (5.15)$$

Similarly, the Laplace transform of Eq. (5.8) results as follows:

$$\left. \frac{\partial \tilde{T}_N(x, 0, s)}{\partial x} = \frac{2K_r}{\rho_f c_f v w} \frac{\partial \tilde{T}_N(x, y, s)}{\partial y} \right|_{y=0} \quad (5.16)$$

5.3.3. Boundary Integral Equation Formulation

Based on the Green's function approach, the temperature in the reservoir due to a continuous point heat source of magnitude Q can be given as follows (Minkowycz et al., 2006):

$$\frac{K_r}{\rho_r c_r} \left(\frac{\partial^2 \tilde{G}}{\partial x^2} + \frac{\partial^2 \tilde{G}}{\partial y^2} \right) - s \tilde{G} = -\frac{Q}{s} \delta(\mathbf{x} - \mathbf{x}') \quad (5.17)$$

where \tilde{G} is the Green's function, δ is the Dirac delta function, \mathbf{x} and \mathbf{x}' are the locations of the source and field points, respectively. The fundamental solution of Eq. (5.17) is given as follows (Banerjee, 1994):

$$\tilde{G} = \frac{1}{2\pi K_R} K_0(\beta R) \quad (5.18)$$

where,

$$\beta = \sqrt{\frac{\rho_r c_r s}{K_r}}$$

where K_0 is the modified Bessel function of the second kind of zero order (Greenberg, 1998),

$R = \|\mathbf{x} - \mathbf{x}'\|$ is the distance between the source and field point. The temperature in the reservoir due to a distribution of line source along the fracture length is given as (Cheng et al., 2001):

$$\tilde{T}_N(x, y, s) = \frac{1}{2\pi K_R} \int_0^L \tilde{q}(x', s) K_0(\beta R) dx' \quad (5.19)$$

where $\tilde{q}(x', s)$ represent the Laplace transform of the line source intensity function. Equation (5.19) represents two-dimensional heat extraction equation for an EGS reservoir. The reservoir domain extends to infinite distance; however, a finite fracture length has been used to facilitate evolution of the integrals. The unknown source function $\tilde{q}(x', s)$ in the above equations can be

written in terms of the heat flux. Assuming that heat lost by the reservoir is equal to the heat gain by the fracture; the line source intensity can be represented using Eq. (5.19) as follows:

$$\tilde{q}(x',s) = -2K_r \left. \frac{\partial \tilde{T}_N}{\partial y} \right|_{y=0} = -2w^v \rho_f c_f \frac{d\tilde{T}_N}{dx} \quad (5.20)$$

Substitution of Eq. (5.20) in Eq. (5.19) results as follows:

$$\tilde{T}_N(x,y,s) = -K \int_0^L \frac{d\tilde{T}_N(x',s)}{dx'} K_0(\beta R) dx' \quad (5.21)$$

where ,

$$K = \frac{w^v \rho_f c_f}{\pi K_r}$$

5.3.4. Integral Equation Solution

Integrating Eq. (5.21) by parts and applying the boundary condition as in Eq. (5.15), results as follows (Ghassemi, 2003):

$$\tilde{T}_N(x,y,s) = K \left[-\tilde{T}_N(L,s) K_0 \left(\beta \sqrt{(x-L)^2 + y^2} \right) + \frac{1}{s} K_0 \left(\beta \sqrt{x^2 + y^2} \right) + \beta \int_0^L \tilde{T}_N(x',s) \frac{(x-x')}{\sqrt{(x-x')^2 + y^2}} K_1(\beta R) dx' \right] \quad (5.22)$$

where K_1 is the modified Bessel function of the second kind of first order (Greenberg, 1998).

Equation (5.22) forms a boundary integral equation solution for two-dimensional heat extraction problem. By applying appropriate boundary conditions and an appropriate numerical integration scheme, Eq. (5.22) can be solved for the unknown temperature at any location in the reservoir or on the fracture surface. Implementing Eq. (5.22) along the fracture surface, $y=0$ and $0 \leq x \leq L$ results as:

$$\tilde{T}_N(x,s) = K \left[-\tilde{T}_N(L,s) K_0(\beta(x-L)) + \frac{1}{s} K_0(\beta x) + \beta \int_0^L \tilde{T}_N(x',s) \frac{(x-x')}{|x-x'|} K_1(\beta|x-x'|) dx' \right] \quad (5.23)$$

The above equation represents a Fredholm equation of second kind (Hall, 1994), which has a weak singularity of $O(R^{-1})$ in the Bessel function K_1 .

5.3.5. Numerical Implementation

Before proceeding for numerical implementation of Eq. (5.23), the singularity in the Bessel's function needs to be regularized. This singularity can be removed using singularity regularization method as suggested by Delves & Mohamed (1985). An analytical integration of singular parts can be given as follows:

$$\beta \int_0^L \tilde{T}_N(x', s) \frac{(x-x')}{|x-x'|} K_1(\beta|x-x'|) dx' = \tilde{T}_N(x, s) [K_0(\beta(L-x)) - K_0(\beta x)] \quad (5.24)$$

Subtraction of Eq. (5.24) from Eq. (5.23) results as follows:

$$\left[\frac{1}{K} - K_0(\beta(L-x)) + K_0(\beta x) \right] \tilde{T}_N = \left[-\tilde{T}_N(L, s) K_0(\beta(L-x)) + \frac{1}{s} K_0(\beta x) + \beta \int_0^L [\tilde{T}_N(x', s) - \tilde{T}_N(x, s)] \frac{(x-x')}{|x-x'|} K_1(\beta|x-x'|) dx' \right] \quad (5.25)$$

Equation (5.25) is regularized and can be solved numerically to determine the Laplace space temperature along the fracture and reservoir boundary. Though, the above equation is regularized, but it still gives numerical instability when the source point is equal the field point $x \rightarrow x'$. This singular situation can handled using Hospital's rule as suggested by Xiang & Zhang (2012). A discretization of Eq. (5.25) based on the Simpson 3/8- numerical integration scheme (Press et al., 1992) can be given as follows (Cheng et al., 2001):

$$\left[\frac{1}{K} - K_0(\beta(L-x_i)) + K_0(\beta x) \right] \tilde{T}_i = \left[-\tilde{T}_N(L, s) K_0(\beta(L-x_i)) + \tilde{T}_0 K_0(\beta x_i) + \beta \frac{L}{N} \sum_{j=0}^N w_j (\tilde{T}_j - \tilde{T}_i) \frac{(x_i-x_j)}{|x_i-x_j|} K_1(\beta|x_i-x_j|) \right] \quad (5.26)$$

where N is the number of equal intervals, w is the weights for the Simpson's 3/8-rule. The above equation can be satisfied at N collocation points, which results in the linear system of equations of order $N \cdot N$. The resultant system of equations can solved using standard Gauss elimination method. Once, the temperature along the fracture surface is known from numerical solution of

equation (5.26), temperature at any point (x, y) in the reservoir can be directly estimated as follows (Baston, 2008):

$$\tilde{T}_i(x, y, s) = K \left[\begin{array}{l} -\tilde{T}_N K_0 \left(\beta \sqrt{(L-x)^2 + y^2} \right) + \tilde{T}_0 K_0 \left(\beta \sqrt{x^2 + y^2} \right) + \dots \\ \beta \frac{L}{N} \sum_{j=0}^N w_j (\tilde{T}_j - \tilde{T}_i) \frac{(x-x_j)}{\sqrt{(x-x_j)^2 + y^2}} K_1 \left(\beta \sqrt{(x-x_j)^2 + y^2} \right) \end{array} \right] \quad (5.27)$$

5.3.6. Numerical Inverse of the Laplace Transform

Once the unknown temperatures in terms of the Laplace transform parameter is obtained from solution of Eq. (5.26) or Eq. (5.27), it can be inverted back in the real time domain using a suitable numerical Laplace inversion scheme. Stehfest (1970) transform technique is mostly used for heat conduction problems due to its stability, accuracy and simplicity for implementation. Following the Stehfest inversion scheme, the Laplace transform of a function $F(s_n)$ can be given as follows (Divo & Kassab, 2003):

$$f(t) = \frac{\ln 2}{t} \sum_{n=1}^N K_n F(s_n) \quad (5.28)$$

where $f(t)$ is the function in time variable, N are the number of terms used in summation. The Laplace transform parameter and coefficient K_n are defined as follows:

$$s_n = n \frac{\ln 2}{t} \quad (5.29a)$$

$$K_n = (-1)^{n+N/2} \left[\sum_{k=\frac{n+1}{2}}^{\min(n, N/2)} \frac{k^{(N/2)} \cdot (2k)!}{(N/2-k)! \cdot k! \cdot (k-1)! \cdot (n-k)! \cdot (2k-n)!} \right] \quad (5.29b)$$

For the stability of results, the values N should be taken between 8-14. The results from different values of N should be checked to verify its accuracy and smoothness (Erhart et al., 2006). A

stability analysis of Laplace inversion scheme for different values of N is given in Table 5-2, which shows a accuracy and smoothness in the results.

Table 5-2. Normalized temperature after 1 year ($L=300$ m)

No.	N	Near injection well	Middle of fracture	At extraction well
1	8	0.9559	0.1518	0.0023
2	10	0.9558	0.1555	0.0024
3	12	0.9558	0.1555	0.0025
4	14	0.9559	0.1555	0.0025

5.3.7. Numerical Examples

For numerical implementation of Eq. (5.26), an injection and extraction well system connected by a single fracture is considered as shown in Figure 5.5. The input parameters for this model are listed in Table 5-3.

Table 5-3. Input Parameters for 2D heat extraction model

No	Parameter	Unit	Value
1	Young's modulus (E)	GPa	60
2	Poisson's ratio (ν)	-	0.25
3	Coefficient of linear expansion (α_T)		0.0000085
4	Thermal diffusivity (K_r)	W/m ⁰ C	2
5	Rock density (ρ_r)	kg/m ³	2700
6	Water density (ρ_w)	kg/m ³	1000
7	Specific heat of rock (c_r)	J/kg ⁰ K	1000
8	Specific heat of water (c_w)	J/kg ⁰ K	4200
9	Fracture length (L)	m	300
10	Fracture width (b)	m	0.003
11	Fluid velocity (v)	m/sec	0.005
12	Reservoir Temperature (T_r)	⁰ C	270
13	Water temperature (T_w)	⁰ C	40

The variation of the fracture temperature with time for a fixed fracture length is shown in Figure 5.6. A cooling of the fracture surfaces with time is observed. The rate of cooling is initially fast; however, it decreases with time. A variation of fracture temperature with time for fixed fracture length is shown in Figure 5.7. For model verification based on analytical solution for one-dimensional heat flow, the results are as follows (Lowell, 1976):

$$T_N(x, y, t) = \operatorname{erfc} \left[\frac{(2K_r L + vw\rho_f c_f y)x}{2Lvw\rho_f c_f} \sqrt{\frac{\rho_r c_r}{K_r t}} \right] \quad (5.30)$$

where *erfc* represent the complementary error function, *L* is the domain length, and all other variables are same as defined earlier. Application of above equation to the fracture surface (*y=0*) results as follows:

$$T_N(x, 0, t) = \operatorname{erfc} \left[\frac{K_r x}{vw\rho_f c_f} \sqrt{\frac{\rho_r c_r}{K_r t}} \right] \quad (5.31)$$

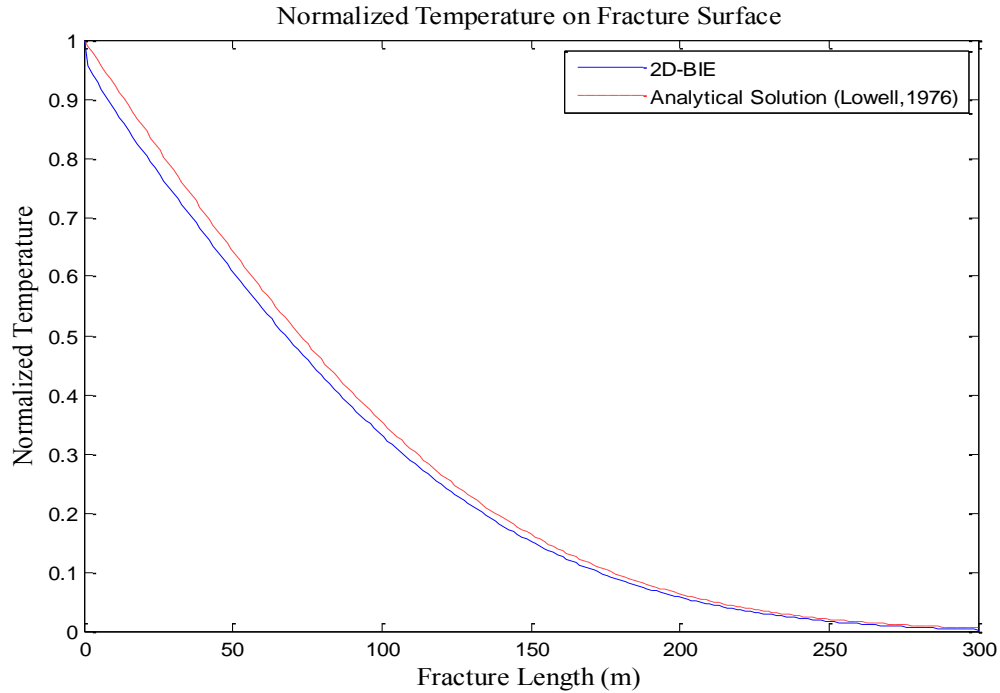


Figure 5.6. Comparison of fracture temperature variation for fixed fracture length (After 1 year)

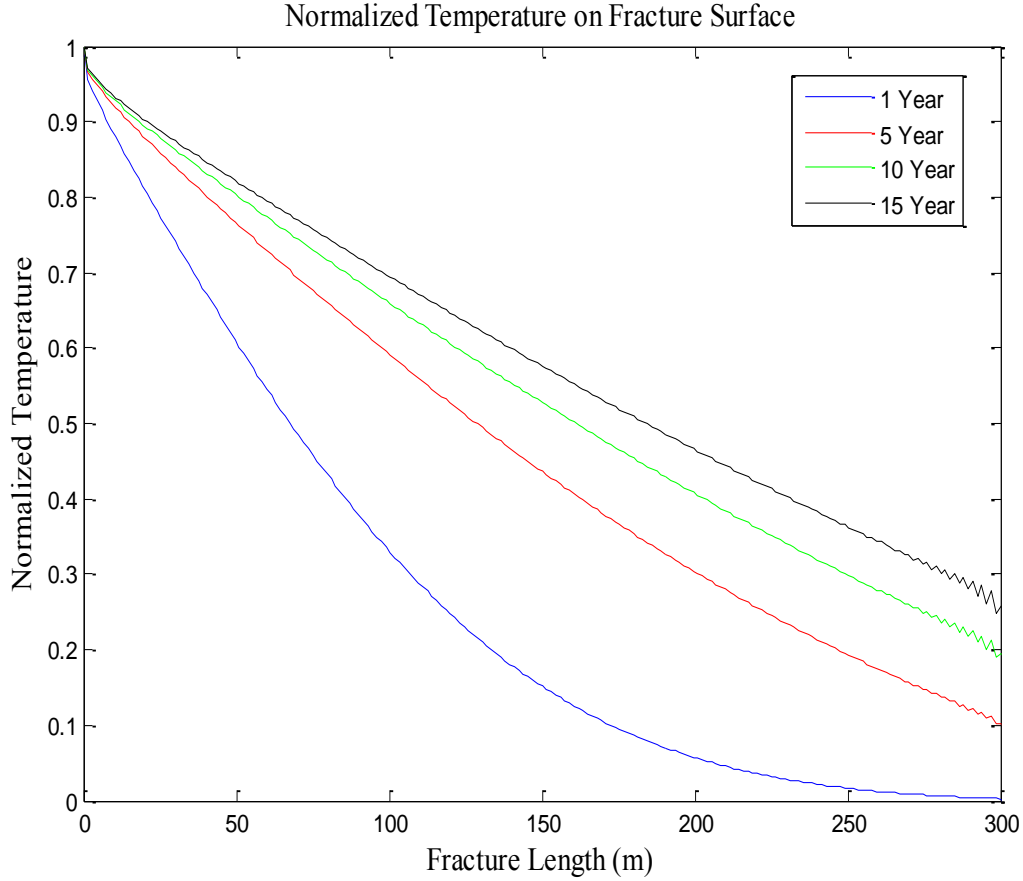


Figure 5.7. Variation of fracture temperature with time for fixed fracture length

1. Estimation of Thermal Induced Stresses

Mossop & Segall (2001) suggested that the thermal induced stresses in this case can be given as follows:

$$\Delta\sigma_{ij}^T = M_i^{-0.5} \left[\frac{1}{3} \Delta T G \beta_s (c^* \cdot t)^{0.25} \right] \cdot \delta_{ij} \quad (5.32)$$

and where M is the fluid mass injection rate, β_s is the solid thermal expansivity, c^* is the thermal diffusivity, and ΔT represents the change in the temperature. The input values of these parameters are given in Table 5.4. A plot of thermal induced stresses is shown in Figure 5.8, which shows a maximum stress change of 45 MPa near the injection well it tends to zero as we approach to extraction well.

Table 5-4. Input parameters for 2D thermal induced stresses (Ghassemi, 2003)

No	Parameter	Unit	Value
1	Fluid mass injection rate (M)	Kg/sec	10
2	Solid thermal expansivity (β_s)	m/°C	$2.4 \cdot 10^{-0.5}$
3	Thermal diffusivity (c^*)	m ² /sec	$5.5 \cdot 10^{-0.6}$

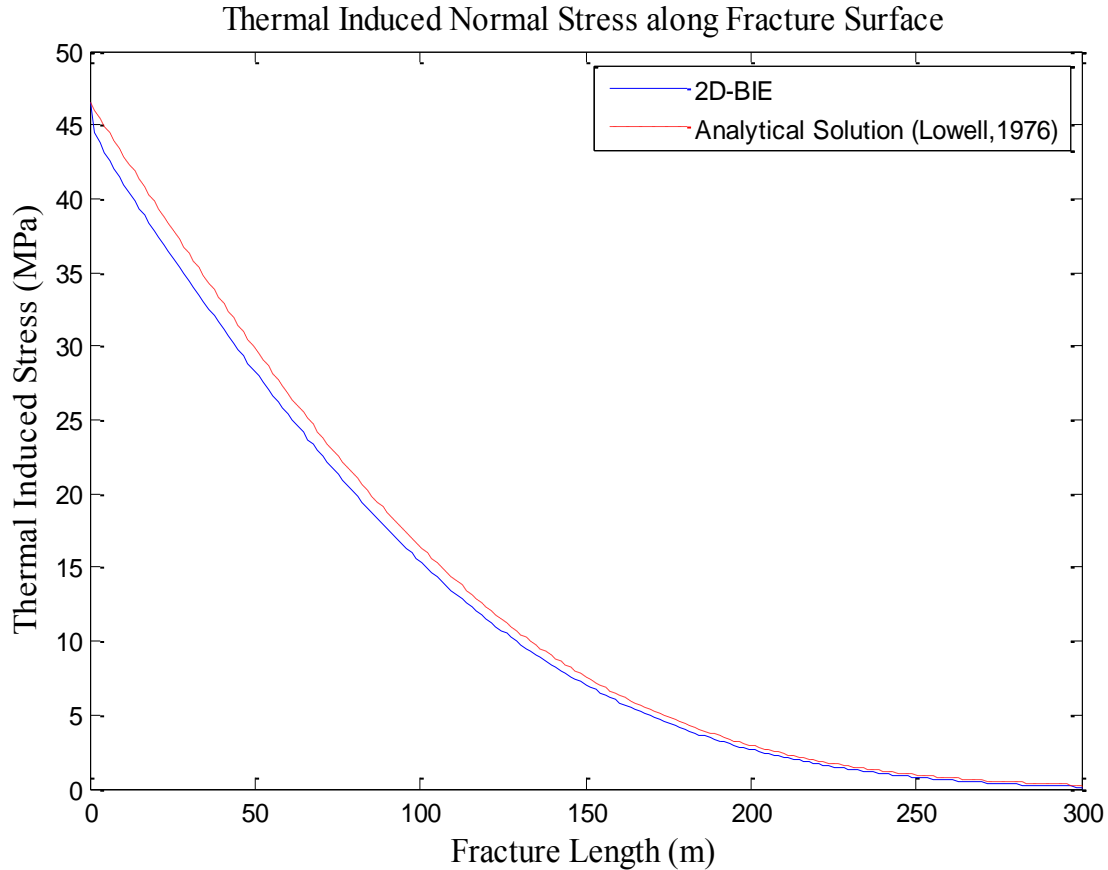


Figure 5.8. Variation of thermal-induced stresses for a fixed fracture length (After 1 year)

5.4. Three-dimensional Heat Extraction Model

A three-dimensional heat extraction model with a pair of injection well and production well is considered in this section. The rock physical and thermal properties are similar as discussed for two-dimensional heat extraction model. A long planar fracture is connecting the

injection and production well. A schematic of three-dimensional heat extraction model from a planar fracture is shown in Figure 5.9. The governing equations for three-dimensional heat flow and the boundary integral formulation and its numerical implementation procedure are discussed in the following section.

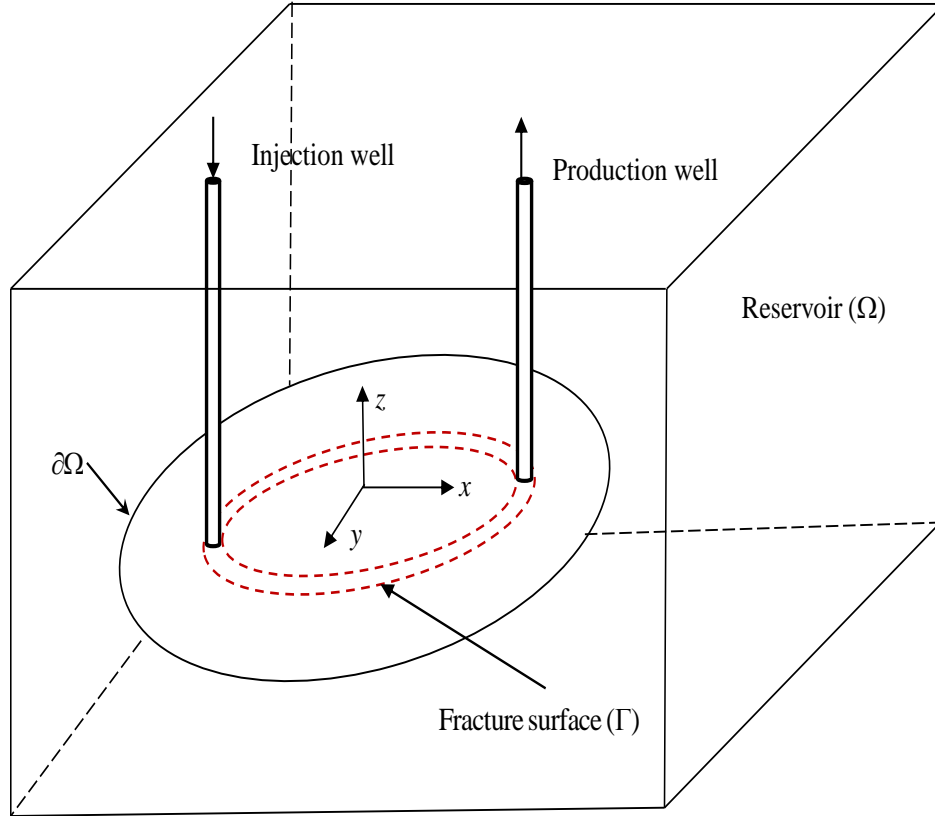


Figure 5.9. Schematic of three-dimensional heat transport flow between the injection and extraction wells (Ghassemi et al., 2003)

5.4.1. Governing Equations

The heat flow process inside the fracture similar to two-dimension flow is governed by advection-diffusion process. The governing equation for heat flow inside the fracture can be written as (Ghassemi et al., 2003):

$$\nabla \cdot [\mathbf{q}(x, y)T(x, y, 0, t)] = \frac{2K_r}{\rho_f c_f} \frac{\partial T(x, y, z, t)}{\partial z} \Big|_{z=0^+}; \quad x, y \in \Gamma \quad (5.33)$$

where $\mathbf{q}(x, y)$ is the fracture fluid flow vector, Γ represents the fracture surface as shown in Figure 5.9 and all other variables are same as defined for two-dimensional heat flow equations.

The heat conduction between the fracture surface and reservoir rocks can be given using three-dimensional diffusing equation as follows (Minkowycz et al., 2006):

$$\nabla^2 T(x, y, z, t) = \frac{\rho_r c_r}{K_r} \frac{\partial T(x, y, z, t)}{\partial z}; \quad x, y, z \in \Omega \quad (5.34)$$

where Ω represents the reservoir domain as shown in Fig. 5.9. The above equations are subjected to initial and boundary conditions as follows:

$$T(x, y, z, 0) = T_r \quad ; \text{ Reservoir temperature} \quad (5.35)$$

$$T(x_i, y_i, 0, t) = T_f \quad ; \text{ Injection fluid temperature}$$

5.4.2. Boundary Integral Equation (BIE) Formulation

Based on temperature normalization as in defined in Eq. (5.13) and application of Laplace transformation to Eqs. (5.30) and (5.34) a BIE solution results as follows:

$$\mathbf{q}(x, y) \cdot \nabla \tilde{T}_N(x, y, 0, s) = \frac{2K_r}{\rho_r c_r} \frac{\partial \tilde{T}_N(x, y, z, s)}{\partial z} \Big|_{z=0^+} \quad (5.36a)$$

$$\nabla^2 \tilde{T}_N(x, y, z, s) = \frac{\rho_r c_r s}{K_r} \tilde{T}_N(x, y, z, s) \quad (5.36b)$$

Equation (5.36) represents the modified Helmholtz equation. The fundamental solution of modified Helmholtz equation for a continuous point heat source of magnitude Q located at point \mathbf{x}' can be given using Green's function as follows (Banerjee, 1994):

$$\tilde{G} = \frac{Q(\mathbf{x}')}{4\pi K_r} \frac{1}{R} \exp(-\beta R) \quad (5.37)$$

where $R = \|\mathbf{x} - \mathbf{x}'\|$ is the distance between the source and field point, and coefficient β is same as defined in Eq.(5.18). The reservoir temperature due to distributed sources over the fracture surface Γ can be given as follows (Ghassemi et al., 2003):

$$\tilde{T}_N(x, y, z, s) = \frac{1}{4\pi K_r} \int_{\Gamma} \tilde{q}(x', y', s) \frac{1}{R} \exp(-\beta R) dx' dy' \quad (5.38)$$

where \tilde{q} is the source intensity, which can be obtained based on the assumption that for the impermeable reservoirs, the heat lost in the reservoir is equal to the heat gain by the fracture fluid through the walls. Hence, the heat source strength can be written as follows:

$$\tilde{q}(x, y, s) = -2K_r \left. \frac{\partial \tilde{T}_N(x, y, z, s)}{\partial z} \right|_{z=0^+} \quad (5.39)$$

Based on Eq. (5.33) and (5.39), the source strength is given as follows:

$$\tilde{q}(x, y, s) = -\rho_f c_f \mathbf{q}(x, y) \cdot \nabla \tilde{T}_N(x, y, 0, s) \quad (5.40)$$

Substitution of Eq. (5.40) in Eq. (5.38) results as follows:

$$\tilde{T}_N(x, y, z, s) = -\frac{\rho_f c_f}{4\pi K_r} \int_{\Gamma} [\mathbf{q}(x', y') \cdot \nabla \tilde{T}_N(x', y', 0, s)] \frac{1}{R} \exp(-\beta R) dx' dy' \quad (5.41)$$

Application of above equation for the fracture surface $z=0$ results as follows:

$$\tilde{T}_N(\mathbf{x}, s) = -\frac{\rho_f c_f}{4\pi K_r} \int_{\Gamma} [\mathbf{q}(\mathbf{x}') \cdot \nabla \tilde{T}_N(\mathbf{x}', s)] \frac{1}{R} \exp(-\beta R) d\mathbf{x}' \quad (5.42)$$

where $\mathbf{x} = (x, y)$ and $\mathbf{x}' = (x', y')$ represents the source and field points, respectively. Expanding divergence operator in Eq. (5.42) results as:

$$\tilde{T}_N(\mathbf{x}, s) = -\frac{\rho_f c_f}{4\pi K_r} \int_{\Gamma} \left[q_x(\mathbf{x}') \frac{\partial T(\mathbf{x}', s)}{\partial x} + q_y(\mathbf{x}') \frac{\partial T(\mathbf{x}', s)}{\partial y} \right] \cdot \frac{1}{R} \exp(-\beta R) d\mathbf{x}' \quad (5.43)$$

5.4.3. Numerical Implementation

For numerical implementation of Eq. (5.43), the fracture surface is discretized using 4-noded quadrilateral elements. The linear variation of the geometry and variables over elements is assumed. Following isoparametric transformation, the elements in the global coordinates system (x, y) are mapped into the local coordinates system $\{\xi, \eta | -1 \leq \xi, \eta \leq 1\}$ using appropriate shape functions as defined in Chapter 3. The discretized form of Eq. (5.43) based on the point collocation technique can be given as follows (Ghassemi et al. 2003):

$$\tilde{T}_N(\mathbf{x}^i, s) = -\frac{\rho_f c_f}{4\pi K_r} \sum_{e=1}^{NE} \int_{\Gamma^e} \left[q_x[\mathbf{x}'(\xi, \eta)] \frac{\partial \tilde{T}_N[\mathbf{x}'(\xi, \eta), s]}{\partial \xi} + q_y[\mathbf{x}'(\xi, \eta)] \frac{\partial \tilde{T}_N[\mathbf{x}'(\xi, \eta), s]}{\partial \eta} \right] \cdot \varpi[\mathbf{x}^i, \mathbf{x}'(\xi, \eta)] d\xi d\eta \quad (5.44)$$

$$\varpi[\mathbf{x}^i, \mathbf{x}'(\xi, \eta)] = \frac{1}{R[\mathbf{x}^i, \mathbf{x}'(\xi, \eta)]} \exp\left(-\beta R[\mathbf{x}^i, \mathbf{x}'(\xi, \eta)]\right) \cdot J[\mathbf{x}'(\xi, \eta)]; \quad i = 1: NP \quad (5.44a)$$

where NE is the total number of elements, NP is the total number of nodes, \mathbf{x}^i represents the coordinates of collocation point, $\mathbf{x}'(\xi, \eta)$ are the mapped coordinates of the field points, J is the Jacobian of transformation from global coordinates system to local coordinates system. The nodal fluid flow components in Eq. (5.44) can be obtained by solving the fluid flow equations; however, the nodal temperature gradient can be estimated by a combination of the forward and backward finite difference approximation based on the nodal fluid velocity direction as suggested by Ghassemi et al. (2005).

5.4.4. Numerical Integration

The fundamental solution kernel in Eq. (5.43) shows a singularity of $O(R^{-1})$ when the distance between the source and field point $R = \|\mathbf{x} - \mathbf{x}'\| \rightarrow 0$. In mathematical term, this case is known as weak singular integration, which can be evaluated using Cauchy principal-value integrals (Aliabadi & Brebbia, 1993). Similar to the elasticity problems discussed in Chapter 3,

the integrand in Eq. (5.43) can be divided in non-singular and singular integrals depending on the location of the source and field point as shown in Figure 5.10.

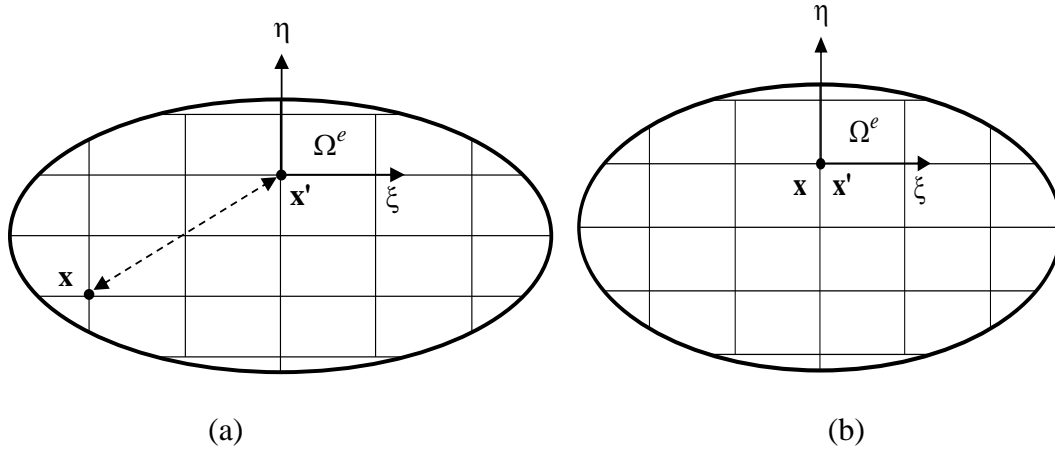


Figure 5.10. Non-singular and singular elements on a discretized fracture surface

1. Non-Singular Integration

In the case, when the source point \mathbf{x} and field point \mathbf{x}' lies on different elements (Figure 5.9a), the integrand is non-singular and well-behaved. The discretized form of Eq. (5.37) in terms of local coordinates can be written as follows:

$$\tilde{T}_N(\mathbf{x}^j, s) = -\frac{\rho_f c_f}{4\pi K_r} \sum_{e=1}^{NE} \left\{ \int_{-1}^1 \int_{-1}^1 \sum_{j=1}^N \left[q_x^j[\mathbf{x}'(\xi, \eta)] \frac{\partial \tilde{T}_N^j[\mathbf{x}'(\xi, \eta), s]}{\partial \xi} + q_y^j[\mathbf{x}'(\xi, \eta)] \frac{\partial \tilde{T}_N^j[\mathbf{x}'(\xi, \eta), s]}{\partial \eta} \right] \cdot \omega d\xi d\eta \right\} \quad (5.45)$$

where N represents number nodes per element. The above equation can be integrated using standard Gauss quadrature numerical integration.

2. Weak Singular Integration

In the case, when the source point \mathbf{x} and field point \mathbf{x}' lies on the same integration element, then integrand is unbounded as $R = \|\mathbf{x} - \mathbf{x}'\| \rightarrow 0$. An accurate evaluation of these integrals is critically important in the BEM implementation. Several methods such as polar coordinates transformation (Cruse, 1977), singularity subtraction method (Guiggiani et al., 1992), and variable transformation (Lachat & Watson, 1976) have been proposed to deal with the

weak singular integration in the boundary element implementation. The variable transformation technique is adopted in this research. This technique suggests division of square of rectangular element into triangular sub-elements and subsequently transformation of each triangular sub-element element in a square domain centered about the singular node such that Jacobian of transformation exactly cancels out the singularity (Aliabadi et al., 1987). The number of triangular subdivisions depends on the location of the singular node as shown in Figure 5.11.

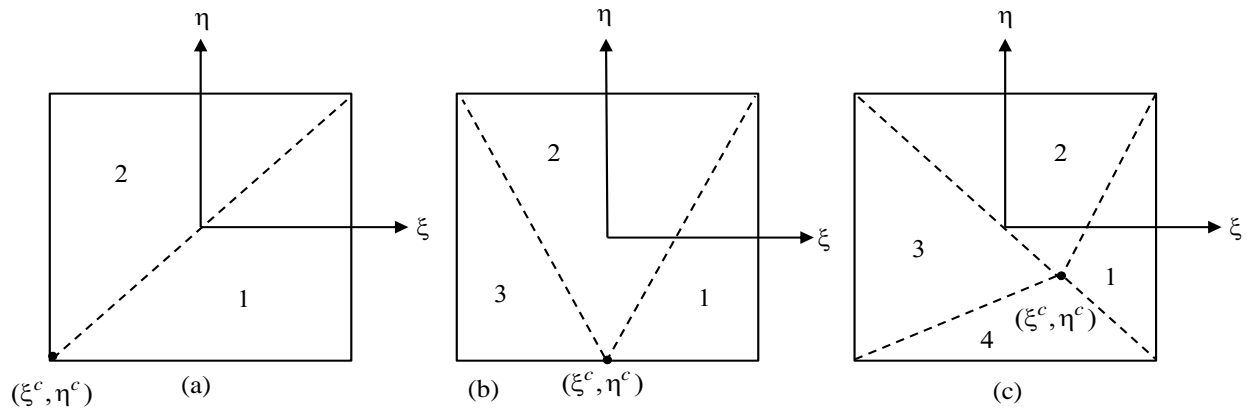


Figure 5.11. Sub-division of quadrilateral element into triangular sub-elements

Consider, a case where the singularity corresponds to corner node 1 (-1,-1) as shown in Figure 5.11(a). The singular element is divided into two sub-elements and each triangular element can be transformed to a degenerated square element as shown in Figure 5.12 using variable transformation as follows (Hall, 1994):

$$\xi = \tilde{\xi}_1 ; \eta = \frac{1}{2} \left[(1 + \tilde{\xi}_1) \tilde{\eta}_1 - (1 - \tilde{\xi}_1) \right] ; \text{ Subtriangle 1} \quad (5.46a)$$

$$\xi = \frac{1}{2} \left[(1 + \tilde{\xi}_2) \tilde{\eta}_2 - (1 - \tilde{\xi}_2) \right] ; \eta = \tilde{\eta}_2 ; \text{ Subtriangle 2} \quad (5.46b)$$

where $(\tilde{\xi}_1, \tilde{\eta}_1)$ and $(\tilde{\xi}_2, \tilde{\eta}_2)$ represents the local coordinates for the degenerated square elements for sub-triangle 1 and 2, respectively. Based on the above transformation, Eq. (5.44) can be written for each triangular sub-division as follows (Aliabadi & Rooke, 1991):

$$I_1 = -\frac{\rho_f c_f}{4\pi K_r} \sum_{e=1}^{NE} \left\{ \int_{-1}^1 \int_{-1}^1 \sum_{j=1}^N \left[q_x^j[\mathbf{x}'(\xi, \eta)] \frac{\partial \tilde{T}_N^j[\mathbf{x}'(\xi, \eta), s]}{\partial \xi} + q_y^j[\mathbf{x}'(\xi, \eta)] \frac{\partial \tilde{T}_N^j[\mathbf{x}'(\xi, \eta), s]}{\partial \eta} \right] \cdot \varpi J_c(\tilde{\xi}_1) d\tilde{\xi}_1 d\tilde{\eta}_1 \right\} \quad (5.47a)$$

$$I_2 = -\frac{\rho_f c_f}{4\pi K_r} \sum_{e=1}^{NE} \left\{ \int_{-1}^1 \int_{-1}^{\eta} \sum_{j=1}^N \left[q_x^j[\mathbf{x}'(\xi, \eta)] \frac{\partial \tilde{T}_N^j[\mathbf{x}'(\xi, \eta), s]}{\partial \xi} + q_y^j[\mathbf{x}'(\xi, \eta)] \frac{\partial \tilde{T}_N^j[\mathbf{x}'(\xi, \eta), s]}{\partial \eta} \right] \cdot \varpi J_c(\tilde{\eta}_2) d\tilde{\xi}_2 d\tilde{\eta}_2 \right\} \quad (5.47b)$$

where new the Jacobians of transformations are defined as follows:

$$J_c(\tilde{\xi}_1) = \frac{(1 + \tilde{\xi}_1)}{2} \quad (5.47c)$$

$$J_c(\tilde{\eta}_2) = \frac{(1 + \tilde{\eta}_2)}{2} \quad (5.47d)$$

These new Jacobian functions in Eqs. (5.47c) and (5.47d) exactly cancels out weak singularity of integrand and results in regular integrand, which can be evaluated using standard Gaussian quadrature method. Finally, the singular integration can be given by summations of Eqs. (5.47a) and (5.47b).

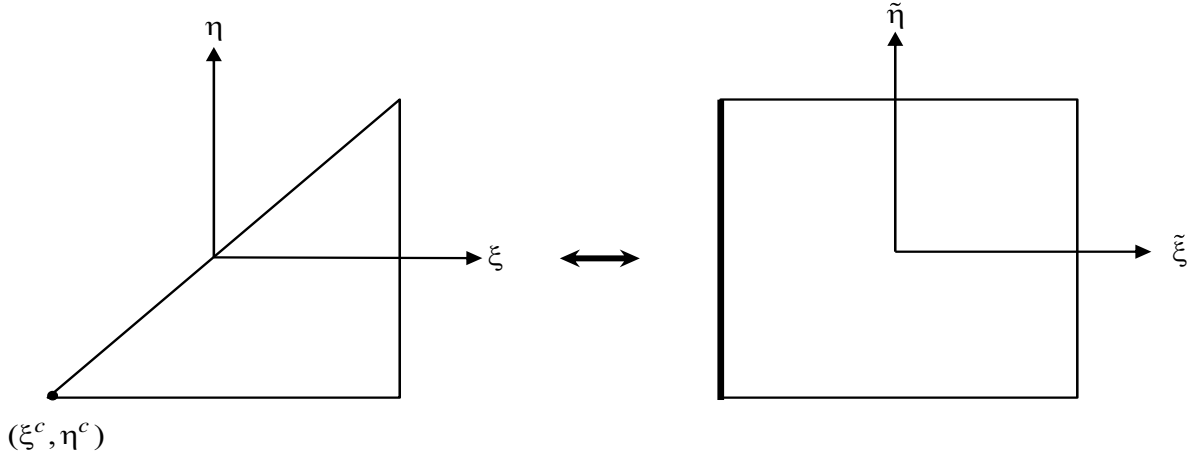


Figure 5.12. Transformation of a triangular sub-element to a degenerated square domain

5.4.5. Linear Equations of Discretized System

By applying the point collocation to each node and using numerical integration over each element, Eq. (5.45) results in a linear system of equations as follows:

$$[\mathbf{A}]\{\mathbf{T}\} = \{\mathbf{b}\} \quad (5.48)$$

where \mathbf{A} represents the coefficient matrix of numerical integration of Eq.(5.45), \mathbf{b} is the right hand side vector which is a resultant of the initial and boundary conditions, and \mathbf{T} is the unknown nodal temperature vector. The above equation is subjected to the boundary condition at the injection well, which is maintained at constant temperature. The coefficient matrix \mathbf{A} results a fully populated unsymmetrical matrix. Gauss elimination scheme is applied to solve the matrix equation (Griffiths & Smith, 2006). A MATLAB computer program has been developed for three-dimensional DDM extraction model in this research and a detailed flow chart for program is provided in Figure 5.13.

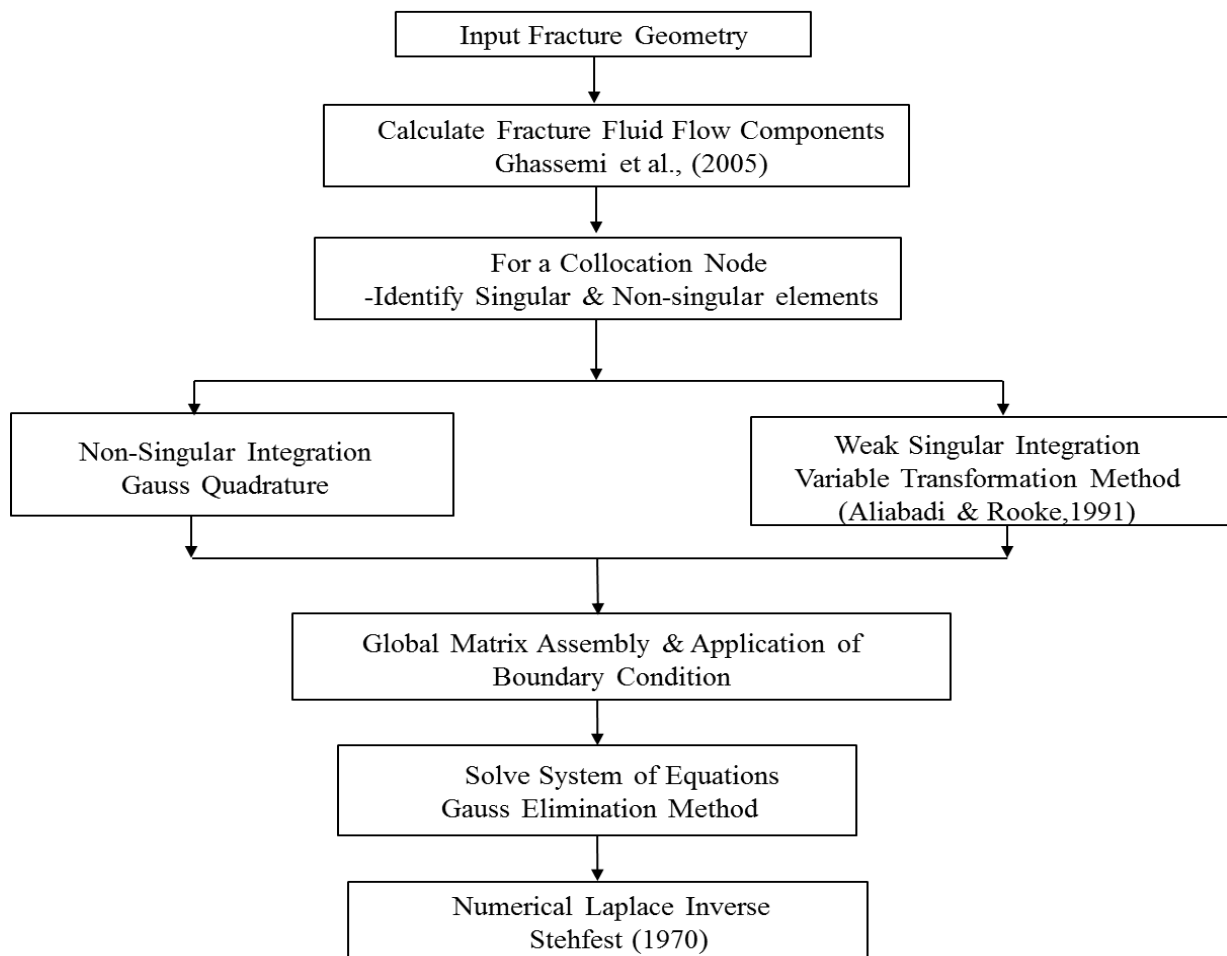


Figure 5.13. Flow chart for three-dimensional heat extraction model

5.4.6. Numerical Examples

For numerical implementation of Eq. (5.48) an EGS system with the injection and production well system is considered. A single long square fracture is assumed to connecting the injection and production wells. The injection well is located at (-25, 0) and production well at (+25, 0). The reservoir rock and the fluid data as listed in Table 5-5.

Table 5-5. Input Parameters for 3D heat extraction model (Yamaguchi, 1992)

No.	Parameter	Unit	Value
1	Young's modulus (E)	MPa	6000
2	Poisson's ratio (ν)	-	0.25
3	Injection rate (Q_i)	kg/sec	16.7
4	Fluid density (ρ_w)	kg/m ³	1000
5	Rock density (ρ_r)	kg/m ³	2700
6	Specific heat of fluid (c_w)	J / kg °K	4200
7	Specific heat of rock (c_r)	J / kg °K	900
8	Rock thermal conductivity (K_r)	W / m °K	3.00
9	Injection temperature (T_f)	°C	55
10	Reservoir temperature (T_r)	°C	250

A surface plot of temperature distribution after 10 years is shown Figure 5.14. As seen from the Figure 5.14, as we move away from the injection well, the fracture temperature is increasing. The production well temperature after 10 years is recorded equal to 200 °C. A change of temperature between the injection and the production well with time is shown in Figure 5.15, which shows reservoir cooling with time. At time $t=25$ years, the production well temperature was recorded equal to 190 °C.

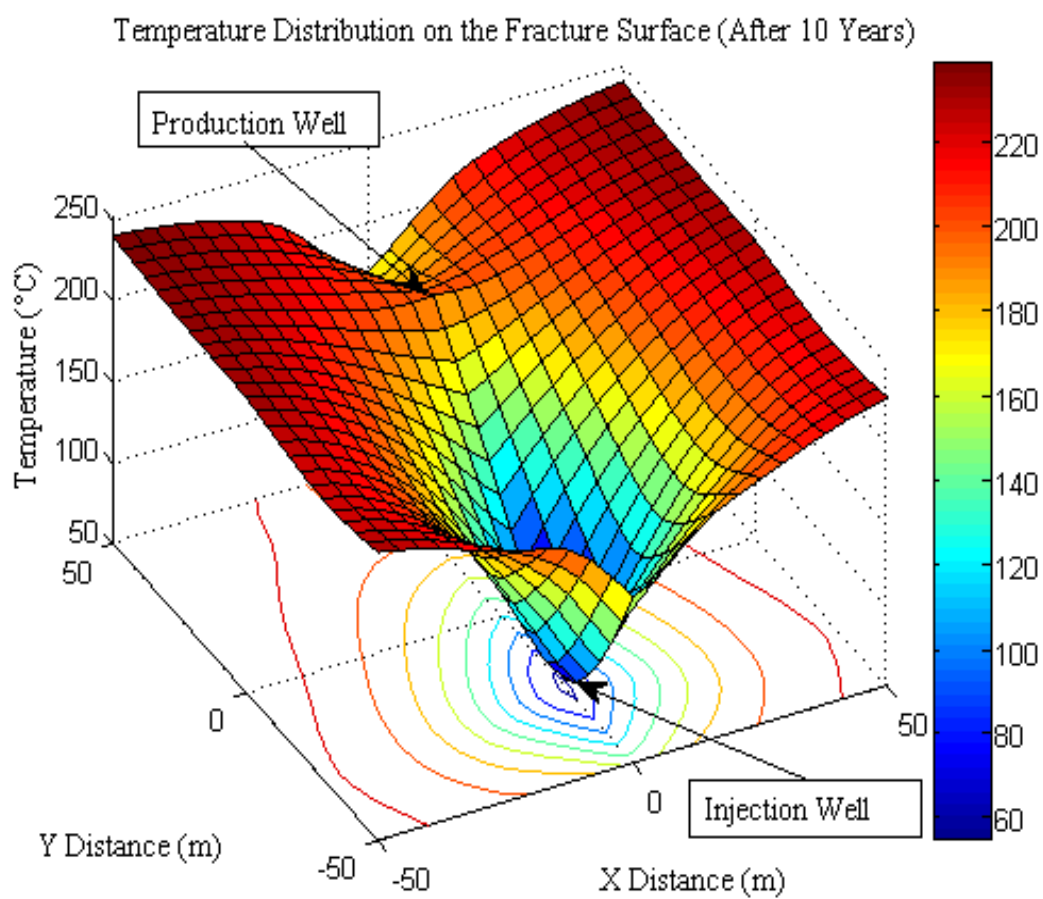


Figure 5.14. Surface plot of temperature distribution over the fracture surface

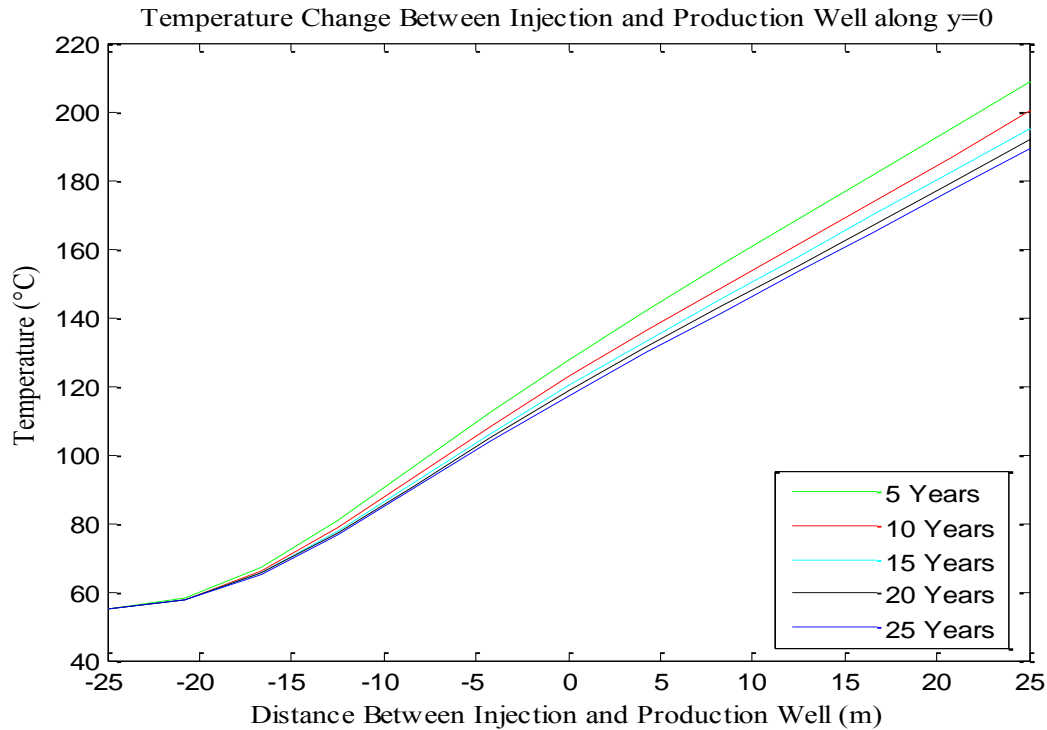


Figure 5.15. Change of temperature with time between injection and production well

5.5. Chapter Summary

The two-dimensional heat flow model developed presents a simple numerical model to estimate the effect of thermal-stresses on the fracture initiation and propagation processes. The moving boundary conditions can be easily accounted in the model by changing the fracture length. The heat extraction models using boundary integral equations presents an efficient method for heat extraction modeling both in terms of accuracy and computational efficiency. Since; only the fracture surface discretization is required. The heat extraction models presented, don't assume essentially one-dimensional heat conduction perpendicular to the fracture surfaces; hence, these models overcome traditional one-dimensional heat conduction approach in the earlier heat extraction models.

CHAPTER 6.

COUPLED HYDRO-THERMO-MECHANICAL FRACTURE MODELING

The chapter presents explicit hydro-mechanical and explicit thermo-mechanical coupling processes during hydraulic fracturing for functional EGS reservoir correction. For hydro-mechanical coupling, one-dimensional Newtonian flow for compressible fluid is solved using implicit Finite Difference method and subsequently the fluid pressures are applied as boundary conditions for the two-dimensional constant displacement discontinuity model. For thermo-mechanical coupling two cases are considered: first coupling between thermal induced stresses with the constant height KGD model and second coupling between the thermal stresses from the two-dimensional boundary integral solution with two-dimensional DDM model. The governing equations for each processes and their numerical implementation are provided in the following section.

6.1. Introduction

The coupled hydro-thermo-mechanical process is an essential issue which needs to be analyzed for hydraulic fracturing in case of EGS. Since, the high reservoir temperature, as discussed earlier in Chapter 2 can affect both the fracture fluid flow and the fracture initiation and propagation. Due to continuous fluid injection through the fracture networks a differential cooling of the reservoir rocks occurs which can change the stress state. The change of the stresses state induced secondary fracture formation and even in some cases can initial seismic activities. The basic concept of the hydro-mechanical coupling and thermo-mechanical coupling has been introduced in this chapter.

6.2. Hydro-Mechanical Coupling

The fracture fluid flow and fracture deformation processes form highly non-linear system which needs to be solved in coupled manner. An inter-dependency of the fracture fluid pressure and fracture aperture is shown in Figure 6.1. The fracture aperture which is an output of the DDM model goes as an input parameter for the fluid flow model. The fluid pressure goes back to the DDM model as an applied load on the fracture surface. Hence, the fracture deformation and the fluid flow are solved either iteratively or sequentially. A sequential explicit coupling is consider in this research

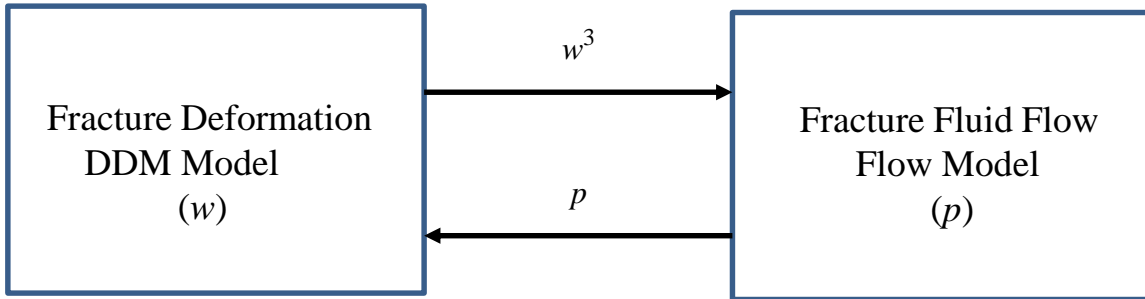


Figure 6.1. Schematic of explicit coupling between the fracture aperture and fluid flow

6.2.1. Governing Equations

This section presents the governing equations for the one-dimensional fracture fluid flow and coupled fracture stress-deformation behavior.

1. Fluid flow in a Fracture

The one-dimensional fluid flow for a compressible fluid inside a fracture can be given based on the mass balance equation as follows (Jalali & Dasseault, 2011):

$$\frac{\partial(\rho_f n w q_x)}{\partial x} = -\frac{\partial M}{\partial t} \pm \rho_f n w q_s \quad (6.1)$$

where ρ_f is the fluid density, q_x is the volumetric fluid flow rate, n is the porosity, w is the fracture aperture, M is the mass of fluid per unit length Δx and q_s represent the source or sink term. The derivative of fluid mass with respect to time can be given as follows:

$$\frac{\partial(\rho_f n w)}{\partial t} = n w \frac{\partial \rho_f}{\partial p} \frac{\partial p}{\partial t} + \rho_f \left(n \frac{\partial w}{\partial t} + w \frac{\partial n}{\partial t} \right) \quad (6.2)$$

For a constant fracture element length, constant fluid density and constant porosity, the above equation can be given as follows:

$$\frac{\partial q_x}{\partial x} = -C_f \frac{\partial p}{\partial t} - \frac{1}{w} \frac{\partial w}{\partial t} \pm q_s \quad (6.3)$$

where C_f represent the fluid compressibility, which is defined as follows:

$$C_f = \frac{\partial \rho_f}{\partial p} \quad (6.4)$$

For laminar fluid flow, the fluid flow rate can be given using cubic law as discussed in Chapter 2:

$$q_x = -\frac{w^3}{12\mu} \frac{\partial p}{\partial x} \quad (6.5)$$

where μ is the fluid viscosity. Substituting, Eq. (6.5) in Eq. (6.3) results as follows:

$$\frac{w^3}{12\mu} \frac{\partial^2 p}{\partial x^2} = -C_f \frac{\partial p}{\partial t} - \frac{1}{w} \frac{\partial w}{\partial t} \pm q_s \quad (6.6)$$

The change in the fracture width in Eq. (6.6) can be given based on the fundamental solution of pressurized fracture displacement continuity method as follows (Crouch & Starfield, 1983):

$$\Delta w = \Delta D_n = \frac{\pi(1-\nu^2)\Delta x}{E} \Delta p \quad (6.7)$$

Substitution of above equation in Eq. (6.6) results as follows:

$$\frac{w^3}{12\mu} \frac{\partial^2 p}{\partial x^2} = \left[C_f + \frac{1}{w} \frac{\pi(1-\nu^2)\Delta x}{E} \right] \frac{\partial p}{\partial t} \quad (6.8)$$

The above equation represents the one-dimensional flow inside a pressurized and it is subjected to following initial and boundary conditions:

$$p(x,0) = p_0; \text{ Initial pore pressure} \quad (6.9a)$$

$$-\frac{w^3}{12\mu} \frac{\partial p}{\partial x} = Q_i; \text{ at injection well} \quad (6.9b)$$

$$\frac{\partial p}{\partial x} = 0; \text{ at fracture tip} \quad (6.9c)$$

For fluid pressure distribution inside the fracture, Eq. (6.8) is solved numerically using a dimensional cell-centered implicit Finite Difference scheme for spatial variable and implicit scheme for time variable. The problem domain is discretized using the cell-centered grids as shown in Figure 6.2. The Finite Difference approximation of Eq. (6.8) for i th nodal point can be given as follows (Zhang & Bennett, 2002):

$$\frac{p_{i-1}^{n+1} - 2p_i^{n+1} + p_{i+1}^{n+1}}{(\Delta x)^2} = \frac{12\mu}{w^3} \left[C_f + \frac{1}{w} \frac{\pi(1-\nu^2)\Delta x}{E} \right] \frac{p_i^{n+1} - p_i^n}{\Delta t} \quad (6.10)$$

where p_i^{n+1} and p_i^n represents the fluid pressure at i th node at $(n+1)$ th and n th time steps, respectively, and Δt is the time increment. The derivative boundary condition of Eq. (6.9b) is implemented using a fictitious node approach as discussed in Chapter 4.

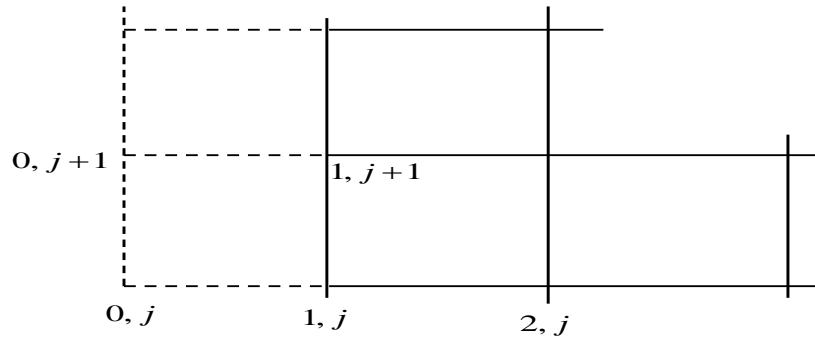


Figure 6.2. Cell-centered Finite Difference discretization of 1D problem

2. Coupled Fracture Stress-Deformation Behavior

Assuming, linear variation of joint model as shown in Figure 6.3, the normal stress and shear stress are related to the normal and shear components of the displacement discontinuities as follows (Andrew, 2000):

$$\Delta\sigma_s = -K_s\Delta D_s \quad (6.11a)$$

$$\Delta\sigma_n = -K_n\Delta D_n \quad (6.11b)$$

where K_s and K_n represent the shear and normal stiffness of a fracture, respectively, ΔD_s and ΔD_n are the change in the shear and normal components of the displacement discontinuity, respectively.

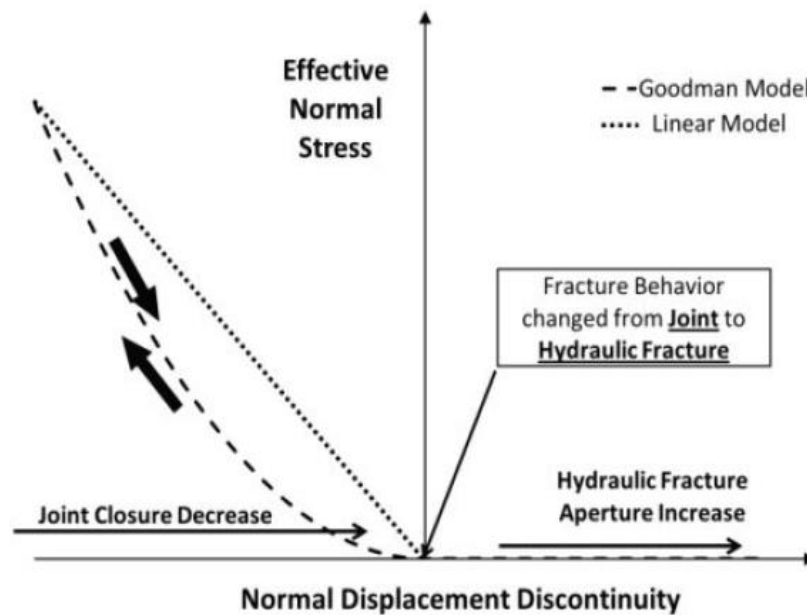


Figure 6.3. Goodman joint model and a linear joint model (Sesetty & Ghassemi, 2013)

The effective normal stress is defined as follows:

$$\sigma_n' = \sigma_n + \alpha p \quad (6.12)$$

where $\alpha = 1 - K_m / K_s$ is the Biot's coefficient as defined in Chapter 2. For a fracture with bulk modulus of matrix K_m much less than the solid bulk modulus K_s , the Biot's coefficient $\alpha = 1$; hence, Eq. (6.12) can be written as follows:

$$\sigma_n^i = \sigma_n + p \quad (6.13)$$

Substituting, above equation in Eq. (6.12), the effective stresses on a fracture element as shown in Figure 6.2 can be written as follows (Andrew, 2000):

$$\Delta \sigma_s^i = -K_s \Delta D_s \quad (6.14a)$$

$$\Delta \sigma_n^i = -K_n \Delta D_n - \Delta p \quad (6.14b)$$

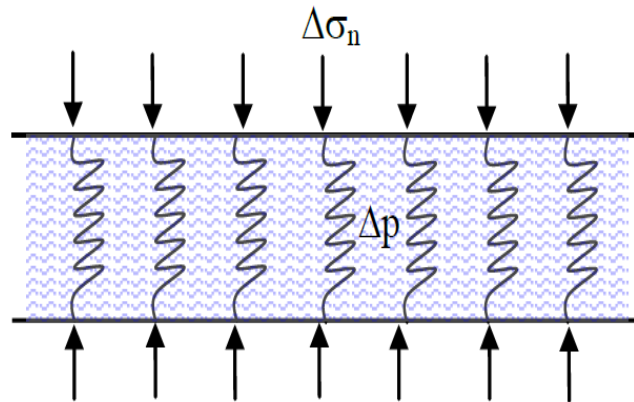


Figure 6.4. Representation of effective stress acting on a fracture element (Tao, 2010)

6.2.2. Explicit Coupling of Fracture Fluid Flow and Deformation

The fracture fluid flow and fracture deformation are coupled explicitly based on Finite Difference solution of flow and the displacement discontinuity method for deformation. The fluid flow changed is substituted in the DDM model to estimate the changes in the fracture deformation. For both fluid and DDM model, the fracture surface is divided in the NE number of small elements. The constant two-dimensional DDM equations as discussed in Chapter 3 can be

rewritten for i th element in terms of the increment stresses and DD's as follows (Crouch & Starfield, 1983):

$$\sum_{j=1}^{NE} A_{ss}^{ij} \Delta D_s^j + \sum_{j=1}^{NE} A_{sn}^{ij} \Delta D_n^j + K_s \Delta D_s^i = 0 \quad (6.15a)$$

$$\sum_{j=1}^{NE} A_{ns}^{ij} \Delta D_s^j + \sum_{j=1}^{NE} A_{nn}^{ij} \Delta D_n^j + K_n \Delta D_n^i = -\Delta p^i \quad (6.15b)$$

where Δp^i is the fluid pressure increment from Eq. (6.10). The above equation is solved for the change in the normal and shear deformations. For next time step, the fracture aperture is updated as follows:

$$w_i^{n+1} = w_i^n - \Delta D_n^i \quad (6.16)$$

where w_i^{n+1} and w_i^n are the fracture aperture for the i th node at $(n+1)$ th and n th time step, respectively, ΔD_n^i represents the change in normal opening of i th node. The new fracture aperture from Eq. (6.16) is substituted in Eq. (6.10) and the new fluid pressure changes are estimated. The new fluid pressure is again substituted in Eq. (6.15) and the subsequent change in the fracture aperture is estimated from Eq. (6.16). This process is repeated till the desired time is reached. A flow chart for explicit coupling method discussed in this section is shown in Figure 6.5. In the explicit coupled model the fracture length is kept constant and the fracture is allowed to dilate only. As obvious from the mass conservation law, the injected fluid volume should be equal to the summation of the fracture volume change and fluid leak-off through reservoir rocks. No fluid leak-off is assumed in this case.

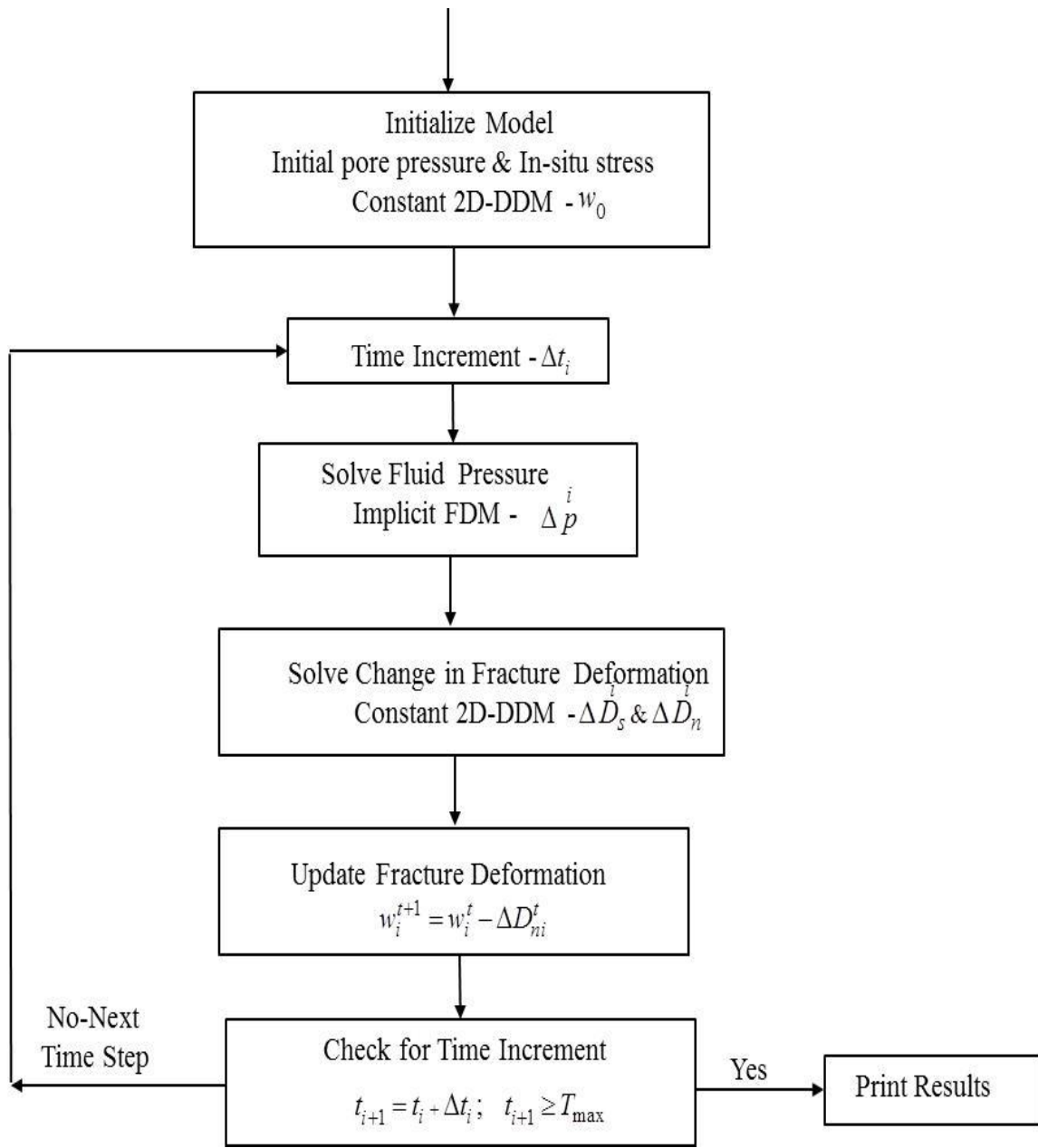


Figure 6.5. Flow chart for explicit coupled hydro-mechanical model

6.2.3. Numerical Example

For numerical implementation of explicit coupled model, a case of two-dimensional pressurized fracture has been considered. For numerical stability of the model a very small time step equal to 0.001 sec is taken. The variations of the fracture fluid pressure and fracture aperture with respect to the fracture length for different injection times are analyzed. Figures 6.6 and 6.7 represent the fluid pressure and fracture width variation after 1 sec. Figures 6.8 and 6.9 represent the fluid pressure and fracture width variation after 2 sec. It can be observed from these results that with time fracture are dilating, which is giving rise to both the pressure and aperture. The input parameters for this model are listed in Table 6-1.

Table 6-1. Input parameters for explicit hydro-mechanical coupled model

No	Parameter	Unit	Value
1	Young's modulus (E)	GPa	15
2	Poisson's ratio (ν)	-	0.25
3	Normal stiffness (K_n)	GPa	10
4	Shear stiffness (K_s)	GPa	10
5	Vertical In-situ stress (σ_3)	MPa	15
6	Horizontal stress (σ_1)	MPa	20
7	Initial fluid pressure (P)	MPa	10
8	Initial fracture width	m	0.001
9	Fracture length (L)	m	2
10	Time increment(dt)	sec	0.001
11	Fluid viscosity (μ)	cp	1

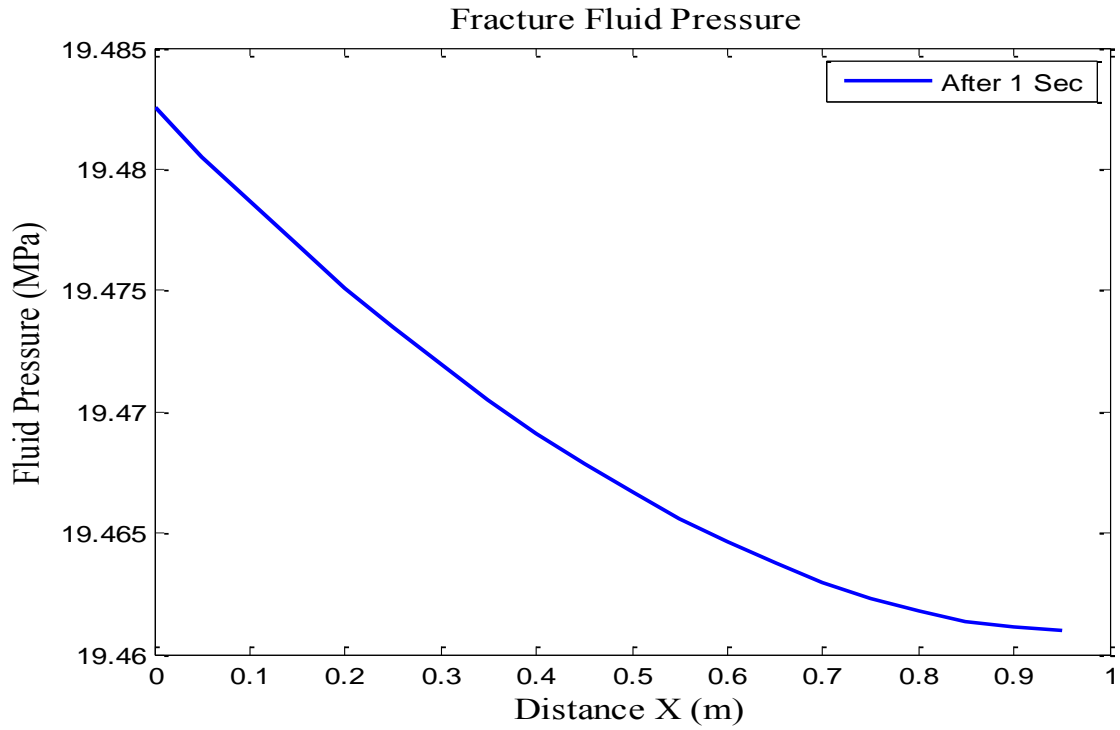


Figure 6.6. Fracture fluid pressure after 1 sec of fluid injection

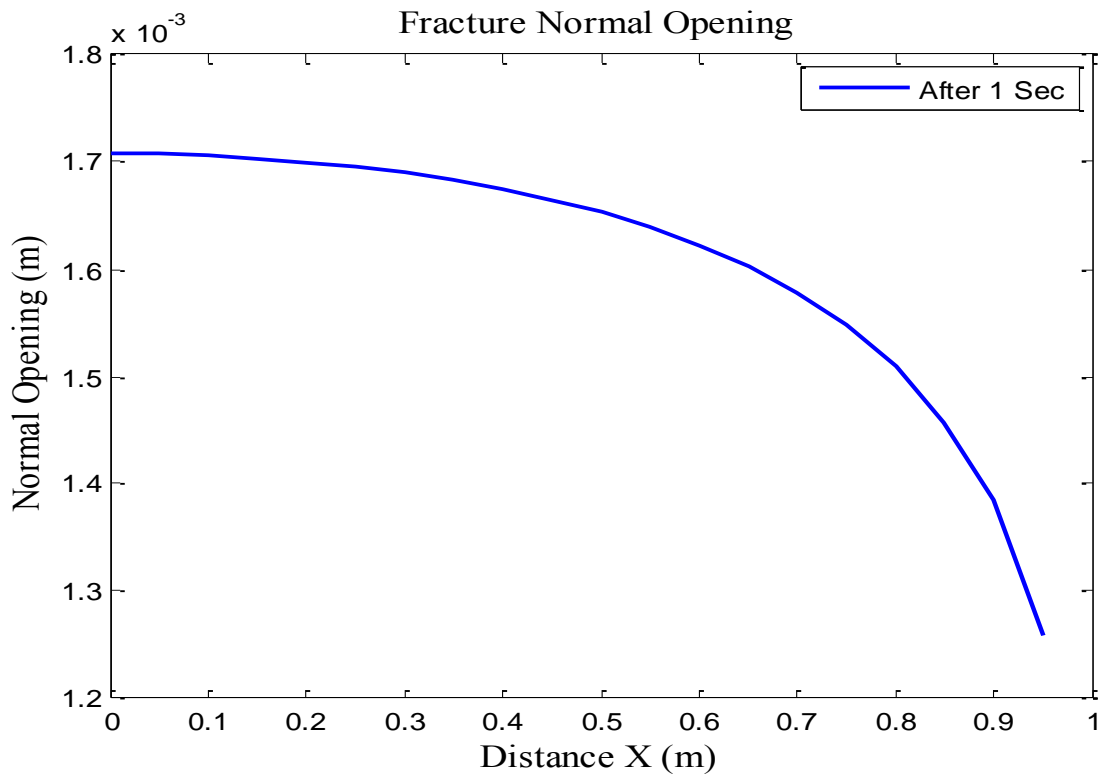


Figure 6.7. Fracture width after 1 sec of fluid injection.

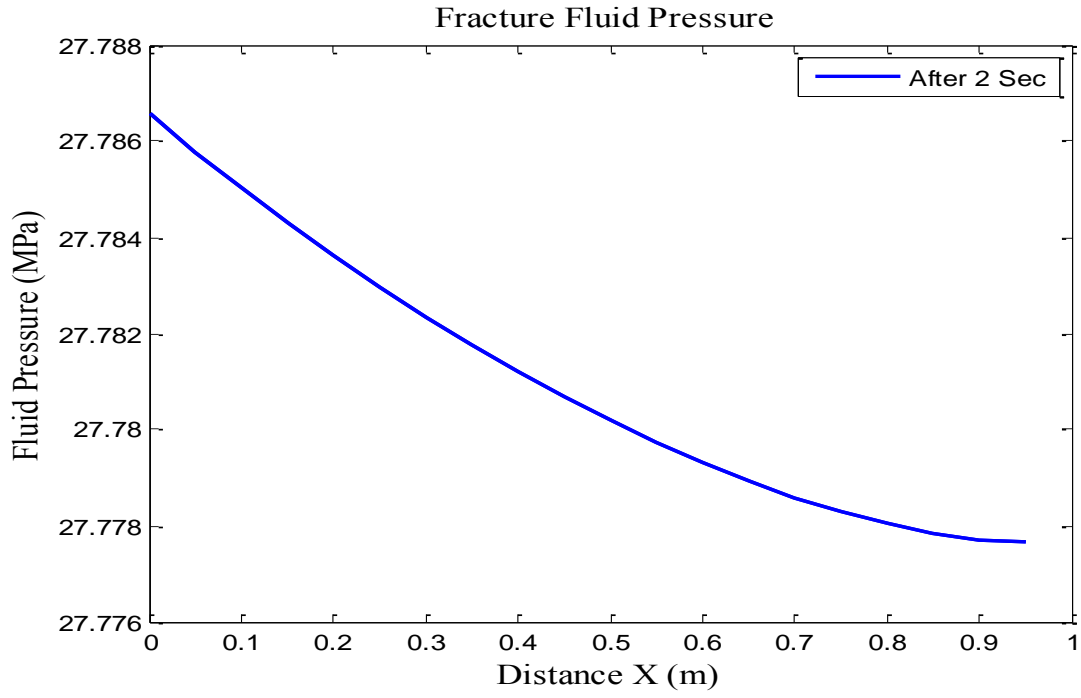


Figure 6.8. Fracture fluid pressure after 2 sec of fluid injection

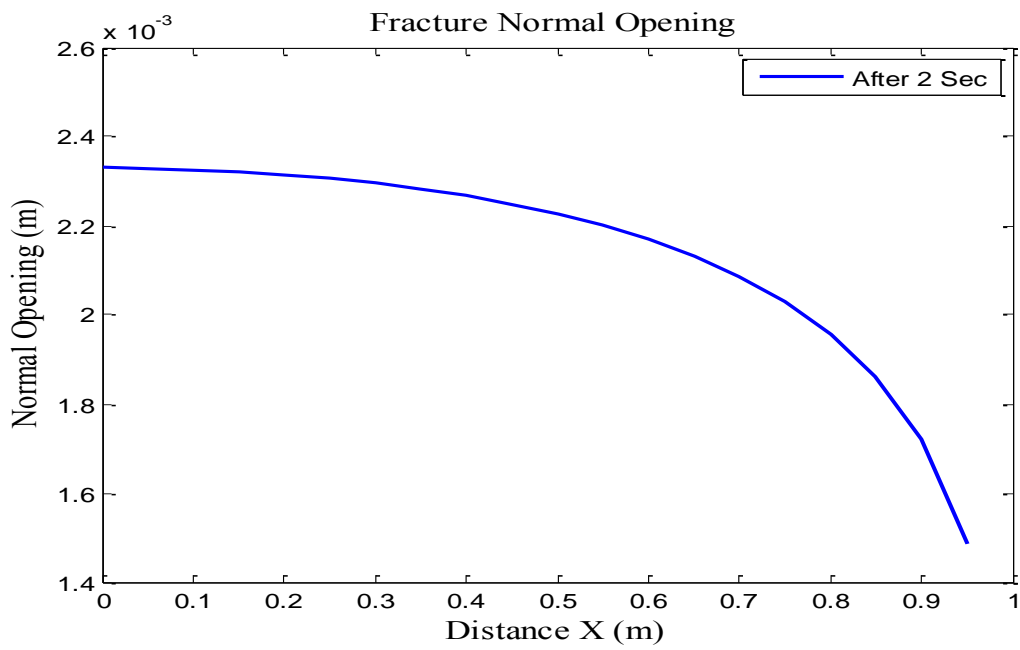


Figure 6.9. Fracture width after 2 sec of fluid injection

6.3. Thermo-Mechanical Coupling

The effects of thermal-induced stresses on the fracture geometry have been estimated on two types of fracture models: first on constant height KGD model and second on the constant two-dimensional DD model. A description of thermal induced stresses coupling is discussed in following sections.

6.3.1. Effect of Thermal Stresses on KGD Model

To evaluate effect of the thermal induced stress, an initial fracture geometry is generated for two-dimensional KGD model based on the analytical solution as discussed in Chapter 2 is developed using a computer program from Gidley et al. (1989). The input parameters for this model are summarized in Table 6-2. The generated initial fracture width and length for the KGD model are shown in Figures 6.10 and 6.11. After 250 min of fluid injection maximum fracture length is recorded as 280 m and maximum fracture width at wellbore is equal to 3.4 cm.

Table 6-2. Input parameters for the KGD model

No.	Parameter	Unit	Value
1	Elastic Modulus (E)	GPa	37.5
2	Poisson's ratio (ν)	-	0.25
3	Fluid injection rate (Q_i)	m ³ /min	1.8
4	Fluid viscosity (μ)	cp	100
5	Fluid injection time (t)	min	250
6	Constant fracture height	h_f	100

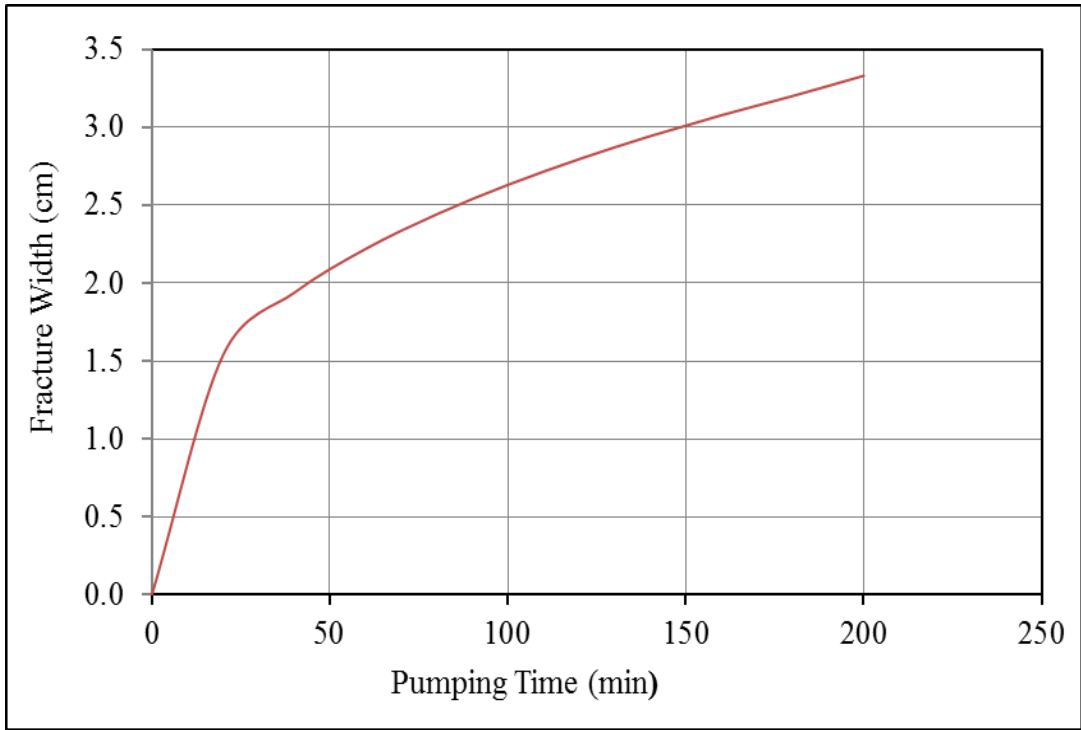


Figure 6.10. Initial fracture width from the KGD model

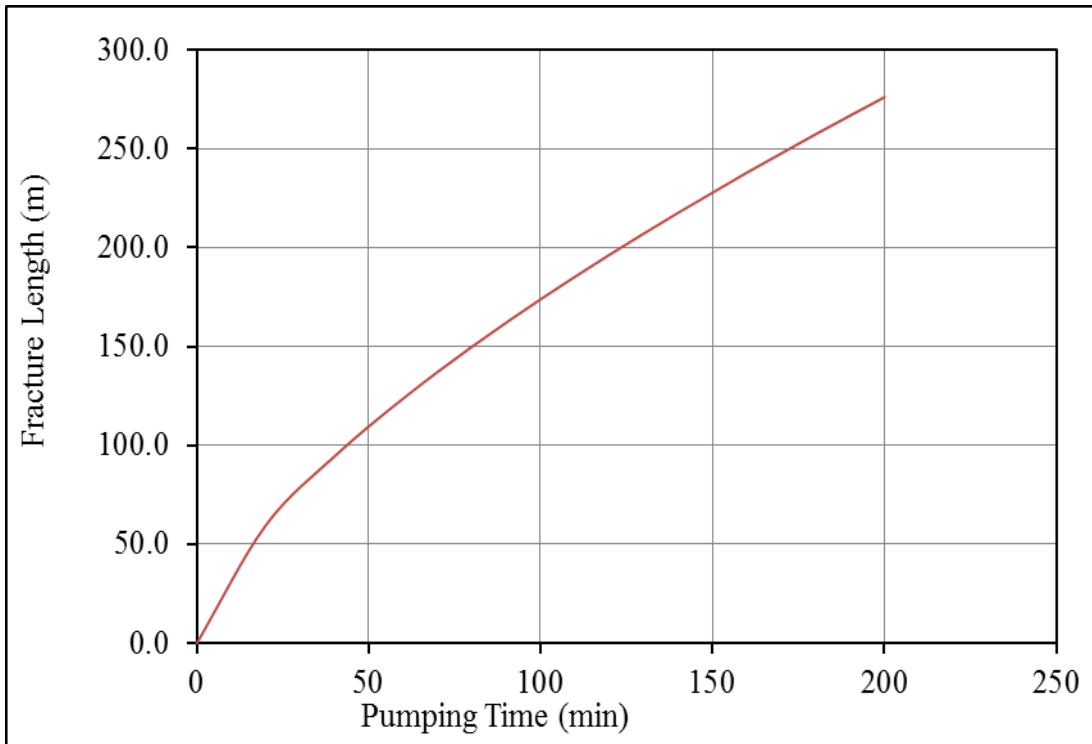


Figure 6.11. Initial fracture length the KGD model

To evaluate the effect of thermal stresses on the fracture geometry, the heat flow models as discussed in the Sec. 5.1 after 10 days were considered. The input parameters are same as in Table 5-1 except to the fluid velocity, which is approximated as $v=Q/2w$, where w is the average fracture width generated by hydraulic fracture models. The thermal induced changes in the fracture length and volume can be estimated as follows:

$$dL_f = \int_0^1 \alpha_T \Delta T(x,0) dx; \text{ Fracture length} \quad (6.17a)$$

$$dA = \int_0^1 \int_0^1 \alpha_T \Delta T(x,y) dx dy; \text{ Fracture area} \quad (6.17b)$$

where dL_f and dA are the change the in fracture length and fracture area due to thermal induced stresses, α_T is the coefficient of the linear thermal expansion, $\Delta T(x,0)$ and $\Delta T(x,y)$ represents the change in temperature along the fracture length and any point in fracture area, respectively. All the calculations in this model have been performed for normalized fracture geometry. For calculation of normalized thermal-induced volume change unit fracture height is assumed. The effect of thermal-induced stresses on the fracture width and fracture volume for the KGD modes is Figures 6.12 and 6.13, respectively. As can be seen from Figure 6.12, the change in the fracture width due to temperature change is much smaller compared to the change is fracturing width due to the hydraulic pressure. As can be seen from Figure 6.13, despite the small change in fracture width due to temperature change, its contribution to the total fracture volume is not negligible. This is because of the large fracture height and length of the fracture, which when multiplied with the change in fracture width results in significant volume contribution. Due to very less thermal expansion coefficients of geothermal reservoirs rocks, it was found that the thermal-induced stresses effects fracture length insignificantly as compare to its width. For better estimation of thermal-induced fracture geometry change, these models need to run longer time duration.

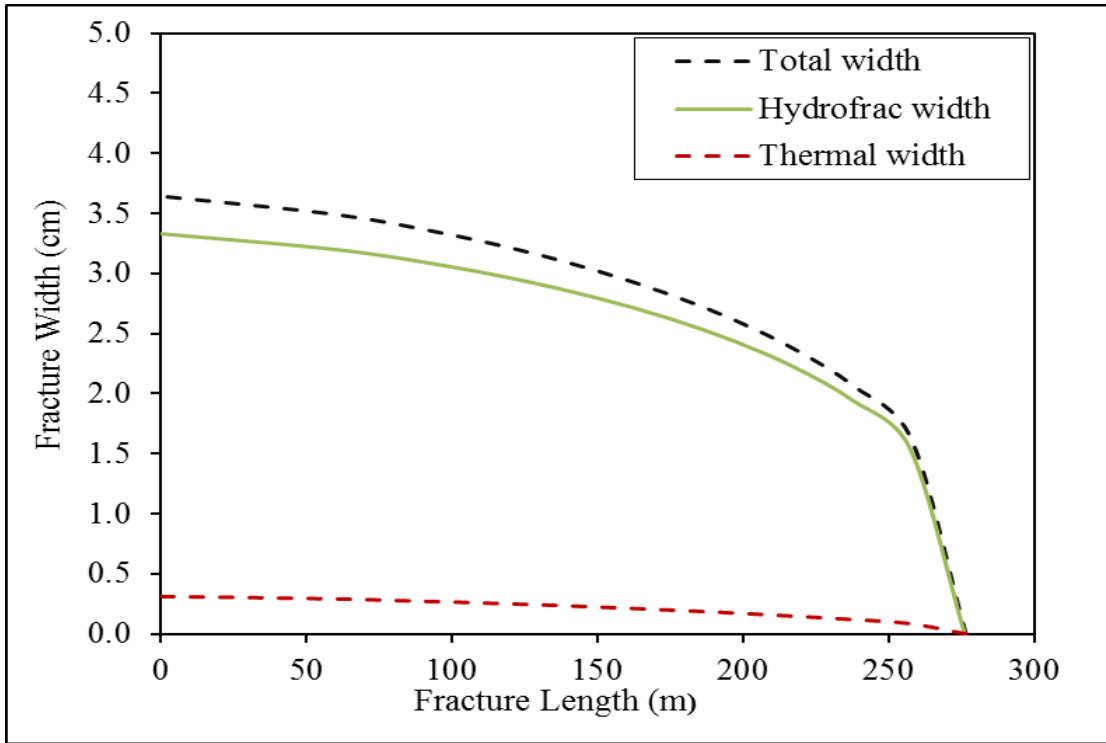


Figure 6.12. Change in the fracture width due to thermal-induced stress (KGD model)

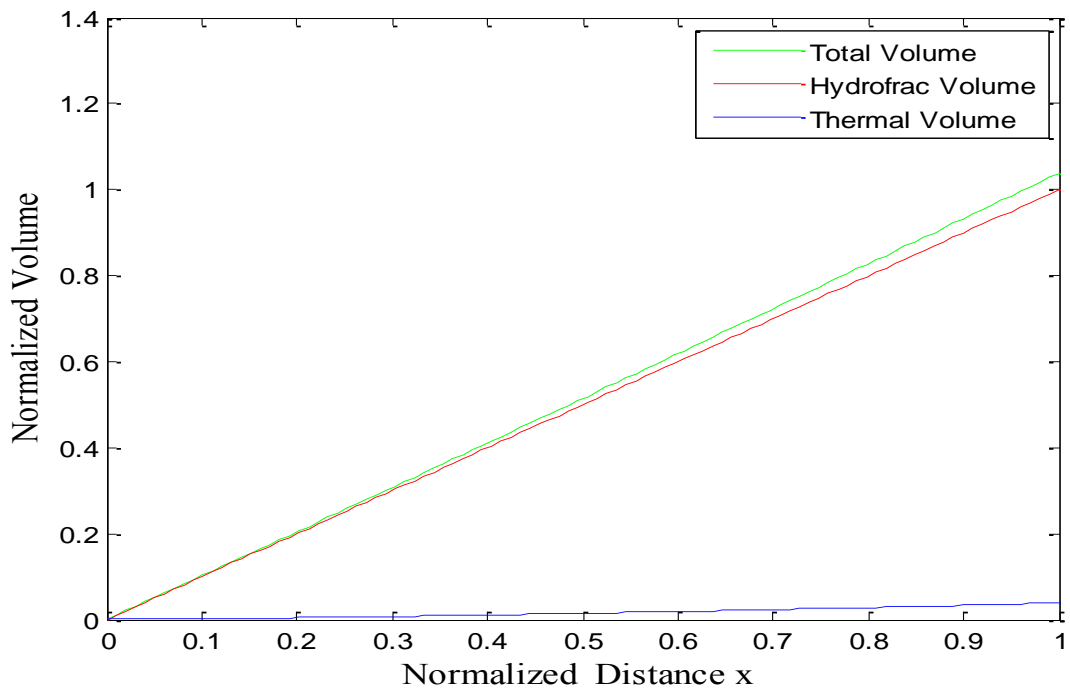


Figure 6.13. Change in fracture volume due to thermal-induced stress (KGD model)

6.3.2 Effect of Thermal Induced Stresses on 2D-DDM Model

The effects of the thermal induced stresses in second case are evaluated using constant two-dimensional DD model for fracture aperture and two-dimensional integral equation model for heat flow as discussed in the Sec. 5.3. In this case, first the fracture geometry is generated with using DDM model and then fluid is circulated for 10 days. The effects of the thermal induced stresses on the fracture aperture after 10 days are estimated. The reservoir rock properties and fluid properties are take same as in Table 5-2. The fracture aperture in this case is taken equal to average fracture opening from the initial model. The fracture length is considered equal to 100 m. In order to couple the thermal stresses in the DDM model, first the thermal stresses are evaluated using the boundary integral solution as shown in Figure 6.14, then the normal and shear stresses acting on each element is updated as follows (Zhou et al., 2010):

$$\sigma_n^i = \sigma_{n0}^i - p^i + \sigma_{nt}^i \quad (6.18a)$$

$$\sigma_s^i = \sigma_{s0}^i + \sigma_{st}^i \quad (6.18b)$$

where σ_{n0}^i and σ_{s0}^i are the normal and shear in-situ stresses on the i th element, respectively, p^i represent the fluid pressure on the i th element, σ_{nt}^i and σ_{st}^i represent the thermal induced normal and shear stresses on the i th element, respectively. The thermal induced stresses are contractive (or tensile) in nature; hence, these stresses help in the fracture opening. A plot of comparison between the fracture normal opening at initial stage and after coupling thermal stresses is shown in Figure 6.15. It can be observed that the maximum effect of thermal induced stresses occurs near the wellbore, which is maintained at constant fluid injection temperature. A maximum fracture opening change equal to 0.0106 (m) in the fracture normal opening is recorded in this case.

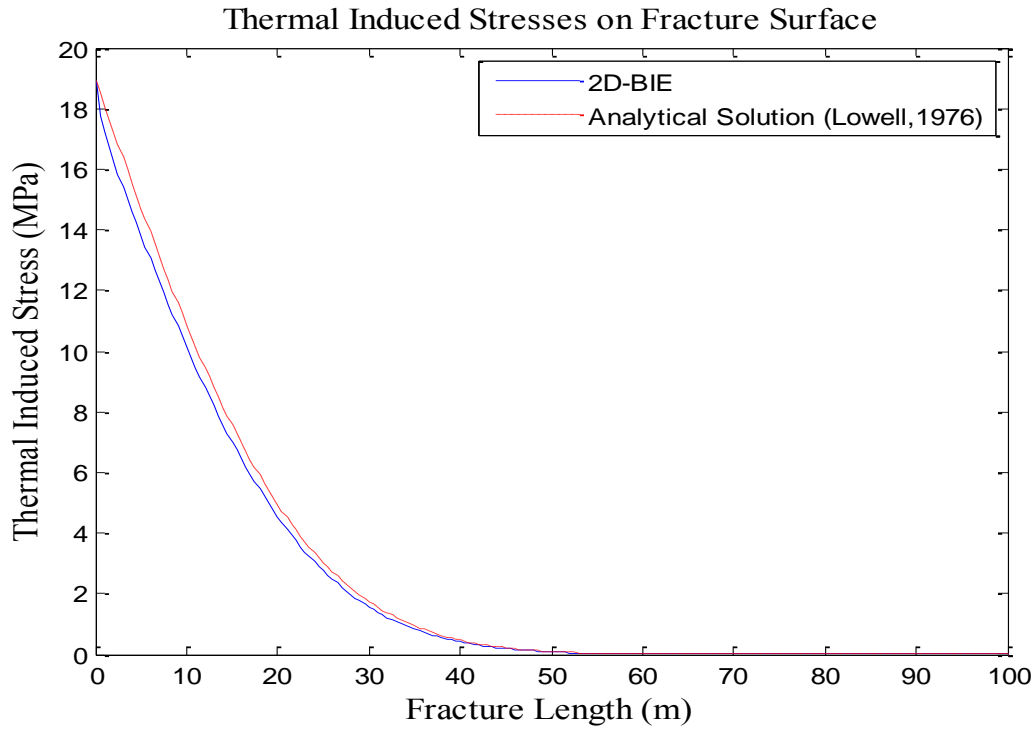


Figure 6.14. Thermal induced stresses after 10 days from boundary integral solution

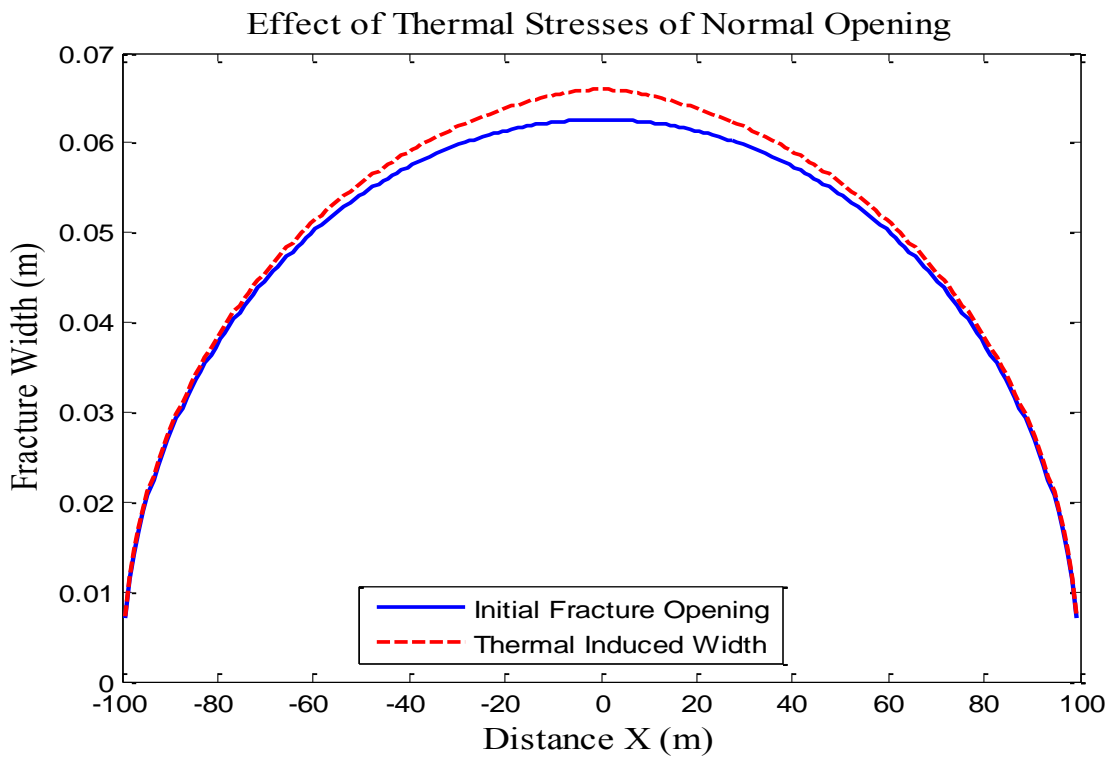


Figure 6.15. Effect of the thermal induced stresses on the fracture normal opening in the 2D-DD model

6.4. Chapter Summary

The two-dimensional heat flow model developed for during fracturing process, presents a simple numerical model to estimate effect of thermal-stresses on the fracture initiation and propagation processes. The moving boundary conditions can be easily accounted in the model by changing the fracture length. The heat extraction models using boundary integral equations presents an efficient method for heat extraction modeling both in terms of accuracy and computational efficiency. Only the fracture surface discretization is required. It over comes traditional one-dimensional heat conduction approach in heat extraction models.

CHAPTER 7.

MODEL VALIDATION

This chapter presents laboratory field validation of the water circulation test, and experimental validation of the hydraulic test using results of laboratory scale model test of hydraulic fracture. For validation circulation test a 90-day circulation test from the Hijiori EGS site is taken. The experimental validation is considered for laboratory scale hydraulic fracturing in the EGS triaxial cell. Details of the validation procedures are discussed in the following sections.

7.1. Field Validation of Circulation Test

For the field validation of heat flow model, 90-day circulation test from the Hijiori EGS site was selected. A layout of the Hijiori EGS site which was developed by the New Energy and Industrial Development Organization (NEDO) is shown in Figure 7.1. This EGS site was developed in two levels; shallow reservoir at 1800 m depth and deep reservoir at 2200 m. A 90-days circulation test which involves 4 well systems in shallow reservoir in 1991 was reported by Yamaguchi (1992). The water was injected in well SKG-2 and produced from well HDR-1, HDR-2 and HDR-3, respectively. The distances from well SKG-2 to well HDR-1, HDR-2, and HDR-3 were about 40, 50, and 55 m, respectively at approximate 1800 m depth. The reservoir initial temperature was 250°C and injection water temperature was 55°C. This test is a unique circulation test in development of the EGS reservoirs, which involved multiple wells and multiple production zones for heat recovery. The rock and fluid properties are same as listed in Table 5-5. The data for 90-days circulation test are listed in Table 7-1, which were used for the heat flow simulation model.

Table 7-1. 90-day circulation test data (Yamaguchi, 1992)

No.	Parameter	Symbol	Unit	Value
1	Injection rate	Q_i	kg/sec	16.7
4	Injection pressure	P	MPa	3
5	Injection temperature	T_f	°C	55
6	Reservoir temperature	T_r	°C	250
7	Production temperature range		°C	160-180
8	Pumping duration		days	90
9	Fluid recovery	%		77
10	Thermal output		MW	8.5

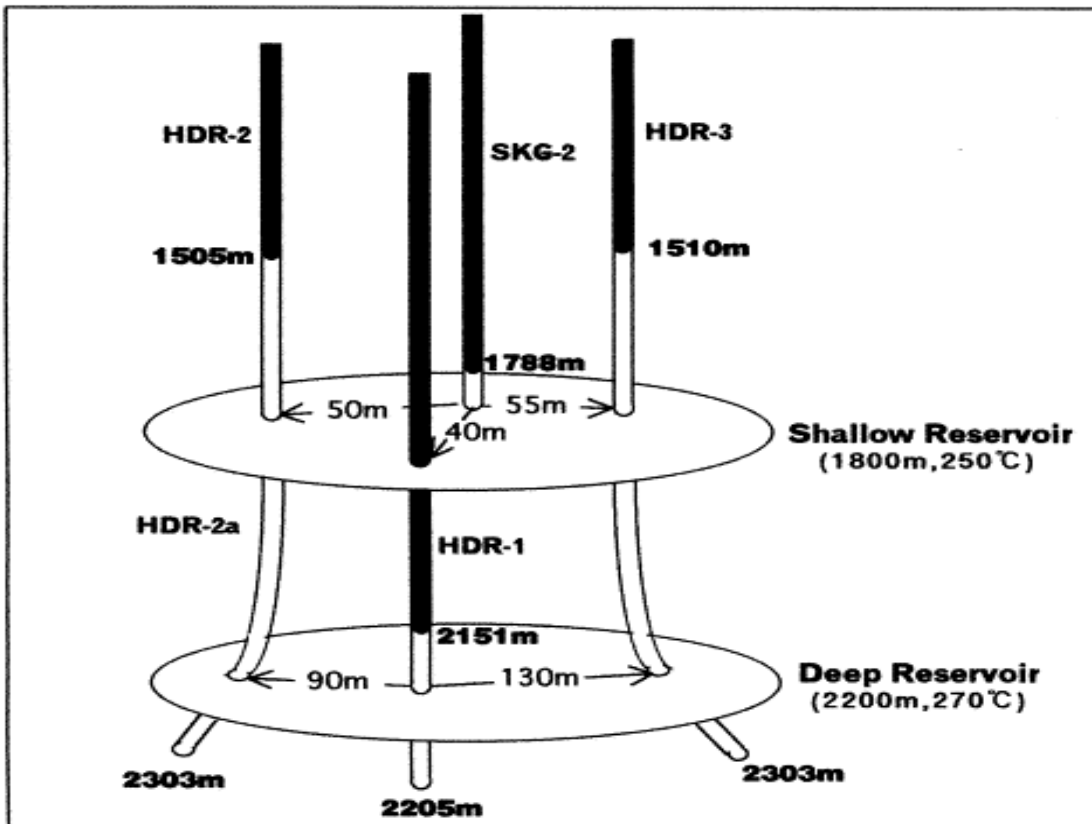


Figure 7.1. Layout of position of wells and reservoirs at Hijiori EGS site (Kuriyagawa & Tenma, 1999)

A three-dimensional heat extraction model assuming 100% fluid recovery was developed for this 90-days circulation test using injection and extraction wells geometrical locations as shown in Figure 7.1. The location of wells coordinates are SKG-2 (0, 0), HDR-1(0,-20), HDR-2 (-24,-16), and HDR-3 (56,-4), respectively. A long rectangular fracture with small uniform fracture width was assumed connecting all 4-wells. A surface plot of temperature at end of circulation test is shown in Figure 7.2. The model generated some higher range production wells temperature as 182-224°C; whereas the field production temperature range was 160-180°C. Several reasons might be responsible for deviation of numerical results from the actual results. First, several main fractures for fluid circulation might be existing in real field scenario. The model doesn't account for the fluid leak-off, by incorporating the fluid leak-off in the flow models, this problem can be rectified. Other important reason might be heterogeneity in the reservoir rocks, because the model assumes a homogenous rock mass.

1. Electrical Energy Output Estimation

The electric energy output or geothermal power output by fluid circulation between the injection well and production wells can be given as follows (Gringarten et al., 1975):

$$W = \rho_f c_f Q (T - T_f) \quad (7.1)$$

where Q is the fluid injection rate, ρ_f and c_f are the fluid density and specific heat, respectively, T_f represents the fluid temperature, and T is temperature at any given time. The cumulative heat energy output over a time period t can be given as follows:

$$W = \int_0^t \rho_f c_f Q (T_R - T_f) \cdot \left(1 - \frac{T_R - T}{T_R - T_f} \right) dt \quad (7.2)$$

The calculated heat thermal energy form model result is about 6.13 MW, which is less than actual heat produced during circulation test. The reason for low energy production form the numerical result is justified, because the model predicted the higher operating temperature range.

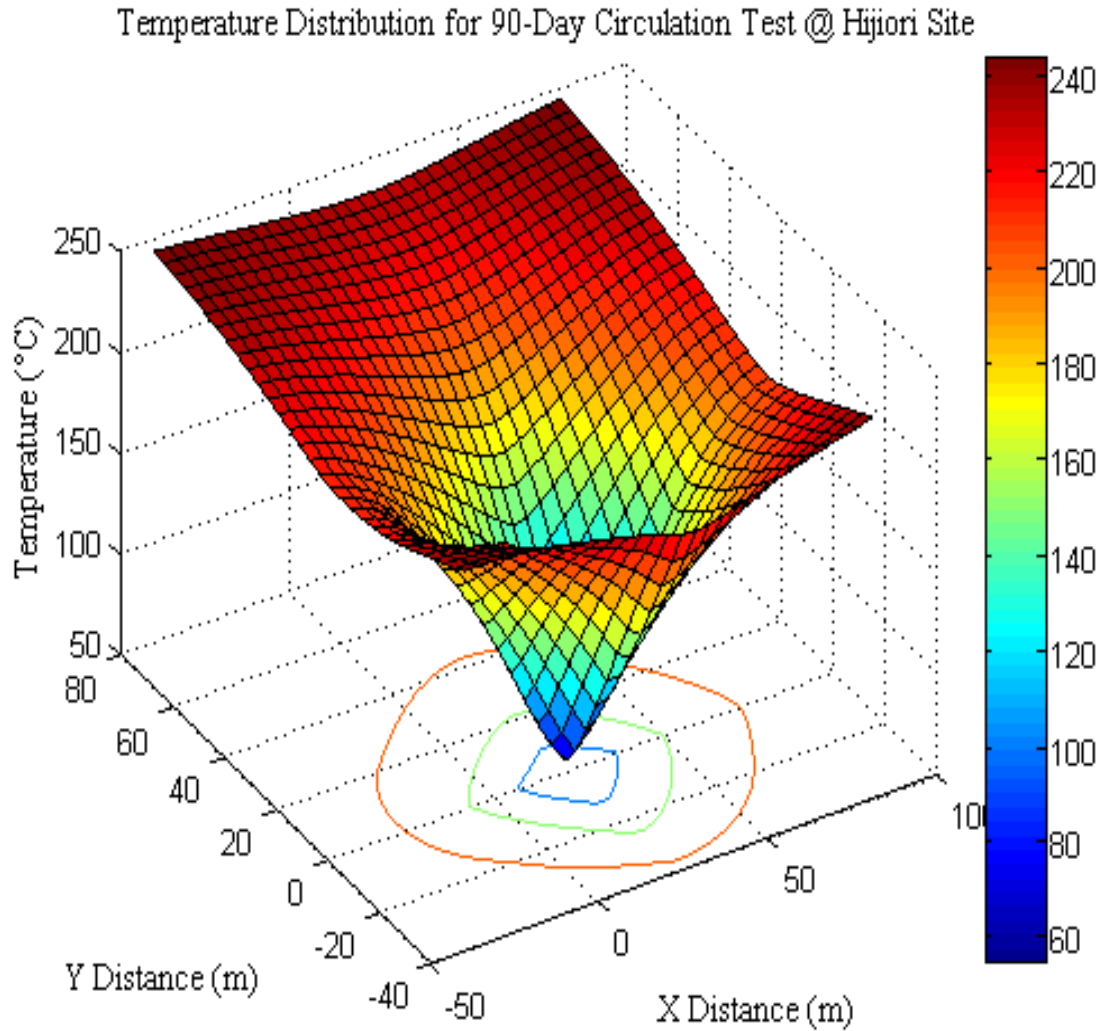


Figure 7.2. Surface plot of temperature distribution for 90-day circulation test

7.2. Experimental Validation of Fracture Model

For experimental validation of numerical hydraulic fracture model was done using a laboratory scale model test of hydraulic fracturing in rocks. An experimental setup of the EGS triaxial cell developed at Civil & Environmental Engineering Department of Colorado School of Mines (CSM). The schematic of the tri-axial cell for the laboratory hydraulic fracturing test is shown in Figure 7.3. The cell has capacity to test cubical rock same of $30 \times 30 \times 30 \text{ cm}^3$ under high three-dimensional stress ($>12.2 \text{ MPa}$) and high temperature ($>100^\circ\text{C}$) conditions. A drawback of laboratory tests is that only small scale models can be tested and it will be necessary to extrapolate results and observations to field scale. However, laboratory tests can be carried out under prescribed and well-controlled conditions, and the results can be directly used in validation of computer models.

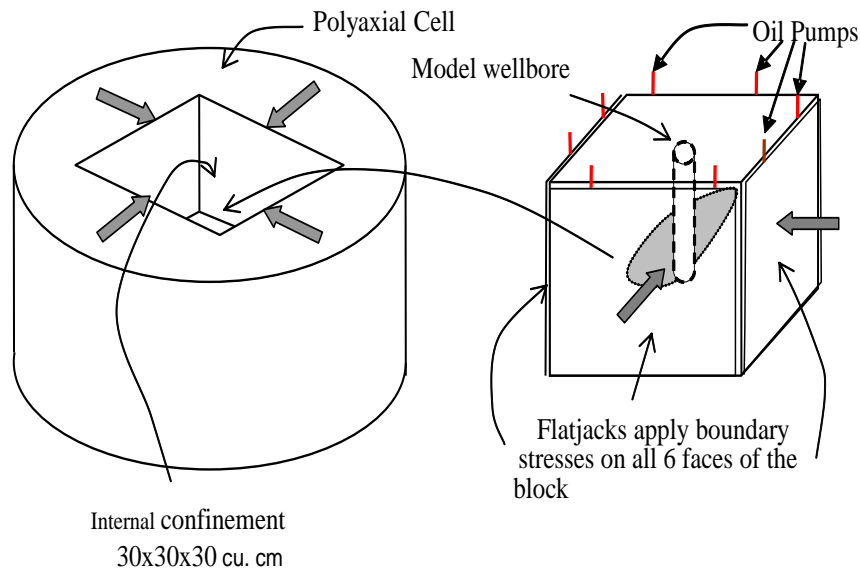


Figure 7.3. Schematic of the tri-axial cell for laboratory hydraulic fracturing test

An experiment hydraulic fracture test on the granite is considered in this section. The input parameters for this test are listed in Table 7-2. The variation of the fluid pressure with time and fluid injection rate is shown in Figure 7.4.

Table 7-2. Input parameters for experimental hydraulic fracture test

No	Parameter	Unit	Value
1	Young's modulus (E)	GPa	56.9
2	Poisson's ratio (ν)	-	0.25
3	Average fluid injection rate (Q_i)	mL/min	1.5
4	Fluid viscosity (μ)	cP	21.18
5	Fracture propagation start time	min	172
6	Total pumping time	min	1000

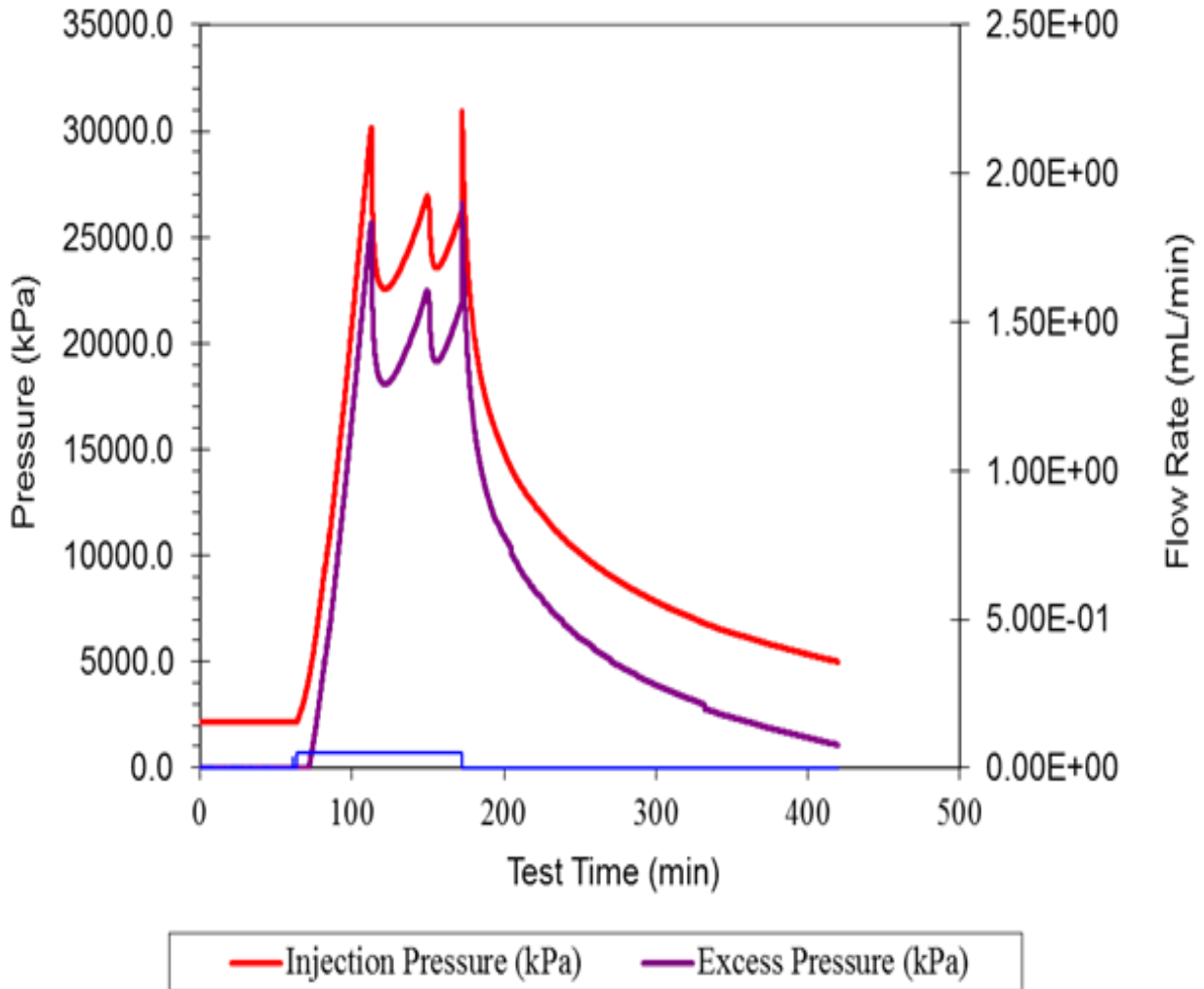


Figure 7.4. Variation of the fluid pressure with time during experimental hydraulic fracturing in triaxial cell (Frash, 2012)

A numerical validation of the above experiment is analyzed using the KGD analytical model as discussed in Chapter 2. For completeness rewriting the variation of fluid pressure, fracture width, and length with time based for the KGD model as follows (Dahi, 2009):

$$p_w(t) = \sigma_3 + 1.09 \left[\mu E'^2 \right]^{1/3} t^{1/3} \quad (7.3a)$$

$$W_o(t) = 2.36 \left[\frac{\mu q_0^3}{E'} \right]^{1/6} t^{1/3} \quad (7.3b)$$

$$L(t) = 1.078 \left[\frac{E' q_0^3}{\mu} \right]^{1/3} t^{2/3} \quad (7.3c)$$

where E' is the plane-strain modulus of elasticity, q_0 is the fluid injection rate per unit height of the fracture, μ represents the fluid viscosity and σ_3 is the minimum in-situ stress. Since, the KGD model is based on the constant fracture; hence constant fracture height equal to 20 cm is assumed in the experimental test. Other basic assumption of this model is the constant fluid injection rate; hence, an average fluid injection rate from the experimental test was taken. A variation of the wellbore pressure and the fracture width for experimental test based on the KGD model is shown in Figures 7.5 and 7.6, respectively. In the numerical model the fluid pressure only after the fracture creation is considered. Based on comparison of Figures 7.4 and 7.5, it can be observed that there is big difference in the fracture fluid pressure between experimental and numerical results. However, the fracture width variation in Figure 7.6 is reasonable for small laboratory scale fracture. It can be concluded from the comparison of the experimental and the result from the KGD model, that more accurate three-dimensional model is required for the validation purpose.

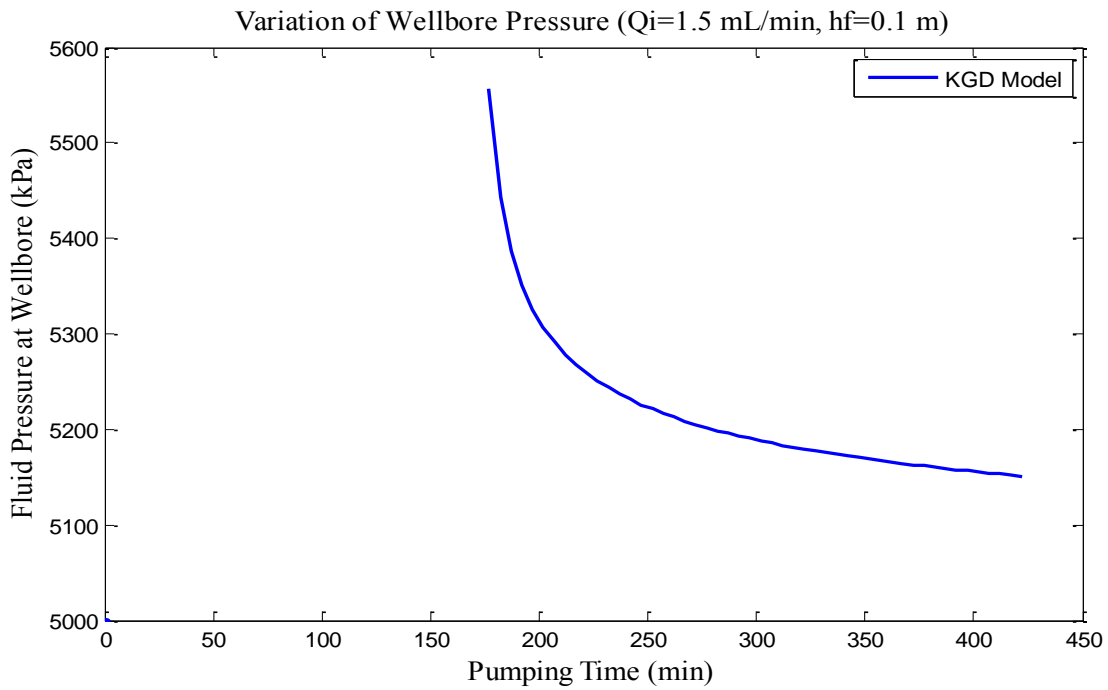


Figure 7.5. Variation of the fluid pressure with time during experimental hydraulic fracturing in triaxial cell (Frash, 2012)

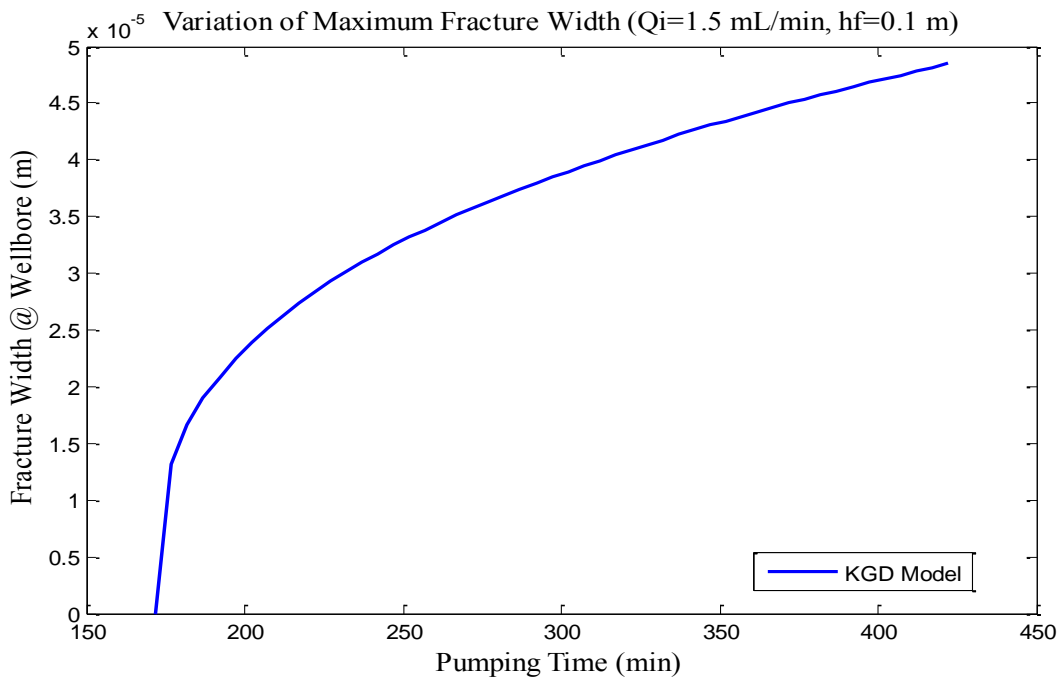


Figure 7.6. Variation of the fluid pressure with time during experimental hydraulic fracturing in triaxial cell (Frash, 2012)

7.3. Chapter Summary

The chapter presented validation of the field heat extraction model and experimental hydraulic fracture model. First validation for heat extraction model shows some higher operating range for production temperature. But by considering multiple connected fractures and incorporating the fluid leak-off in the numerical model, the heat extraction models can simulate the field circular test more efficiently. However, the pressure difference between the experimental hydraulic fracture results and the numerical results from the KGD model suggests that advanced fully three-dimensional numerical model is required.

CHAPTER 8.

SUMMARY, CONCLUSIONS AND RECOMMENDATIONS

The fundamental aspects of the hydraulic fracture mechanics and the fluid and heat flow processes in an Enhanced Geothermal System (EGS) have been presented in this study. The research was motivated by the need for an advanced hydraulic fracture prediction model for the EGS as the existing fracture simulator models from the oil and gas industry have either limited or not directly applicable for EGS reservoir creation.

8.1. Summary

The study presented the development and validation of numerical models for the hydraulic fracture geometry prediction and heat extraction through the created fracture networks in EGS. Analytical validations based on some simplified cases have been included for each model. The models were developed using: (1) the Displacement Discontinuity (DD) Method for three hydraulic fracturing, (2) Finite Element Method (FEM) for fracture fluid flow, and (3) the Boundary Integral formulations for the heat extraction modeling based on the advective-convective heat flow equation. A coupled hydro-thermo-mechanical approach was used to integrate the fracturing, fluid flow and heat flow models into one system hydro-thermo-mechanical fracturing code.

The concepts of the Boundary Element Method and its applications to the fracture mechanics problems were addressed in detail. Two types of the DD models: constant strength DD model for two- and three-dimensional and the DD model based on the Kelvin's fundamental solution for three-dimensional elasticity problem were developed. For the constant two-dimensional DD model, analytical solution for constant line strength was used and the fracture

tip singularity of stresses were calculated using parabolic tip element, which accounted for stress variation based on the LEFM (Linear Elastic Fracture Mechanic). The model was verified using pressurized planar and oriented fractures. For generalized three-dimensional DD model, the fundamental solution for elasticity and numerical integration based point collocation technique was used. The 4-node continuous quadrilateral elements for the fracture domain and semi-discontinuous elements for the fracture front were utilized. The semi-discontinuous element in this case satisfied the LEFM criterion for the fracture front elements. The hyper-singularity of the elasticity kernel function was addressed based on the singularity subtraction approach and the non-singular integration is optimized using the adaptive Gaussian integration. This model was applied to the pressurized penny shaped fracture and verified using the analytical solution for the fracture normal opening and variation of normal stresses near the fracture tip.

The fracture fluid flow was been modeled for the steady and transient cases. The steady-state fluid flow components were used as input parameters for the heat extraction models. The steady state flow was solved based on the source and sink analogy at the injection and extraction well. An implicit Finite Difference approximation was used in this case. The transient fluid flow was solved for a component in the coupled fracture model. In this, Galerkin's Finite Element approximation was used. The computer code for this model was verified using pore pressure distribution in a reservoir.

The heat flow models were developed to address two main concerns in the EGS: how the thermal induced stresses can influence the fracturing process and what is thermal output from a continuous water circulation for certain time. For first case, a two-dimensional heat flow model was developed based on the sequential approach: first the variation of temperature inside the fracture was solved using the analytical solution for one-dimensional advection-diffusion

process, and then the temperature inside the fracture is substituted as a boundary for the heat conduction between the fracture surfaces and reservoir. To address the second concern of the EGS, two- and three-dimensional heat extraction models based on the boundary integral equation formulation were developed. The detailed mathematical approach and numerical implementation schemes for both the models were presented in the thesis. The numerical issue of weak singularity was addressed in both formulations. The time variable in the both models have been transferred to a constant parameter using the Laplace transformation and the temperatures are solved in terms of this constant parameters. Finally, using a numerical Laplace inversion scheme, the temperatures in the real time domain was obtained. The methodologies to estimate the thermal energy output and the thermal induced stress have been presented.

Coupled hydro-thermo-mechanical fracture models for two-dimensional case were developed. The hydro-mechanical processes were modeled based on explicit coupling between the fluid flow and the fracture deformation. The fracture fluid flow in this case was solved using cell centered one-dimensional implicit scheme; whereas the fracture deformation is modeled two-dimensional constant DD formulation for a linear joint model. Two cases for hydro-mechanical coupling: the classical KGD model and the two-dimensional DD model were considered. For the KGD model, the effect of the thermal induced stresses on the fracture aperture and volume was estimated. For two-dimensional DD model, the thermal induced stresses from the 2D integral equation formation are coupled with applied stresses on the fracture-surfaces and its effect on the fracture aperture was estimated.

Finally, the three-dimensional heat extraction model was validated using data from field circulation test data. In this case, a 90-day circulation test from the Hijiori (Japan) EGS site was utilized in the validation. The validation of the hydro-thermo-fracturing model used test results

from scale model testing of hydraulic fracturing of rock sample using cubical triaxial rig developed at the Civil & Environmental Engineering laboratory at Colorado School of Mines.

8.2. Conclusion

The main conclusions from this research are as follows:

1. The DD model based on the Kelvin's fundamental solution presents a generalized and efficient method for the fracture mechanics problems. This method over comes the shortcoming of constant DD models; because there is no restriction on the type of geometry to be modeled and on the type of elements used to discretized the boundary surfaces. This method is basically based on the node sharing scheme; hence, it reduces the number of variable for the same problem if it has been modeled using the constant strength DD method. The 4-node semi-discontinuous elements used for the fracture front elements present a relatively simple scheme without compromising with numerical efficiency as compared to quadratic 8- or 9- node elements. The singularity subtraction technique used for hyper-singular cases presents a generalized scheme which can be easily extended to any order of singularity just by selecting the appropriate terms in the Taylor's series expansion for the singular integrand.
2. The two-dimensional sequential heat model presents a simpler scheme to incorporate the moving mesh boundary conditions in the hydraulic fracture propagation. Both the two-dimensional and three-dimensional boundary integral models present a computationally efficient and accurate numerical approach for the EGS heat exaction modeling. Since, the boundary integral formulation completely eliminates the domain discretization. Once, the temperatures are known over the fracture surface, the domain temperatures can be directly obtained by super-position method. The Laplace transform scheme used in the

boundary integral equations present an efficient scheme to handle time variable; since it converts time variable to a constant parameters.

3. The thermo-mechanical coupling with the KGD model and with the DDM model shows that thermal induced stresses have significant influence on the fracture geometry.
4. The extension of the boundary integral solution to the large scale field problems presents an efficient method for the heat extraction modeling. By accounting for some shortcomings in the current model, it can be very good numerical tool for the heat extraction modeling for the EGS sites.
5. The validation of experimental hydraulic fracture test using the KGD model predicts a reasonable fracture aperture variation for small test; however, a big difference in the fluid pressure variation is observed. Hence, it can be concluded that advanced fully coupled three-dimensional model is required for accurate validation of experimental results.

The main novel contributions from this research are as follows:

1. The research presented a simple and efficient heat flow model, which can easily adopt the moving fracture boundary conditions and can estimate the effects of temperature change on the fracture propagation process and on rock and fluid physical properties.
2. The successfully implementation of the 4-node semi-discontinuous element for the fracture front elements, gives computationally efficient scheme for the large fracture modeling problems.
3. The implementation of weak-singularity treatment in case of three-dimensional heat extraction model gives more accurate results.
4. The extension of boundary integral heat extraction model, for the field EGS case study, presents a computationally efficient scheme for long terms heat extraction modeling.

Once, the temperature is known over the fracture surface, the reservoir temperature at any location can be estimated as a secondary variable from the model.

8.3. Future Recommendations

The numerical methodologies and codes developed in this study presents basis for future research in this area. The main topics which I would like to recommend for future work in this research area are as follows:

1. The fracture process is a complex fully coupled non-linear problem; hence, expansion of the codes for fully-coupled hydro-thermo-mechanical model is required.
2. The objective of a hydraulic fracturing process is to create a fracture and keep it open for long time; hence, addition of the proppant flow and transport process in the model is recommended.
3. Mostly, the hydraulic fracturing is done for deviated well bore; hence, it is important to include mixed mode fracture initiation and propagation which can account for the fracture turning and twisting.
4. Since, mostly the reservoirs are not homogenous; it is recommended to include reservoir heterogeneity and multilayer properties in model.
5. Since, in real hydraulic fracturing process, a main fracture along with cluster of small fractures initiates from a wellbore. Hence, simulate accurate fracturing process, numerical modeling of the multiple fracture should be considered
6. In case of the EGS, the thermal induced stresses, not only affects the stresses state in the reservoir, but can also change the rock and fluid physical and thermal properties. Hence, it is important to include the change in the properties in the model.

REFERENCES CITED

- Adachi, J., Siebrits, E., Peirce, A., & Desroches, J. (2006). Computer simulation of hydraulic fractures. *Int. J. of Rock Mechanics & Mining Sciences*, Vol. 44, Issue 5, pp.739-757.
- Aliabadi, M.H., and Brebbia, C.A. (1993). *Advanced formulations in boundary element methods*. Computational Mechanics Publications, Elsevier Applied Science, 289 pp.
- Aliabadi, M.H., Hall, W.S., & Plemister, T.G. (1985). Taylor expansions for singular kernels in the boundary element method. *Int. J. for Num. Methods in Engg.*, Vol. 21, pp.2221-2236.
- Aliabadi, M.H., Hall, W.S., & Hibbs, T.T. (1987). Exact cancelling for potential kernel in the boundary element method. *Commun. In Num. Methods in Engineering*, Vol.3, pp.123-128.
- Aliabadi, M.H., & Rooke, D.P. (1991). *Numerical fracture mechanics*. Kluwer Academic Publisher, 276 pp.
- Ameen, M. (2005). *Computational Elasticity: theory of elasticity, finite and boundary element methods*. Alpha Science International Ltd., 530 pp.
- Andrew, W. (2000). *A dual boundary element formulation for three-dimensional fracture analysis*. WIT Press, Southampton, Boston, 227 pp.
- American Petroleum Institute (2009). Hydraulic fracturing operations-well construction and integrity guidelines. 1st Ed., pp. 1-36.
- Banerjee, P.K. (1994). *The boundary element method in engineering*. McGraw-Hill Company Europe, 496 pp.
- Banerjee, P.K., & Butterfield, R. (1981). *Boundary element methods in engineering science*. McGraw Hill Publication, 452 pp.

- Barsoum, R.S. (1976). On the use of isoparametric finite elements in linear fracture mechanics. *Int. J. for Num. methods in Engineering*. Vol.10, pp.25-37.
- Becker, E.B., Graham, F.C., & Oden, J.T. (1981). Finite elements: An introduction. Prentice-Hall Inc., Vol. I, 258 pp.
- Becker, A.A. (1992). *The boundary element method in engineering: A complete course*. McGRAW-Hill Book Company, 337 pp.
- Beer. G. (2001). *Programming the boundary element method*. John Wiley & Sons, Ltd, 457 pp.
- Ben-Naceur, K., Thiercelin, M., & Touboul, E. (1989). Simulation of fluid flow in hydraulic fracturing: implications for 3D propagation. *SPE Prod Eng J.*, SPE-16032, pp.133-141.
- Benzley, S.E. (1974). Representation of singularities with isoparametric finite element. *Int. J. of Num. Meth. In Engineering*, Vol. 8(3), pp.537-545.
- Blandford, G.E., Ingraffea, A.R., & Liggett, J.A. (1981). Two-dimensional stress intensity factor computation using the boundary element method. *Int. J. for Num. Methods for Engineering*, Vol.17, pp.387-404.
- Boston, D.P. (2008). *Analytical and numerical modeling of thermal conductive heating in fractured rocks*. MS. Thesis, Queen's University, Canada, 148 pp.
- Brebbia, C.A., Telles, J.C.F., & Wrobel, L. (1984). Theory and applications in boundary element techniques in Engineering, Springer, 1st Ed., 464 pp.
- Carslaw, H.S., & Jaeger, J.C. (1959). *Conduction of heat in solids*. Oxford University Press, 510 pp.
- Carter, B.J., Desroches, J., Ingraffea, A.R., & Wawrzynek, P.A. (2000). Simulating fully 3D hydraulic fracturing. *Modeling in Geomech.*, John Wiley & Sons, New York, pp.1-36.

- Carter, R.D. (1957). Derivation of general equation for estimating the extent of fracture area. *Drilling and Prod. Practice*, API, pp. 261-270.
- Chan, S.K., Tuba, I.S., & Wilson, W.K. (1970). On the finite element method in linear fracture mechanics. *Engineering Fracture Mechanics*, Vol. 2, pp. 1-17.
- Chapra, S.C., & Canale, R.P. (2006). *Numerical methods for engineers*. 5th Ed. McGraw Hill Companies, New York, 926 pp.
- Cheng, AH-D., Ghassemi, A., & Detournay E. (2001). A two-dimensional solution for heat extraction from a fracture in hot dry rock. *Int. J. Num. Anal. Methods Geomech*, Vol. 25, pp.1327-1338.
- Cleary, M.P., Kavvadas, M., & Lam, K.Y. (1983). Development of a fully three-dimensional simulator for analysis and design of hydraulic fracturing. *SPE/DOE Low Permeability Gas Reservoir Symposium*, Denver, pp. 1-12.
- Clifton, R.J., & Abou-Sayed, A.S. (1981). A variational approach to prediction of the three-dimensional geometry of hydraulic fractures. *SPE/DOE Low Permeability Gas Reservoir Symposium*, Denver, pp. 457-465.
- Clifton, R.J. (1989). Three-dimensional fracture propagation models. *SPE Monograph*, Vol.12, pp. 96-108.
- Crouch, S.L., & Starfield, A.M. (1983). *Boundary element methods in solid mechanics*. George Allen& Unwin, London, 322 pp.
- Crouch, S. L. (1976). Solution of plane elasticity problems by displacement discontinuity method. *Int. J. Num. Methods Engineering.*, Vol. 10, pp. 301-343.
- Cruse, T.A. (1988). *Boundary element analysis in computational fracture mechanics*. Springer, 162 pp.

- Cruse, T.A. (1977). Mathematical foundations of the boundary integral equation method in solid mechanics. *Technical Report, AFOSR-TR-77-1002*, Pratt and Whitney Aircraft Group, 120 pp.
- Cruse, T.A. (1978). Two-dimensional BEM fractures mechanics analysis. *Applied Mathematical Modeling*, Vol.2, pp.287-293.
- Currie, I.G. (2003). *Fundamental of fluids*. 3rd Ed., Mechanical Engineering, CRC Press, Vol.154, 548 pp.
- Dahi, A.L. (2009). An Analysis of hydraulic fracture propagation in fractured reservoirs: an improved model for the interaction between induced and natural fracture. *PhD dissertation, Graduate School-University of Texas at Austin*, 215 pp.
- Davis, T.G., & Bu, S. (1995). Effective evaluation of non-singular integrals in 3D BEM. *Advances in Engineering Software*, Vol. 23, pp.121-128.
- Davis, T.G., & Gao, X.W. (2006). Three-dimensional elasto-plastic analysis via the boundary element method. *Computers and Geotechnique*, Vol. 33, pp.145-154.
- Dell'Erba, D.N. (2002). *Thermo-elastic fracture mechanics using boundary elements*. WIT Press, Topic is engineering, Vol. 39, 146 pp.
- Delves, L., & Mohamed, J. (1988). *Computational methods for integral equations*. Cambridge University Press, 392 pp.
- Divo E.A., & Kassab A.J. (2003). *Boundary element methods for heat conduction: with applications in non-homogeneous media*. *WIT Press Topics in Engineering*, Vol. 44, 245 pp.

- Dong, C.Y., & Pater de, C.J. (2001). Numerical implementation of displacement discontinuity method and its application in hydraulic fracturing. *Computer Methods in Applied Mechanics and Engineering*, Vol. 191, pp.745-760.
- Economides, M. J., & Nolte, K.G., 2000. *Reservoir stimulation*. John Wiley & Sons, Ltd., 3rd Ed., 1-1 to 20-13 pp.
- Elswoth, D. (1989). Theory recovery from a spherically stimulated hot dry rock reservoir. *Journal of Geophysical Research*, Vol.94, pp.1927-1934.
- Erdogan, F., & Sih, G.C. (1963). On the crack extension in plates under plane loading and transverse shear. *Journal of Basic Engineering*, Vol. 85, pp. 519-527.
- Frash, L.P. (2012). Laboratory simulation of an enhanced geothermal reservoir. *M.S. Thesis, Colorado School of Mines*.
- Erhart, K., Divo E., & Kassab, A.J. (2006). A parallel domain decomposition boundary element method approach for the solution of large-scale transient heat conduction problems. *Engineering Analysis with Boundary Elements*, Vol. 30, pp. 553-563.
- Inglis, C.E. (1913).Stresses in a plate due to the presence of cracks and sharp corners. 54th session of the Institution of Naval Architects, March 14, pp.221-241.
- Gao, X.W., & Davis, T.G. (2000). Adaptive integration in elasto-plastic boundary element analysis. *Journal of the Chinese Institute of Engineers*, Vol. 3, pp. 349-356.
- Geertsma, J. & de Klerk, F. (1969).A rapid method of predicting width and extent of hydraulically induced fractures. *Journal of Petroleum Technology*, Volume 21, pp. 1571-1581.
- Ghassemi, A., Zhou ,X.X., & Rawal ,R C., 2010. 3D poro-elastic analysis of rock failure around a hydraulic fracture. 44th *US Rock Mechanics Symposium*, Salt Lake City, Utah, pp. 1-7.

- Ghassemi, A., Nygren, A., & Cheng, A-HD. (2008). Effects of heat extraction on fracture aperture: A poro-thermo-elastic analysis. *Geothermics*, Vol. 37, pp. 525-539.
- Ghassemi, A., Tarasovs, S., Cheng, AH-D. (2003). An integral equation method for modeling three-dimensional heat extraction from a fracture in hot dry rock. *Int. J. Num. Anal. Method Geomech*, Vol. 27, pp. 989-1004.
- Ghassemi, A., Tarasovs, S., & Cheng, AH-D. (2005). Integral equation solution of heat extraction stress induced thermal in enhanced geothermal systems. *Int. J. Num. Anal Methods in Geomech*, Vol. 29, pp. 829-841.
- Gidley, J.L., Holditch, S.A., Nierode, D.E., & Veatch Jr., R.W. (1989). Recent advances in hydraulic fracturing. *SPE Monograph Series*, Vol.12, 452 pp.
- Greenberg, M. (1998). *Applied Engineering Mathematics*. Pearson Publisher, 1324 pp.
- Griffith, A.A. (1921). The theory of rupture and flow in solids. *Phil. Trans. Roy. Soc. London*, pp. 163-197.
- Griffiths, D.V., & Smith. I.M. (2006). *Numerical method for engineers*. 2nd Ed, *Chapman & Hall/CRC, Taylor & Francis Group*, 479 pp.
- Gringarten, A.C., Witherspoon, P.A., & Ohnishi, Y. (1975). Theory of heat extraction from fractured hot dry rock. *Journal of Geophysical Research*, Vol. 80, pp.1120-1124.
- Gringarten, A.C., & Sauty, J.P. (1975). A theoretical study of heat extraction from aquifers with uniform regional flow. *Journal of Geophysical Research*, Vol. 80, pp. 4956-4962.
- Guiggiani, M., Krishnasamy, G., Rudolphi, T.J., & Rizzo, F.J. (1992). A general algorithm for the numerical solution of hyper-singular boundary integral equation. *Journal of Applied Mechanics*, Vol. 59, pp. 604-614.

- Guiggiani, M. (1998). Formulation and numerical treatment of boundary integral equations with hyper-singular kernels. Chapter 3: Singular Integral in Boundary Element Methods by V. Sladek & J Sladek, *Computational Mechanics Publications*, pp.86-124.
- Gutierrez, M., & Hansteen, H. (1994). Fully coupled analysis of reservoir compaction and subsidence. *SPE-28900*, pp.1-9.
- Guzina, B. B., Pak, R.Y.S., & Castro A.E.M. (2006). Singular boundary elements for three-dimensional elasticity problems . *Engineering Analysis with Boundary Elements*, Vol. 30, pp. 623-629.
- Hartranft, R.J., and Sih, G.C. (1969). The use of eigenfunction expansions in the general solution of the three-dimensional crack problems. *Journal of Mathematics and Mechanics*, Vol. 19, pp.123-138.
- Hall, W.S. (1994). The boundary element method. *Solid Mechanics and its Applications*, Kluwer Academic Publishers, 227 pp.
- Harr, M.E. (1962). *Ground water and seepage*. McGraw-Hill, New York. 336 pp.
- Henshell, R.D., & Shaw, K.G. (1975). Crack tip elements are unnecessary. *Int. J. for Num. Methods*, Vol. 9, pp.495-509.
- Herget, G. (1988). *Stresses in rocks*. A.A. Balkema Publication, Rotterdam, Netherlands, 179 pp.
- Hongren, G. (1987). A study of propagation of hydraulic induced fracture. *PhD. Thesis*, University of Texas at Austin, 145 pp.
- Hubbert, M.K., & Willis, D.G. (1957). *Mechanics of hydraulic fracturing*. *SPE Journal*, Vol. 210, pp. 153-168.

- Hussain, M.A., Pu, S.L., & Underwood, J. (1974). Strain energy release rate for a crack under combined Mode-I and Mode-II in Fracture Analysis. *Proc. of the 1973 Nat. Symp. On fracture mechanics*, Part II, pp. 2-28.
- Jaeger, J., Cook, N.G., & Zimmerman, R., 2007. Fundamentals of rock mechanics. Wiley-Blackwill, 4th Ed., 488 pp.
- Jalali, M.S., & Dusseault, M.B.(2011). Hydro-mechanical modeling of fractures with a finite difference-displacement discontinuity method. *45th US Rock Mechanics Sym, San Francisco, CA.*, pp.1-8.
- Khristianovic, S.A., & Zheltov, Y.P. (1955). Formation of vertical fractures by means of highly viscous fluids. *Proc.of World Petroleum Congress*, Rome, pp. 579-586.
- Kolditz, O. (1995). Modeling flow and heat transfer in fractured rocks: conceptual model of a 3-d deterministic fracture network. *Geothermics*, Vol. 24, pp. 451-470.
- Kolditz, O., & Clauser, C. (1998). Numerical simulation of flow and heat transfer in fractured crystalline rocks: Application to the hot dry rock site in Rosemanowes (U.K). *Geothermics*, Vol. 27, pp.1-23.
- Kuriyagawa M., & Tenma N. (1999). Development of hot dry rock technology at the Hijiori test site. *Geothermics*, Vol. 28, pp. 627-636.
- Kutt, H.R. (1975). Quadrature formulae for finite-part integrals. *National Research Inst. for Mathematical Science*, Pretoria (South Africa), WISK 178, 156 pp.
- Kwon, Y.W., & Bang, H. (2000). *The finite element method using MATLAB*. CRC Press, 2nd Ed., 624 pp.
- Lachat, J.C., & Watson, J.O. (1976). Effective numerical treatment of boundary integral equations. *Int. J. Num. Meth. In Engineering*, Vol.10, pp. 991-1005.

- Lauwerier, H.A. (1955). The transport of heat in an oil layer caused by the injection of hot fluid. *Applied Science Research*, Vol. A5, pp. 145-150.
- Li, H., Liu, C.L., Mizuta, Y., & Kayupov, M.A. (2001). Crack edge element of three-dimensional displacement discontinuity method with boundary division into triangular leaf elements, *Commun. Numer. Meth. in Engineering*, Vol. 17, pp. 365-376.
- Liggett, J.A., & Liu, P.L. (1983). *The boundary integral equation method for porous media flow*. George Allen & Unwin (Publisher) Ltd, 253 pp.
- Love, A.E.H. (1944). *A treatise on the mathematical theory of elasticity*. Dover Publications, New York, 672 pp.
- Lowell, R.P. (1976). Comments on - Theory of heat extraction from fracture hot dry rock by A.C. Gringarten, P.A., Witherspoon, and Y., Ohnishi. *J. Geophys. Res.*, Vol. 81, pp. 359-360.
- Mack, M.G. (1992). Three dimensional dynamic displacement discontinuity: Theory and applications. *Pure and Applied Geophysics*, Vol.139, Issue 3-4, pp.763-779.
- Mi, Y. (1996). *Three-dimensional analysis of crack growth*. Computational Mechanics Publications, Southampton UK and Boston, USA, Vol.28, 1-184 pp.
- Mi, Y., & Aliabadi, M.H. (1992). Dual boundary element method for three-dimensional fracture mechanics analysis. *Engg. Anal. with Boundary Elements*, Vol. 10, pp.167-171.
- Minkowycz W.J., Sparrow E.M., & Murthy J.Y. (2006). Handbook of numerical heat transfer. *2nd Edition*, John Wiley and Sons, Inc., 968 pp.
- Mossop, A., & Segall. P. (2001). Induced seismicity in geothermal fields-I: A thermo-elastic injection model.

- Mustoe, G.G.W. (1984). Advanced integration schemes over boundary elements and volume cells for two-and three-dimensional non-linear analysis. In Banerjee P. K., Mukherjee S., Editors, *Developments in boundary element methods*, Vol. 3, pp. 213-270.
- Nasab, H.H., & Marji, M.F. (2007). Semi-infinite higher order displacement discontinuity method and its application to quasi-static analysis of radial crack produced by blasting. *J. of Mech. of Material and Structures*, Vol. 2(3), pp. 1-22.
- Nordgren, R. P. (1972). Propagation of a Vertical Hydraulic Fracture. *45th Annual Fall Meeting, SPE Journal*, pp. 306-314.
- Ogata, A., & Banks, R.B. (1961). A solution of the differential equations of longitudinal dispersion in porous media. *U.S. Geological Survey Professional paper*, 411-A.
- Orowan, E. (1952). Fundamental of brittle behavior of metals. *In Fatigue and Fracture of Metals* (Ed. W.M. Murray), New York, Wiley, pp.139-167.
- Ouyang, S., Carey, G.F., & Yew, C.H. (1997). An adaptive finite element scheme for hydraulic fracturing with proppant transport. *International Journal for Numerical Methods in Fluids*, Vol. 24. pp. 645-670.
- Pande, G.N., Beer, G., & Williams, J.R. (1990). Numerical methods in rock mechanics. West Sussex: John Wiley & Sons Ltd., 376 pp.
- Paterson, A.R. (1983). A first course in fluid Dynamics. *Cambridge University Press*, 540 pp.
- Perkins, T.K., & Kern, L.R. (1961). Widths of hydraulic fractures. *J. Pet. Tech. Trans. AIME*, Vol. 222, pp.937-949.
- Portela, A. (1992). Dual boundary element incremental analysis of crack growth. *PhD Thesis Wessex Institute of Technology*, Portsmouth University, Southampton.

- Portela, A., Aliabadi, M.H., & Rooke, D.P. (1992). The dual boundary element method: effective implementation for crack problems. *Int. J. Num. Methods in Engineering*, Vol.33, pp.1269-1287.
- Portela, A., Aliabadi, M.H., & Rooke, D.P., 1993. Dual boundary element incremental analysis of crack propagation. *Computer and Structures*, Vol. 46(2), pp.237-247.
- Prats, S. (1981). Effect of burial history on the subsurface horizontal stress of formations having different material properties. *Society of Petroleum Engineers Journal*, SPE-9017, pp.658-662.
- Press, W.H., Teukosky, S.A., Vetterling, W.T., & Flannery, B.P. (1992). Numerical Recipe in FORTRAN, the Art of Scientific Computing. 2nd Ed., Cambridge Press, 993 pp.
- Reddy, J.N., & Gartling, D.K. (1994). *The finite element in heat transfer and fluid dynamics*. CRC Press, 1-469 pp.
- Rice, J.R. (1968). *Mathematical analysis in the mechanics of fracture*. In fracture, an advance treatise, Vol.II, pp.191-311.
- Rizzo, F.J., & Shippy, D.J. (1970). A method of solution for certain problems of transient heat conduction. *AIAA Journal*, Vol. 8, pp.2004-2009.
- Rizzo, F.J., & Shippy, D.J. (1977). An advanced boundary integral equation method for three-dimensional thermo-elasticity. *Int. J. for Num. Methods in Engineering*, Vol. 11, pp.1753-1768.
- Salamon, M.D.G. (1963). Elastic analysis of displacements and stresses induced by the mining of seam or reef deposits. Part-I, *J. S. Afr. Inst. Min. Metall.*, Vol.65, pp. 319-338.
- Schmidt, D.R., & Zoback, M.D. (1989). Poro-elasticity effects the determination of minimum horizontal principal stress in hydraulic fracturing tests: A proposed breakdown equation

- employing a modified effective stress relationship for tensile failure. *Int. J. of Rock Mech. Min.Sci. and Geomech.*, Vol.26, pp.499-506.
- Sessety, V., & Ghassemi, A. (2013). Numerical simulation of sequential and simultaneous hydraulic fracturing. *Intech Open Science*, pp.1-14.
- Settari, A. (1979). Simulation of hydraulic fracturing process. *SPE Journal* 7693, pp. 487-500.
- Shah, S. (1992). Practical implementation of direct boundary element method three-dimensional stress analysis of underground excavations. *PhD Thesis, University of Toronto*, 278 pp.
- Shou, K.J., & Crouch, S.L. (1995). A higher order displacement discontinuity method for analysis of crack problems. *Int. J. Mech. Min. Sci. & Geomech.* Vol. 32, pp. 49-55.
- Sih, G.C., & Cha, B.C.k. (1974). A fracture mechanics criterion for three-dimensional crack problems. *J. of Engg. Fracture Mechanics*, Vol.6, pp.699-732.
- Skelland, A.H.P. (1967). Non-Newtonian flow and heat transfer. *Wiley Press in New York*, 469 pp.
- Sneddon, I.N. (1946). The distribution of stress in the neighborhood of a crack in an elastic solid. *Proc. Roy. Soc.*, Vol.187, pp. 229-238.
- Sneddon, I.N., & Elliot, H.A. (1946). The opening of a Griffith crack under internal pressure. *Quarterly*, Vol. 4, pp. 262-267.
- Stehfest, H. (1970). Numerical inversions of Laplace transform. *Commun. ACM* 13, pp.47-49.
- Strack, O.D.L. (1989). *Groundwater mechanics*. Prentice Hall, 732 pp.
- Sun, C.T., & Jin, Z.H. (2012). *Fracture Mechanics*. Elsevier Inc., 311 pp.
- Sutradhar A., Paulino G.H., & Gray L.J. (2002). Transient heat conduction in homogeneous and non-homogeneous materials by the Laplace transform Galerkin boundary element

- method. *Engineering Analysis with Boundary Element Methods*, Vol. 26, and pp. 119-132.
- Sutradhar A., Paulino G.H., & Gray L.J. (2008). *Symmetric Galerkin's Method* ". Springer, 276 pp.
- Snyder, M. D., & Cruse, T.A. (1975). Boundary integral equation analysis of cracked anisotropic plates. *Int. Journal of Fracture*, Vol.11, pp. 315-328.
- Tao, Q. (2010). Numerical modeling of fracture permeability change in naturally fractured reservoirs using a fully coupled displacement discontinuity method. *PhD. Thesis, Texas A & M University*, 168 pp.
- Telles, J.C.F. (1987). A self-adaptive coordinate transformation for efficient numerical evaluation of general boundary integrals. *Int. J. for Num. methods in Engineering*, Vol. 24, pp. 959-973.
- Timoshenko, S.P., & Goodier, J.N. (1982). *Theory of Elasticity*. McGraw-Hill London, 608 pp.
- Yamaguchi T. (1992). 90-day circulation test at the Hijiori HDR test site. *16th Trans. Geoth. Res. Council* , pp. 417-422.
- Yamamoto, K., Gutierrez, M., Shimamoto, T., & Maezumi, S. (2000). Verification of a 3D hydraulic fracturing model against a field study. *SPE/DOE Improved Oil Recovery Symposium, Tulsa, SPE-59373*, pp.1-12.
- Yamamoto, K., Shimamoto, T., & Sukermura, S. (2004). Multiple fracture propagation model for a three-dimensional hydraulic fracture simulator. *Int. J. Geomech*, Vol.4, pp.1-12.
- Wang, H.F., & Anderson M.P. (1982). *Introduction to groundwater modeling: Finite difference and finite element methods*. W.H. Freeman and Company, New York, 233 pp.

- Warpinski, N.R., Abou-Sayed, A.S., Moschovidis, Z. & Parker C. (1993). Hydraulic fracture model comparison study: Complete results. *Sandia National Laboratories, report no. SAND93-7042.*
- Weaver, J. (1977). Three-dimensional crack analysis. *Int. J. of Solids and Structures*, Vol.13, pp.321-330.
- Wen, P.H. (1996). Dynamic fracture mechanics: displacement discontinuity method. *Computational Mechanics Publications*, Southampton, UK & Boston, USA, Vol.29, 202 pp.
- Wiles, T.D., & Curran, J.H. (1982). A general 3-D displacement discontinuity method. *Proc. 4th Int. Conference for Num. Method in Geomech.*, pp.103-111.
- Wiles, T.D. (1986). Modeling of hydraulic fracture propagation in a discontinuous rock mass using displacement discontinuity method. *PhD. Thesis, University of Toronto*, 168 pp.
- Williams, M.L. (1957). On the stress distribution at the base of a stationary crack. *J. Applied Mech.*, Vol. 24, pp. 109-114.
- Witherspoon, P.A., Wang, J.S.Y., Iwai, K., & Gale, J.E. (1980). Validity of cubic law for fluid flow in a deformable rock fracture. *Water Resources*, 6(6), pp. 016-1024.
- Whittaker, E. (1985). *Theory and application of drilling fluid hydraulics*. Springer 1st, 213 pp.
- Wright, C.A., & Tanigawa, J.J. (1994). Real-time and post-frac 3D analysis of hydraulic fracture treatments in geothermal reservoirs. *Nineteenth workshop on geothermal reservoir engineering*, pp. 179-186.
- Valko, P., & Economides, M.J., 1989. *Hydraulic fracturing mechanics*. John Wiley & Sons Inc., New York, 298 pp.

- Vandamme, L., & Curran, J.H. (1989). A three-dimensional hydraulic fracturing simulator. *Int. J. Num. Method in Engineering*, pp. 909-927.
- Xiao, H.T., & Yue, Z.Q. (2011) .A three-dimensional displacement discontinuity method of crack problems in layered rocks. *Int. J. of Rock Mechanics and Mining Sciences*, Vol. 48, pp. 412-420.
- Yew, C.H. (1997). *Mechanics of hydraulic fracturing*. Gulf Publishing Company, Houston, Texas, 183 pp.
- Zheng, C., & Bennet, G.D. (2002). *Applied contaminant transport modeling*. 2nd Edition, John Wiley & Sons, 621 pp.
- Zhou, X., Aydin, A., Liu, F., & Pollard, D.D. (2010). Numerical modeling of secondary thermal fractures in hot dry geothermal reservoirs. *25th workshop on Geothermal Reservoir Engineering*, Stanford University, pp. 1-7.
- Zienkiewicz, O.C. (1971). *The finite element method*. McGraw-Hill, New York.
- Zienkiewicz, O.C., Taylor, R.L., & Zhu, J.Z. (2005). *The finite element method: its basis and fundamentals*. 6th Ed., Butterworth-Heinemann, 752 pp.

APPENDIX A

A 1.1. Derivatives of Function for Constant Strength 2D-DD Formulation (Crouch & Starfield, 1983):

$$f_x(x, y) = \frac{-1}{4\pi(1-\nu)} \left[y \left\{ \arctan\left(\frac{y}{x-a}\right) - \arctan\left(\frac{y}{x+a}\right) \right\} - \left[(x-a) \text{Ln}\sqrt{(x-a)^2 + y^2} + (x+a) \text{Ln}\sqrt{(x+a)^2 + y^2} \right] \right] \quad (\text{A1})$$

$$f_{,x}(x, y) = \frac{1}{4\pi(1-\nu)} \left[\text{Ln}\sqrt{(x-a)^2 + y^2} - \text{Ln}\sqrt{(x+a)^2 + y^2} \right] \quad (\text{A2})$$

$$f_{,y}(x, y) = \frac{-1}{4\pi(1-\nu)} \left[\arctan\left(\frac{y}{x-a}\right) - \arctan\left(\frac{y}{x+a}\right) \right] \quad (\text{A3})$$

$$f_{,xy}(x, y) = \frac{1}{4\pi(1-\nu)} \left[\left(\frac{y}{(x-a)^2 + y^2} \right) - \left(\frac{y}{(x+a)^2 + y^2} \right) \right] \quad (\text{A4})$$

$$f_{,xx}(x, y) = -f_{,yy}(x, y) = \frac{1}{4\pi(1-\nu)} \left[\left(\frac{x-a}{(x-a)^2 + y^2} \right) - \left(\frac{x+a}{(x+a)^2 + y^2} \right) \right] \quad (\text{A5})$$

$$f_{,xyy}(x, y) = -f_{,xxy}(x, y) = \frac{1}{4\pi(1-\nu)} \left[\left(\frac{(x-a)^2 - y^2}{\{(x-a)^2 + y^2\}^2} \right) - \left(\frac{(x+a)^2 - y^2}{\{(x+a)^2 + y^2\}^2} \right) \right] \quad (\text{A6})$$

$$f_{,yyy}(x, y) = -f_{,xyy}(x, y) = \frac{2y}{4\pi(1-\nu)} \left[\left(\frac{x-a}{\{(x-a)^2 + y^2\}^2} \right) - \left(\frac{x+a}{\{(x+a)^2 + y^2\}^2} \right) \right] \quad (\text{A7})$$

APPENDIX B

B 1.1. Taylor's Series Expansion for 3D Elasticity Problems (Guiggiani, 1998)

1. Derivatives of the distance between the source and field points

$$x_i - y_i = \left[\frac{\partial x_i}{\partial \xi} \Big|_{(\xi_0, \eta_0)} (\xi - \xi_0) + \frac{\partial x_i}{\partial \eta} \Big|_{(\xi_0, \eta_0)} (\eta - \eta_0) \right] + \left[\frac{\partial^2 x_i}{\partial \xi^2} \Big|_{(\xi_0, \eta_0)} \frac{(\xi - \xi_0)^2}{2} + \frac{\partial^2 x_i}{\partial \xi \partial \eta} \Big|_{(\xi_0, \eta_0)} (\xi - \xi_0)(\eta - \eta_0) + \frac{\partial^2 x_i}{\partial \eta^2} \Big|_{(\xi_0, \eta_0)} \frac{(\eta - \eta_0)^2}{2} \right] \quad (\text{B1})$$

In terms of polar coordinates, the distance vector is given as:

$$x_i - y_i = \rho \left[\frac{\partial x_i}{\partial \xi} \Big|_{(\xi_0, \eta_0)} \cos \theta + \frac{\partial x_i}{\partial \eta} \Big|_{(\xi_0, \eta_0)} \sin \theta \right] + \rho^2 \left[\frac{\partial^2 x_i}{\partial \xi^2} \Big|_{(\xi_0, \eta_0)} \frac{\cos^2 \theta}{2} + \frac{\partial^2 x_i}{\partial \xi \partial \eta} \Big|_{(\xi_0, \eta_0)} \cos \theta \sin \theta + \frac{\partial^2 x_i}{\partial \eta^2} \Big|_{(\xi_0, \eta_0)} \frac{\sin^2 \theta}{2} \right] \quad (\text{B2})$$

Or

$$x_i - y_i = \rho A_i(\theta) + \rho^2 B_i(\theta) + O(\rho^3) \quad (\text{B3})$$

where $A_i(\theta)$ and $B_i(\theta)$ are the simple trigonometric functions.

Distance derivatives can be given as:

$$R_{,i} = \frac{A_i}{A} + \rho \left(\frac{B_i}{A} - A_i \frac{C}{A^3} \right) + O(\rho^2) \quad (\text{B4})$$

where

$$A(\theta) = \left\{ \sum_{k=1}^3 [A_k(\theta)]^2 \right\}^{1/3} > 0 \quad (\text{B5})$$

$$C(\theta) = \sum_{k=1}^3 A_k(\theta) B_k(\theta)$$

The distance in polar coordinates is given as:

$$\frac{1}{R^3} = \frac{1}{\rho A} - \frac{3C}{\rho^2 A^5} + O\left(\frac{1}{\rho}\right) \quad (\text{B6})$$

2. Derivatives of Jacobian function

$$J_h = J_h(\xi_0, \eta_0) + \rho \left[\frac{\partial J_h}{\partial \xi} \Big|_{(\xi_0, \eta_0)} \cos \theta + \frac{\partial J_h}{\partial \eta} \Big|_{(\xi_0, \eta_0)} \sin \theta \right] + o(\rho^2) \quad (\text{B7a})$$

$$J_h = J_{h0} + \rho J_{h1}(\theta) + o(\rho^2) \quad (\text{B7b})$$

3. Derivatives of shape functions

$$\phi^a = \phi^a(\xi_0, \eta_0) + \rho \left[\frac{\partial \phi^a}{\partial \xi} \Big|_{(\xi_0, \eta_0)} \cos \theta + \frac{\partial \phi^a}{\partial \eta} \Big|_{(\xi_0, \eta_0)} \sin \theta \right] + o(\rho^2) \quad (\text{B8a})$$

$$\phi^a = \phi_0^c + \rho \phi_1^c(\theta) + o(\rho^2) \quad (\text{B8b})$$

4. Radius of neighborhood of the singular node

$$\varepsilon = \rho A(\theta) + \rho^2 \frac{C(\theta)}{A(\theta)} + O(\rho^3) \quad (\text{B9a})$$

$$\rho = \alpha(\varepsilon, \theta) = \frac{\varepsilon}{A(\theta)} - \varepsilon^2 \frac{C(\theta)}{A^4(\theta)} + O(\varepsilon^3) \quad (\text{B9b})$$

$$\rho = \alpha(\varepsilon, \theta) = \varepsilon \beta(\theta) + \varepsilon^2 \gamma(\theta) + O(\varepsilon^3) \quad (\text{B9c})$$

where ,

$$\beta(\theta) = \frac{1}{A(\theta)} \quad ; \quad \gamma(\theta) = -\frac{C(\theta)}{A^4(\theta)}$$

B 1.2. Functions for Singularity Subtraction

Considering, the hyper-singular integrands as:

$$F_{ijk}(\rho, \theta) = V_{ijk} \phi^a J \rho = \frac{1}{R^3} Q_{ijk} \phi^a J \rho \quad (\text{B10})$$

Substituting, first two terms form Eqs. (B6), (B7b), and (B8b) in above equation results as:

$$F_{ijk}(\rho, \theta) = \rho Q_{ijk} \left(\frac{1}{\rho A} - \frac{3C}{\rho^2 A^5} + O\left(\frac{1}{\rho}\right) \right) \cdot (J_{h0} + \rho J_{h1}(\theta) + o(\rho^2)) \cdot (\phi_0^c + \rho \phi_1^c(\theta) + o(\rho^2)) \quad (\text{B11})$$

Collection of constant terms and terms of ρ is the above equation results as given below:

$$S_{-2}(\rho, \theta) = \left[\frac{J_{h0} \phi_0^c}{A} \right] \quad (\text{B12a})$$

$$S_{-1}(\rho, \theta) = \left[-\frac{3C}{A^5} (J_{h1}(\theta) \phi_0^c + J_{h0} \phi_1^c(\theta)) \right] \quad (\text{B12b})$$

The above terms with coefficients in Eq. (B9c) provides required terms in the Taylor's series expansion for the hyper-singular evaluation.

B 1.3. Semi-Analytical Treatment

As from Eq. (3.71), the first term becomes regular which can be estimated using standard Gauss quadrature; however, the second and third terms are still singular which needs special treatment. A semi-analytical scheme as developed by Guiggiani et al. (1992) is presented in this section.

Case (1): Considering Eq. (3.71b) as:

$$I_{-1} = \lim_{\varepsilon \rightarrow 0} \int_0^{2\pi} \int_{\alpha(\varepsilon, \theta)}^{R(\theta)} \frac{F_{-1}(\theta)}{\rho} d\rho d\theta \quad (\text{B13})$$

Integrating above equation analytically with respect to ρ results as follows:

$$= \lim_{\varepsilon \rightarrow 0} \int_0^{2\pi} F_{-1}(\theta) [\ln |R(\theta)| - \ln |\alpha(\varepsilon, \theta)|] d\theta \quad (\text{B14})$$

Using Eq.(3.69), the above equation can be written as:

$$= \int_0^{2\pi} F_{-1}(\theta) \ln |R(\theta)| d\theta - \lim_{\varepsilon \rightarrow 0} \int_0^{2\pi} F_{-1}(\theta) \ln |\varepsilon \beta(\theta)| d\theta \quad (\text{B15})$$

Or,

$$= \int_0^{2\pi} F_{-1}(\theta) \ln \left| \frac{R(\theta)}{\beta(\theta)} \right| d\theta - \lim_{\varepsilon \rightarrow 0} \left\{ \ln \varepsilon \int_0^{2\pi} F_{-1}(\theta) d\theta \right\} \quad (\text{B16})$$

For a singular point inside the element, considering:

$$\int_0^{2\pi} F_{-1}(\theta) d\theta = 0 \quad (\text{B17})$$

Substituting, the above equation in Eq.(B16), the I_{-1} can be given as:

$$I_{-1} = \int_0^{2\pi} F_{-1}(\theta) \ln \left| \frac{R(\theta)}{\beta(\theta)} \right| d\theta \quad (\text{B18})$$

This equation is only function of θ , which can be evaluated using one-dimensional Gaussian quadrature.

Case (2): Considering Eq. (3.71c) as:

$$I_{-2} = \lim_{\varepsilon \rightarrow 0} \left\{ \int_0^{2\pi} \int_{\alpha(\varepsilon, \theta)}^{R(\theta)} \frac{F_{-2}(\theta)}{\rho^2} d\rho d\theta + \phi^a(\xi^c, \eta^c) \frac{b_{ijk}(\mathbf{x})}{\varepsilon} \right\} \quad (\text{B19})$$

Integrating above equation analytically with respect to ρ results as follows:

$$= \lim_{\varepsilon \rightarrow 0} \left\{ \int_0^{2\pi} F_{-2}(\theta) \left[-\frac{1}{R(\theta)} + \frac{1}{\alpha(\varepsilon, \theta)} \right] d\theta + \phi^a(\xi^c, \eta^c) \frac{b_{ijk}(\mathbf{x})}{\varepsilon} \right\} \quad (\text{B20})$$

Using Eq.(3.69), the above equation can be written as:

$$= \lim_{\varepsilon \rightarrow 0} \left\{ \int_0^{2\pi} \frac{F_{-2}(\theta)}{\varepsilon \beta(\theta)} \left[1 - \varepsilon \frac{\gamma(\theta)}{\beta(\theta)} \right] d\theta + \phi^a(\xi^c, \eta^c) \frac{b_{ijk}(\mathbf{x})}{\varepsilon} \right\} - \int_0^{2\pi} \frac{F_{-2}(\theta)}{R(\theta)} d\theta \quad (\text{B21})$$

Rearranging the terms, results as:

$$= \lim_{\varepsilon \rightarrow 0} \left(\frac{1}{\varepsilon} \right) \left\{ \int_0^{2\pi} \frac{F_{-2}(\theta)}{\beta(\theta)} d\theta + \phi^a(\xi^c, \eta^c) \frac{b_{ijk}(\mathbf{x})}{\varepsilon} \right\} - \int_0^{2\pi} F_{-2}(\theta) \left[\frac{\gamma(\theta)}{\beta^2(\theta)} + \frac{1}{R(\theta)} \right] d\theta \quad (\text{B22})$$

Taking the limits of above equation and assuming:

$$\int_0^{2\pi} \frac{F_{-2}(\theta)}{\beta(\theta)} d\theta + \phi^a(\xi^c, \eta^c) \frac{b_{ijk}(\mathbf{x})}{\varepsilon} = 0 \quad (\text{B23})$$

Substituting, the above equation in Eq.(B23), the I_{-2} can be given as:

$$I_{-2} = -\int_0^{2\pi} F_{-2}(\Theta) \left[\frac{\gamma(\Theta)}{\beta^2(\Theta)} + \frac{1}{R(\Theta)} \right] d\Theta \quad (\text{B24})$$

This equation is also only function of θ , which can be evaluated using one-dimensional Gaussian quadrature.